University of Strathclyde

Biomolecular and Chemical Physics (Photophysics)

SURFACE-ENHANCED RAMAN SCATTERING OF METAL NANOPARTICLE ASSEMBLY IN AGAROSE AND HIGHLY ORDERED METAL NANOROD ARRAYS

MARTIN KEATING

A thesis presented in fulfilment of the requirements for the degree of Doctor of Philosophy to the University of Strathclyde,

Department of Physics

2015

This thesis is the result of the author's original research. It has been composed by the author and has not been previously submitted for examination which has led to the award of a degree.

Signed:

Martin Keating

Date:

Previously-published-work statement

I confirm that parts of this PhD thesis, "Surface-enhanced Raman scattering of metal nanoparticle-agarose and highly ordered metal nanorod arrays fabricated by guided oblique angle deposition", are derived from the following published papers:

Paper 1: M. Keating, S. Song, G. Wei, D. Graham, Y. Chen, and F. Placido, "Ordered silver and copper nanorod arrays for enhanced Raman scattering created via guided oblique angle deposition on polymer," *J. Phys. Chem. C*, vol. 118, no. 9, pp. 4878–4884, 2014.

Paper 2: M. Keating, Y. Chen, I. A. Larmour, K. Faulds, and D. Graham, "Growth and surface-enhanced Raman scattering of Ag nanoparticle assembly in agarose gel," *Meas. Sci. Technol.*, vol. 23, no. 8, p. 084006, 2012.

Paper 3: S. Song, M. Keating, Y. Chen, and F. Placido, "Reflectance and surface enhanced Raman scattering (SERS) of sculptured silver films deposited at various vapor incident angles", *Meas. Sci. Technol.*, vol. 23, no. 8, p. 084007, 2012.

Section 2.3 in the thesis, "Growth and surface-enhanced Raman scattering of Ag nanoparticle assembly in agarose gel", pages 69-87, is based on Paper 2, for which I conducted all research and created all non-cited graphics, save the TEM images which are courtesy of Mr Colin How, School of Physics and Astronomy, University of Glasgow.

Section 5.1 in the thesis, "Varying the deposition angle of Ag nanorods on silicon: the link between film porosity, surface roughness and SERS", pages 160-171, is based on Paper 3, for which I conducted the SERS experiment and SERS data analysis. All other research, including production and reflectance analysis of Ag film samples, and all non-cited graphics (excepting figure 5.4 which was created by me), are courtesy of Dr Shigeng Song, Thin Film Centre (TFC), University of the West of Scotland (UWS).

Section 5.2 in the thesis, "Ordered silver and copper nanorod arrays for enhanced Raman scattering created via guided oblique angle deposition on polymer", pages 171-198, is based on Paper 1, for which I, in collaboration with Dr Shigeng Song (TFC,UWS), conducted most of the SERS experimental work. Dr Song contributed to the SERS experiments and was ultimately responsible for supplying all Ag and Cu nanorod array samples, as well as SEM imaging of the same. Figures 5.8 (b), 5.10, and 5.22 (a), are all courtesy of Dr Song. Mr Guoke Wei, Photophysics, University of Strathclyde, conducted all nanorods simulation work, and figures 5.9, 5.16, 5.17, 5.18, 5.19, 5.21, and 5.24 are all courtesy of Mr Wei. All other non-cited graphics are by me.

All remaining research and non-cited graphics derived from such were produced by me.

Signed:

Martin Keating

Date:

To Mum, Dad, Johanna, Louise and Rosalyn, for their love, support and generosity

Acknowledgements

My profound thanks goes to my first supervisor Dr Yu Chen, from the Photophysics group at the University of Strathclyde, for her guidance, patience and support over the course of my PhD. Our many discussions on how to approach different aspects of my work were illuminating and helped shape my research for the better. Likewise, I am very grateful to my second supervisor, Prof Duncan Graham and his colleague Dr Karen Faulds, both from the Centre for Nanometrology, the University of Strathclyde, who made many very helpful suggestions regarding my approach to SERS spectroscopy.

A considerable debt of gratitude is owed to Prof Frank Placido, and his colleague Dr Shigeng Song, both from the Thin Film Centre (TFC), University of the West of Scotland, for their including me at every level of the nanorods project. Dr Song worked with me several times on a one-to-one basis, allowing me to benefit immensely from his considerable knowledge and experience. Thanks must also go to technician Mr Andrew Bunyan, for fabrication of the metal nanorod samples, and Dr Liz Porteous for SEM imaging of the same, both also from the TFC.

I am indebted to my co-student, Mr Guoke Wei from the Photophysics group at the University of Strathclyde, for his painstaking nanorods simulations work which forms an important part of this thesis, and to Prof David Birch, Dr Jens Sutter and Dr Olaf Rolinski, all from Photophysics, who offered helpful and constructive feedback on regular oral presentations of my research. Thanks also to technicians Mr John Revie and Mr Bob Dawson, for their valuable assistance in several practical aspects of the work. I am very grateful to anyone else who has assisted me in any way over the past few years.

Heartfelt thanks goes to my close friend Gayle who regularly gave me indispensable advice, support and encouragement. I also warmly thank my close friend Audrey for her kindness and encouragement throughout and am particularly thankful to both of my friends for their much-needed and timely support at the end of my PhD. Finally, my sincere thanks goes to my family; to my parents Henry and Teresa and to my sisters Johanna, Louise and Rosalyn, all of whom were a huge support throughout my studies and beyond. Words cannot convey my appreciation for all they have done and continue to do, especially my mother and father. I am always grateful.

This research is generously supported by an Engineering and Physical Sciences Research Council (EPSRC) Doctoral Training Grant.

Abstract

This thesis examines metal nanoparticle/agarose (MNPA) gel composites and highly ordered metal nanorod arrays, fabricated by guided nucleation during oblique angle deposition (OAD), as surface-enhanced Raman scattering (SERS) substrates. The effectiveness of MNPA has been effectively demonstrated previously using silver nanoparticles (AgNPs), but it is poorly understood how different NP growth conditions affect the SERS response.

SERS intensity of gold and silver NPA is examined in detail as a function of salt and (by default) reducing solution concentration, and the effect of using different reductants is also investigated; reproducibility of selected gels is carefully explored. In addition, SERS of highly ordered Ag and copper (Cu) nanoarrays is examined in depth.

Normally, OAD generates a random nanorod distribution on flat supports, where nucleation is a random process. This however hinders the control of geometrical parameters such as rod separation and diameter which directly affect the SERS response, an effect mitigated by introducing a guiding element to influence nucleation. Until recently, only semiordered SERS-active Ag nanorod arrays had been accomplished by OAD. These however depended on time-consuming and expensive electron beam lithography (EBL) to write a template to guide nucleation and the subsequent growth of nanorods. Importantly, lengthy fabrication times force a practical upper size limit on the substrate, meaning it is exceedingly small which drastically reduces its potential for sensing applications. It also severely restricts the number of substrates which can be produced in a given time.

This thesis addresses these issues via the construction of highly ordered, SERS-active, large-area Ag and Cu nanorod arrays, using a cheap, large-scale, nano-imprinted polymer template to influence nucleation during the initial stages of OAD. Moreover, OAD is a high throughput method, as it permits the simultaneous fabrication of several substrates during a relatively short deposition cycle.

Contents

Table of abbreviations

%RSD	percentage relative standard deviation
Ag	silver
$AgNO_3$	silver nitrate
AgNP	silver nanoparticle
Au	gold
AuNP	gold nanoparticle
CRSC	citrate-reduced silver colloid
Cu	copper
CuNP	copper nanoparticle
DDA	discrete dipole approximation
EBL	electron beam lithography
EM	electromagnetic
H	hydroxylamine
HH	hydroxylamine hydrochloride
HR	hydroxylamine-reduced
MNP(A)	metal nanoparticle (agarose)
$NaBH_4$	sodium borohydride
NIL	nanoimprint lithography
NP	nanoparticle
OAD	oblique angle deposition
RSE	relative standard error
SB	sodium borohydride
SBR	sodium borohydride-reduced
SEM	scattering electron micrograph/microscopy
SERRS	surface-enhanced resonant Raman scattering
SERS	surface-enhanced Raman scattering
TEM	transmission electron micrograph/microscopy

List of tables

List of figures

Chapter 1 General introduction

1.1 Background and motivation for the thesis

It is remarkable that as SERS comes of age, the challenges, which until relatively recently prevented its widespread adoption in applications, have been largely overcome. Problems such as an incomplete understanding of the theory, and obtaining reliable and reproducible measurements, previously conspired to hinder SERS in becoming a comprehensively used scientific technique. Given the impressive progress made on these fronts, it might be expected that the desire for novel substrates has quietened in recent years, but evidently, the opposite is true. In contrast, there has been an explosion in the literature during the last decade concerning novel, nanostructured materials which maximise signal strength without sacrificing reproducibility. This seemingly endless demand emanates in part from experimental requirements, and overall from the continuing quest for improved SERS sensitivity, reproducibility and inter-batch repeatability. In SERS, "one size" most certainly does not fit all.

Two SERS substrates which have garnered a lot of interest within the last decade are metal nanoparticle agarose (MNPA) and metal nanorod arrays created via oblique angle deposition (OAD). In MNPA, particularly Ag-agarose gel, the porous structure permits silver nanoparticles (AgNPs) to form *in situ* inside nano-sized pores within the agarose matrix. AgNPs are naturally situated close enough to one another to facilitate coupling of localised surface plasmons, thus dispensing with the need for aggregating agents to engage SERS activity which can potentially alter the analyte spectrum. Moreover, the matrix constrains the nanoparticles, hindering aggregation

so that capping agents are not required which might otherwise seriously interfere with molecular adsorption on the nanoparticle surface. In such a substrate, analytes with a low affinity for noble metals can be mechanically trapped in the vicinity of the NPs during shrinkage of the matrix either by physical or chemical means, thus permitting detection of substances previously impenetrable using SERS.

However, the influence of nanoparticle growth conditions, in aqueous solution, on Ag-agarose structure and the associated SERS response is not clear. If the gel is to find eventual utility in applications therefore, it is first necessary to examine how these parameters affect the SERS response. This thesis investigates the impact of different growth conditions on nanoparticle morphology, gel homogeneity, SERS signal intensity and reproducibility.

The second group of substrates – metal nanorod arrays fabricated using OAD, and their success as SERS substrates, is well documented. Diameter and gap size however, two geometrical parameters which crucially affect the SERS response, are difficult to control, as nucleation is a random process on flat, blank supports, meaning the resultant nanorods are randomly distributed. One way to mitigate this effect is to introduce a template to guide nucleation during the initial stages, with a view to creating a high-order rod structure. Up until recently however, only semiordered Ag nanorods arrays had been realised for SERS using OAD, a disappointing result further compounded by the microscopic substrate size, constrained by the practical limits inherent to the electron beam lithography (EBL) technology used to write such a template. In other words, EBL is not appropriate as part of a large-scale, high-throughput sensor fabrication process. This thesis investigates the use of large-scale, pre-patterned polymer as a template to tightly

control nucleation and, in turn, the subsequent growth of Ag (and Cu) nanorods during OAD, to construct large-scale, highly ordered SERS-active nanorod arrays.

1.2 Structure of the thesis

This chapter serves as a general introduction to the thesis; it discusses the theory of molecular vibration and how the interplay between it and incident light is responsible for the Raman Effect – an inelastic scattering process where scattered photons gain or lose a portion of energy exactly matching that of a specific molecular vibrational mode. The Raman/SERS spectrum is introduced which comprises peaks, also known as "bands", at different intensities corresponding to specific vibrational modes, the combination of which forms a unique SERS profile. A classical mathematical model of Raman scattering is presented, after which SERS enhancement mechanisms are discussed which act to amplify the desperately weak Raman signal, allowing probe molecules at very low concentrations to be studied.

Coupled localised surface plasmons are then explored, as these are crucial for the most important enhancement mechanism in SERS, namely electromagnetic enhancement. The single molecule enhancement factor or the E^4 approximation (probably the most important equation in SERS) arising from electromagnetic enhancement is covered and the dielectric function of metals is derived; this function is intimately linked with the ability of a metal nanoparticle to magnify an incident alternating electric field, crucial for SERS.

Aqueous-solution-based nucleation and nanoparticle growth are then considered in depth towards the end of the chapter, providing the theoretical

background for Ag- and Au-agarose SERS substrate fabrication discussed in chapters two to four.

Chapter two begins with a general review of SERS substrates, and focusses on results for Ag-agarose. The ability of the substrate to qualitatively detect various probes is investigated and the effect of varying the growth conditions of the metal/gel nanocomposite with regard to SERS signal strength and reproducibility is examined.

A review of metal/gel nanocomposites is included in chapter three, to present MNPA in this context. The review refocusses on MNPA, which is highly pertinent to this thesis, concentrating on its applicability to SERS. SERS of gels formed using sodium borohydride and hydroxylamine (an adapted method for salt-gel reduction), is compared. The importance of characterising any substrate in terms of SERS before addition of the analyte is highlighted; this helps to avoid potential confusion during data analysis caused by distortion to an analyte spectrum arising from a poor choice of aggregating agent – something that is not an issue for the substrates in this thesis which do not rely on such an agent to engage SERS activity.

Chapter four is an extension of chapter three, in that SERS of gels formed exclusively by hydroxylamine reduction is examined. Some samples with the best reproducibility are investigated further in depth using Raman mapping to obtain a more accurate view of gel uniformity.

Chapter five deals with the manufacture of metal nanorod arrays using OAD and their role as SERS substrates. It begins by investigating the relationship between film surface roughness, porosity and the associated SERS response before examining SERS of highly ordered silver and copper arrays, formed on pre-patterned polymer templates. The SERS response of Ag nanorod arrays of various structures is

investigated alongside results obtained from discrete dipole approximation simulations.

Finally, chapter six gives a summarisation of and conclusion to the thesis and outlines possible future work regarding MNPA and ordered OAD nanorod arrays as SERS substrates.

1.3 Surface-enhanced Raman scattering (SERS): origins and theory

1.3.1 Vibrational spectroscopy

Over the last hundred years or so, science has continuously exploited the interaction between electromagnetic radiation (light) and matter, to probe at the deepest level the stuff from which we, our world, and ultimately the Universe are made. Whether they interact with a sample in the laboratory or objects strewn throughout the vastness of space, photons help unlock Nature's secrets via this crucial interaction, without which we would metaphorically and literally be left in the dark.

At the smaller end of the scale, several disciplines have proven critical to our understanding of molecular structure and dynamics. Vibrational spectroscopy in particular, which encompasses principal techniques such as mid-infrared (IR), near-IR, and Raman spectroscopy, has yielded an abundance of information in this regard. Both Raman and mid-IR spectroscopy generate spectra from specific fundamental molecular vibrations, while near-IR spectroscopy measures the higher frequency mode combination and overtone bands of certain fundamental vibrations –

fundamental, combination and overtone bands in the context of Raman scattering or more accurately SERS, are discussed later in this chapter [1].

Mid-IR and Raman spectroscopy are complementary in nature, and in most cases, both are required to completely ascertain the vibrational modes of a molecule. However, the two techniques emerge from different selection rules and processes. IR spectroscopy for example, tends to be best-suited to the study of asymmetric vibrations of polar groups, where incident radiation of a specific energy is absorbed, inducing a transition (identical in energy) between molecular vibrational energy levels and a change in the dipole moment of the polar molecule – the latter being a prerequisite for a mode to be IR-active. This process involves *absorption* of photons, in contrast with Raman spectroscopy on the other hand which is best-suited to the study of symmetric vibrations of groups which are non-polar, where photons are Raman-*scattered* [1].

In Raman scattering, a photon imparts a fraction of its energy to or subtracts it from a molecular vibrational mode, generating a Stokes or anti-Stokes shift in frequency respectively, and so is inelastically scattered. The Stokes shift lines are much more intense [2] (which will be explained later) and the change in polarisability along a specific vibrating molecular bond must be non-zero for that bond, and by extension, those bonds comprising a specific vibrational mode, to be Raman-active [1].

A simple way to picture molecular vibration which gives rise to the characteristic bands in Raman spectra, is by use of a mechanical model such as the simple harmonic oscillator in figure 1.1, which represents a simple heteronuclear

diatomic molecule with the molecular bond depicted by a spring. Both atoms with masses $m_1 < m_2$, oscillate at the same frequency towards and away from a common centre of mass represented by the dotted line. The spring incorporates mutual repulsion between positive nuclei as the atoms move closer to one another (the nuclei cannot touch each other) plus an attractive restoring force between the nucleus of one atom and the electrons of the other as the atoms move further apart.

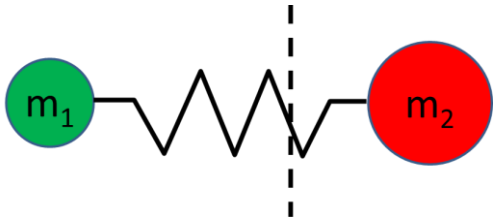

Figure 1.1. A heteronuclear diatomic molecular model.

For simplification, the masses can be combined to form a reduced mass $\mu = m_1 m_2 / (m_1 + m_2)$ so that now the molecular bond can be modelled as in figure 1.2.

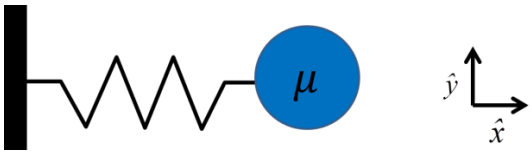

Figure 1.2. Reduced mass representation of a heteronuclear diatomic molecule.

The magnitude of force on μ directed along the x-axis as the bond stretches and contracts is given by $F = -kx$, where k is the spring constant, with the equilibrium

position of μ situated at the origin for convenience. The classical vibrational frequency for the diatomic molecule is [1]:

$$\nu_{vib} = (1/2\pi)\sqrt{k/\mu} \tag{1.1}$$

Eq. (1.1) shows explicitly that the vibrational frequency of a molecular bond is intimately related to both the masses of the atoms in the molecule (μ) and the strength of the molecular bond (k). In vibrational spectroscopy, wavenumber units, $\bar{\nu}_{vib}$ are more commonly used and Eq. (1.1) becomes [1]:

$$\bar{\nu}_{vib} = (1/2\pi c)\sqrt{k/\mu} \tag{1.2}$$

where $\bar{\nu}_{vib}$ is in waves per centimetre and the speed of light *c* is in cm s^{-1}.

It is precisely because the Raman Effect is a *scattering* rather than an *absorption* phenomenon that it is possible for a fraction of photon energy to be relinquished to the vibrating molecular mode, as opposed to all or none, befitting a specific electronic transition (absorption). However, there exists a resonance effect known as 'resonant Raman scattering' (RRS), where the energy exchange is a substantial fraction of the total photon energy due to an overlap between the excitation wavelength of the laser and an electronic transition of the probe molecule under observation [3]. RRS in addition to the phenomenon known as "surface-enhanced Raman scattering" (SERS), as well as the two combined, "surface-enhanced resonant Raman scattering" (SERRS), are all used in experiments and applications to massively increase the magnitude of the Raman signal which happens

to be exceptionally weak. This thesis discusses several fabricated structures which give rise to the SERS effect.

1.3.2 Vibrational energy levels in molecules

The way in which light interacts with molecules is chiefly determined by the energy levels of the degrees of freedom of the molecule, which can either be linked to the motion of atoms within the molecule (translational, rotational, or vibrational energy levels) or motion of the electrons (electronic energy levels, perhaps further characterised by their spin) [4]. Molecular motion arising from specific vibrations depends upon the internal degrees of freedom N of the molecule, given by the rules of thumb: $N = 3n - 6$ and $N = 3n - 5$ for non-linear and linear molecules respectively where n is the number of atoms, with each atom possessing three degrees of freedom [1]. An easy way to visualise the energy levels in a molecule is by use of a Jablonski diagram as in figure 1.3 (adapted from [5]); the diagram represents some possible energy states of a molecule.

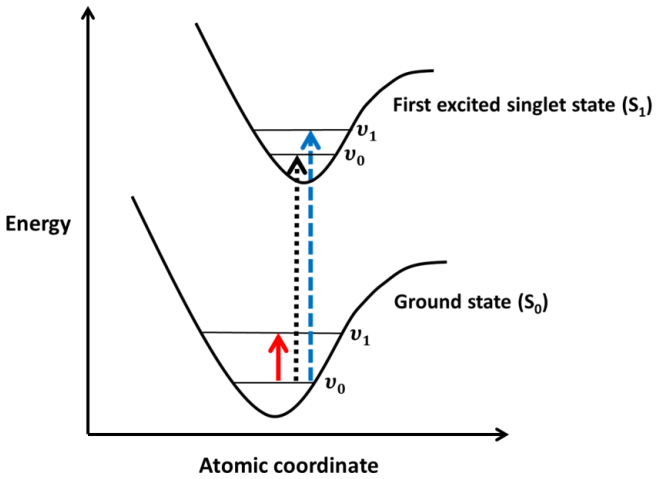

Figure 1.3. Jablonski diagram illustrating electronic and vibrational energy levels, adapted from [5].

Electronic states (the highest-energy motional states), S_0 (the ground state) and S_1 (the first excited state), are shown as bold curves and are a function of atomic coordinates (internuclear distance in the case of a diatomic molecule). Within the electronic states, and represented by thin horizontal lines are the vibrational states, v_0 and v_1 which are much lower in energy. Only two electronic and vibrational states are shown for clarity in figure 1.3, but higher energy states obviously exist for each. Superimposed on the vibrational states, but not shown, are the rotational states which are the least energetic and arise from molecular rotation.

Several molecular energy transitions are allowed [4], [5], but for the sake of simplicity only photon *absorption* is considered here. For a given electronic state, a fundamental vibration is excited when one relatively low-energy photon (in the infrared for example) is absorbed by the molecule, raising the vibrational energy from v_0 to v_1, with the difference in energy exactly matching that of the absorbed photon, represented here by the "solid red arrow" transition in the ground state in figure 1.3. A purely electronic transition takes place if, for example, there is an energy increase from v_0 in S_0 to v_0 in S_1 (represented by the black dotted arrow), while a vibrational coupled with an electronic transition takes place if, for example, there is an increase from v_0 in S_0 to v_1 in S_1 (represented by the blue dashed arrow). The rotational states, which are not shown, are of course also involved in these transitions. Despite recognition of three distinct energy states, the distinction is slightly superficial in that the vibrational and rotational states are weakly coupled to the electronic states [6].

1.3.3 The discovery of the Raman Effect

In 1925, Smekal theoretically predicted frequency-shifted lines in the spectrum of scattered light, which were first observed in 1928 by Sir Chandrasekhara Venkata Raman. The frequency shifts in relation to the excitation source, in this case natural light, corresponded to the vibrational and rotational frequencies of the scattering molecules and were independent of the excitation frequency, being instead a unique property of the scattering molecules themselves [2]. This phenomenon, which would later become known as the Raman Effect, forms the basis of all forms of Raman spectroscopy.

1.3.4 Raman instrumentation

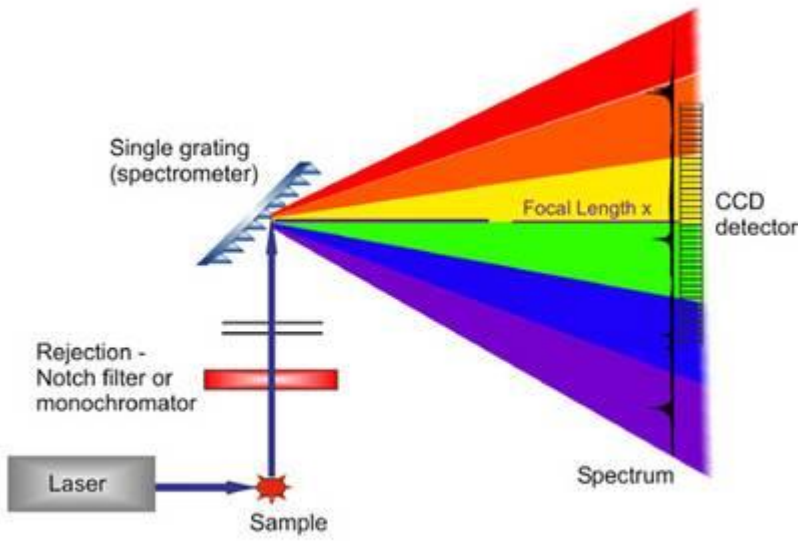

Figure 1.4. A schematic of a Raman spectrometer from [7].

Figure 1.4 shows a schematic of a Raman spectrometer. In this work, the monochromatic laser beam is focussed onto the sample by a microscope objective,

and is 180° back-scattered and collected by the same objective, illustrated separately in figure 1.5.

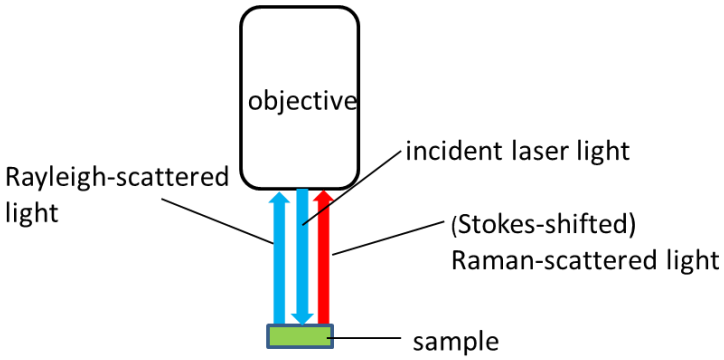

Figure 1.5. Raman excitation and collection in a 180° back-scattering configuration.

The coloured arrows in figure 1.5 have been used to emphasise the shift in frequency from Rayleigh to Raman-scattered light, although the frequency shift would of course be significantly less than that corresponding to a colour change from blue to red. Such a shift would necessitate an electronic transition rather than merely a change in vibrational energy. Additionally, it should be remembered that scattering occurs in random directions, which has been omitted in the diagram for convenience.

In figure 1.4, laser light strikes the sample, after which Rayleigh and Raman-scattered light is directed through a filter to reject almost all of the Rayleigh portion (which would otherwise swamp the signal) and to allow chiefly the Raman-scattered light access to a diffraction grating. The frequency-shifted light is now separated by the grating into its constituent frequencies and absorbed by a charge-coupled device which records the different intensities, creating a Raman spectrum.

1.3.5 The Raman spectrum

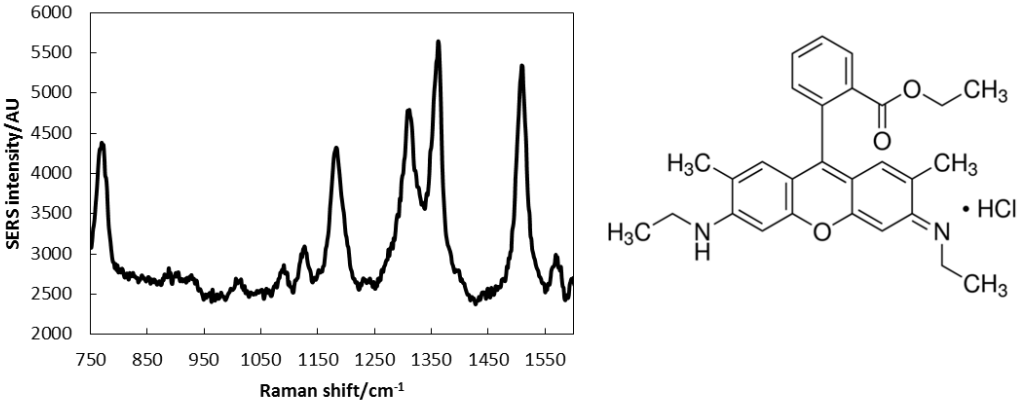

Figure 1.6. Left: SERS spectrum of 10^{-5} M rhodamine 6G in Ag-agarose gel at 633 nm excitation, taken over 1s at approximately 1 mW power. Right: molecular structure of R6G [8].

The (surface-enhanced) Raman spectrum of a common SERS probe molecule, rhodamine 6G (R6G) is shown in figure 1.6. As mentioned earlier, the Raman signal happens to be extremely weak, but it can thankfully be magnified by many orders of magnitude by the agency of metal nanoparticles, a phenomenon known as electromagnetic (EM) enhancement which generates a so-called SERS spectrum. Peaks, also known as "bands", in the spectrum correspond to specific vibrational modes, the combination of which forms a unique R6G SERS profile, or a molecular fingerprint. The main peaks at 770, 1188, 1312, 1362 and 1503 cm^{-1} in the spectrum are the most prominent, matching those in the literature. 770 and 1188 cm^{-1} correspond to the C – H out-of-plane bend and C – C stretching modes respectively, while 1312, 1362 and 1503 cm^{-1} correspond to the symmetric in-plane C – C stretching modes [9]. Bands in the SERS spectrum may be slightly shifted with respect to the normal Raman spectrum due to the molecule being adsorbed onto the metal NP surface, causing small alterations in normal vibrational energy transitions.

The SERS substrate used to create the R6G spectrum in figure 1.6 is Ag nanoparticle agarose gel, the production and SERS characteristics of which will be described in detail later in chapter two. Briefly, AgNPs are embedded in an agarose gel matrix. The metal-gel composite is immersed in the R6G solution prior to SERS analysis, permitting the adsorption of R6G molecules onto AgNP surfaces. After removal from the solution, the R6G@AgNP-agarose undergoes SERS analysis, delivering a vastly-enhanced Raman signal of R6G.

The *x*-axis in figure 1.6, labelled "Raman shift" (measured in wavenumber units of cm^{-1}), corresponds to the difference between the laser excitation wavenumber and the vibrational mode wavenumber. A spectrum can go from negative values (anti-Stokes, not shown), where laser photons gain energy from vibrational modes, through zero, which is the laser line and has a Raman shift of zero, to positive values where laser photons relinquish portions of energy to specific vibrational modes. The further from zero a peak is on either side, the more energetic the mode, but, as shall be explained later, the anti-Stokes lines (negative *x*-axis) are always much less intense than the Stokes lines, even though one set is a mirror image of the other. For example, an anti-stokes shift of say negative 1200 cm^{-1}, corresponds to the exact same vibrational mode and hence the same modulus of energy difference as the corresponding Stokes shift of positive 1200 cm^{-1}.

Eq. (1.2) gives the classical wavenumber (and indirectly the vibrational frequency) for a diatomic molecule, and although it is a simple equation derived from the simple harmonic oscillator, it is important in introducing and helping to depict the concept of molecular vibration in a straightforward way. A more general

equation however, which determines the wavenumber for the vibrational mode of any type of molecule (and adapted from [10]) is:

$$\bar{v}_{vib} = \hbar\omega_{vib} / hc \tag{1.3}$$

where h and $\hbar$ are Planck's constant and Planck's constant divided by 2π respectively, c is the speed of light and ω_{vib} is the angular frequency of the vibrational mode.

1.3.6 A classical model of Raman scattering

To simplify the following model of Raman scattering, molecular rotations are not considered, and it is assumed that molecules exhibit vibrations only. The classical description of the Raman Effect begins with a description of Rayleigh scattering which originates from the force exerted on the electron clouds of a molecule by the electric field vector of incident radiation $\mathbf{E}(t) = E_0 \cos(2\pi\nu_p t)\hat{\mathbf{c}}$ [2]. E_0 is the amplitude of the electric field, ν_p the frequency of the wave and $\hat{\mathbf{c}}$ an arbitrary unit vector. When incident EM radiation impinges on a molecule, an oscillating dipole moment with identical frequency is induced [2]:

$$\mathbf{p}(t) = \alpha\mathbf{E}(t) = \alpha E_0 \cos(2\pi\nu_p t)\hat{\mathbf{c}} \tag{1.4}$$

acting as a Hertztian dipole and reradiating a wave of identical frequency. α is the polarisability, a measure of the electron clouds' susceptibility to an external electric field, which in the general case is a tensor, allowing for the possibility that $\mathbf{p}$ and $\mathbf{E}$ are not aligned. An induced dipole moment arises from a displacement of the

negative electron clouds relative to the positive nuclear charges and because it is induced, molecules such as N_2 or H_2 which under $\mathbf{E} = \mathbf{0}$ conditions do not possess a dipole, acquire one [2].

Rayleigh scattering is an elastic process where the energies of the incident and scattered photons are identical, and it can be most commonly observed for example when light in the blue part of the visible spectrum is strongly scattered in the atmosphere, rendering the sky blue. Conversely, Raman scattering is an inelastic process and is extremely weak – about 1000 times weaker than Rayleigh scattering, and the energy of the scattered photon differs to that of the incident photon [11].

If the molecule is already vibrating in one of its fundamental modes, then induced dipole oscillations are amplitude modulated at the frequency ν_{vib} of the mode, assuming that polarisability α of the molecule changes with respect to internuclear distance R of the vibrating atomic nuclei. For small perturbations (which occur in molecules) the polarisability can be expanded in a Taylor series [2]:

$$\alpha(R) = \alpha(R_0) + (R - R_0)\left.\frac{d\alpha}{dR}\right|_{R_0} + \textit{higher order terms} \tag{1.5}$$

where vibrational equilibrium is at $R = R_0$. Because the molecular bond is vibrating, R is time-dependent, obeying the equation [2]:

$$R = R_0 + q_0 \cos(2\pi\nu_{vib}t) \tag{1.6}$$

where q_0 is the amplitude of vibration about R_0, meaning [2]:

$$R - R_0 = q_0 \cos(2\pi\nu_{vib}t) \tag{1.7}$$

Combining Eqs. (1.4), (1.5) and (1.7) and omitting higher order terms gives a dipole moment of magnitude [2]:

$$p(t) = \alpha E = \left[\alpha(R_0) + q_0 \cos(2\pi \nu_{vib} t) \frac{d\alpha}{dR}\bigg|_{R_0} \right] E_0 \cos(2\pi \nu_p t) \qquad (1.8)$$

Using the trigonometric identity,

$$\cos\alpha \cos\beta = \frac{1}{2}\left[\cos(\alpha+\beta) + \cos(\alpha-\beta)\right] \qquad (1.9)$$

and $\cos(\theta) = \cos(-\theta)$ this becomes [2]:

$$p(t) = \alpha(R_0) E_0 \cos(2\pi \nu_p t) + \frac{1}{2}\frac{d\alpha}{dR}\bigg|_{R_0} E_0 q_0 \left\{ \cos\left[2\pi(\nu_p + \nu_{vib})t\right] + \cos\left[2\pi(\nu_p - \nu_{vib})t\right] \right\} \qquad (1.10)$$

It can be seen from Eq. (1.10) that sidebands form part of the scattered light spectrum, having frequencies $\nu_p \pm \nu_{vib}$, producing the so-called 1st order Raman effect. With decreasing intensity, other Raman frequencies are generated: $\nu_p \pm 2\nu_{vib}$, $\nu_p \pm 3\nu_{vib}$ and so on, known as the 2nd and 3rd order Raman effects respectively. These are the overtone bands which originate from the higher order terms in the Taylor expansion of $\alpha(R)$ in Eq. (1.5) [2]. If two vibrational frequencies ν_1 and ν_2 combine, then combination bands are produced as $\nu_p \pm (\nu_1 \pm \nu_2)$ [12]. A vibrating bond is considered Raman-active therefore if $d\alpha/dR \neq 0$; as stated earlier, the polarisability of the bond must alter as a function of internuclear distance during the

vibration [2]. This again applies, by extension, to all bonds present in a Raman-active vibrational mode. If this is not so then Eq. (1.10) reverts to Eq. (1.4) which is simply the equation for Rayleigh scattering.

The classical theory of Raman scattering given here explains many experimental observations well, but breaks down when the Stokes and anti-Stokes intensities are compared. Classical theory dictates that the intensities are equal, which is not observed experimentally. Indeed, the Stoke lines are always considerably more intense. This phenomenon is accounted for by a full quantum-mechanical treatment of the Raman Effect which is beyond the scope of this thesis. Briefly however, in this theory, the intensities of both types of lines have the relationship [2]:

$$\frac{I_{anti\text{-}Stokes}}{I_{Stokes}} = \frac{n(\upsilon = 1)}{n(\upsilon = 0)} = \exp\left(-h\nu_{vib}/kT\right) \tag{1.11}$$

where $\upsilon = 0$ and $\upsilon = 1$ are vibrational quantum numbers of the ground and excited states respectively. The intensity ratio between anti-Stokes and Stokes lines in Eq. (1.11) is dependent on the occupation probabilities *n* which are calculated from the Boltzmann factor in thermal equilibrium, where *h* is Planck's constant, *k*, Boltzmann's constant and *T* the temperature in Kelvin. This means that the intensity of the anti-Stokes lines decays exponentially with decreasing temperature, since the presumption here is that the molecule is initially in an excited vibrational state and the number of such molecules is reduced as temperature is decreased. To illustrate just how comparatively weak the anti-Stokes lines are, if a wavenumber of say, $\bar{\nu}_{vib} = 1000\ \text{cm}^{-1}$ is chosen at room temperature, $T = 300\ K$, then the relative

intensity of anti-Stokes to Stokes is merely 0.7% which cannot be explained using the classical description [2].

1.3.7 Amplification of the Raman signal

As mentioned in section 1.3.6, Raman scattering is an inherently weak process – about 1000 times weaker than its Rayleigh counterpart, no matter the vibrational mode considered. Nevertheless, the Raman spectrum is an extremely useful analytical tool, as it can be considered a molecular fingerprint due to the presence of distinct narrow bands arising from specific molecular vibrations. However, the paucity of Raman-scattered light automatically precludes standard Raman spectroscopy from any manner of low-concentration or trace analysis which, for example, is routinely required by disciplines such as bio- and chemical analysis. Consequently, viable standard Raman samples are usually limited to solids or relatively high-concentration liquids so that sufficient molecules might exist collectively to generate a discernible Raman signal. If however, Eq. (1.10) is re-examined, it becomes evident that one way to boost the signal might be to magnify the incident electric field strength, E_0, and/or to increase the change in polarisability with respect to internuclear distance, i.e. to increase $d\alpha/dR$, both of which happen to be the enhancement mechanisms in SERS.

1.3.8 The discovery of SERS and the associated enhancement mechanisms

In 1974, Fleischmann *et al.* [13] were the first to observe the phenomenon of what would subsequently become known as "surface-enhanced Raman scattering".

Whilst collecting potential-dependent surface Raman spectra from pyridine adsorbed onto an electrochemically roughened silver electrode, it was noted that the Raman signal seemed inordinately high. This was mistakenly attributed to a much greater number of pyridine molecules becoming adsorbed onto the roughened electrode due to a vastly-increased surface area, which in turn, produced a substantially elevated signal. After making careful calculations and conducting an experiment however, Van Duyne *et al.* proved that even when factoring in the increased surface area and concomitant increased adsorption, the intensity of the signal still remained anomalously high, of order $10^5 - 10^6$ times, but their results would not be accepted by the scientific establishment for another three years. Finally in 1977, Jeanmaire and Van Duyne published their paper around the same time that Albrecht and Creighton independently reported a similar result. It was now apparent that what was being observed was an actual *enhancement* of the Raman signal itself by, as yet, some unknown mechanism. The discovery of SERS would have considerable implications for surface science and spectroscopy, as the intrinsically weak signal which had long-plagued Raman analysis, could now be boosted by several orders of magnitude, opening the door to a wider study of surface vibrational phenomena, previously impenetrable using standard Raman spectroscopy [14].

As mentioned earlier, two enhancement mechanisms come into play, one which magnifies the incident electric field strength E_0, and another which increases the change in polarisability with respect to internuclear distance during a vibration, i.e., increases $d\alpha/dR$. These are known as the "electromagnetic" (EM) and "chemical" (CH) enhancement mechanisms respectively.

1.3.8.1 Chemical enhancement

Of the two mechanisms, CH enhancement contributes by far the least enhancement in SERS, probably only about 10 – 100 times [15] and the main mechanism behind it is thought to be some mode of charge transfer, of which there is thought to be three types. Type I is the simplest and occurs when the molecular probe does not covalently bind to the metal NP. Here, the metal slightly disrupts the electronic structure of the molecule, affecting a change in polarisability and ultimately, in the Raman efficiency of a vibrational mode.

Type II can be represented by the schematic in figure 1.7 from [16].

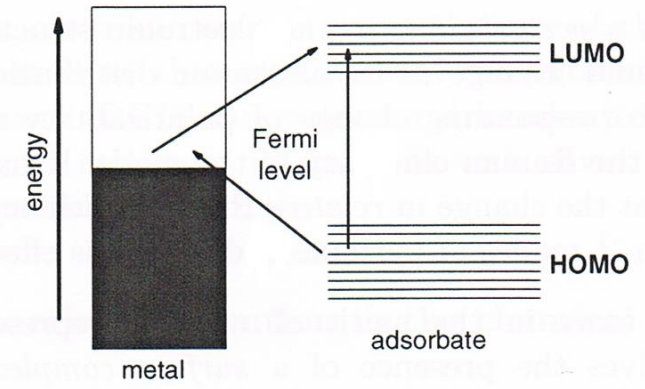

Figure 1.7. Surface complex of a metal NP and molecule with a HOMO-LUMO gap from [16].

This type of charge transfer involves a surface complex comprising the metal and the molecule which are either directly and covalently bound to one another, or indirectly bound via the mediation of an electrolyte ion, e.g. chloride. This is capable of inducing a substantial change in the intrinsic polarisability of the molecule, whose magnitude depends crucially on the available optical transitions. The new indirect transitions resulting from the overlap of molecular orbitals generate pathways for

modification of the polarisability. Moreover, the surface complex may also create a novel electronic state which is in, or almost in resonance with the laser, creating a kind of resonance Raman scattering.

Type III involves photons driving charge in the analyte from the highest occupied molecular orbital (HOMO) to the lowest unoccupied molecular orbital (LUMO) even if the energy of the laser is substantially lower than the HOMO-LUMO gap. Mediation by the nanoparticle in the (chemisorbed) surface complex, allows an electron to be driven firstly from the HOMO to the Fermi level of the NP within the complex and then, by another photon, to the LUMO of the analyte, meaning that the laser can be in resonance with the HOMO-LUMO gap providing signal amplification; however, the Fermi level must lie halfway between the gap limits for this to be possible [17].

1.3.8.2 Electromagnetic enhancement

In EM enhancement, the Raman signal is boosted on average by a considerable factor of about 10^6 – 10^8 [15], far greater than that created by CH enhancement, and since the latter makes only a minor contribution to the overall SERS enhancement factor (EF), it is discussed no further. The incident electric field in EM enhancement is amplified by the intense electric fields created by localised surface plasmons (LSPs) – coherent oscillations of the conduction electrons of metal NPs, induced by incident photons as illustrated in figure 1.8 from [18].

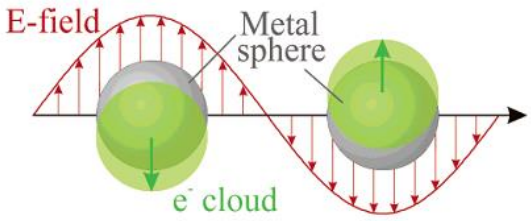

Figure 1.8. LSPs of two metal NPs showing the displacement of the conduction electron clouds relative to positive nuclei in response to an incident alternating electric field [18].

Strong electric fields generated by LSPs are at their most intense when two or more NPs lie close enough to one another, in the order of nm, so that their respective LSPs become coupled. Moreover, this effect is maximised when the LSP oscillation and excitation frequencies are the same. i.e. resonance occurs [19]. Figure 1.9 from [20] is a simulation of two different arrangements of spherical Au NPs in an alternating E-field with the associated electric field distributions arising from LSPs.

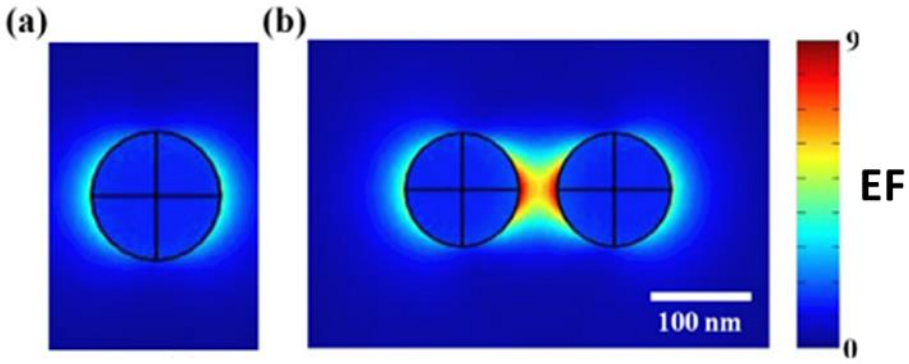

Figure 1.9 adapted from [20]. Simulated electric field distributions of (a) a single Au NP and (b) Au NP dimer (two NPs close together). In (a), the region in which the field is enhanced is limited to less than 10 nm from the surface, whereas in (b), the whole region between the two NPs is enhanced; the two individual NP LSPs have become coupled within this region, creating an extremely intense electric field, otherwise known as a "hotspot". The single particle has an enhancement factor (EF) of about 4 which is lower than that of the dimer at about 9.

The physics of LSPs is discussed in detail later, as the importance of metal nanostructures which generate EM enhancement in SERS via LSP coupling cannot be overstated as they are universal in the field. The famous "E^4 approximation" equation for EM enhancement however is presented in the next paragraph before that discussion to conclude this section on SERS enhancement mechanisms.

There are two types of EM signal augmentation during light scattering by a molecule which multiply to produce an overall SMEF (single molecule enhancement factor). Firstly, the intensity of incident light is magnified by coupled NP LSPs, producing a local field enhancement factor, $M_{\mathrm{Loc}}(\omega_L)$, in the vicinity of the molecule, which excites Raman modes of the analyte, increasing the Raman-scattered signal [21]:

$$M_{\mathrm{Loc}}(\omega_L) = \frac{\left|\mathbf{E}_{\mathrm{Loc}}(\omega_L)\right|^2}{\left|E_0\right|^2} \tag{1.12}$$

where $\mathbf{E}_{\mathrm{Loc}}$ is the local electric field which is a function of the angular frequency of the laser ω_L, and E_0 is the incident electric field. Raman-scattered light is then further boosted by the same coupled LSPs, generating a directional radiation enhancement factor, the equation for which has been adapted from [22]:

$$M^{d}_{\mathrm{Rad}}(\omega_R) = \frac{\left|\mathbf{E}_{\mathrm{Rad}}(\omega_R)\right|^2}{\left|E_0\right|^2} \tag{1.13}$$

where the superscript "*d*" emphasises that this is the radiation enhancement factor in the direction of detection of the SERS signal. $\mathbf{E}_{\mathrm{Rad}}$ is the electric field of the Raman-

scattered light which is a function of the angular frequency of this light, ω_R. The local field enhancement factor, $M_{\text{Loc}}(\omega_L)$, can be found relatively easily by solving the electromagnetic problem for a given set of excitation conditions with incident electric field E_0; this yields the local field, $\mathbf{E}_{\text{Loc}}$ everywhere. Calculating M_{Rad}^d on the other hand proves very challenging, as it is necessary to solve the inherently difficult electromagnetic problem of dipolar emission rather than external excitation, presenting obstacles both theoretically and numerically. This necessitates solving the problem for each possible position (and for at least three perpendicular orientations) of the dipole, rendering it unsolvable in most cases. One way around this difficulty, is to assume that $M_{\text{Rad}}^d(\omega) \approx M_{\text{Loc}}(\omega)$, meaning that the SERS SMEF can be expressed simply as [22]:

$$\text{SMEF}(\omega_L,\omega_R) \approx M_{\text{Loc}}(\omega_L) M_{\text{Loc}}(\omega_R) \approx \frac{\left|\mathbf{E}_{\text{Loc}}(\omega_L)\right|^2}{\left|E_0\right|^2} \frac{\left|\mathbf{E}_{\text{Loc}}(\omega_R)\right|^2}{\left|E_0\right|^2} \quad (1.14)$$

Eq. (1.14) is extensively used in the literature and is known as the "E^4 approximation". When the frequencies of Raman-scattered light and laser light are roughly equal, i.e. the Raman shift is fairly small, Eq. (1.14) simplifies to [22]:

$$\text{SMEF}(\omega_L) \approx \frac{\left|\mathbf{E}_{\text{Loc}}(\omega_L)\right|^4}{\left|E_0\right|^4} \quad (1.15)$$

which is an even more famous expression of the E^4 approximation, an expression which, it can be argued, is in fact the most important in SERS.

1.3.9 Bound and free electrons in an electromagnetic field

As was discussed in the previous section, EM enhancement avails itself of the intense electric fields produced by coupled LSPs of two or more closely situated metal NPs. In order to better understand the origin of LSPs, the response of free electrons in bulk metal to an EM field is examined in this section, with an initial discussion on the interaction between an EM wave and a "normal" dielectric, i.e. one which allows the permeation of an electric field and one where all the electrons are bound to their respective nuclei. For electromagnetic waves *in vacuo*, the magnetic field component has magnitude $|\mathbf{B}| = |\mathbf{E}|/c$ where **E** is the electric field component and *c* the speed of light. When an electron responds to an alternating E-field in free space therefore, the magnetic contribution to the Lorentz force ($-e\mathbf{v}\times\mathbf{B}$) where **v** is the velocity of the electron with charge $-e$ is v/c times the electric contribution, meaning the magnetic component can be ignored with confidence. In a normal dielectric, the restoring force of an electron displaced from its positive nucleus is $-a\mathbf{r}(t)$, where a is the effective spring constant and $\mathbf{r}$, the displacement from equilibrium at time *t*. Energy loss can be introduced via a friction force $-b\mathbf{v}(t) = -b\,d\mathbf{r}(t)/dt$, which creates a viscous drag directly proportional to the instantaneous speed $v(t) = dr/dt$. Under the influence of a passing EM wave, the bound electron experiences a force $-e\mathbf{E}(\mathbf{r}(t),t)$ which is evaluated locally at its position $\mathbf{r}(t)$ [23].

It is assumed that the nucleus of the atom is fixed, which is justified at relatively high frequencies as the nucleus is thousands of times more massive than

the electron, and so exhibits a much greater inertia. Combining these factors, the equation of motion for a bound electron of mass *m* in a dielectric is [23]:

$$m\frac{d^2\mathbf{r}(t)}{dt^2} = -a\mathbf{r}(t) - b\frac{d\mathbf{r}(t)}{dt} - e\mathbf{E}\left(\mathbf{r}(t),t\right) \tag{1.16}$$

Since the electron displacement from equilibrium will be << 1 nm, i.e. much smaller than the size of an atom and the wavelength of visible light, λ >> 1 nm $\mathbf{E}\left(\mathbf{r}(t),t\right)$ can be replaced by $\mathbf{E}(\mathbf{0},t)$ because the field can be considered constant, to a high approximation, over the region in which the electron moves. Using complex exponential notation, the driving field with angular frequency ω is [23]:

$$\mathbf{E}(\mathbf{0},t) = \mathbf{E}_0 \exp\left[-i\omega t\right] \tag{1.17}$$

which simplifies the equation of motion to [23]:

$$m\frac{d^2\mathbf{r}(t)}{dt^2} + a\mathbf{r}(t) + b\frac{d\mathbf{r}(t)}{dt} = -e\mathbf{E}_0 \exp\left[-i\omega t\right] \tag{1.18}$$

Eq. (1.18) is the equation of motion for a bound electron in a dielectric. To consider the same for a conduction electron in bulk metal, it is merely necessary to set the spring constant, *a* to zero, as (free) conduction electrons are not bound and experience no restoring force from individual nuclei, so for such an electron, the equation of motion will be [24]:

$$m\frac{d^2\mathbf{r}(t)}{dt^2} + b\frac{d\mathbf{r}(t)}{dt} = -e\mathbf{E}_0 \exp\left[-i\omega t\right] \tag{1.19}$$

Steady-state solutions of this forced oscillator equation take the form [23]:

$$\mathbf{r}(t) = \mathbf{r}_0 \exp[-i\omega t] \tag{1.20}$$

where $\mathbf{r}_0$ is the amplitude of the oscillation. Eqs. (1.19) and (1.20) arise from the Drude-Sommerfeld model which assumes that the optical response of a metal can be arrived at by modelling external forces on one free conduction electron and then multiplying this effect by the number of electrons in the system to gain the macroscopic response [24]. The next section uses this model to obtain the dielectric function of a metal.

When an electric field $\mathbf{E}_0$ is applied to a conductor, the free conduction electrons quickly rearrange themselves on the surface to create an internal electric field which exactly cancels the applied field, preventing the existence of any electric field within the interior of the conductor as shown in figure 1.10.

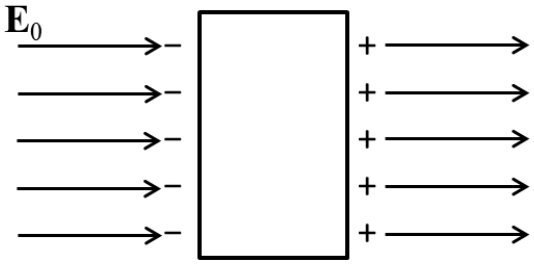

Figure 1.10. The electric field within a conductor is zero.

This means however that despite this "non-dielectric" behaviour, the conductor can still possess an overall polarisation arising from the induced charge imbalance upon the surface. There are no dipole moments created within the body of the metal (as in a dielectric) due to unfettered movement of the conduction electrons to the metal surface. However, a free electron, whilst not subject to a restoring force issued by a

particular nucleus, will still feel such a force from the positive ionic lattice as a whole, as it is displaced from the lattice to the surface of the metal by an EM field.

1.3.10 The dielectric function of bulk metals

According to the Drude-Sommerfeld theory, the conduction electrons within a metal can be modelled as a plasma, i.e. a free electron "gas". Since the dynamics of the electrons are intimately linked to the optical properties of metals and both can be entirely described using a (complex) relative dielectric function, $\varepsilon(\omega)$ [25], this section focusses on derivation of the function. It shall be shown later in 1.3.12 (in the case of a small metal sphere) how the function is directly related to amplification of an incident, alternating E-field, which as discussed earlier, is the EM enhancement mechanism crucial for SERS.

For simplicity, only isotropic media are considered, i.e. polarisation, $\mathbf{P}$ is parallel to $\mathbf{E}$. Substituting Eq. (1.20) into Eq. (1.19), collecting terms and cancelling $\exp[-i\omega t]$ on both sides, the equation for the amplitude of the displacement of a single free electron from the positive ionic lattice in a time-dependent E-field is [23]:

$$\left[-m\omega^2 - i\omega b\right]\mathbf{r}_0 = -e\mathbf{E}_0 \tag{1.21}$$

The notation can be simplified by the introduction of a friction parameter, $\gamma = b/m$. $\mathbf{r}_0$ then becomes [23]:

$$\mathbf{r}_0 = -\frac{e\mathbf{E}_0}{m}\frac{1}{\left(-\omega^2 - i\omega\gamma\right)} \tag{1.22}$$

Eq. (1.22), describing the response of a single electron to an EM field, is used to determine the aggregate response of a system containing many free electrons which experience the restoring force of the positive lattice. The electric field induces a polarisation $\mathbf{P}(t)$ due to the displacement of the electrons with number density *n* [23]:

$$\begin{aligned}\mathbf{P}(t) &= -ne\mathbf{r}(t) \\ &= -ne\mathbf{r}_0 \exp[-i\omega t] \\ &= \frac{ne^2}{m}\frac{1}{\left(-\omega^2 - i\omega\gamma\right)}\mathbf{E}_0 \exp[-i\omega t] \\ &= \omega_p^2 \frac{1}{\left(-\omega^2 - i\omega\gamma\right)}\varepsilon_0\mathbf{E}_0 \exp[-i\omega t]\end{aligned} \tag{1.23}$$

where [23]

$$\omega_p = \sqrt{\frac{ne^2}{m\varepsilon_0}} \tag{1.24}$$

is the natural frequency of oscillation, known as the plasma frequency. Since the polarisation can also be written [23]:

$$\mathbf{P}(t) = \chi_E \varepsilon_0 \mathbf{E}(t) \tag{1.25}$$

where the electric susceptibility $\chi_E = \varepsilon - 1$, the dielectric function can be written [23]:

$$\varepsilon(\omega) = 1 + \omega_p^2 \frac{1}{\left(-\omega^2 - i\omega\gamma\right)} \tag{1.26}$$

Eq. (1.26) can be separated into real and imaginary parts, $\varepsilon_1(\omega)$ and $\varepsilon_2(\omega)$ respectively, to give:

$$\varepsilon_1(\omega) = 1 - \frac{\omega_p^2}{\omega^2 + \gamma^2} \tag{1.27}$$

and

$$\varepsilon_2(\omega) = \frac{\omega_p^2 \gamma}{\omega(\omega^2 + \gamma^2)} \tag{1.28}$$

For $\omega >> \gamma$, the real and imaginary parts of $\varepsilon(\omega)$ for free electron metals can be written as:

$$\varepsilon_1(\omega) \approx 1 - \frac{\omega_p^2}{\omega^2}, \quad \varepsilon_2(\omega) \approx \frac{\omega_p^2 \gamma}{\omega^3} \tag{1.29}$$

Eq. (1.29) shows that ω is equal to the plasma frequency ω_p for $\varepsilon_1(\omega) = 0$.

For simplicity, only the role of the free conduction electrons has up until now been considered with regard to the optical properties of metals. Importantly however, bound core electrons also contribute to the dielectric function and electrons which experience interband transitions contribute additively, $\chi^{IB} = \chi_1^{IB} + i\chi_2^{IB}$ to the susceptibility. The imaginary part, χ_2^{IB}, describes energy dissipation and is large only for the relatively short wavelengths of interband transitions, whereas the real part, χ_1^{IB}, is also important for longer wavelengths [26]. The complex dielectric

function encapsulating all optical material properties in the visible region arising from both bound and free electrons is given by [27]:

$$\varepsilon(\omega) = 1 + \chi^{IB}(\omega) + \chi^{DS}(\omega) \tag{1.30}$$

where the superscript "*DS*" (Drude-Sommerfeld) has been used to denote the electric susceptibility arising from the free electrons.

1.3.11 Light penetration in metals

In the low-frequency approximation, light penetrates the surface of a metal to a characteristic depth, known as the 'skin depth' given by [28]:

$$\delta = \sqrt{\frac{2}{\mu_0 \sigma \omega}} \tag{1.31}$$

where μ_0 is the magnetic permeability of free space, and σ and ω are the electrical conductivity of the metal and the angular frequency of the incident light respectively. Both the high conductivity of the metal and the high angular frequency of visible light combine to ensure that field penetration is restricted to the surface in bulk metal, normally in the order of 10s of nm. For this reason, in metal NPs below about 10 nm diameter, field attenuation is negligible, whereas in larger NPs it becomes increasingly important, as electrons within the body of the particle are better-screened from the impinging E-field, with only the *surface* electrons reacting to it [29], generating the so-called localised *surface* plasmons introduced earlier.

1.3.12 The response of a small metal sphere to a quasistatic electric field

To illustrate the response of a metal NP to a light wave, a simple shape, in this case a sphere, is used along with the quasistatic approximation, i.e. $R \leq 0.01\ \lambda$ where R is the radius of the particle and λ, the excitation wavelength, meaning that NP radii of around 5 nm are used in the model with visible frequency excitation [30]. The massive, positive nuclei in the NPs are considered immobile, with negative charges, i.e. the much less-massive conduction electrons, being displaced by the E-field. The quasistatic approximation ensures that retardation effects arising from the phase shift of the wave can be ignored, restricting excitation of the conduction electrons to a dipolar as opposed to a multipolar electric mode. Using boundary conditions at the sphere surface (which are not stated here), the (complex) internal electric field is [29]:

$$E_i = E_0 \frac{3\varepsilon_m}{\varepsilon(\omega) + 2\varepsilon_m} \tag{1.32}$$

where ε_m is the dielectric constant of the embedding medium. This solution for the internal electric field works well for small spheres subject to an oscillating E-field in the quasistatic regime, a regime characterised by maintaining the time but not the spatial dependence of the E-field. The sphere experiences a field therefore with spatially constant, but time-dependent, phase as illustrated in figure 1.11 (a) from [31].

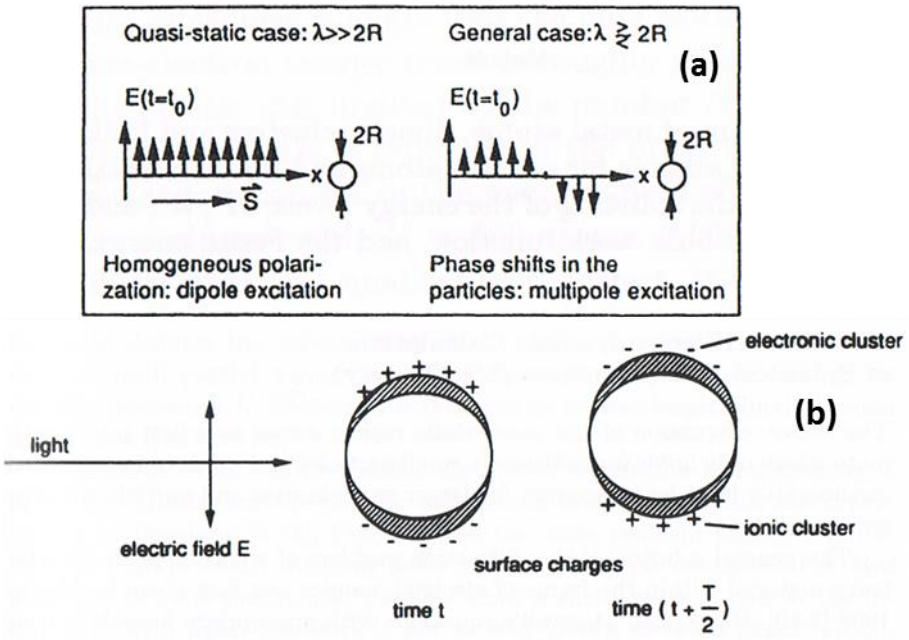

Figure 1.11 from [31]: (a) schematic comparison of the quasistatic regime and the general case. (b) excitation of a dipolar LSP.

The displacement of negative charge due to the E-field induces polarisation charges at the NP surface which generate a linear restoring force, determining the eigenfrequency of the system. The conduction electrons in a spherical NP therefore act as a simple harmonic oscillator (SHO) system, whereas those in bulk metal behave in a relaxatory way [32].

The fact that the real part of the dielectric function in metals, i.e. $\varepsilon_1(\omega)$, is negative in the visible region, implies a very small refractive index (less than 1 and close to 0) and conversely a reflection coefficient close to ~ 1. This is responsible for many of the optical properties of metals, specifically those which give rise to plasmon-related effects. The important part in Eq. (1.32) is the denominator. As it tends to zero, a condition fulfilled if $\varepsilon(\omega) \approx -2\varepsilon_m$ (ε_m is always positive), a resonance is set up between the SHO-NP system and the driving E-field, reflected by

a gross inflation of the fraction in Eq. (1.32) [33]. This corresponds to a characteristic extinction spectrum or "plasmon band" as seen in figure 1.12.

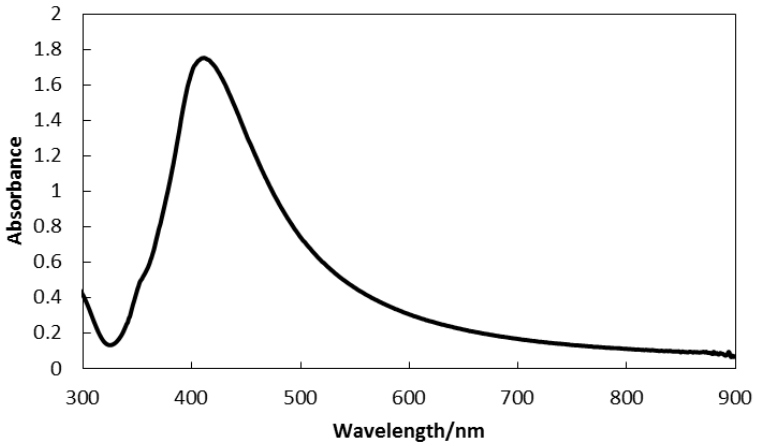

Figure 1.12. Extinction spectrum of silver colloid with the plasmon band centred on 411 nm.

Figure 1.12 shows the extinction spectrum of Ag colloid fabricated for this thesis (the synthesis of which is described later in chapter three) with the characteristic Ag LSP band or "plasmon band" at around 400 nm [34] (411 nm in the diagram). Extinction comprises a combination of absorption and scattering and generally, the larger a metal NP is, the more it tends to scatter radiation rather than absorb it. The wavelength maximum is the resonant wavelength corresponding to the eigenfrequency of the system.

While standard dielectrics can only have positive $\varepsilon_1(\omega)$ values between about 1 and 10, resonance occurs in metal NPs if the negative, real part of the dielectric function, $\varepsilon_1(\omega) \approx -2\varepsilon_m$ *and* energy losses are small, i.e. $\varepsilon_2(\omega) \approx 0$. While the possibility of resonance is chiefly dependent on the value of $\varepsilon_1(\omega)$, its

magnitude is crucially affected by how "lossy" a metal is; the less lossy it is, the closer $\varepsilon_2(\omega)$ is to zero and the larger the resonance becomes [33].

The simple case of a small sphere in an oscillating EM field under quasistatic conditions has been presented here to help elucidate the way in which metal NPs interact with light, but many other NP geometries exist which, despite exhibiting similar resonance effects, produce different equations describing the internal electric field; this leads to resonance conditions governed in part by geometry. In other words, optical resonances in metal NPs do not arise solely from the material properties of metals, but rather from both these *and* the specific NP geometry. Consequently, two NPs of the same metal but with different structures will each exhibit different resonances, corresponding to distinct extinction spectra [33].

To optimise the SERS performance of a metal NP substrate therefore, one or more of the material properties, geometry, and interstitial gap size can be altered to provoke a change in the plasmonic response of the substrate, allowing its resonance to be tuned to the desired laser excitation wavelength for maximum effect (maximum SERS intensity). Some of the most widely used substrates are reviewed in the next chapter.

1.4 Nucleation and growth of metal nanoparticles in aqueous solution

Chapters 2 – 4 discuss the reduction of Ag- and Au-salt agarose gels, using different chemicals, to form MNPA SERS substrates. Ag and AuNP size, density

and dispersity within the gel depend critically on particle nucleation and subsequent growth, both of which are influenced by the attendant physical and chemical environmental factors. This section therefore covers nucleation theory in detail.

1.4.1 Classical nucleation theory

In any chemical reaction, the Gibbs free energy (ΔG) of a closed system is that amount of total energy available for useful work [35]:

$$\Delta G = \Delta H - T\Delta S \tag{1.33}$$

where ΔH and ΔS are changes in enthalpy and entropy respectively. The sign of ΔG determines the outcome of a chemical reaction [35]:

- $\Delta G < 0$: The reaction is spontaneous in the written direction, releasing free energy (exergonic).
- $\Delta G = 0$: The system is in equilibrium, meaning there is no overall change in either the forward or reverse direction.
- $\Delta G > 0$: The reaction flows spontaneously in the reverse direction, requiring input of free energy (endergonic).

The word "free" signifies the maximum useful work that is available in a reversible process at constant pressure and temperature which is not involved in expansion, and when energy is transferred, the system can do work on its surroundings ($\Delta G < 0$), or the surroundings can do work on the system ($\Delta G > 0$) [35]. ΔG therefore is an excellent way to predict the evolution of a complex system such as nucleation, growth and dissolution of metal nanoparticles in a single-solute solution.

At the initial stage of nanoparticle growth, solute atoms (A) collide, merging together to form small clusters in solution atom-by-atom [36]:

$$A_n + A \leftrightarrow A_{n+1} \tag{1.34}$$

The double arrow indicates that just as atoms aggregate to form nanoclusters, they also re-dissolve back into solution. The average number of clusters with radius $r(N_r)$ can be determined by the following equations, taken from [36]:

$$N_r = N_0 \exp\left(-\frac{\Delta G_r}{RT}\right) = N_A [A]_{eq} S_n \exp\left(-\frac{\Delta G_r}{RT}\right) \tag{1.35}$$

$$\Delta G_r = 4\pi r^2 \gamma + \frac{4}{3}\pi r^3 \Delta G_V \tag{1.36}$$

$$\Delta G_V = -\frac{RT \ln S_n}{V_m} \tag{1.37}$$

$$S_n = \frac{[A]_s}{[A]_{eq}} \tag{1.38}$$

where N_0 is the number of free solute atoms per unit volume in the system (m^{-3}), ΔG_r is the excess free energy of nanocluster formation (J mol^{-1}), γ is the surface free energy per nanocluster unit surface area (J mol^{-1} m^{-2}), ΔG_V is the difference in free energy between solute atoms in solution and unit volume of the bulk crystal (J mol^{-1}), V_m is the molar volume of bulk crystal (m^3), T is the reaction temperature (K), N_A is Avogadro's constant (mol^{-1}), R is the ideal gas constant (J K^{-1} mol^{-1}), and

S_n is the supersaturation ratio, the ratio between solute concentration at supersaturation, $[A]_s$ and at equilibrium (normal saturation), $[A]_{eq}$.

ΔG_r (the excess free energy of nanocluster formation) comprises two competing terms; one is normally positive, relating to newly formed interfaces between nanoclusters and their environment which is unfavourable ($4\pi r^2\gamma$), and the other arises from bond formation between nuclei, whose sign depends on the value of S_n, $(4/3)\pi r^3\left(-RT\,ln\,S_n/V_m\right)$ [36]. As more and more solute atoms are added to solution, solute concentration increases up to and beyond normal saturation (the equilibrium saturation) to become supersaturated. If $S_n<1$, the solution is not supersaturated, and ΔG_V, and ΔG_r therefore is positive, increasing with nanocluster growth. Thermodynamic instability increases with cluster size in such a system, preventing nanocluster formation. Only when a solution is supersaturated i.e. $S_n>1$, does ΔG_r decrease with increasing nanocluster radius, making the formation of solute crystals energetically preferable [36].

Under this condition ($S_n>1$), ΔG_r initially increases (the activation energy barrier) then decreases as a function of nanocluster radius, as illustrated in figure 1.13. The critical radius r^*, occurs at a local maximum of free energy, ΔG^*, meaning there exists a critical number of atoms n^* in a cluster A_n^* of radius r^*. If $r<r^*$, the system reduces its free energy via dissolution of the cluster which is thermodynamically unstable, from which new, embryonic clusters $\left(A_n<A_n^*\right)$ are generated through spontaneous collisions. If, during the collisions, the radius of an

embryo becomes large enough, $r > r^*$, it becomes stable and is referred to as a "nucleus". The expressions for critical radius r^*, and maximum excess free energy of nanocluster formation, ΔG^*, can therefore be obtained by setting $d\Delta G_r / dr$ to zero [36].

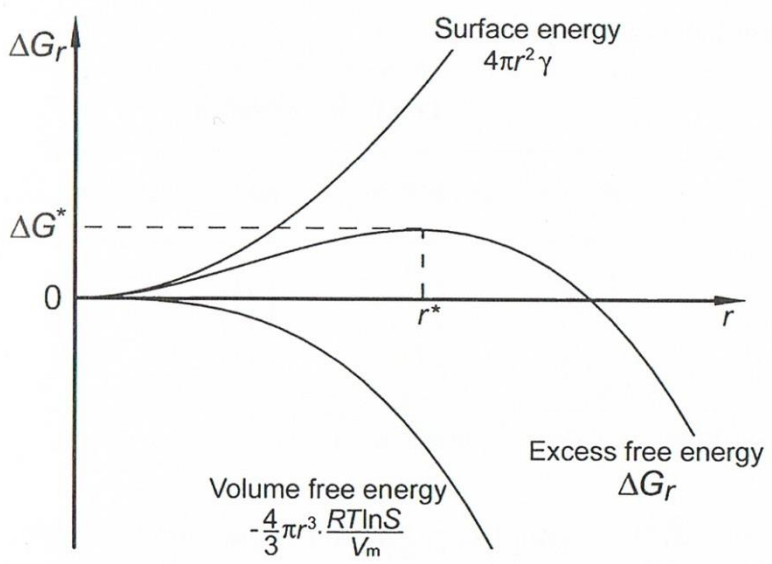

Figure 1.13. The change in Gibbs free energy versus nanoparticle radius, taken from [37]. "*S*" in the Volume Free Energy equation is denoted "S_n" in the text.

The critical radius and maximum excess free energy of nanocluster formation are therefore given respectively by [36]:

$$r^* = \frac{2\gamma V_m}{RT\ln S_n} \tag{1.39}$$

and [36]

$$\Delta G^* = \frac{16\pi\gamma^3 V_m^2}{3\left(RT\ln S_n\right)^2} \tag{1.40}$$

In a similar way, the number of nanoclusters acquiring critical radius, N_{r^*} and the nucleation rate, dN_{r^*}/dt can be given by the following equations [36]:

$$N_{r^*} = N_A[A]_{eq} S_n \exp\left(-\frac{16\pi\gamma^3 V_m^2}{3(RT)^3 (\ln S_n)^2}\right) \tag{1.41}$$

where Eq. (1.40) for ΔG^* has been substituted into the right hand side of Eq. (1.35) for N_r, and

$$\frac{dN_{r^*}}{dt} = f_0 N_A[A]_{eq} S_n \exp\left(-\frac{16\pi\gamma^3 V_m^2}{3(RT)^3 (\ln S_n)^2}\right) \tag{1.42}$$

where f_0 is the ratio of nanoclusters with critical radius becoming stable nuclei and a function of variables such as the vibration frequency of the atoms, the activation energy of diffusion in liquid and the surface area of critically sized nuclei.

Parameters r^*, ΔG^*, N_{r^*}, and dN_{r^*}/dt, describe how easy (or difficult) it is for a solute to nucleate. For small values of $r^*$and ΔG^*, the system readily produces nuclei because the energy barrier to nanocluster formation is quite small, and few atoms are needed to form a stable nanocluster. If, on the other hand, $r^*$and ΔG^* are large, stable nucleation is difficult, and only a relatively small number of nanoclusters can grow to form stable nuclei and a slow nucleation rate is observed [36].

1.4.2 Controlled nucleation

Surface free energy per nanocluster unit surface area (γ), reaction temperature (T), degree of supersaturation (S_n) and the ratio of nanoclusters with critical radius becoming stable nuclei (f_0) are the important variables which impact nucleation, and what the end results will be therefore with regard to nanoparticle size and dispersity. Of the four parameters, f_0 is quite complex, representing variables which cannot be easily controlled experimentally, but the others are managed relatively simply to guide nucleation and growth. The impact that changing one parameter has on the other and the resultant effect on nucleation is summarised in table 1.1, taken from [38].

Table 1.1 reproduced from [38]. The symbols '$\uparrow(\downarrow)$' indicate the increase (decrease) of a parameter.

Experimental parameters			**Effects on nucleation**			
γ	**T**	**S_n**	**r^***	**ΔG^***	**N_r^***	**dN_r^*/dt**
$\uparrow(\downarrow)$	–	–	$\uparrow(\downarrow)$	$\uparrow(\downarrow)$	$\downarrow(\uparrow)$	$\downarrow(\uparrow)$
–	$\uparrow(\downarrow)$	–	$\downarrow(\uparrow)$	$\downarrow(\uparrow)$	$\uparrow(\downarrow)$	$\uparrow(\downarrow)$
–	–	$\uparrow(\downarrow)$	$\downarrow(\uparrow)$	$\downarrow(\uparrow)$	$\uparrow(\downarrow)$	$\uparrow(\downarrow)$

A large surface free energy hinders nucleation due to the need for unstable nanoclusters to acquire a large critical radius to overcome a high energy barrier and so become nuclei. Consequently, only a small number of nanoclusters will attain critical size which results in a reduced nucleation rate. In contrast, increasing the reaction temperature and supersaturation ratio has the effect of reducing critical size,

increasing the number of nanoclusters attaining critical size, and lowering the energy barrier which greatly increases the nucleation rate [36].

1.4.3 Types of nucleation

There are three known types of nucleation: homogenous, heterogeneous, and secondary nucleation. Homogenous nucleation is the most common, with nuclei being able to form without need of any external additives such as pre-prepared seeds for example. The system is thermodynamically unstable when critical supersaturation occurs, and the overall energy of the system is reduced via the formation of stable nuclei. Homogeneous nucleation is well-explained by classical nucleation theory, covered in section 1.4.1, and is applicable to the fabrication of MNPA.

In heterogeneous nucleation, some surface energy is released when the solution forms interfaces with contaminants or structures added purposely such as seeds. These interfaces tend to lower the energy barrier to a value less than that required for corresponding homogeneous nucleation. The presence of such structures increases the nucleation rate, and the equations which describe heterogeneous nucleation are similar to those of homogenous (classical) nucleation theory. The equations however (which are not stated here), must be altered slightly to accommodate the presence (and number) of the structures and their geometric relationship with the solute, as well as their ability to reduce the energy barrier.

The third type of nucleation is secondary nucleation, where nuclei are generated by experimental conditions such as stirring. The nuclei can continue onto

the growth stage, but as yet, there has been no complete theory to describe secondary nucleation [36].

1.4.4 Growth

As discussed in section 1.4.2, certain parameters (*S, γ,* and *T*) can be controlled experimentally to influence nucleation, and La Mer's theory of "burst nucleation" followed by diffusion-led growth is generally used to manipulate these parameters during experimental design. La Mer's theory is illustrated in figure 1.14, adapted from [39].

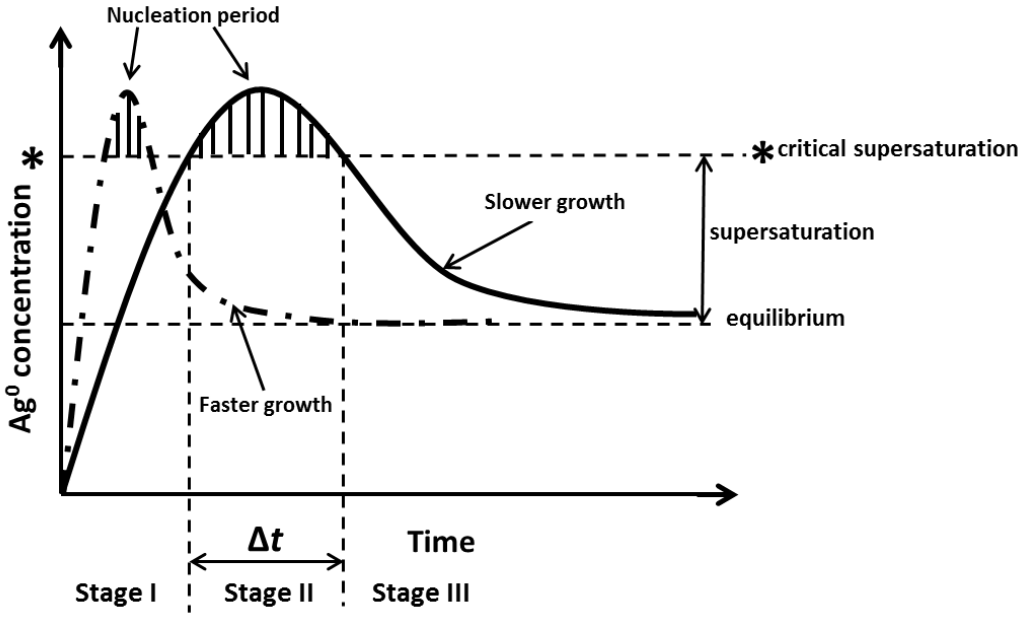

Figure 1.14 adapted from [39]. The change in supersaturation ratio versus time, showing the three stages of nanoparticle formation for the "solid line" La Mer plot.

The fabrication process can be divided into three stages. In stage I, free solute atoms form either by reduction of a metal precursor or nanocluster dissolution, thereby increasing the solute concentration beyond the critical supersaturation threshold.

Nucleation now occurs explosively, simultaneously producing a large number of stable nuclei (stage II). This process rapidly depletes solute atoms, bringing the solute concentration below critical supersaturation and ceasing nucleation, after which the growth stage (stage III) becomes dominant. At this stage, nuclei grow by cannibalising free solute atoms and unstable clusters whose radii are below the critical radius. Figure 1.14 shows two La Mer plots for different nucleation periods, with the three fabrication stages marked for the "solid line" plot. This plot represents a relatively long nucleation period, indicated by Δt on the time-axis, while the "dot-dash" plot represents a shorter one.

In general, nanoparticle growth is either diffusion- or reaction-limited. In solution, a diffusion-limited process normally prevails, and the rate of particle growth is given by [36]:

$$\frac{dr}{dt} = K\left(\frac{1}{r} + \frac{1}{\delta}\right)\left(\frac{1}{r^*} - \frac{1}{r}\right) \tag{1.43}$$

where t is the reaction time, δ the thickness of the diffusion layer, and K a constant proportional to the diffusion constant of the solute.

1.4.5 Size focussing and defocussing

According to Eq. (1.43) the diffusion-limited growth rate is very dependent on nanoparticle size. The larger a nanoparticle, the slower the growth rate, while unstable nanoclusters with a radius below the critical value disappear. Both these phenomena lead to a narrowing of the size distribution, and the combined process is known as "size focussing", which occurs at the beginning of the growth stage (stage

III), where nucleation has ended but S_n is still relatively high but below the critical supersaturation value. At this stage, the radii of many newly-formed nuclei are only marginally greater than the critical radius r^*. Some of these nuclei grow by absorbing solute atoms and unstable clusters, quickly reducing S_n, and causing r^* and ΔG^* to increase. Previously stable nanoparticles which have not grown, perhaps due to a localised lack of solute, are now below the new critical size and suffer instability and dissolve, becoming fewer in number while larger nanoparticles continue to grow. This nanoparticle dissolution therefore, directly results from the increase in critical radius due to reduction of the supersaturation ratio within the growth period, and can be explained by the equations for S_n, r^* and ΔG^* [36]. In contrast, "size defocussing", a process independent of particle concentration known as Ostwald ripening also takes place. This promotes the growth of larger nanoparticles at the expense of smaller ones, and tends to broaden the size distribution. Importantly, Ostwald ripening is *not* continued growth of all nanoparticles as a function of supersaturation, but is instead a redistribution of mass from smaller nanoparticles of higher curvature (higher solubility) to those of lower curvature (lower solubility). This is explicit in the modified Kelvin equation [40]:

$$c(r) = c_\infty \exp(\alpha / r) \tag{1.44}$$

where $c(r)$ and c_∞ are the solubility and bulk solubility of the nanoparticles respectively, and $\alpha \equiv 2\gamma V_m / RT$ [40]. Ultimately, Oswald ripening will result in an overall defocussing, causing the particle size distribution to broaden.

The most favourable scenario for achieving a monodisperse distribution of nanoparticles is a short nucleation period, followed by a distinct growth period. The shorter the nucleation period, the narrower the size distribution can be, and rapid reduction is one way to achieve this goal. Free solute atoms are released into solution in a very short space of time, hiking the solute concentration substantially above the critical supersaturation threshold, giving rise to an intense and very short burst of nucleation. As a result, most of the solute atoms are depleted, and growth abruptly ends after nucleation. The newly formed seed particles increase in size during a separate growth phase, as outlined in the description of heterogeneous nucleation in section 1.4.3.

1.5 Summary

In this chapter, the motivation was laid out for research into SERS of both MNPA and highly ordered metal nanorod arrays created via guided OAD. The influence of nanoparticle growth conditions on Ag-agarose structure and the associated SERS response is not clear. If the gel is to find eventual utility in applications therefore, it is necessary to examine how SERS intensity and reproducibility evolve in different growth scenarios. With respect to SERS-active, metal nanorod arrays created via OAD, until recently, and despite best efforts, only very small, semiordered substrates had been realised. This thesis investigates the use of large-scale, pre-patterned polymer as a template to tightly control nucleation and, in turn, the subsequent growth of Ag (and Cu) nanorods during guided OAD, to construct large-scale, highly ordered SERS-active nanorod arrays.

This chapter also examined theoretical aspects underpinning the thesis, beginning with a discussion on the theory of molecular vibration and how the interplay between it and incident light is responsible for the Raman Effect. The Raman/SERS spectrum was introduced which comprises peaks at different intensities corresponding to specific vibrational modes, the combination of which forms a unique SERS profile. A classical mathematical model of Raman scattering was then presented, after which SERS enhancement mechanisms were discussed which are responsible for Raman signal amplification.

Coupled localised surface plasmons were explored, as these are crucial for the most important enhancement mechanism in SERS, namely electromagnetic enhancement. The single molecule enhancement factor or the E^4 approximation was covered and the dielectric function of metals was derived as it is intimately linked to the ability of a metal nanoparticle to magnify an incident alternating electric field which gives rise to SERS.

Aqueous solution-based nucleation and nanoparticle growth were then considered, providing the theoretical background for Ag- and Au-agarose SERS substrate fabrication discussed in chapters two to four.

References

[1] P. J. Larkin, *Infrared and Raman Spectroscopy: Principles and Spectral Interpretation*. Waltham: Elsevier, 2011, pp. 1–11.

[2] H. Haken and H. C. Wolf, *Molecular Physics and Elements of Quantum Chemistry*, Second Ed. Berlin: Springer, 2004, pp. 257–261.

[3] M. Fan and A. G. Brolo, "Silver nanoparticles self assembly as SERS substrates with near single molecule detection limit," *Phys. Chem. Chem. Phys.*, vol. 11, no. 34, pp. 7381–7389, 2009.

[4] E. C. Le Ru and P. G. Etchegoin, *Principles of Surface-Enhanced Raman Spectroscopy and related plasmonic effects*. Oxford: Elsevier, 2009, p. 33.

[5] E. C. Le Ru and P. G. Etchegoin, *Principles of Surface-Enhanced Raman Spectroscopy and related plasmonic effects*. Oxford: Elsevier, 2009, p. 34.

[6] E. C. Le Ru and P. G. Etchegoin, *Principles of Surface-Enhanced Raman Spectroscopy and related plasmonic effects*. Oxford: Elsevier, 2009, p. 35.

[7] Horiba, "Raman spectrometer schematic." [Online]. Available: http://www.horiba.com/uk/scientific/products/raman-spectroscopy/raman-academy/raman-faqs/hardware-required/. [Accessed: 27-Aug-2014].

[8] Sigma-Aldrich, "Rhodamine 6G schematic." [Online]. Available: http://www.sigmaaldrich.com/catalog/product/aldrich/252433?lang=en&region=GB. [Accessed: 16-Apr-2015].

[9] G. Upender, R. Satyavathi, B. Raju, K. Shadak Alee, D. Narayana Rao, and C. Bansal, "Silver nanocluster films as novel SERS substrates for ultrasensitive detection of molecules," *Chem. Phys. Lett.*, vol. 511, no. 4–6, pp. 309–314, 2011.

[10] E. C. Le Ru and P. G. Etchegoin, *Principles of Surface-Enhanced Raman Spectroscopy and related plasmonic effects*. Oxford: Elsevier, 2009, p. 44.

[11] P. J. Larkin, *Infrared and Raman Spectroscopy: Principles and Spectral Interpretation*. Waltham: Elsevier, 2011, pp. 16–17.

[12] E. C. Le Ru and P. G. Etchegoin, *Principles of Surface-Enhanced Raman Spectroscopy and related plasmonic effects*. Oxford: Elsevier, 2009, p. 98.

[13] M. Fleischmann, P. J. Hendra, and A. J. McQuillan, "Raman spectra of pyridine adsorbed at a silver electrode," *Chem. Phys. Lett.*, vol. 26, no. 2, pp. 163–166, 1974.

[14] Z.-Q. Tian, B. Ren, J.-F. Li, and Z.-L. Yang, "Expanding generality of surface-enhanced Raman spectroscopy with borrowing SERS activity strategy," *Chem. Commun.*, no. 34, pp. 3514–3534, 2007.

[15] M. Keating, Y. Chen, I. A. Larmour, K. Faulds, and D. Graham, "Growth and surface-enhanced Raman scattering of Ag nanoparticle assembly in agarose gel," *Meas. Sci. Technol.*, vol. 23, no. 8, p. 084006, 2012.

[16] E. C. Le Ru and P. G. Etchegoin, *Principles of Surface-Enhanced Raman Spectroscopy and related plasmonic effects*. Oxford: Elsevier, 2009, p. 259.

[17] E. C. Le Ru and P. G. Etchegoin, *Principles of Surface-Enhanced Raman Spectroscopy and related plasmonic effects*. Oxford: Elsevier, 2009, pp. 259–260.

[18] K. L. Kelly, E. Coronado, L. L. Zhao, and G. C. Schatz, "The optical properties of metal nanoparticles: the influence of size, shape, and dielectric environment," *J. Phys. Chem. B*, vol. 107, no. 3, pp. 668–677, 2003.

[19] L.-L. Tay, J. Hulse, D. Kennedy, and J. P. Pezacki, "Surface-enhanced Raman and resonant Rayleigh scatterings from adsorbate saturated nanoparticles," *J. Phys. Chem. C*, vol. 114, no. 16, pp. 7356–7363, 2010.

[20] X. Zhang, Y. L. Chen, R.-S. Liu, and D. P. Tsai, "Plasmonic photocatalysis," *Reports Prog. Phys.*, vol. 76, no. 4, p. 046401, 2013.

[21] E. C. Le Ru and P. G. Etchegoin, *Principles of Surface-Enhanced Raman Spectroscopy and related plasmonic effects*. Oxford: Elsevier, 2009, p. 212.

[22] E. C. Le Ru and P. G. Etchegoin, *Principles of Surface-Enhanced Raman Spectroscopy and related plasmonic effects*. Oxford: Elsevier, 2009, p. 217.

[23] J. Bolton, N. Braithwaite, S. Freake, B. Lambourne, T. Smith, and M. Thorpe, *SMT359 Book 3 Electromagnetism: Electromagnetic Waves*. Cambridge: The Open University, 2006, pp. 92–95.

[24] U. Kreibig and M. Vollmer, *Optical Properties of Metal Clusters*. Berlin: Springer, 1995, pp. 14–15.

[25] E. C. Le Ru and P. G. Etchegoin, *Principles of Surface-Enhanced Raman Spectroscopy and related plasmonic effects*. Oxford: Elsevier, 2009, p. 135.

[26] U. Kreibig and M. Vollmer, *Optical Properties of Metal Clusters*. Berlin: Springer, 1995, p. 16.

[27] U. Kreibig and M. Vollmer, *Optical Properties of Metal Clusters*. Berlin: Springer, 1995, p. 17.

[28] J. Benford, J. A. Swegle, and E. Schamiloglu, *High Power Microwaves*, Second Ed. Boca Raton, FL: Taylor and Francis, 2007, p. 129.

[29] U. Kreibig and M. Vollmer, *Optical Properties of Metal Clusters*. Berlin: Springer, 1995, pp. 22–23.

[30] U. Kreibig and M. Vollmer, *Optical Properties of Metal Clusters*. Berlin: Springer, 1995, p. 8.

[31] U. Kreibig and M. Vollmer, *Optical Properties of Metal Clusters*. Berlin: Springer, 1995, p. 25.

[32] U. Kreibig and M. Vollmer, *Optical Properties of Metal Clusters*. Berlin: Springer, 1995, p. 24.

[33] E. C. Le Ru and P. G. Etchegoin, *Principles of Surface-Enhanced Raman Spectroscopy and related plasmonic effects*. Oxford: Elsevier, 2009, pp. 128–129.

[34] I. A. Larmour and D. Graham, "Surface-enhanced optical spectroscopies for bioanalysis," *Analyst*, vol. 136, no. 19, pp. 3831–3853, 2011.

[35] T. M. Devlin, *Textbook of Biochemistry With Clinical Correlations*, Seventh Ed. India: Wiley, 2011, p. 544.

[36] Z. Peng, S. Yang, and H. Yang, "Approaches to the Synthesis and Characterization of Spherical and Anisotropic Platinum Nanomaterials," in *Nanomaterials for the Life Sciences Vol. 1: Metallic Nanomaterials*, C. Kumar, Ed. Weinheim: Wiley-VCH, 2009, pp. 359–365.

[37] Z. Peng, S. Yang, and H. Yang, "Approaches to the Synthesis and Characterization of Spherical and Anisotropic Platinum Nanomaterials," in *Nanomaterials for the Life Sciences Vol. 1: Metallic Nanomaterials*, C. Kumar, Ed. Weinheim: Wiley-VCH, 2009, p. 361.

[38] Z. Peng, S. Yang, and H. Yang, "Approaches to the Synthesis and Characterization of Spherical and Anisotropic Platinum Nanomaterials," in *Nanomaterials for the Life Sciences Vol. 1: Metallic Nanomaterials*, C. Kumar, Ed. Weinheim: Wiley-VCH, 2009, p. 362.

[39] Z. Peng, S. Yang, and H. Yang, "Approaches to the Synthesis and Characterization of Spherical and Anisotropic Platinum Nanomaterials," in *Nanomaterials for the Life Sciences Vol. 1: Metallic Nanomaterials*, C. Kumar, Ed. Weinheim: Wiley-VCH, 2009, p. 364.

[40] Y. Liu, K. Kathan, W. Saad, and R. Prud'homme, "Ostwald ripening of β-carotene nanoparticles," *Phys. Rev. Lett.*, vol. 98, no. 3, p. 036102, 2007.

Chapter 2 Surface-enhanced Raman scattering of Ag nanoparticle assembly in agarose gel

This chapter begins with a general review of SERS substrates and focusses on Ag-agarose gel, which has captured a lot of attention recently due to its excellent molecular trapping capabilities and strong SERS. Ag-agarose is initially tested with several molecular probes to confirm the findings of previous work which proved it a viable SERS substrate [1], findings reinforced here by the qualitative detection of nanomolar concentrations of the dye Nile blue A (NBA) using SERRS. Despite its obvious potential however, the influence of nanoparticle growth conditions on gel structure and the resultant SERS intensity and reproducibility is not clear. The effect of altering these parameters on the SERS response is systematically investigated.

2.1 A review of SERS substrates

Broadly speaking, SERS substrates can be divided into three classes [2]:

- Metallic nanoparticles, such as colloidal solutions.
- Arrays of metallic nanostructures on a planar substrate, such as glass or silicon.
- Metallic electrodes.

The importance of electrodes leading to the discovery of SERS in the early 70s by Fleischmann *et al*. [3] is undisputed (see chapter one, section 1.3.8), but due to the relatively poor Raman enhancements they deliver, they shall not be discussed further; it is worth pointing out though that they do still find utility in investigations of chemical enhancement, and the monitoring of specific electrochemical reactions.

Of the other two classes, metallic colloidal suspensions (sols), mainly fabricated from gold or silver, are amongst the most easily produced and widely used substrates in the SERS community, and therefore have a firmly established history. Crucially, in aqueous solution or deposited on a planar surface, they lay-claim to the first ever detection of single-molecule SERS [2]. Typically, they rely on stabilising agents to prevent uncontrolled aggregation, and ultimately precipitation. Uncontrolled aggregation is highly undesirable, as it generates time-dependent and irreproducible results. Nonetheless, the largest Raman enhancements derive from small colloidal clusters (even dimers prove adequate), due to coupling of localised surface plasmons, meaning that *controlled* aggregation is sought via the deployment of aggregating agents [2]. The metal nanoparticle agarose (MNPA) gel used in this thesis, which can in some ways be considered a colloid frozen in a gel matrix, does not require such agents to engage SERS activity; the nanoparticles are held close enough to one another naturally within the matrix to facilitate coupling of localised surface plasmons. As shall be discussed in chapter three, a poor choice of aggregating agent can result in an intrinsic distortion of an analyte spectrum with potential ramifications for analysis, an obstacle which is automatically avoided when using gel substrates.

Colloid can be used to form 2D substrates by dipping, for example, planar functionalised glass or silicon supports in the colloid solution and allowing it to dry [4]. The functional groups chemisorbed to the support can fix NPs, forming a foundational monolayer, to which bifunctional ligands can be attached with one end free to fix more NPs from solution. This process can be repeated the desired number of times, to tune the substrate to a specific excitation wavelength and maximise

SERS intensity. Such substrates have a fixed geometry, in contrast with the possibly complex dynamics present in Ag or Au colloidal solutions.

Another type of planar substrate is fabricated using electron beam lithography (EBL), and shown in figure 2.1 from [4].

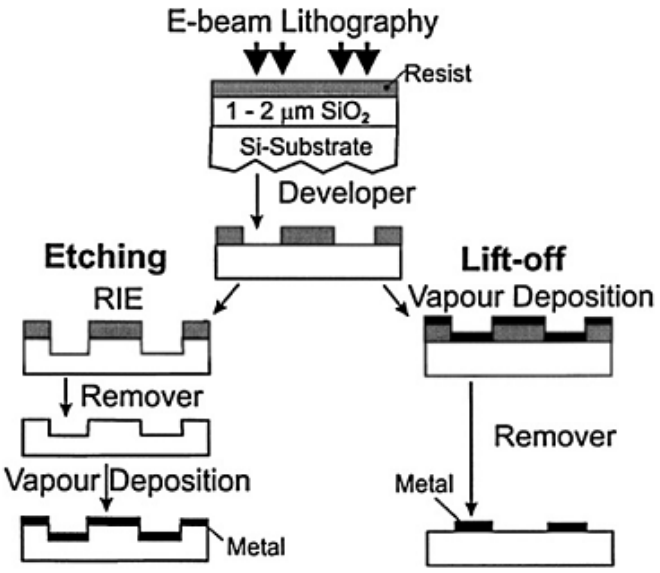

Figure 2.1. Two schemes for manufacture of SERS substrates using EBL, taken from [4].

Figure 2.1 shows two variations of the EBL technique where a nano-pattern is written onto a substrate using an electron beam, upon which metal is ultimately overlaid rendering the substrate SERS-active. Substrates of this type achieve tight control over geometry and homogeneity (reproducibility), but, contrary to the planar metallic nanoarrays described later in this thesis, this comes at a cost of low throughput, high expense, and small working areas (in the order of 10s of square micrometres) which are not amenable to applications such as sensing [5]. In contrast, arrays such as the silver and copper nanorod arrays produced for this thesis, achieve both high uniformity and large surface areas (in the order of square centimetres).

In addition to EBL, two other lithography techniques, namely "island lithography" and "nanosphere lithography" are commonly used to construct SERS nanoarrays. The main difference between these and EBL, is that these arrays form via self-assembly as opposed to being written onto a blank substrate. Island lithography for example, produces an array on a blank support by electron beam evaporation (sputtering), resulting in the growth of metal "islands" on the surface whose interstitial gaps promote LSP-coupling under laser excitation [6]. While this technique produces strong and reproducible SERS, it should be highlighted that unlike ordered metallic nanorod arrays for example, whose construction and SERS properties are explored in chapter five, the geometries of the metal islands laid down are random. This immediately makes it more difficult to control island and gap size, two geometrical parameters crucial to the SERS response.

Nanosphere lithography is another technique which uses self-assembly to construct substrates. The particular procedure is illustrated in figure 2.2 (taken from [7]).

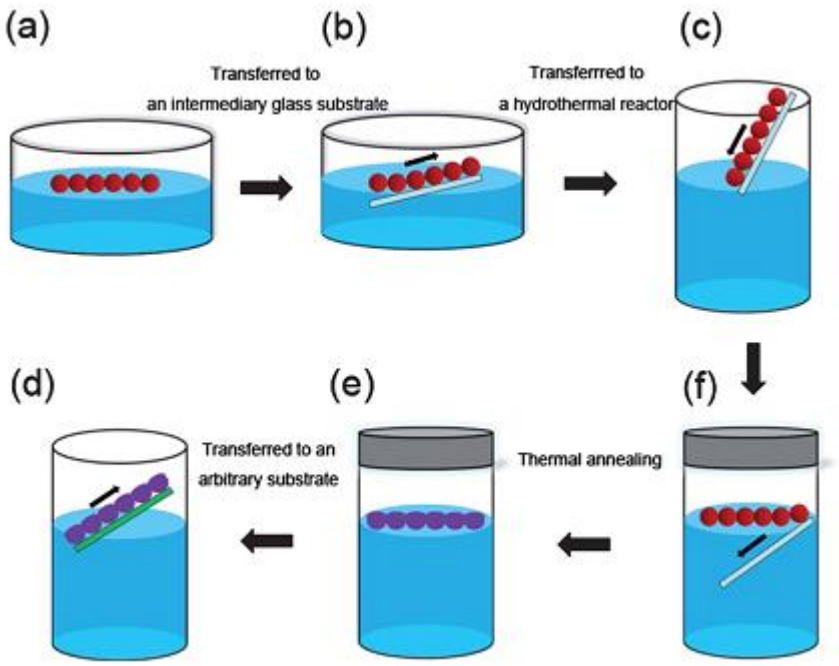

Figure 2.2. Schematic of the nanosphere lithography fabrication process in [7].

Dielectric polystyrene nanospheres suspended in solution, self-assemble into a hexagonal lattice at the air/water interface, and are transferred to a temporary glass substrate to transport them to a hydrothermal reactor. The sealed reactor permits water inside to be heated to above 100^{o}C and annealing of the polystyrene lattice takes place. The newly annealed polystyrene spheres can then be transferred to a chosen support. By controlling the annealing time and temperature, the size and shape of the interstitial gaps can be optimised prior to metal deposition. Evaporation of metal onto the mask-array (at 0^{o} to the substrate normal) is conducted, after which the mask is removed from the support, leaving behind an ordered array of SERS-active metallic nanostructures whose shape and volume precisely mirror those of the previously existing interstices.

While the authors effectively demonstrate that nanosphere lithography is highly capable of producing ordered Ag arrays on a large scale, which clearly has implications for SERS and plasmonics in general, they nonetheless do not present detailed results concerning the SERS part of the experiment. They do correlate the maximum SERS signal to an optimised substrate, and provide detailed information concerning the SERS setup as well as displaying the relative SERS intensities of different substrates, but they fail to give any indication as to the reproducibility of the substrate, optimised for intensity. One of the key parameters in SERS for applications, and one of the most difficult to control, is reproducibility. Without this information, it is impossible to judge properly just how effective the substrate might be or gauge its potential suitability for applications.

In addition, there is a note of caution regarding the cleaning protocols for the substrates prior to nanosphere deposition. To maximise hydrophobicity, the substrate is cleaned in piranha solution (98% H_2SO_4 + 30% H_2O_2 in a 3:1 volume ratio). This cocktail is excellent at removing any remaining dirt from glass in the final stages of cleaning, but great caution must be exercised when using it in the lab, as the solution is extremely toxic and becomes explosive with trace quantities of organics. Only small amounts should be used therefore with the utmost care [8], [9]. This contrasts with the cleaning protocols described in this thesis, which only required a comparatively benign 3% solution of DECON 90 and distilled water for immersion and rinsing of glassware and other apparatus respectively.

One final sub-class of planar substrates which has attracted great interest over the last few years is metal nanorods deposited via oblique angle deposition (OAD). Chapter five concentrates on these in detail, and they are mentioned here only briefly

to complete the all-round picture of SERS substrates under discussion. Figure 2.3 schematically depicts the fabrication process and displays an SEM surface image of Ag nanorods deposited on a glass substrate, both taken from [10].

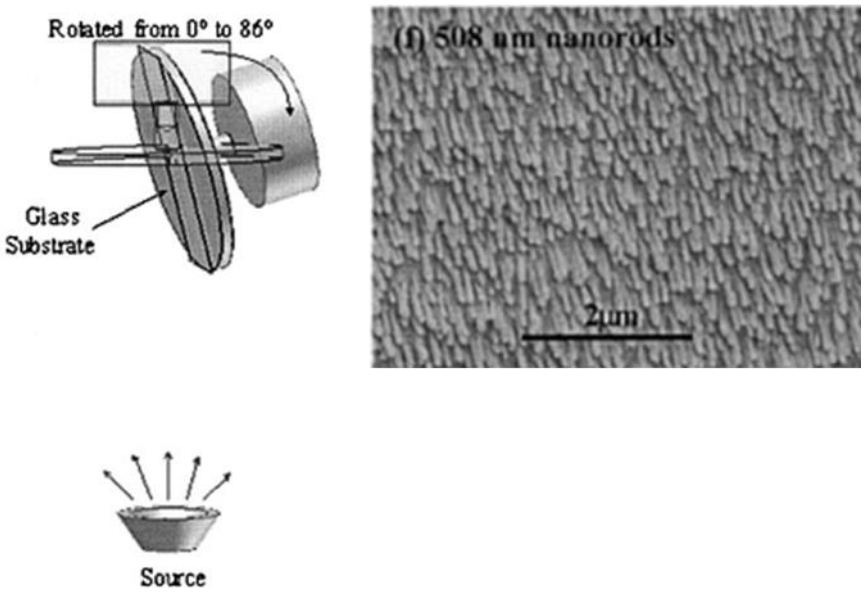

Figure 2.3. Left: setup to fabricate metal nanorods using OAD (adapted from the original image). Right: SEM surface image of Ag nanorods; both images are from [10].

Metal is placed in the source under high vacuum and irradiated by an electron beam (not shown) which vaporises the metal, creating a plume which travels towards the glass substrate. The substrate can be rotated through 0 to 90 degrees, allowing films of various deposition angles to be constructed.

Particularly, aligned Ag nanorod arrays created by OAD have recently been demonstrated to be highly effective SERS substrates [11]–[14]. Producing strong SERS with high sensitivity, these arrays also show good reproducibility in signal strength and can be fabricated with substantial uniform areas for applications such as sensing. In addition, the OAD approach is relatively straightforward compared with

other methods employed to generate nanostructured arrays, such as photolithography or EBL, and avoids the time-consuming, complex and expensive steps inherent to those methods [15], [16]. Ag nanorods have also been applied successfully in 'real world' applications, for example, in the detection and differentiation of several human pathogens [17]. Moreover, *highly ordered*, SERS-active copper, as well as silver nanorod arrays have been fabricated by OAD, using patterned polymer as a template to guide nucleation [5], which could offer the possibility of tightly controlling nanorod diameter and gap size, two geometrical parameters inextricably linked to the SERS response. Using copper in particular to fabricate ordered SERS arrays, also has a clear financial incentive due to its considerably lower scrap value compared with gold or silver, the two other most commonly used SERS metals [18]. Ordered copper and silver SERS nanorod arrays are discussed in chapter five.

2.1.1 Agarose gel

Another SERS platform which is relatively new but which has already been proven to be highly effective is Ag-agarose gel. Agarose is a linear polysaccharide which, together with a heterogeneous mixture of smaller molecules called agaropectin constitute agar, a substance gained from algae [19], [20].

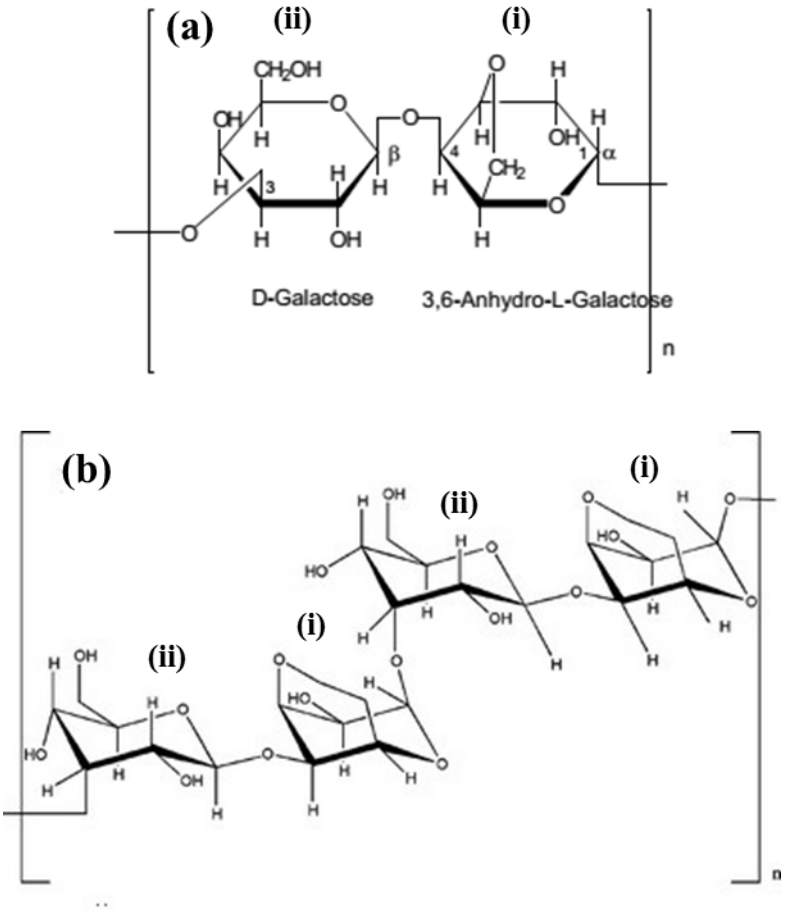

Figure 2.4. (a) A monomer unit of agarose in a Haworth projection consisting of linked sugars, (i) 3,6-Anhydro-L-Galactose and (ii) D-Galactose [21]. Two linked monomers are shown in (b) a "puckered-ring" representation, with the sugars again denoted by Roman numerals (i) and (ii) [22].

The molecular structure of agarose in figure 2.4 (a) shows the monomer unit consisting of linked sugars, (i) 3,6-Anhydro-L-Galactose and (ii) D-Galactose [21]. In figure 2.4 (b), two linked monomers are shown in a "puckered-ring" representation to give a better idea of atomic orientation in space [22]. Various types of agarose have different melting and gelation temperatures. The variety used in this thesis (Type IX-A: Ultra-low Gelling Temperature, Sigma-Aldrich), gelates at very low temperatures (around 8 – 17 ^{o} C depending on the concentration), which is why it

was always placed in the fridge at 4^{o}C to set. Before it can set, agarose must be heated in water to a high enough temperature in order to dissolve. When hot, it exhibits semi-flexible polymer characteristics, and upon cooling, individual polymer chains wind themselves into double helices that come together to form fibrils, producing a water-filled gel. Fibrils arrange themselves to form a matrix which regulates gel pore size as a function of agarose concentration [23].

2.1.2 Ag-agarose as a SERS substrate

The porous gel structure permits silver nanoparticles (AgNPs) to form *in situ* inside nano-sized pores within the agarose matrix, with larger nanoparticles being trapped in the water phase of the gel while smaller nanoparticles pepper the polymeric network [1]. AgNPs are naturally situated close enough to one another to facilitate coupling of localised surface plasmons, thus dispensing with the need for aggregating agents to engage SERS activity; moreover, the matrix constrains the nanoparticles, hindering aggregation so that capping agents are not required which might otherwise seriously interfere with molecular adsorption on the nanoparticle surface [24], [25]. In addition to providing significant nanoparticle stability, preparation of metal NPs within a confined area such as the polymeric network of a gel offers a high degree of control over NP size, morphology and overall 3-dimensional structure [26], [27], with a gel matrix proving to be a superb molecular trap. Ag-agarose for example has been shown to detect analytes such as the potent environmental toxin dichlorodiphenyl-trichloroethane (DDT) which does not adsorb onto gold or silver, a characteristic which up until now has precluded it from SERS analysis [1]. In such cases, analytes with a low affinity for noble metals can be

mechanically trapped in the vicinity of the NPs during shrinkage of the matrix either by physical or chemical means, thus permitting detection [1], [28]. An in-depth review of the role of metal/gel nanocomposites as SERS substrates, particularly those comprised of metal/agarose, is given in chapter three.

Added to its efficacy in SERS analysis is the inexpensive and straightforward production of metal nanocomposite agarose. This plus its ease of preparation and sample handling, combine to make it a robust SERS platform with great potential.

2.2 Testing SERS activity of Ag-agarose

2.2.1 Introduction

Ag-agarose was initially fabricated to replicate work by Aldeanueva-Potel *et al.* [1], where they successfully used silver nanoparticle-agarose (AgNPA), or simply "Ag-agarose", as a SERS substrate to detect the presence of several molecular probes. Numerous advantages of this relatively novel substrate have already been highlighted, and part of the review later in chapter three discusses metal/gel SERS substrates in general with a special emphasis on SERS-active metal-agarose.

2.2.2 Experimental

2.2.2.1 Preparation of Ag-agarose

All chemicals were purchased from Sigma Aldrich and used without further purification: Sodium borohydride (SB, $NaBH_4$ – purum p.a., ≥ 96% (gas-volumetric)), silver nitrate ReagentPlus grade ($AgNO_3$ ≥ 99.0% titration), agarose

type IX-A (ultra-low gelling temperature), *trans*-1,2-bis(4-pyridyl)ethylene (BPE – assay 97%), D-amphetamine-d_3 sulfate salt (amphetamine, 98 atom % D), Nile blue A (NBA, dye content, ≥75%), rhodamine 6G (R6G, dye content, 99%).

Silver-loaded agarose gels were prepared using a method similar to that used by Aldeanueva-Potel *et al*. [1]. A 5.4% w/v solution of agarose gel was prepared by placing 0.54 g of agarose powder in 10 ml of distilled water. The mixture was heated to about 90 ^{o}C and stirred gently until it began to boil, after which it was poured carefully into a standard plastic cuvette (path length 10 mm) and placed in the fridge, where it cooled for 1 h at 4 ^{o} C. Once solidified, the gel was carefully removed from the cuvette with a thin spatula, and a sharp blade was used to cut samples about 1.5 × 10 × 20 mm^3. To ensure that silver ions had diffused uniformly throughout the gel and that they had been completely reduced, gel samples were immersed for 24 h each in 15 mM silver nitrate and 500 mM SB (1 sample per 6 ml), resulting in gels of a light yellowish-brown. Upon removal from the SB solution, Ag-agarose was washed in distilled water and dialysed for 20 h before being placed in an analyte solution (6 ml) overnight prior to SERS analysis.

2.2.2.2 UV-VIS spectroscopy

Absorption spectra were recorded on a Jasco V-660 UV-VIS spectrometer, using the same method as Aldeanueva-Potel *et al.* [1], whereupon a small piece of blank agarose gel was compressed between two fused silica slides and used as a baseline.

2.2.2.3 SERS analysis

SERS spectra of three probe molecules – NBA, R6G and amphetamine were recorded on a Leica DM/LM microscope equipped with an Olympus 20x/N.A. 0.4 long-working distance objective to collect 180^{o} backscattered light. The spectrometer was a Renishaw Ramascope System 2000 with the 632.8 nm line of a helium-neon laser as the excitation source. At 100% power, the unfocussed output at the sample was measured to be approximately 4 mW. Dielectric edge filters were used to reject the Rayleigh scattered light. The following laser powers and collection times were used in section 2.2.3.2: NBA (approximately 0.5 mW, 0.5 s), R6G (approximately 2 mW, 2 s) amphetamine (approximately 2 mW, 1s). For the qualitative limit-of-detection experiment in 2.2.3.3, the power and collection time were approximately 0.5 mW, and 0.5 s

2.2.3 Results and discussion

2.2.3.1 UV-VIS spectroscopy

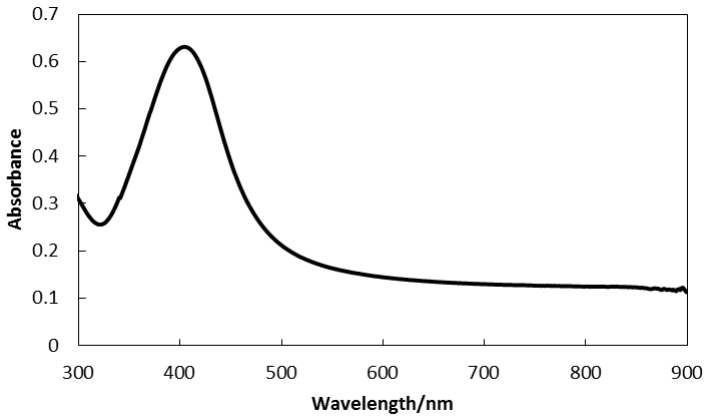

Figure 2.5. An absorption spectrum of 15 mM Ag-agarose gel.

Figure 2.5 is an absorption spectrum of 15 mM Ag-agarose, displaying the characteristic Ag nanoparticle plasmon band around 400 nm [29], signifying that silver-loading by reduction of Ag^{+} ions has taken place.

2.2.3.2 Testing SERS activity of Ag-agarose

Fifteen mM Ag-agarose was tested qualitatively for SERS activity using two common SERS probes, Nile blue A (NBA) and rhodamine 6G (R6G), in addition to an atypical probe, namely amphetamine sulphate, a class B drug in the UK [30]. Figure 2.6 is a SERS spectrum of the Ag-agarose control, recorded over the same wavenumber range as that of the amphetamine spectrum.

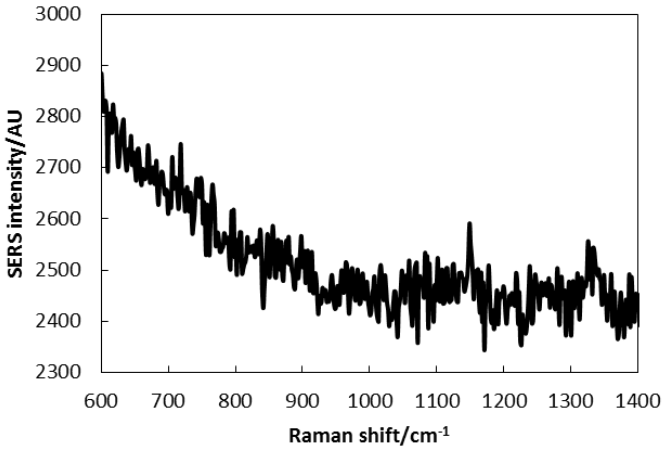

Figure 2.6. A SERS spectrum of Ag-agarose, taken at 633 nm excitation at approximately 2 mW, over 1s.

The spectrum is virtually featureless, and contains none of the distinct peaks present in the "Ag-agarose + amphetamine" spectrum in figure 2.7. Although the control spectra for "Ag-agarose + NBA or R6G or amphetamine" were recorded over

different wavenumber ranges, each was similarly featureless possessing no distinct analyte bands.

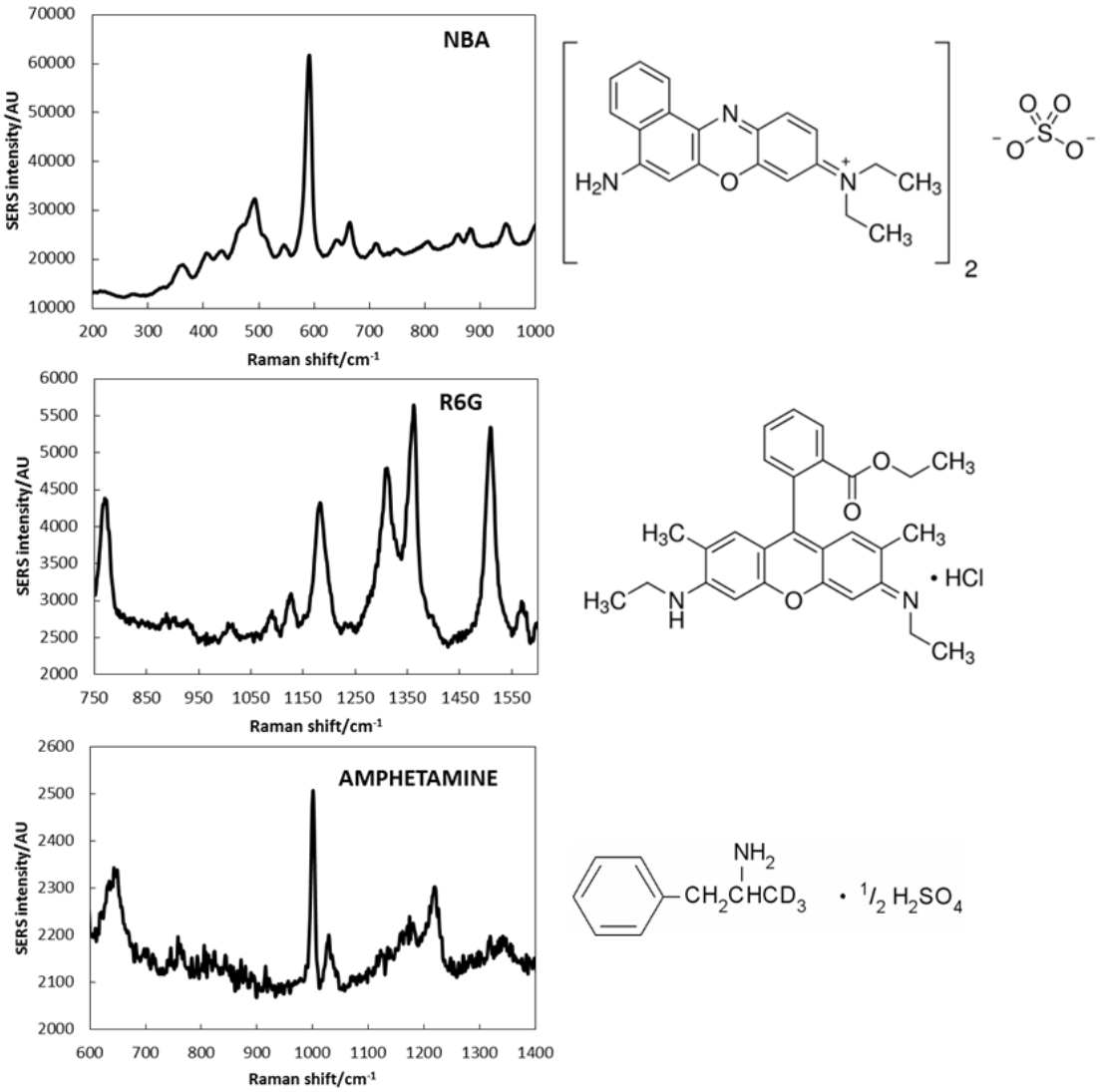

Figure 2.7. Various representative SERS spectra as-labelled using 15 mM Ag-agarose as a substrate. The aqueous concentrations and references for the molecular probe schematics are respectively, 10^{-5} M NBA [31], 10^{-6} M R6G [32] and 10^{-4} M amphetamine sulphate [33]. NBA and R6G are individual representative spectra and amphetamine comprises six averaged spectra. All spectra were recorded using 633 nm excitation with the following laser powers and collection times: NBA (approximately 0.5 mW, 0.5 s), R6G (approximately 2 mW, 2 s), and amphetamine (approximately 2 mW, 1s).

Ag-agarose readily generated SERS spectra for all three analytes as shown in figure 2.7. Molecular schematics are positioned to the right of the spectra: NBA [31], R6G [32] and amphetamine sulphate [33], with characteristic peaks matching those in the literature [18], [34], [35]. Amphetamine sulphate (10^{-4} M (aq)) was chosen as an atypical probe to test the ability of the substrate to qualitatively identify "non-SERS" analytes of potential interest, in this case a class B drug [30]. Six spectra from different locations on the gel were averaged to smooth the signal. While this is a qualitative rather than a quantitative analysis, it does confirm previous findings by Aldeanueva-Potel *et al.* [1] that Ag-agarose is indeed a viable SERS substrate.

2.2.3.3 SERRS of NBA

A short experiment was conducted to qualitatively test the sensitivity of 15 mM Ag-agarose. Concentrations of (8.5 ×) 10^{-6}, 10^{-7}, 10^{-8} and 10^{-9} M (aq) NBA were synthesised by sequential dilution and interrogated using 633 nm excitation.

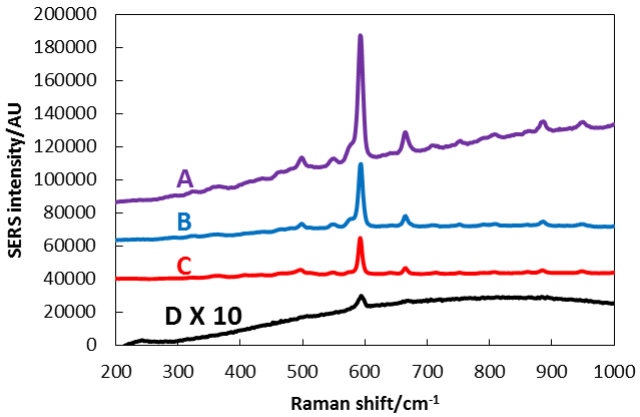

Figure 2.8. SERRS of NBA recorded at approximately 0.5 mW, at 0.5 s with decreasing concentration: (8.5 ×) (A) 10^{-6}, (B) 10^{-7}, (C) 10^{-8} and (D) 10^{-9} M (aq). (A), (B), and (C) are averaged from two spectra collected from the surface of the substrate and (D) is averaged from four. The spectra are not background-corrected, but have been shifted for clarity and (D), 8.5 × 10^{-9} M has been scaled up by a factor of 10.

Figure 2.8 shows surface-enhanced resonance Raman scattering (SERRS) of NBA with decreasing concentration. The main peak at 592 cm^{-1} becomes smaller as the solution becomes less concentrated, although it should be remembered that this is a qualitative rather than a quantitative analysis, and that spectra (A), (B) and (C) in figure 2.8 are averaged from only two individual NBA spectra, so this trend could vary. Only the peak at 592 cm^{-1} remains at 8.5×10^{-9} M. This can be seen more clearly in figure 2.9 (a), where the spectrum is averaged from four spectra. The qualitative SERRS limit of detection (LOD) of NBA in this experiment of around 8.5×10^{-9} M is similar to that observed by Fan and Brolo (5.7×10^{-9} M) [34], who used a multi-layered AgNP assembly on glass with 633 nm excitation. Resonance Raman as opposed to surface-enhanced Raman scattering occurs, because NBA has an electronic transition in the same region as the excitation wavelength of 633 nm [34]. Chemical species which would otherwise fluoresce and interfere with the SERS signal under these resonant conditions however, are effectively quenched if they are bound to the nanoparticle surface. Non-bound molecules however still fluoresce, causing interference [36].

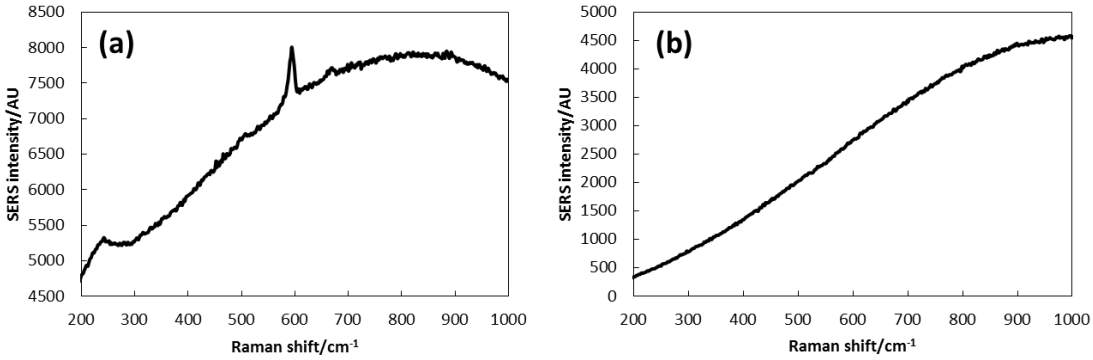

Figure 2.9. SERRS at 633 nm, at approximately 0.5 mW, over 0.5 s of (a) 8.5×10^{-9} M NBA averaged from four spectra collected from across the substrate, and (b) a single featureless spectrum of 8.5×10^{-10} M NBA.

Figure 2.9 (a) shows the just-observable 592 cm^{-1} peak of NBA (larger than 3 standard deviations of the fluorescent background noise of the molecule [37]) at 8.5 × 10^{-9} M concentration, which is about to be swamped by the background. Figure 2.9 (b) shows SERRS of 8.5 × 10^{-10} M NBA; the 592 cm^{-1} peak has disappeared, meaning the LOD must lie somewhere between 8.5 × 10^{-9} and 8.5 × 10^{-10} M.

2.2.4 Conclusion

Ag-agarose gel was fabricated to confirm its viability as a SERS substrate observed in a previous study. The gel readily generated SERS spectra for three molecular probes, NBA, R6G and amphetamine sulphate with characteristic peaks matching those in the literature. Amphetamine (10^{-4} M (aq)) was chosen as an atypical probe to test the ability of the substrate to qualitatively identify "non-SERS" analytes of potential interest, in this case a class B drug. NBA at nanomolar concentrations was qualitatively detected using SERRS, reinforcing the viability of the substrate.

2.3 Growth and surface-enhanced Raman scattering of Ag nanoparticle assembly in agarose gel

2.3.1 Introduction

As mentioned at the beginning of the chapter, the influence of nanoparticle growth conditions on Ag-agarose structure and the associated SERS response is not clear. If the gel is to find utility in applications, it is first necessary to examine how SERS intensity and reproducibility evolve under different growth scenarios. In this

section, the effect of silver nitrate feed solution concentration on nanoparticle morphology, gel homogeneity, SERS signal intensity and reproducibility is systematically investigated.

2.3.2 Experimental

All chemicals were purchased from Sigma Aldrich, used without further purification and are listed in section 2.2.2.1. Blank agarose squares (≈ 1.5 × 10 × 10 mm^3) were fabricated using the method described in section 2.2.2.1. Samples were immersed sequentially overnight in $AgNO_3$ and $NaBH_4$ solutions (each 1 square per 3 ml, with a molar ratio [$AgNO_3$]:[$NaBH_4$] = 1:1, and concentrations 10, 20, 40, 60, 80, 100, 150, 200, 250, 300, 350, 400, 450 and 500 mM). During reduction, the higher-concentration samples of 250 mM and above produced so much gas so quickly to varying degrees that they "inflated", and the next day there existed a white froth on the top of the solution upon which the samples floated. Samples were dialysed for 20 h and placed overnight in *trans*-1,2-bis(4-pyridyl)ethylene (BPE) before SERS analysis. The [$AgNO_3$]:[$NaBH_4$] molar ratio was chosen to be in line with that used by Aldeanueva-Potel *et al.* [1].

2.3.2.1 SERS of Ag-agarose

Trans-1,2-bis(4-pyridyl)ethylene (BPE) was chosen as a SERS probe, as its absorbance maximum is around 280 nm with absorbance tending to zero at around 325 nm [38], well away from the excitation wavelength of 633 nm used in the experiment. This prevents contributions to SERS intensity originating from resonance effects (electronic transitions of the probe molecule which overlap the

excitation wavelength), so that signal strength arises purely from the size and arrangement of AgNPs within the agarose matrix. SERS spectra were recorded using the same setup as in 2.2.2.3. At 100% power, the unfocussed output was measured to be approximately 4.8 mW at the sample. SERS intensity of BPE was recorded by measuring the height of the 1200 cm^{-1} peak. Analysis was carried out using OriginPro 8.5 software and the peak height was averaged from 25 baseline-corrected spectra per silver nitrate concentration taken from different locations on the gel sample. Laser power was maintained at 1.2 mW and integration time was adjusted from 5 to 0.2 s to prevent signal saturation. It should be noted that under these conditions, no evidence of gel scorching was observed upon examination through the microscope. All samples were gently patted dry on filter paper before analysis. All spectra were corrected to an integration time of 1 s for comparison. In an attempt to shorten the fabrication period, a comparative blank gel sample was immersed for 3 h each in 250 mM silver nitrate and SB, followed by rinsing and dialysis in distilled water for 45 minutes.

2.3.2.2 TEM and UV-VIS spectroscopy

Absorption spectra were taken using a Jasco V-660 UV-VIS spectrometer. The samples were prepared using the same method as Aldeanueva-Potel *et al.* [1]. A small piece of blank agarose gel was compressed between two fused silica slides and used as a baseline. The same was done for silver gels of each silver nitrate feed concentration and their spectra recorded. Transmission electron micrographs were taken with a FEI Tecnai T20 TEM with a LaB_6 filament and an accelerating voltage of 200 kV. Images were captured with a Megaview Soft Imaging System and a

Gatan Image Filter with an exposure time of 2.0 s. Gel samples were positioned on carbon-coated copper grid substrates and vacuum dried before analysis. ImageJ, the public domain software (version 1.46a), was used to measure nanoparticle size. Size distributions are quoted as the mean measurement ± the standard deviation.

2.3.3 Results and discussion

A representative absorption spectrum, in this case silver agarose from a 100 mM silver nitrate feed solution or 100 mM gel for ease of reference, is shown in figure 2.10.

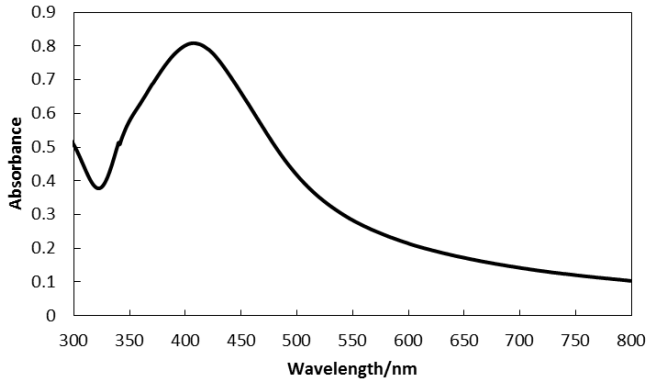

Figure 2.10. UV-vis absorption spectrum of 100 mM Ag gel.

Spectra were taken of all silver nitrate concentration gels, which confirmed that silver-loading by reduction of Ag^+ ions had taken place as shown by the presence of the plasmon band around 400 nm. The gels were yellowish to dark brown depending on the concentration of the $AgNO_3$ feed solution. Due both to the nature of the gel and sample preparation, it was not possible to make a quantitative comparison in the absorption intensity, but this is not the subject of the present study. After confirmation of silver-loading, SERS was conducted on the Ag-gels using 1.00×10^{-5} M BPE (aq) as a Raman reporter. A representative SERS spectrum of

BPE using Ag gel, along with the molecular schematic of BPE (inset) is shown in figure 2.11.

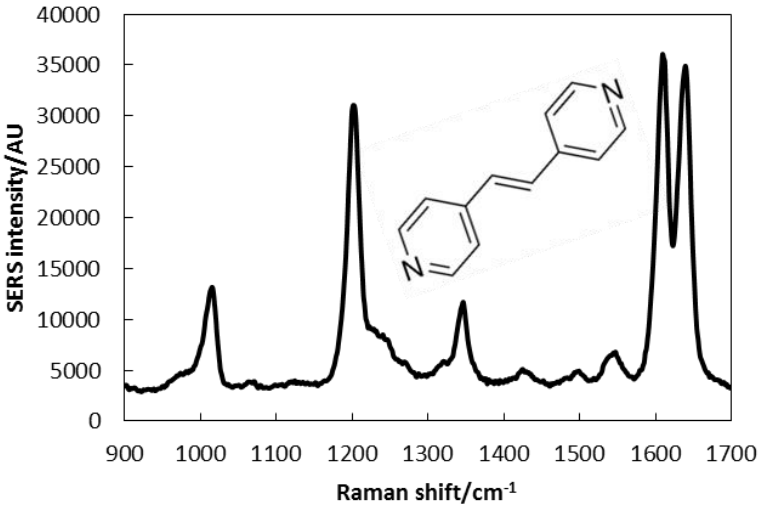

Figure 2.11. Representative SERS spectrum of 10^{-5} M BPE in 200 mM gel, along with the molecular structure of BPE (inset – taken from [38]).

The most prominent vibrational modes of BPE appear in figure 2.11 at 1200, 1607, and 1637 cm^{-1} corresponding to the C = C stretching, aromatic ring stretching and in-plane ring mode respectively [39]. A plot of SERS intensity versus $AgNO_3$ concentration is shown in figure 2.12

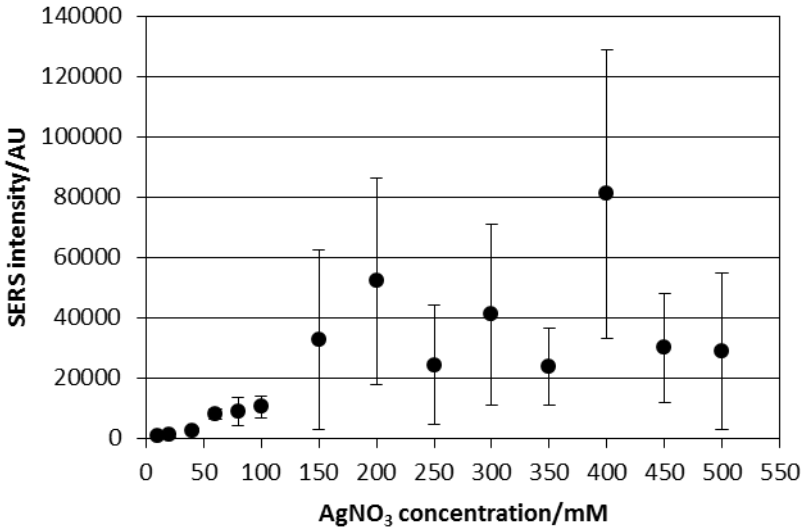

Figure 2.12. SERS intensity of the 1200 cm^{-1} peak of BPE versus $AgNO_3$ concentration.

Error bars on the graph in figure 2.12 are the standard deviations of 25 SERS intensity measurements. The graph shows that intensity rises substantially as a function of silver nitrate feed solution concentration. There is a steady rise between 10 and 100 mM, magnified for clarity in figure 2.13, after which values fluctuate with no subsequent overall increase after 150 mM.

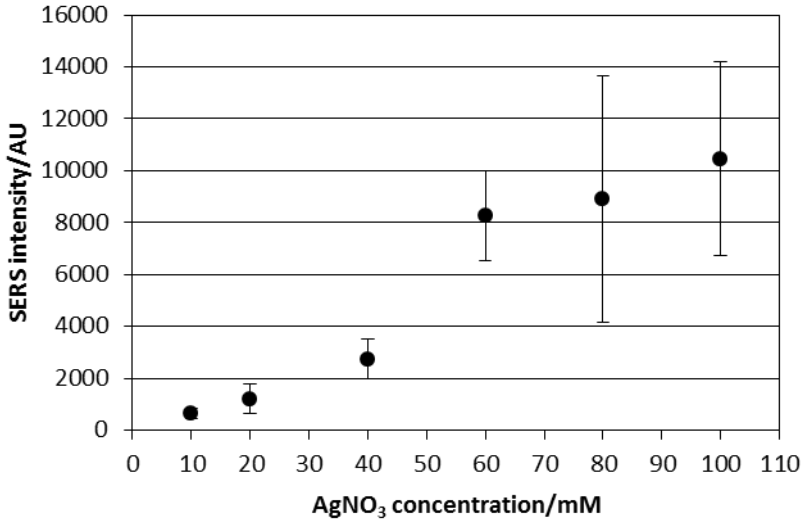

Figure 2.13. SERS intensity for the range 10 – 100 mM $AgNO_3$.

It is interesting at this point to note that 250 mM Ag-agarose prepared in the control experiment with greatly reduced gel immersion and dialysing times provided a similar average SERS intensity (merely 13% less) compared with gel fabricated using the established method. In addition, the SERS signal intensity % relative standard deviations (%RSDs) for both methods were also very similar, being about 56% and 49% respectively. This shows that fabrication time can be greatly reduced from days to hours without seriously impacting the SERS response.

Further structural study using TEM analysis was carried out to understand the rise in signal strength with feed concentration. Figure 2.14 shows TEM micrographs taken from gels of various $AgNO_3$ concentrations together with their corresponding size distributions.

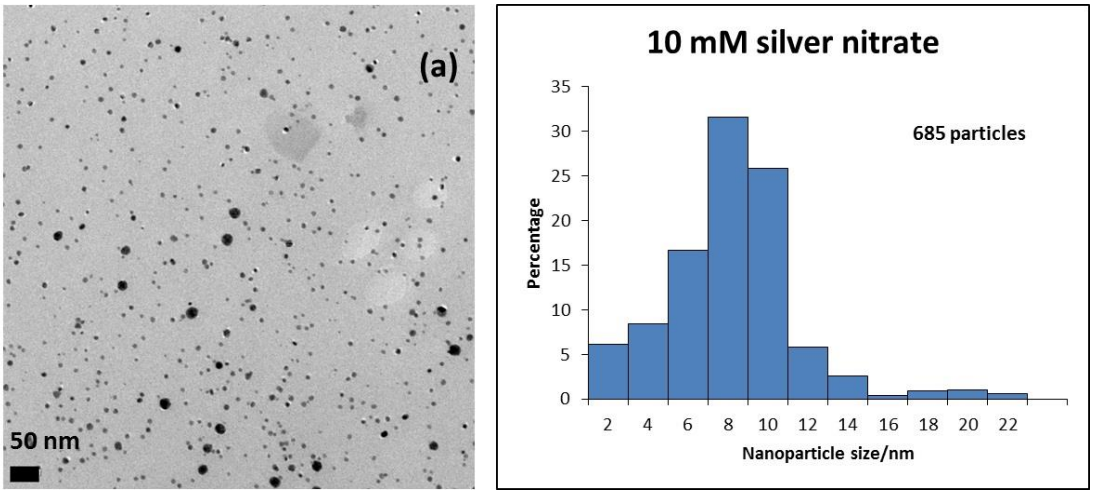

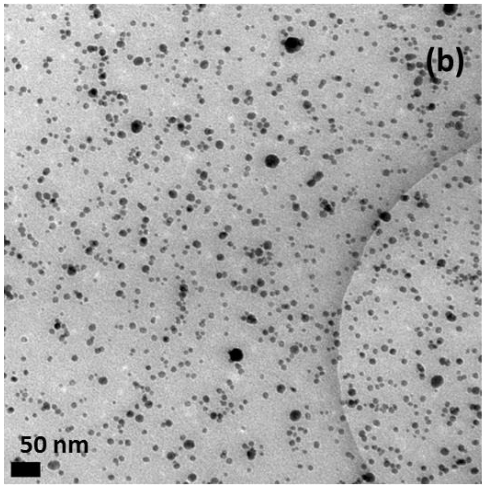
(b)
50 nm

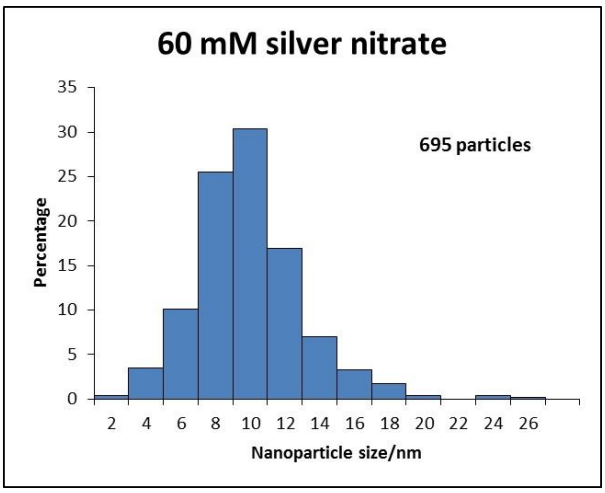
60 mM silver nitrate
695 particles
Percentage
Nanoparticle size/nm
0
5
10
15
20
25
30
35
2 4 6 8 10 12 14 16 18 20 22 24 26

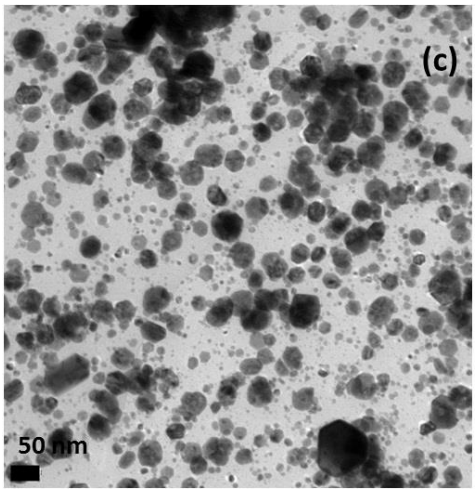
(c)
50 nm

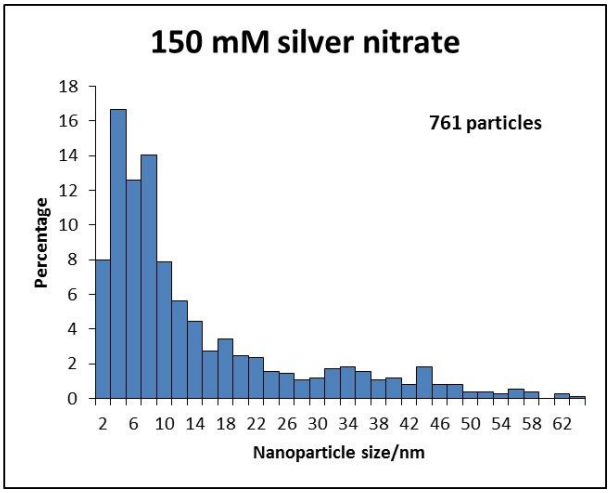
150 mM silver nitrate
761 particles
Percentage
Nanoparticle size/nm
0
2
4
6
8
10
12
14
16
18
2 6 10 14 18 22 26 30 34 38 42 46 50 54 58 62

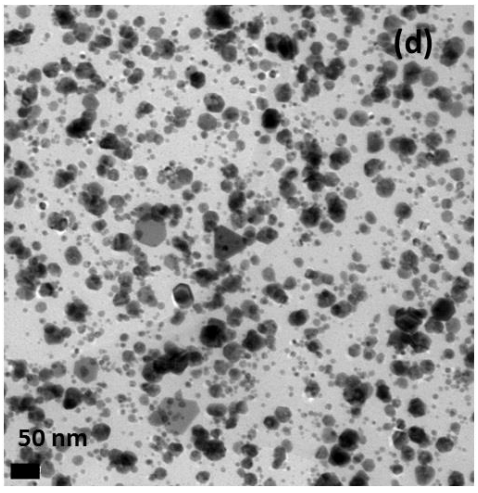
(d)
50 nm

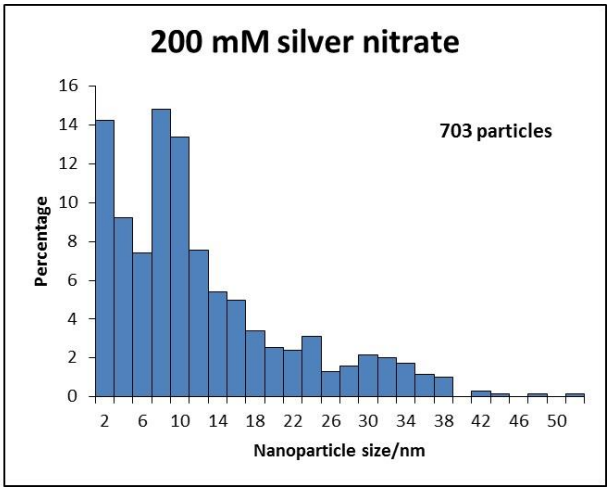
200 mM silver nitrate
703 particles
Percentage
Nanoparticle size/nm
0
2
4
6
8
10
12
14
16
2 6 10 14 18 22 26 30 34 38 42 46 50

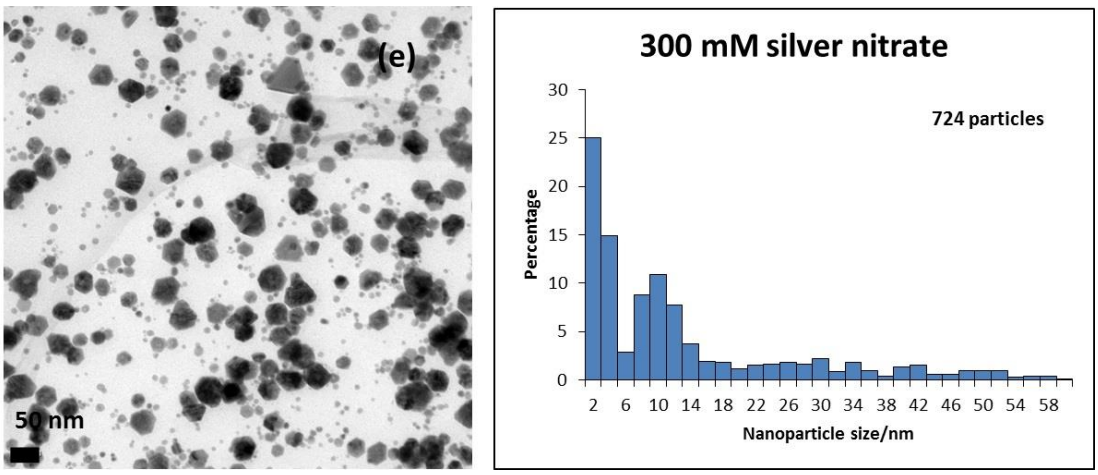

Figure 2.14. TEM images of (a) 10, (b) 60, (c) 150, (d) 200 and (e) 300 mM gels with their corresponding size distributions and the number of particles measured for each. All images are at the same scale. The scale bar on the bottom left is 50 nm.

Table 2.1 The size distribution of nanoparticles in Ag gel from different $AgNO_3$ concentrations.

$AgNO_3$ concentration/mM	Average size/nm	Standard deviation/nm	%RSD
10	7.2	3.2	44.8
60	9.0	3.2	36.2
150	13.4	13.7	102.1
200	11.4	10.4	91.1
300	12.1	13.6	112.4

Average particle size, standard deviation and % relative standard deviation are summarised in table 2.1. There is an increase in size from 7.2 ± 3.2 nm to 11.4 ± 10.4 nm from the 10 mM to the 200 mM gel – the concentration at which maximum SERS intensity occurs (excluding the 400 mM outlier). The average nanoparticle size peaks at 13.4 ± 13.7 nm for the 150 mM gel. Generally, the larger a metal nanoparticle is, the greater its capability of Raman enhancement [40] so an increase in average particle size, although modest, does contribute towards the rise in SERS intensity. More important however, are the shapes of the size distributions

themselves. The distributions of the lower-concentration gels, namely the 10 and 60 mM gels, closely approximate a normal curve with comparatively small %RSDs around 40% and maximum particle size around 20 nm. Those of the higher-concentration gels, namely the 150, 200 and 300 mM gels however are all highly skewed, having much larger %RSDs at around 100% and tails covering a wide range of up to 50 nm or more. Although the higher concentration gels possess significantly large numbers of small nanoparticles, they have what the 10 and 60 mM gels lack – particles of up to and over 50 nm.

As nanoparticles become larger and greater in number, the rise in signal strength may originate from either greater molecular adsorption with increasing nanoparticle surface area or increased 'hotspot' density via increasing aggregation or a combination of the two. Figure 2.15 plots the ratio of average SERS intensity to total nanoparticle surface area (with nanoparticles modelled as simple spheres) per unit area of gel measured, as a function of feed concentration.

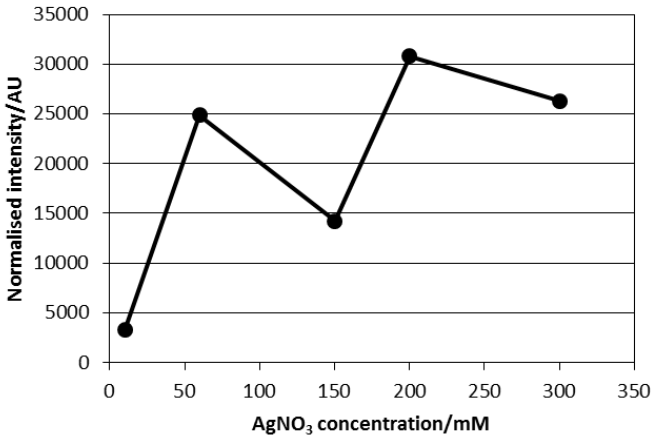

Figure 2.15. The ratio of average SERS signal intensity to total nanoparticle surface area per unit area of gel measured (with nanoparticles modelled as simple spheres), as a function of feed concentration for (10, 60, 150, 200 and 300 mM gels).

An overall increasing trend implies that the rise in signal strength originates mainly from the enhanced local electromagnetic field within ‘hotspots’.

Indeed, larger particles produce a stronger SERS response on their own compared to their smaller solitary counterparts and are found solely in the higher-concentration gels where they have a much stronger tendency to aggregate. Formation of clumps and chains with each other and with smaller particles means they generate significantly more hotspots than smaller, less-aggregated particles in lower-concentration samples. In addition, the geometry of larger particles most likely increases the number of hotspots even further via the so-called ‘lightning rod effect’ [41]. Lower-concentration gels consist of mainly spheres, while higher-concentration gels include a significant proportion of nonspherical crystals. The electromagnetic field for spherical particles is evenly distributed over the entire surface, but in nonspherical particles the distribution is uneven [29], with fields at sharp metallic structures being significantly stronger [41]. Therefore, the geometry of these structures must also make some contribution towards Raman enhancement.

Agglomerations in the lower-concentration gels also exist, but as stated, these samples lack larger particles and are much less prone to aggregation. However, the 60 mM sample produces an intensity of about 13 times that of the 10 mM sample. Figure 2.14 (a) and (b) suggests that this stronger response must originate mainly from a combination of increased particle loading and moderate aggregation. In respect of the higher-concentration gels, the 200 mM sample produces a signal about 80 and 6 times that of the 10 mM and 60 mM samples respectively. TEM images confirm that SERS intensity in higher-concentration samples is undoubtedly linked to large aggregates which give rise to a higher density of ‘hotspots’. Figure 2.16

illustrates the different degrees of aggregation in lower- and higher-concentration gels.

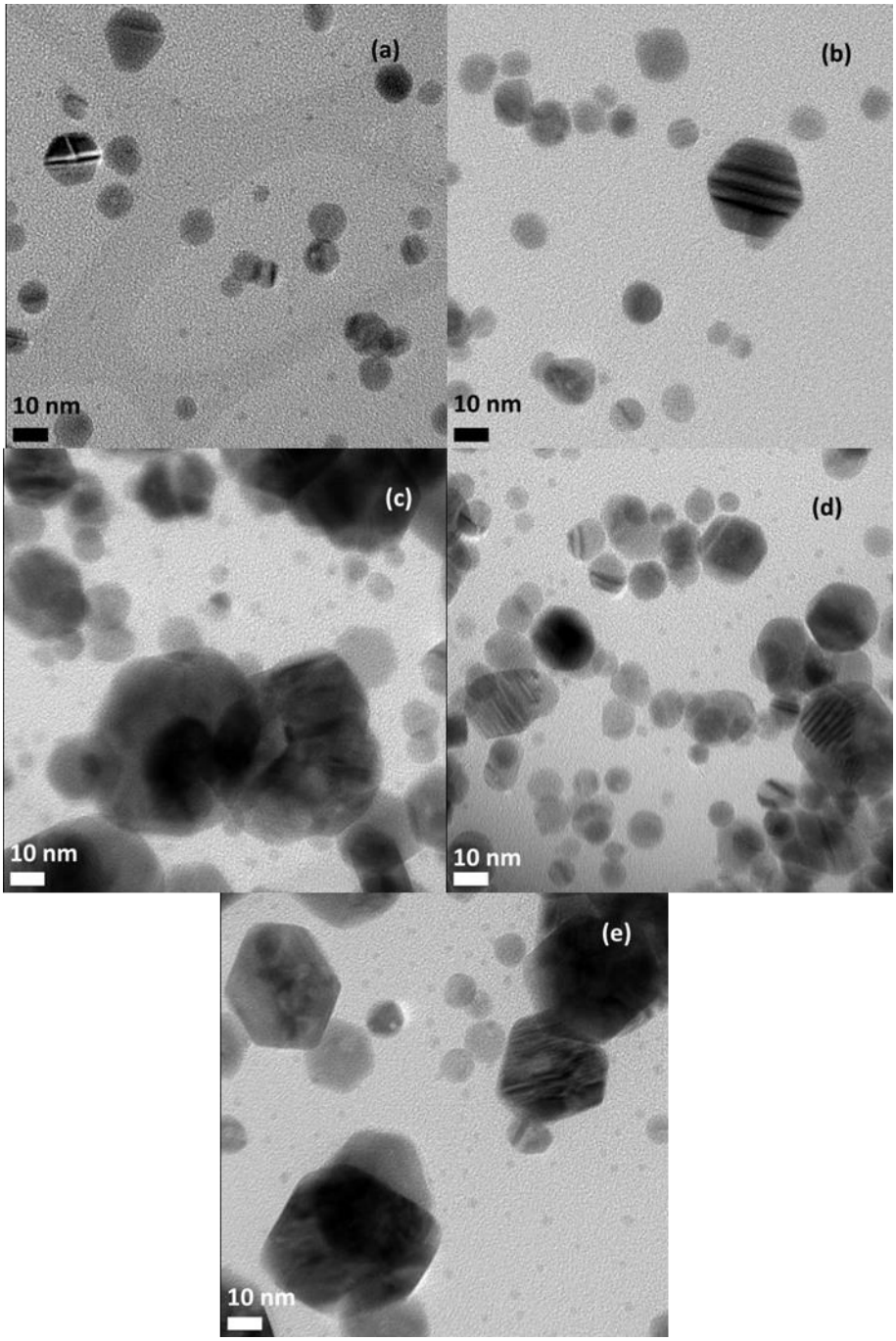

Figure 2.16. High-magnification TEM images of (a) 10, (b) 60, (c) 150, (d) 200 and (e) 300 mM samples. All images are at the same scale and the scale bar on the bottom left is 10 nm.

Immediately obvious is the greater degree of aggregation in higher-concentration gels which is conducive to 'hotspot' generation, giving rise to comparatively stronger SERS. Going from lower- to higher-concentration samples, the signal becomes stronger as the size distribution broadens, generating larger particles which tend to produce sizeable aggregates. Broadening however also has the effect of increasing spot-to-spot signal variation on the gel surface. Figure 2.17 shows graphs of the %RSDs of particle size and SERS signal strength.

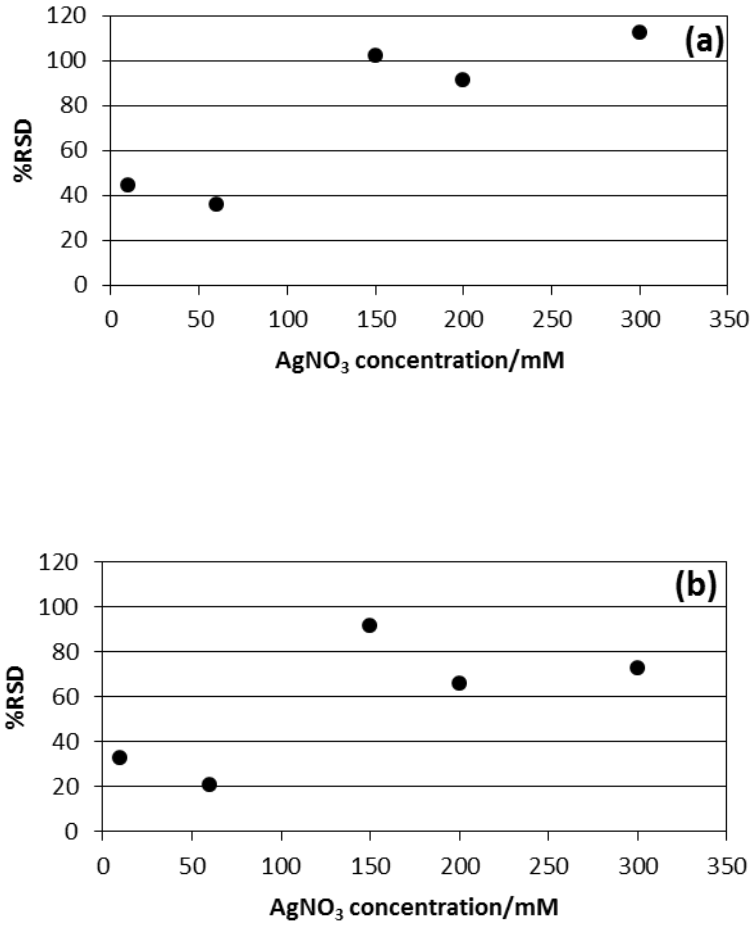

Figure 2.17. (a) Nanoparticle size and (b) SERS signal strength %RSDs for 10, 60, 150, 200 and 300 mM gels.

As seen in figure 2.17, the trends in both the size and signal graphs are very similar. This points to a close correlation between broadening of the size distribution and the general increase in the spread of SERS intensity measurements. As feed concentration rises, there is an overall increase in the particle size %RSD, making the sample less homogeneous and producing a larger spot-to-spot variation in signal strength on the gel surface.

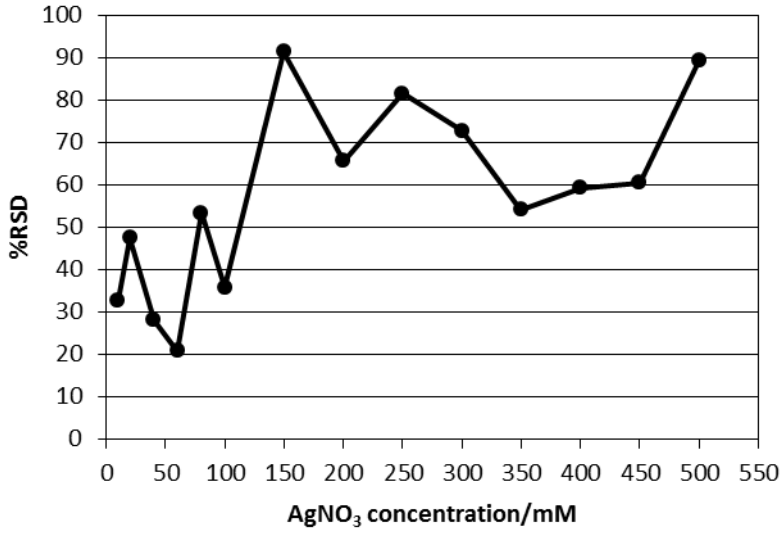

Figure 2.18. %RSD in intensity of the 1200 cm^{-1} peak of BPE (measured from 25 spectra per point), showing a division between lower- and higher-concentration gels.

This finding is reinforced when the %RSDs of all $AgNO_3$ concentrations are considered in figure 2.18, which shows an overall division in signal uniformity between lower- and higher-concentration gels. It is noteworthy that the 60 mM Ag-gel yields a %RSD of 20.8%, which is marginally above the upper-limit of 20% for detection and identification purposes [42], [43]. This shows that even without further refinement, the upper-limit is practically achievable, and that this result may well be improved upon.

The absence of an overall rise in SERS intensity beyond 150 mM can be explained by the lack of an appreciable increase in the number of larger particles beyond this concentration. To optimise silver agarose gel as a SERS substrate therefore, it would be necessary to maximise the number of larger particles whilst simultaneously narrowing the size distribution. This should have the combined effect of producing a stronger SERS response and reducing signal variation.

Sample homogeneity depends critically on how the silver nanoparticles form and grow. Although the science behind particle nucleation and growth is complicated, being governed by thermodynamics and kinetics [44], [45] the La Mer model can adequately explain the evolution of the size distribution in lower- to higher-concentration gels. The reduction of silver nitrate using sodium borohydride to form a critical concentration of silver seed nuclei, can be explained by La Mer's burst nucleation theory which was described in detail in chapter one. Figure 1.14 from chapter one, adapted from [46] and reproduced in figure 2.19 is a reminder of the principles of nucleation theory.

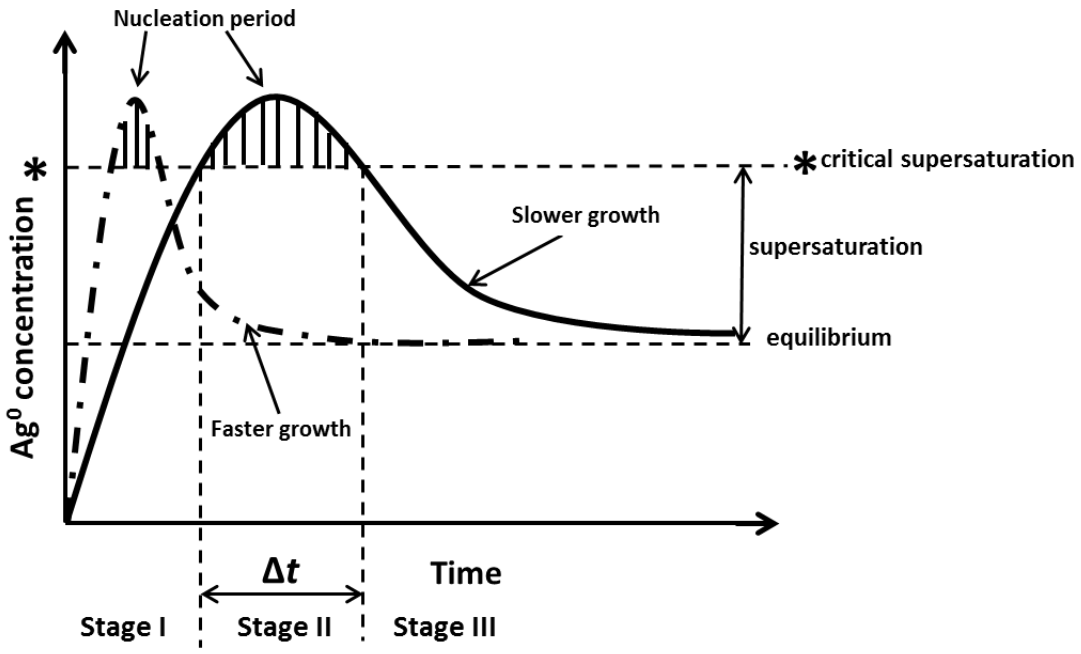

Figure 2.19. La Mer model of burst nucleation theory showing the different stages for the "solid-line" plot, adapted from [46].

As more and more silver is added to solution during reduction, its concentration rises sharply beyond the equilibrium concentration so that the solution becomes "supersaturated" (stage I for the "solid-line" plot). Formation of silver seed nuclei occurs instantaneously and homogeneously when silver reaches a critical supersaturation (CS) concentration. Above CS, nucleation continues until enough silver is removed from solution by seed formation to bring the concentration below critical (stage II for the "solid-line" plot). Seeds then grow layer-by-layer, forming nanoparticles until the concentration falls to the "normal" saturation concentration at equilibrium (stage III for the "solid-line" plot). When there is only a short nucleation period represented by the 'dot-dash' line in figure 2.19, the solution is more monodisperse. During a longer nucleation period however, silver is unevenly depleted from solution leading to the creation of different seed particles at different

times with a wide range of growth rates, resulting in a more polydisperse solution represented by the solid line in figure 2.19. A longer nucleation event could occur for example, if the rate of consumption of silver by growing nanoparticles was less than the rate of addition of silver atoms to solution through $AgNO_3$ reduction. This would force the solution to remain above CS for longer, prolonging the nucleation period until sufficient silver had been exhausted to reduce it below the threshold. Consequently, higher-concentration gels which are more polydisperse experience a longer nucleation period than lower-concentration gels which should be expected as they possess significantly more precursor. This was confirmed qualitatively by observation as all samples were reduced. The reduction of silver nitrate by sodium borohydride is governed by the equation:

$$AgNO_3 + NaBH_4 \rightarrow Ag + \frac{1}{2}H_2 + \frac{1}{2}B_2H_6 + NaNO_3 \qquad (2.1)$$

Borohydride also reacts with water relatively slowly:

$$NaBH_4 + 2H_2O \rightarrow NaBO_2 + 4H_2 \qquad (2.2)$$

Before the silver nitrate gels were added to their respective borohydride solutions, bubbling of hydrogen given off by the reaction with water for all borohydride concentrations was minimal. Immediately after gel immersion, copious quantities of bubbles of hydrogen and diborane were generated with higher-concentration gels producing the gases much more vigorously. The lower-concentration gels ceased gas production after about 10 minutes suggesting the reaction had terminated whereas the higher-concentration gels produced gases for up

to about 25 minutes or longer. This suggests that for higher-concentration gels, new silver was still being produced long after lower-concentration gels had ended their reaction, meaning that the former did experience a longer nucleation period. In addition to the high concentrations of $AgNO_3$ (and by default $NaBH_4$) having the effect of prolonging the nucleation period, there is the possibility that the huge quantities of gas released in the higher-concentration samples somehow disrupt the nucleation and growth processes, contributing to an adverse effect on gel structure. The combined outcome is broadening and skewing of the AgNP size distribution, which negatively impacts gel reproducibility.

2.3.4 Conclusion

The effect of silver nitrate feed solution concentration on the resultant nanoparticle morphology, gel homogeneity, SERS signal intensity and spot-to-spot signal variation in silver agarose gel was examined. Initially, SERS signal strength increased approximately linearly as a function of feed concentration but then fluctuated with no further overall increase. TEM studies confirmed that this rise in lower-concentration gels was due mainly to a higher nanoparticle density along with a modest increase in aggregation. In higher-concentration gels, larger symmetric particles not only produced stronger SERS on their own, but tended to form large aggregates conducive to 'hotspot' formation, further increasing the signal. The overall increasing spot-to-spot signal variation was attributed to the increasing size distribution leading to a decrease in gel homogeneity. Generally, as the size %RSD rose, the less homogeneous a sample was and the larger the spread in SERS measurements became. In addition, no appreciable rise in the number of larger

particles after 150 mM $AgNO_3$ was evident which accounted for the subsequent lack of overall increase in SERS signal strength. La Mer's theory explained why lower-concentration gels had narrower size distributions than higher-concentration gels whose distributions were heavily skewed. It is noteworthy that the 60 mM Ag-gel yielded a %RSD of 20.8%, which is marginally above the upper-limit of 20% for detection and identification purposes. This shows that even without further refinement, the upper-limit is practically achievable, and that this result may well be improved upon. Future work could focus on different reducing solutions, with a view to creating larger, more monodisperse particles which should create a stronger SERS response with less signal variation. This would further optimise a substrate which already holds great potential for SERS analysis.

2.4 SERS of high-concentration Ag-agarose fabricated with varying excess of sodium borohydride

2.4.1 Introduction

Higher-concentration gels do provide notably stronger SERS than those of lower concentration, but it would be better if their size distributions could be narrowed, with the average position shifted towards larger particle size. This should give rise to stronger SERS with less signal variation. One way to achieve this might be to shorten the nucleation period by using a heavy excess of $NaBH_4$. High-concentration Ag-agarose was fabricated using a fixed, high concentration of $AgNO_3$ (200 mM) and a varying ratio of $NaBH_4$ to $AgNO_3$ from 0.01 to 10; the results were then examined in terms of SERS intensity and uniformity.

2.4.2 Experimental

All chemicals were purchased from Sigma Aldrich, used without further purification and are listed in section 2.2.2.1. Blank agarose squares (≈ 1.5 × 10 × 10 mm^3) were fabricated using the method described in section 2.2.2.1. Samples were immersed sequentially overnight in $AgNO_3$ and $NaBH_4$ solutions (1 square per 3 ml, 200 mM $AgNO_3$ (aq) and then 1 square per 2, 20, 100, 200, 500, 1000, 1500, and 2000 mM $NaBH_4$ (aq) concentration). During reduction, the higher-borohydride-oncentration samples of 500 mM and above produced so much gas so rapidly (to varying degrees) that they "inflated", and the next day, a white froth was observed on the top of the solution, upon which the samples floated. In all samples, there was visual evidence of particles leaching into solution as they were being reduced, particularly in the 2 mM sample, before they grew large enough to become trapped by the agarose matrix. Samples were dialysed and placed overnight in *trans*-1,2-bis(4-pyridyl)ethylene (BPE) before SERS analysis.

SERS spectra were recorded using the same setup described earlier in section 2.2.2.3, with the 632.8 nm line of a helium-neon laser as the excitation source. The unfocussed output power was measured to be approximately 1 mW at the sample, with a 1 s collection time. SERS intensity of BPE was recorded by measuring the height of the 1200 cm^{-1} peak. Analysis was carried out using OriginPro 8.5 software and the peak height was averaged from 20 baseline-corrected spectra per sodium borohydride concentration taken from different locations on the gel sample. All samples were gently patted dry on filter paper before analysis. It should be noted that under these conditions, no evidence of gel scorching was observed upon

examination through the microscope. All spectra were corrected to the same collection time for comparison.

2.4.3 Results and discussion

Figure 2.20 is a graph of SERS intensity versus sodium borohydride ($NaBH_4$) concentration, using a fixed $AgNO_3$ concentration of 200 mM. Interestingly, a molar ratio of 1:10 for [$NaBH_4$]:[$AgNO_3$], results in the 20 mM $NaBH_4$ sample producing a SERS signal 2.8 times stronger than a 1:1 ratio (200 mM each of $NaBH_4$ and $AgNO_3$). The greatest intensity occurs when the $NaBH_4$ concentration is less than that of the Ag salt solution, with the exception of the 2 mM sample, whose intensity is so low that it does not even show on the graph. Strangely, there were no SERS spectra of BPE produced at all for the 1500 mM sample.

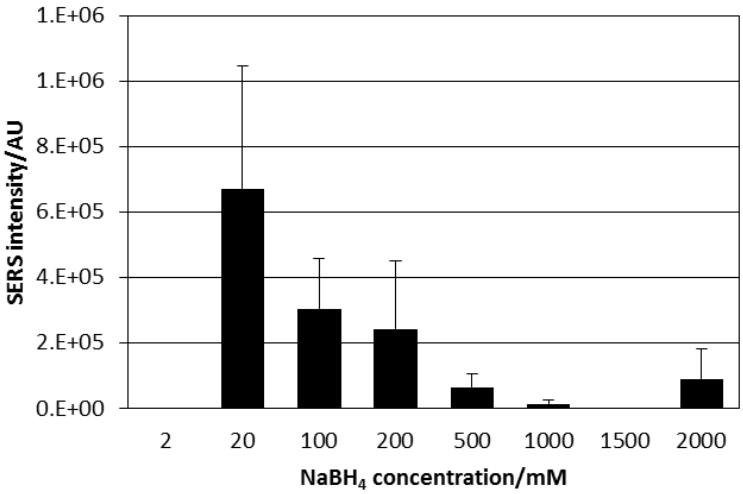

Figure 2.20. SERS intensity of Ag-agarose fabricated from 200 mM $AgNO_3$ and sodium borohydride: 2, 20, 100, 200, 500, 1000, 1500, and 2000 mM. Each bar represents the 1200 cm^{-1} peak height of BPE, averaged from twenty spectra taken from across the sample surface, with error bars representing the standard deviation. The intensity for 2 mM is so slight, it cannot be seen on the graph and there is no result for 1500 mM as no BPE spectra were produced for this sample.

In the case of the 2 mM sample, the $NaBH_4$ concentration is so low in comparison to that of $AgNO_3$, that most of the newly formed Ag nanoparticles end up in solution, confirmed by the solution turning a yellow-green as seen in Lee-Meisel colloids [47]; the other solutions turn varying degrees of muddy-brown. For 2 mM $NaBH_4$, relatively few Ag nuclei form during the nucleation stage (stage II in the "solid-line" La Mer plot in figure 2.19), and those which spontaneously appear and begin to grow, escape the matrix before becoming large enough to become trapped due to an insufficient flux of reductant across the gel surface per unit time. The 2 mM solution is the only one that takes on a yellow-grey appearance, suggesting that the greatest proportion of nanoparticles have abandoned the agarose – something which is confirmed by the gel's resultant virtual transparency, as well as the extremely weak signal for this sample. At 20 mM, many more nuclei form spontaneously and grow quickly enough to become trapped due to an adequate flux of reductant, but the borohydride is still weak enough to ensure that the number is small compared with a high-NaBH4-concentration scenario. This means in contrast that relatively few nuclei act as growth sites, resulting in fewer but larger particles, which produce an elevated signal. The decreasing trend in intensity therefore from 20 to 1500 mM borohydride (the intensity is zero at 1500 mM), probably reflects increasing numbers of nanoparticles being produced, as more nuclei are formed due to an increasing concentration of $NaBH_4$, but so many that there is now insufficient Ag^+ (aq) in the gel to act as a reservoir for growth; this likely culminates in a high nanoparticle density, but very small nanoparticle size with reduced plasmonic activity and a concomitant reduction in signal strength.

Interestingly, intensity recovers at 2000 mM, but why this should be so is not clear. It could simply be that although the particles are almost certainly very small, they are now so densely packed, that the reduction in plasmonic activity is reversed as weak coupling between plasmons begins to reassert itself, generating a small but detectable SERS signal once more.

The reproducibility of the gels was then examined, the results of which are in figure 2.21.

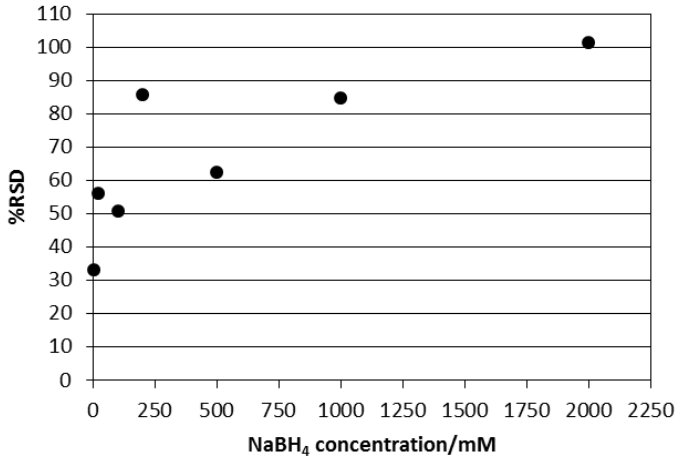

Figure 2.21. %RSD of SERS signal strength of Ag-agarose fabricated from 200 mM $AgNO_3$ and sodium borohydride: 2, 20, 100, 200, 500, 1000, 1500, and 2000 mM. Each point represents the %RSD of the 1200 cm^{-1} peak height of BPE, from twenty averaged spectra taken from the sample surface. There is no result for 1500 mM, as no BPE spectra were produced for this sample.

Figure 2.21 shows counterintuitively that, as the excess of $NaBH_4$ becomes greater, so too does the %RSD in signal strength. It would appear that even if the nucleation period is possibly reduced with increasing excess of $NaBH_4$, NPs become more polydisperse when %RSD in signal strength is used as an indirect measure of NP dispersity. Again, it should be remembered however that $NaBH_4$ must diffuse across

the surface of the gel in order to reduce Ag^+ ions, and this creates a limit as to how fast they can be reduced, even in excess $NaBH_4$. Conceivably this physical barrier, replete with nucleation sites, could adversely alter the dynamics of nucleation and particle growth at higher $NaBH_4$ excesses, just as it might do at higher "[$AgNO_3$]:[$NaBH_4$] = 1:1" concentrations, which also produce comparatively high %RSDs as seen earlier in this chapter.

Previous results in section 2.3.3 and the results presented here show that while the ratio of $NaBH_4$ to $AgNO_3$ concentration does influence gel reproducibility, though in a way opposite to that expected, the concentration of *both* reactants must be kept reasonably low to optimise this parameter. Moreover, there is the possibility that the huge quantities of gas released in the higher-borohydride-concentration samples, somehow disrupt the nucleation and growth processes, adversely affecting gel structure.

One other important point is that $NaBH_4$ may not turn out to be the most suitable choice with respect to reproducibility, even if low-concentration reactants are used. As shall be seen in chapter three, this is indeed the case when $NaBH_4$ is compared with hydroxylamine, which overall, gives rise to significantly better gel uniformity.

2.4.4 Conclusion

High-concentration Ag-agarose was fabricated using a fixed concentration of $AgNO_3$ and heavy excesses of $NaBH_4$, alongside lower concentrations of the reductant as a control. The aim was to construct gels which had undergone a short

nucleation period, and thus possessed better uniformity. The greatest SERS intensity was observed when the $NaBH_4$ concentration was less than that of $AgNO_3$, excepting the 2 mM sample, whose intensity was slight due to heavy leakage of Ag nanoparticles from the gel into solution during reduction. Strangely, there were no SERS spectra of BPE produced at all for the 1500 mM sample, probably because increasing numbers of Ag nanoparticles were produced as more nuclei were formed due to a high concentration of $NaBH_4$, but so many that there was now insufficient Ag^+ (aq) in the gel to act as a reservoir for growth; this likely culminated in a high nanoparticle density, but very small nanoparticle size with reduced plasmonic activity and a concomitant reduction in signal strength.

While the concentration ratio of $NaBH_4$ to $AgNO_3$ did influence gel reproducibility (in a way opposite to that expected), overall reproducibility remained poor whatever the molarity of borohydride, and it would appear that the concentration of *both* reactants must be reasonably low to maximise gel homogeneity. Moreover, vigorous bubbling in the higher-borohydride-concentration samples during reduction might have somehow disrupted the nucleation and growth processes, adversely affecting gel structure. However, $NaBH_4$ may not turn out to be the most suitable choice as regards reproducibility, even if low-concentration reactants are used.

2.5 Summary

Initial testing of Ag-agarose gel successfully replicated previous work in readily producing SERS of various molecular probes. SERRS of NBA at nanomolar

concentrations was detected. The effect of silver nitrate feed solution concentration on resultant nanoparticle morphology, gel homogeneity, SERS signal intensity and spot-to-spot signal variation was examined in depth. Initially, SERS signal strength increased approximately linearly as a function of feed concentration but then fluctuated with no further overall increase. TEM studies confirmed that this rise in lower-concentration gels was due mainly to a higher nanoparticle density along with a modest increase in aggregation. In higher-concentration gels, larger symmetric particles not only produced stronger SERS on their own, but tended to form large aggregates conducive to 'hotspot' formation, further increasing the signal. The overall increasing spot-to-spot signal variation was attributed to the increasing size distribution leading to a decrease in gel homogeneity. Generally, as the size %RSD rose, the less homogeneous a sample was and the larger the spread in SERS measurements became. In addition, no appreciable rise in the number of larger particles after 150 mM $AgNO_3$ was evident which accounted for the subsequent lack of an overall increase in SERS signal strength. La Mer's theory explained why lower-concentration gels had narrower size distributions than higher-concentration gels whose distributions were heavily skewed. Future work could focus on different reducing solutions with a view to creating larger, more monodisperse particles which should create a stronger SERS response with less signal variation. This would further optimise a substrate which already holds great potential for SERS analysis.

High-concentration Ag-agarose was fabricated using a fixed concentration of $AgNO_3$ and heavy excesses of $NaBH_4$, alongside lower concentrations of the reductant as a control. The aim was to construct gels which had undergone a short nucleation period, and thus possessed better uniformity. The greatest SERS intensity

was observed when the $NaBH_4$ concentration was less than that of $AgNO_3$, with the exception of the 2 mM sample whose intensity was exceedingly weak due to heavy leeching of nanoparticles out into solution during reduction. Strangely, there were no SERS spectra of BPE produced at all for the 1500 mM sample; this probably reflected increasing numbers of Ag nanoparticles being produced, as more nuclei were formed due to a high concentration of $NaBH_4$, but so many that there was now insufficient Ag^+ (aq) in the gel to act as a reservoir for growth, resulting in very small nanoparticles with reduced plasmonic activity and a concomitant reduction in signal strength.

While the concentration ratio of $NaBH_4$ to $AgNO_3$ (with a fixed $AgNO_3$ concentration) does influence gel reproducibility (in a way opposite to that expected), overall, it remains poor whatever the molarity of borohydride, and it would appear that the concentration of *both* reactants must be reasonably low to maximise reproducibility. However, even at relatively low reactant concentrations, $NaBH_4$ may not turn out to be the optimum choice as regards reproducibility.

References

[1] P. Aldeanueva-Potel, E. Faoucher, R. A. Alvarez-Puebla, L. M. Liz-Marzan, and M. Brust, "Recyclable molecular trapping and SERS detection in silver-loaded agarose gels with dynamic hot spots," *Anal. Chem.*, vol. 81, no. 22, pp. 9233–9238, 2009.

[2] E. C. Le Ru and P. G. Etchegoin, *Principles of Surface-Enhanced Raman Spectroscopy and related plasmonic effects*. Oxford: Elsevier, 2009, pp. 367–369.

[3] M. Fleischmann, P. J. Hendra, and A. J. McQuillan, "Raman spectra of pyridine adsorbed at a silver electrode," *Chem. Phys. Lett.*, vol. 26, no. 2, pp. 163–166, 1974.

[4] M. Fan, G. F. S. Andrade, and A. G. Brolo, "A review on the fabrication of substrates for surface-enhanced Raman spectroscopy and their applications in analytical chemistry," *Anal. Chim. Acta*, vol. 693, no. 1–2, pp. 7–25, 2011.

[5] M. Keating, S. Song, G. Wei, D. Graham, Y. Chen, and F. Placido, "Ordered silver and copper nanorod arrays for enhanced Raman scattering created via guided oblique angle deposition on polymer," *J. Phys. Chem. C*, vol. 118, no. 9, pp. 4878–4884, 2014.

[6] P. Pavaskar, I.-K. Hsu, J. Theiss, W. Hsuan Hung, and S. B. Cronin, "A microscopic study of strongly plasmonic Au and Ag island thin films," *J. Appl. Phys.*, vol. 113, no. 3, p. 034302, 2013.

[7] C. Geng, L. Zheng, J. Yu, Q. Yan, T. Wei, X. Wang, and D. Shen, "Thermal annealing of colloidal monolayer at the air/water interface: a facile approach to transferrable colloidal masks with tunable interstice size for nanosphere lithography," *J. Mater. Chem.*, vol. 22, no. 42, pp. 22678–22685, 2012.

[8] F.-K. Liu, Y.-C. Chang, F.-H. Ko, T.-C. Chu, and B.-T. Dai, "Rapid fabrication of high quality self-assembled nanometer gold particles by spin coating method," *Microelectron. Eng.*, vol. 67–68, pp. 702–709, 2003.

[9] B. W. Trautner, A. I. Lopez, A. Kumar, D. M. Siddiq, K. S. Liao, Y. Li, D. J. Tweardy, and C. Cai, "Nanoscale surface modification favors benign biofilm formation and impedes adherence by pathogens," *Nanomedicine*, vol. 8, no. 3, pp. 261–270, 2012.

[10] S. B. Chaney, S. Shanmukh, R. A. Dluhy, and Y.-P. Zhao, "Aligned silver nanorod arrays produce high sensitivity surface-enhanced Raman spectroscopy substrates," *Appl. Phys. Lett.*, vol. 87, no. 3, p. 031908, 2005.

[11] J. D. Driskell, S. Shanmukh, Y. Liu, S. B. Chaney, X.-J. Tang, Y.-P. Zhao, and R. A. Dluhy, "The use of aligned silver nanorod arrays prepared by oblique angle deposition as surface-enhanced Raman scattering substrates," *J. Phys. Chem. C*, vol. 112, no. 4, pp. 895–901, 2008.

[12] Y.-J. Liu, Z.-Y. Zhang, Q. Zhao, R. A. Dluhy, and Y.-P. Zhao, "Surface enhanced raman scattering from an Ag nanorod array substrate: the site-dependent enhancement and layer absorbance effect," *J. Phys. Chem. C*, vol. 113, no. 22, pp. 9664–9669, 2009.

[13] Y.-J. Liu, H. Y. Chu, and Y.-P. Zhao, "Silver nanorod array substrates fabricated by oblique angle deposition: morphological, optical, and SERS characterizations," *J. Phys. Chem. C*, vol. 114, no. 18, pp. 8176–8183, 2010.

[14] C. Song, J. L. Abell, Y. He, S. H. Murph, Y. Cui, and Y. Zhao, "Gold-modified silver nanorod arrays: growth dynamics and improved SERS properties," *J. Mater. Chem.*, vol. 22, no. 3, pp. 1150–1159, 2012.

[15] D. L. J. Vossen, D. Fific, J. Penninkhof, T. van Dillen, A. Polman, and A. van Blaaderen, "Combined optical tweezers/ion beam technique to tune colloidal masks for nanolithography.," *Nano Lett.*, vol. 5, no. 6, pp. 1175–1179, 2005.

[16] J. L. Plaza, Y. Chen, S. Jacke, and R. E. Palmer, "Nanoparticle arrays patterned by electron-beam writing: structure, composition, and electrical properties," *Langmuir*, vol. 21, no. 4, pp. 1556–1559, 2005.

[17] J. D. Driskell, S. Shanmukh, Y.-J. Liu, S. Hennigan, L. Jones, Y.-P. Zhao, R. A. Dluhy, D. C. Krause, and R. A. Tripp, "Infectious agent detection with SERS-active silver nanorod arrays prepared by oblique angle deposition," *IEEE Sens. J.*, vol. 8, no. 6, pp. 863–870, 2008.

[18] K. Faulds, W. E. Smith, D. Graham, and R. J. Lacey, "Assessment of silver and gold substrates for the detection of amphetamine sulfate by surface enhanced Raman scattering (SERS)," *Analyst*, vol. 127, no. 2, pp. 282–286, 2002.

[19] C. Lofrumento, M. Ricci, E. Platania, M. Becucci, and E. Castellucci, "SERS detection of red organic dyes in Ag-agar gel," *J. Raman Spectrosc.*, vol. 44, no. 1, pp. 47–54, 2013.

[20] R. Armisen, F. Galatas, and S. A. Hispanagar, "Agar," in *Handbook of Hydrocolloids*, Second Ed., G. O. Phillips and P. A. Williams, Eds. Cambridge: Woodhead Publishing Limited, 2009, pp. 82–89.

[21] Sigma-Aldrich, "Agarose: Product Information." [Online]. Available: http://www.sigmaaldrich.com/content/dam/sigma-aldrich/docs/Sigma-Aldrich/Product_Information_Sheet/a5030pis.pdf. [Accessed: 30-Apr-2014].

[22] N. Benmouhoub, N. Simmonet, N. Agoudjil, and T. Coradin, “Aqueous sol-gel routes to bio-composite capsules and gels,” *Green Chem.*, vol. 10, no. 9, pp. 957–964, 2008.

[23] X. Wang, C. E. Egan, M. Zhou, K. Prince, D. R. G. Mitchell, and R. A. Caruso, “Effective gel for gold nanoparticle formation, support and metal oxide templating,” *Chem. Commun.*, no. 29, pp. 3060–3062, Aug. 2007.

[24] K. A. Stoerzinger, J. Y. Lin, and T. W. Odom, “Nanoparticle SERS substrates with 3D Raman-active volumes,” *Chem. Sci.*, vol. 2, no. 8, pp. 1435–1439, 2011.

[25] S. Abalde-Cela, B. Auguie, M. Fischlechner, W. T. S. Huck, R. A. Alvarez-Puebla, L. M. Liz-Marzan, and C. Abell, “Microdroplet fabrication of silver–agarose nanocomposite beads for SERS optical accumulation,” *Soft Matter*, vol. 7, no. 4, pp. 1321–1325, 2011.

[26] S. Saha, A. Pal, S. Pande, S. Sarkar, S. Panigrahi, and T. Pal, “Alginate gel-mediated photochemical growth of mono- and bimetallic gold and silver nanoclusters and their application to surface-enhanced Raman scattering,” *J. Phys. Chem. C*, vol. 113, no. 18, pp. 7553–7560, 2009.

[27] J.-L. Li, X.-Y. Liu, X.-G. Wang, and R.-Y. Wang, “Controlling nanoparticle formation via sizable cages of supramolecular soft materials,” *Langmuir*, vol. 27, no. 12, pp. 7820–7827, 2011.

[28] R. A. Alvarez-Puebla and L. M. Liz-Marzan, “Traps and cages for universal SERS detection.,” *Chem. Soc. Rev.*, vol. 41, no. 1, pp. 43–51, 2012.

[29] I. A. Larmour and D. Graham, “Surface-enhanced optical spectroscopies for bioanalysis,” *Analyst*, vol. 136, no. 19, pp. 3831–3853, 2011.

[30] NHS, “Drug Misuse (facts about drug misuse),” *NHSinform*, 2014. [Online]. Available: http://www.nhsinform.co.uk/health-library/articles/d/drug-misuse/facts. [Accessed: 17-Sep-2014].

[31] Sigma-Aldrich, “Nile Blue A schematic”, 2015 [Online]. Available: http://www.sigmaaldrich.com/catalog/product/sigma/n5632?lang=en&region=GB [Accessed: 21-May-2015].

[32] Sigma-Aldrich, “Rhodamine 6G schematic”, 2015 [Online]. Available: http://www.sigmaaldrich.com/catalog/product/aldrich/252433?lang=en&region=GB [Accessed: 21-May-2015].

[33] Sigma-Aldrich, “Amphetamine Sulphate schematic”, 2015 [Online]. Available: http://www.sigmaaldrich.com/catalog/product/fluka/a0922?lang=en&region=GB [Accessed: 21-May-2015].

[34] M. Fan and A. G. Brolo, “Silver nanoparticles self assembly as SERS substrates with near single molecule detection limit,” *Phys. Chem. Chem. Phys.*, vol. 11, no. 34, pp. 7381–7389, 2009.

[35] W.-L. Zhai, D.-W. Li, L.-L. Qu, J. S. Fossey, and Y.-T. Long, “Multiple depositions of Ag nanoparticles on chemically modified agarose films for surface-enhanced Raman spectroscopy,” *Nanoscale*, vol. 4, no. 1, pp. 137–142, 2012.

[36] G. McNay, D. Eustace, W. E. Smith, K. Faulds, and D. Graham, “Surface-enhanced Raman scattering (SERS) and surface-enhanced resonance Raman scattering (SERRS): a review of applications,” *Appl. Spectrosc.*, vol. 65, no. 8, pp. 825–837, 2011.

[37] IUPAC, “Limit of detection in analysis,” Gold Book. [Online]. Available: http://goldbook.iupac.org/L03540.html. [Accessed: 21-May-2015].

[38] A. S. Polo, M. K. Itokazu, K. M. Frin, A. O. de Toledo Patrocinio, and N. Y. M. Iha, “Light driven *trans*-to-*cis* isomerization of stilbene-like ligands in fac-$[Re(CO)_3(NN)(trans\text{-}L)]^+$ and luminescence of their photoproducts,” *Coord. Chem. Rev.*, vol. 250, no. 13–14, pp. 1669–1680, 2006.

[39] W. Yang, J. Hulteen, G. C. Schatz, and R. P. Van Duyne, “A surface-enhanced hyper-Raman and surface-enhanced Raman scattering study of *trans*-1,2-bis (4-pyridyl) ethylene adsorbed onto silver film over nanosphere electrodes. Vibrational assignments: Experiment and theory,” *J. Chem. Phys.*, vol. 104, no. 11, pp. 4313–4323, 1996.

[40] S. Abalde-Cela, P. Aldeanueva-Potel, C. Mateo-Mateo, L. Rodriguez-Lorenzo, R. A. Alvarez-Puebla, and L. M. Liz-Marzan, “Surface-enhanced Raman scattering biomedical applications of plasmonic colloidal particles,” *J. R. Soc. Interface*, vol. 7, no. Suppl 4, pp. S435–S450, 2010.

[41] S. A. Maier, *Plasmonics: Fundamentals and applications*. New York: Springer, 2007, pp. 161–162.

[42] X.-M. Lin, Y. Cui, Y.-H. Xu, B. Ren, and Z.-Q. Tian, “Surface-enhanced Raman spectroscopy: substrate-related issues,” *Anal. Bioanal. Chem.*, vol. 394, no. 7, pp. 1729–1745, 2009.

[43] M. Kahraman, I. Sur, and M. Culha, “Label-free detection of proteins from self-assembled protein-silver nanoparticle structures using surface-enhanced Raman scattering,” *Anal. Chem.*, vol. 82, no. 18, pp. 7596–7602, 2010.

[44] C. Burda, X. Chen, R. Narayanan, and M. A. El-Sayed, “Chemistry and properties of nanocrystals of different shapes,” *Chem. Rev.*, vol. 105, no. 4, pp. 1025–1102, 2005.

[45] Z. Peng, S. Yang, and H. Yang, “Approaches to the Synthesis and Characterization of Spherical and Anisotropic Platinum Nanomaterials,” in *Nanomaterials for the Life Sciences Vol. 1: Metallic Nanomaterials*, C. Kumar, Ed. Weinheim, 2009, pp. 359–365.

[46] Z. Peng, S. Yang, and H. Yang, “Approaches to the Synthesis and Characterization of Spherical and Anisotropic Platinum Nanomaterials,” in *Nanomaterials for the Life Sciences Vol. 1: Metallic Nanomaterials*, C. Kumar, Ed. Weinheim: Wiley-VCH, 2009, p. 364.

[47] P. C. Lee and D. Meisel, “Adsorption and surface-enhanced Raman of dyes on silver and gold sols,” *J. Phys. Chem.*, vol. 86, no. 17, pp. 3391–3395, 1982.

Chapter 3 SERS of sodium borohydride- and hydroxylamine-reduced Ag nanoparticle-agarose

This chapter builds on work from chapter two, which gave a general review of SERS substrates and examined the growth conditions of Ag-agarose along with the associated SERS response, as well as the ability of the substrate to qualitatively detect various analytes. In this chapter, SERS of Ag-agarose reduced by sodium borohydride and hydroxylamine is compared, after which the discussion moves on to issues which can arise during spectral analysis. Chapter four is an extension of this chapter, in that SERS of gels reduced exclusively by hydroxylamine are the focus. The following literary review therefore is applicable to both this chapter and chapter four, providing an overview of metal/gel nanocomposites used in SERS, and focussing on in particular, MNPA which is especially pertinent to this thesis.

3.1 Introduction: a review of metal nanoparticle/gel composites for SERS

Recently, there has been a surge of interest in the growth of different varieties of nanoparticle (NP) within the supportive, constraining and protective framework of a host material such as a gel. Inorganic, gold or silver NPs, carbon nanotubes and graphene for example, have all been incorporated into/created within gel matrices with a view to eventually deploying the resultant nanocomposites in advanced applications as diverse as catalysis, sensing, electronics [1]–[3], and the elimination of microbes [4]–[6]. Specifically, the incorporation of pre-fabricated and *in situ*

creation of Au or AgNPs within a gel matrix, as in the case of Ag-agarose discussed previously in chapter two, has garnered a lot of interest recently in the SERS community. Nanoparticles are fixed in and stabilised by the matrix, the porous structure of which readily exposes them to analytes. A variety of materials and techniques have been utilised in the synthesis of hydrogels. Saha *et al*. produced SERS-active Ag and AuNPs, and combinations of these grown on polysaccharide calcium alginate (CA) gel bead cores (about 3.5 and 2.0 mm diameter when wet and dry respectively) which helped stabilise the NPs [7]. Calcium ions act as gelators, and the beads are incubated in metal precursor solutions and subsequently reduced photochemically by UV irradiation. Curiously, Ag-only coated beads fail completely to produce SERS of the molecular probes used in the study, which is in direct contrast with the Ag-agarose substrates produced for this thesis which generated a clear SERS signal. It was found that SERS intensity followed the order Au > Au@Ag > Ag@ Au. Figure 3.1 illustrates the colour changes within the beads due to NP formation as the metal salts are reduced *in situ*.

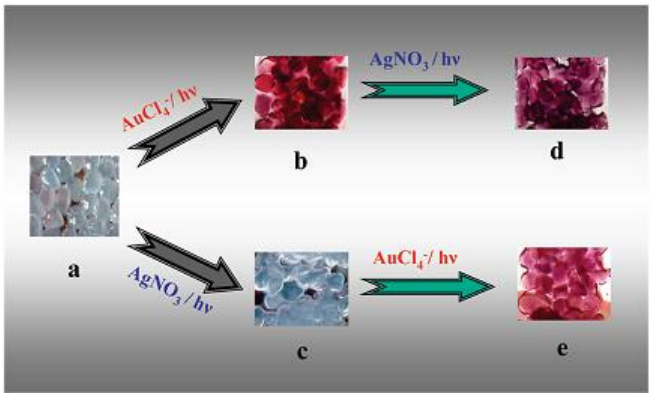

Figure 3.1. Various CA-stabilised metal nanoparticles showing different colour changes in relation to NP species: (a) CA control, (b) Au-CA, (c) Ag-CA, (d) Ag@Au-CA, and (e) Au@Ag-CA beads, as produced by [7].

Much smaller bead-substrates (0.45 mm in diameter when wet and 0.3 mm when dry) were synthesised by Kohler *et al.* [8] using a micro-coflow system as shown schematically in figure 3.2.

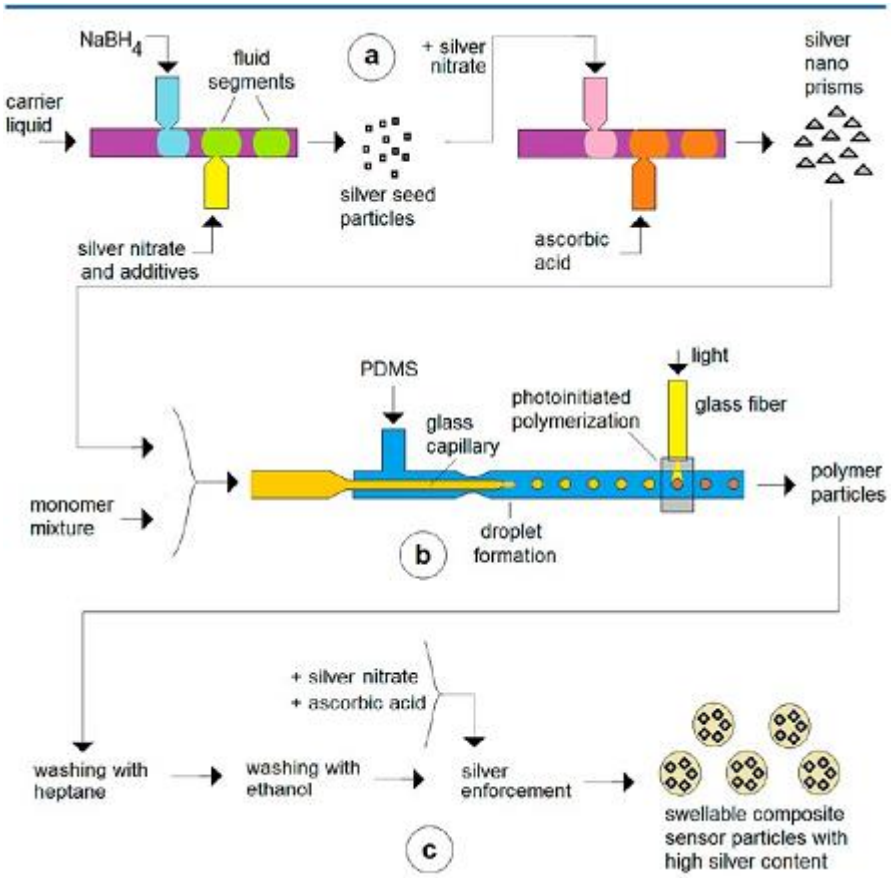

Figure 3.2. Microfluidic arrangement to produce densely packed AgNP-polyacrylamide SERS-active composites as produced by [8].

Briefly, silver seeds in figure 3.2 (a) are fabricated via the reduction of silver nitrate using aqueous sodium borohydride ($NaBH_4$) in microfluidic segments. The seeds grow into silver nanoprisms in contact with additional silver nitrate, and this time ascorbic acid. They are then forced into a glass capillary along with acrylamide monomers, and a cross-linker in figure 3.2 (b), where photo-polymerisation takes place. Figure 3.2 (c) illustrates various washing stages, after which "silver

enforcement" augments the AgNP content in the nanocomposites. The AgNP/polyacrylamide beads are very SERS-active, highly uniform in size and possess a highly homogenous distribution of silver NPs throughout the matrix.

Abalde-Cela *et al.* [9] also used the principal of microfluidics to fabricate SERS-active Ag-agarose nanocomposite beads which exhibited very good reproducibility in size and signal strength. Substrates capable of ultradetection were produced for both probes used in the experiment, and this particular technique involved fewer steps than in the previous paragraph. Ag-agarose microbeads are fabricated in two main stages: (i) the formation of Ag^{+}-agarose beads using a microfluidic setup, and (ii) *in situ* reduction of Ag^{+} using hydrazine, giving rise to 75 μm diameter AgNP microbeads. A single microbead can be adequate for SERS analysis, greatly lowering the detection limit of an analyte, as much less is required to generate an observable SERS signal. However, despite its reducing power hydrazine is extremely toxic, capable of causing instant death or injury and cannot be handled without adequate protective clothing and equipment [10]. In contrast, the reducing agents used in the experiments for this thesis (sodium borohydride and hydroxylamine hydrochloride) are comparatively much more benign, and alternative, less harmful reductants could have perhaps been used instead by [9].

In other work, Yao *et. al.* fabricated poly(vinyl alcohol) (PVA) gel in the same solution as preformed citrate-stabilised gold nanoparticles and NaCl micro-sized seeds, giving rise to microporous SERS-active Au-PVA [11]. Au-PVA has both nano- and micro-sized pores, but enhanced microporosity significantly heightens the SERS response due to the consequent increased number of (Raman) scattering events. Interestingly, the degree of microporosity had previously been

deemed unimportant, something which the authors refute. Moreover, microporous Au-PVA retains its limit of detection (LOD) even after being in storage for up to three months. The method used to record this parameter however is questionable. After collecting twenty random spectra from each substrate, the LODs are compared using the spectrum with the strongest signal from each, alongside the claim that this avoids sampling effects. But, sole reliance on one spectrum as opposed to twenty for LOD determination, would instead appear to expose the results to the incorporation of potential outliers. In addition, there exist numerous time-consuming preparation steps involving, for example, several freeze-thaw cycles of the gel and freeze-drying, amounting to an overall fabrication period of a little under two weeks which is inordinately long. This is in stark contrast with the shortest fabrication period in this thesis of a matter of hours.

Shin *et al.* also produced SERS-active gold hydrogels [12] using the procedure illustrated in figure 3.3.

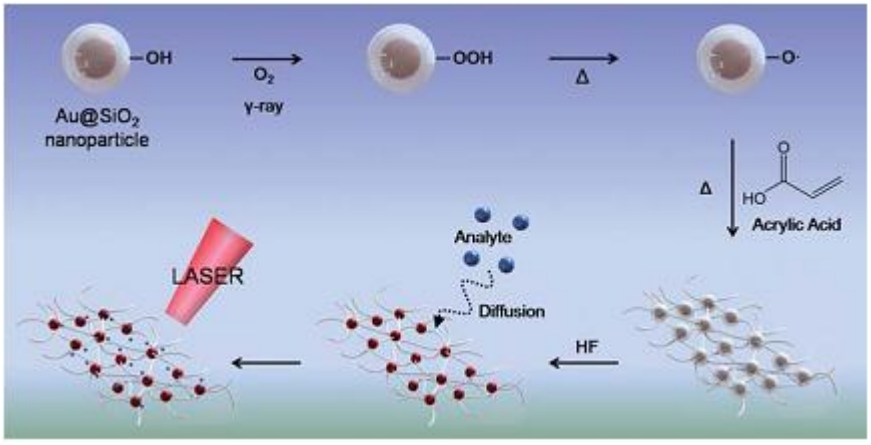

Figure 3.3. Procedure for the fabrication of Au nanoparticle-encapsulated (PAA) hydrogel as prepared by [12].

Briefly, AuNPs are synthesised using the citrate reduction method and coated with silica (SiO_2). $Au@SiO_2$ NPs in aqueous solution are then irradiated by Co^{60} γ-rays (dose rate: 10 kGy h^{-1}) for about 2 hours in ambient conditions to create peroxide groups (–OOH) on the exposed surface of the silica layer. Immediately after, N_2 is bubbled into the solution to eliminate dissolved oxygen and help block reactions between peroxide and oxygen. The solution is then heated to 40^{o} C to decompose peroxides to oxygen radicals which trigger polymerisation of acrylic acid monomers to form an acrylic polymer hydrogel with $Au@SiO_2$ embedded in the matrix. Finally, the silica shell is dissolved from around the AuNPs using hydrofluoric acid, allowing the probe molecules free access to the AuNPs.

Gels prepared in this way, exhibit exceptional reproducibility over the space of a year, but the authors acknowledge that more work is needed to improve SERS sensitivity of the substrate. Interestingly, a large-area laser illumination technique is employed to alleviate the problem of fluctuating SERS signal intensity. Nonetheless, there exist several disadvantages in applying this particular fabrication technique; numerous complex and time-consuming steps are necessary, resulting in a not-inconsiderable fabrication period. A more serious drawback is use of the γ-source Co^{60}, immediately raising health and safety concerns which bring into question the use of such a hazardous substance in this context, especially given the number of safer alternative fabrication methods available. The need for γ-radiation in this experiment makes large-scale adoption of this technique highly unlikely. The method of SERS-active metal-agarose synthesis discussed in this thesis relies on no such hazardous materials or methods, and the chemicals and procedures used are

relatively very safe and uncomplicated, delivering high throughput, SERS-active substrates.

Nanocomposite gels have found use in some experimental applications. Leona *et al.* used a pre-manufactured clear hydrogel to extract chemical information on several dyes from works of art using SERS [13]. Up until now, analytical identification of dyes and pigments in priceless and irreplaceable works of art has necessitated the extraction of a small sample from the work, a procedure which is obviously undesirable even if minimised. The authors managed to invent a non-destructive method of analysis whereupon a small piece of hydrogel is placed on the region of interest of an artwork as shown in figure 3.4

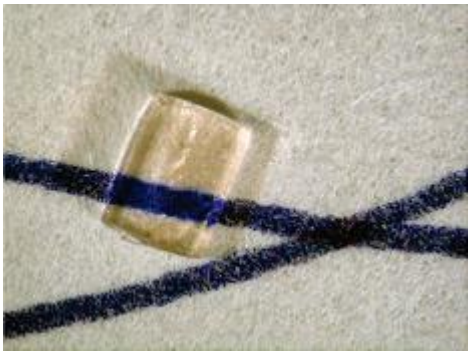

Figure 3.4. A piece of hydrogel in contact with dyed fabric as employed in [13].

Very small amounts of dye are extracted by the solvent-containing gel which is then covered with a drop of pre-prepared Ag colloid, and examined using a Raman microscope. Gel samples can be reduced to a fraction of a mm to minimise the contact area without loss of detailed spectral information, and the colour change in the work after extraction cannot be seen by the naked eye. The technique may also be tailored to the chemical characteristics of the analyte in terms of the type of gel and extraction solution used. Analysis of the samples however could perhaps be

improved upon if the authors were to grow or embed AgNPs within the gel in a manner similar to that described in this thesis, as opposed to applying liquid colloid after dye-transfer. The latter method will further reduce analyte concentration, thus potentially impacting detectability of the molecule.

Another detection method, almost identical to that just discussed, was proposed by Lofrumento *et al.* [14]. The objective once more was to deploy a non-destructive analytical technique for works of art. In this instance however, Ag colloid fabricated using a Lee-Meisel procedure (described in section 3.3), was incorporated into an agar-agar matrix. Agar-agar comprises two components: the linear polysaccharide agarose, the use of which has already been discussed in chapter two and is again in this chapter, and a heterogeneous mixture of smaller molecules called agaropectin [14], [15]. The same dye-transfer approach adopted by [13] was used to gain chemical information on artwork pigments employing SERS.

3.1.1 Agarose gel: general applications and its function as a SERS substrate

Chapter two covered in detail the structure and some of the properties of agarose gel, as well as examining the impact of growth conditions on the SERS response of Ag-agarose composites. This subsection focusses primarily on the role of metal nanoparticle-agarose in SERS, first highlighted in chapter two, as part of the larger class of metal/gel substrates discussed in the preceding review. At high temperatures, aqueous agarose exhibits semi-flexible polymer characteristics; as it cools, individual polymer chains wind themselves into double helices that come together to form fibrils, producing a water-filled gel. Fibrils arrange themselves to

form a matrix, which regulates gel pore size as a function of agarose concentration, a characteristic which has made it highly suitable as chromatographic and electrophoretic media as well as stabilisers and thickeners in the food and pharmaceutical industries [16]. Metal-agarose composites have received much attention lately, not least because of their ease of fabrication and handling [17]–[19], and not solely for their applicability as SERS-active substrates. Electronic transport through gold-agarose has been studied, as its tunable charge-transport characteristics make it suitable for the development of sensors [18]. The porous nature of agarose has also been used to construct "cages" of different dimensions, depending on the concentration of the gel solution, within which growth of metal NPs can be controlled. Restricting growth in this manner, in conjunction with the tailoring of precursor concentrations, can give rise for example to monodisperse selenium and silver nanoparticles of different sizes, and in the case of silver, different morphologies [20].

The properties of agarose make it suitable for lab-on-a-chip studies [21]–[23] and the ability to regulate pore size has long been exploited in electrophoresis [16], especially to separate DNA fragments [24]. Pore size can be controlled in a similar manner to fractionate SERS-active Ag-multi-NP aggregates. A mixture of monomer, dimer, trimer, and higher-order aggregate classes, can be separated out by modulating NP surface charges with capping agents, with a view to enriching whichever class exhibits the greatest SERS intensity [25]. Agarose has also been used as a scaffold for the design of a gold/titania composite that could be used in catalysis [16].

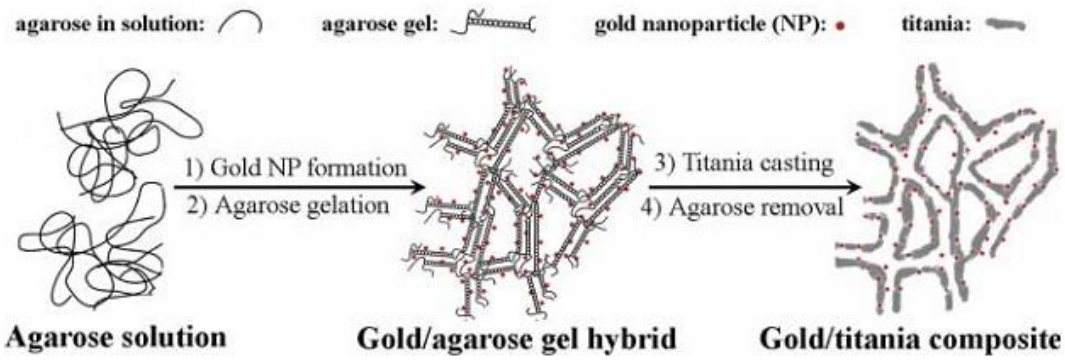

Figure 3.5. Fabrication of a Au/TiO_2 composite, as prepared by [16].

Figure 3.5 summarises the fabrication process for the gold/titania composite. Briefly, AuNPs are incorporated into an agarose matrix which is then infused with a titania precursor to form a network which ultimately replaces the agarose matrix/template by calcination at $450\,^{o}C$. A crystallised titania network peppered with gold NPs acts as a robust, porous catalyst that can withstand the generally high temperatures endured in catalytic reactions.

The application of agarose in microfluidics with respect to the design of highly SERS-active and reproducible agarose/AgNP composite beads has already been discussed in this chapter. In other work, Kattumuri *et al.* used gold NPs formed *in situ* within agarose to successfully fabricate SERS substrates for the detection of DNA nucleosides. It was found that Au-agarose yielded a stronger SERS signal than the gold-colloid-on-film control, due to the capability of agarose to form a network of AuNPs within the matrix for maximal coupling of localised surface plasmon resonances [26].

Raza and Saha [27] fabricated Ag-agarose gel by mixing agarose powder into Ag colloid solution, heating it and then allowing it to cool and gelate. They employed the same dye-transfer technique, discussed in this chapter, to detect

common everyday ink pigments. Interestingly, the authors use a × 20 objective and laser powers of 10 and 30 mW for 514 and 785 nm excitations respectively, and do not make reference to any scorching of the Ag-agarose samples when viewed by the naked eye or even under the microscope. In the experimental work for this thesis however, which also used × 20 magnification, it was found that the power tolerance of both Au- and Ag-agarose in high-to-low concentration gels was much lower, at around 0.1 to 4 mW at 633 nm excitation and around 0.5 to 5 mW at 785 nm excitation, depending on NP density. Generally, for a given power and sample, the shorter wavelength of 633 nm did more damage to the gels than 785 nm. If the power was greater than the tolerance levels, the laser blasted holes in the agarose, and scorching was patently obvious under the microscope, and even sometimes to the naked eye. Too high a laser power can burn samples, distorting the analyte spectrum through the addition of carbon bands [28], [29] and can cause signal deterioration [30], both of which negatively impact spectral reproducibility.

Raza and Saha also produced flexible filter paper strips that were impregnated with Ag-agarose [31]. Gel in the Ag-agarose/filter paper composite, promotes adhesion of plasmonic NPs, which would otherwise only be weakly bound and inhibits diffusion of analyte across and into the paper surface, allowing very low volumes of analyte at low concentration to be analysed with increased accuracy of analysis. In this process, no reducing agent is required; the reducing ends of the agarose polymer reduce the silver salt, forming AgNPs within the matrix, rendering the substrate SERS-active. Figure 3.6 summarises the fabrication process.

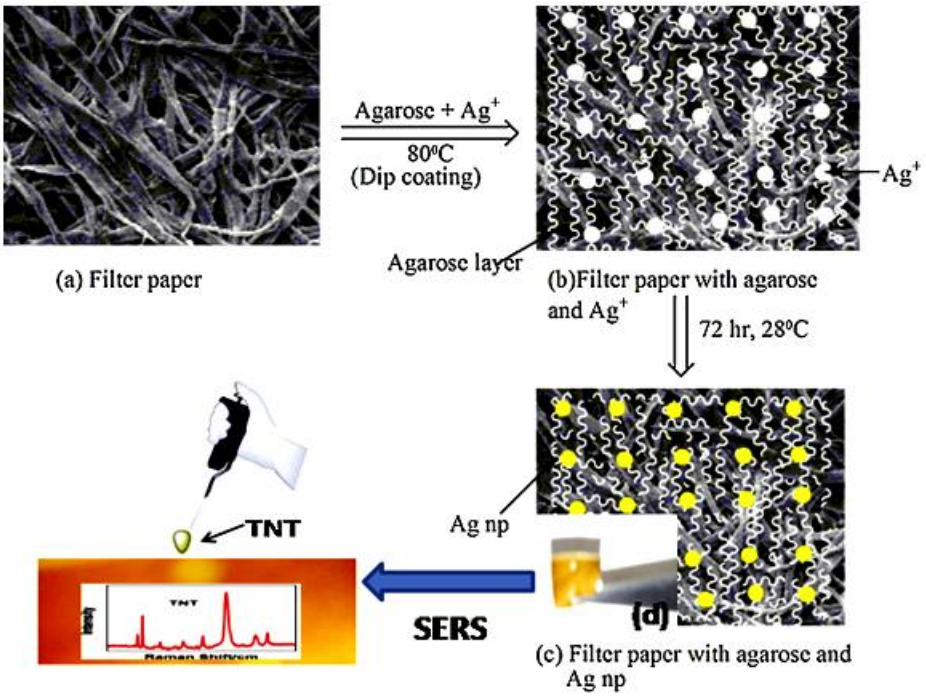

Figure 3.6. (a)-(c) Process for the synthesis of silver NPs in agarose/filter paper, (d) the actual filter paper after 72 h of treatment, as produced by [31].

Notably, the authors used a × 20 objective and a 514 nm laser source at 30 mW, a power which (for reasons given in the previous paragraph) would almost certainly seem intolerably high if burning of the agarose were to be prevented, especially given the shorter wavelength.

Zhai *et al.* employed a different technique to fabricate rigid as well as flexible agarose/AgNP composites [32]. Hot agarose solution is poured onto a glass or flexible substrate to form a thin, dry agarose film which is then functionalised with amines by dipping the substrate into a 3-aminopropyltriethoxysilane (APTES) solution. The procedure is illustrated in figure 3.7.

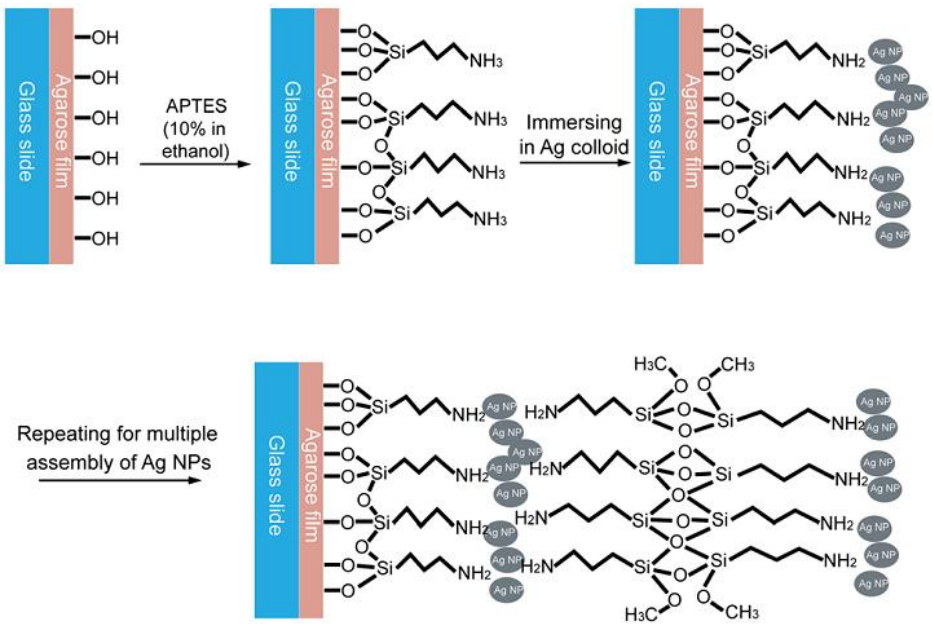

Figure 3.7. Fabrication of the AgNP/APTES/Agar film on a glass slide by [32].

After functionalisation, alternating layers of AgNPs and (APTES) sol-gel can be laid down via Ag colloid and APTES immersion. The substrate retains high sensitivity, good reproducibility and stability for at least 6 months after fabrication; however, there are numerous lengthy preparative treatments of the substrate necessary, in contrast with Ag-agarose production described in this thesis, which simply relies on the immersion of agarose in salt and reducing solutions. As seen in chapter two, altering one or both of these solutions affects the size and arrangement of the AgNPs, potentially allowing the SERS signal to be optimised.

3.2 SERS of Ag-agarose reduced by hydroxylamine and sodium borohydride: a comparison

3.2.1 Introduction

Chapter two section 2.3, showed that the reproducibility of Ag-agarose gel (%RSD in SERS signal strength) is heavily reliant on the growth conditions of AgNPs, in other words, the silver nitrate feed solution concentration and, by default, the sodium borohydride (SB) concentration, both of which were present in a 1:1 ratio. Generally, decreasing concentration narrows the AgNP size distribution, and in turn, the spread in SERS intensity measurements, as lower-concentration gels which experience a shorter nucleation period tend to possess better reproducibility. This chapter introduces a reduction technique, previously employed only in the fabrication of Ag colloids, which employs high-pH hydroxylamine as a reductant in Ag gel production; SERS of both these and samples using benchmark SB production are compared with one another to see if there might be an improvement in gel reproducibility without sacrificing SERS intensity.

Hydroxylamine can, in a high-pH environment, rapidly reduce silver salts to form an Ag colloid [33]. It can also reduce Au^{3+} ions, for example, to Au^{0} – a reaction which quickens if Au seeds are present [34], [35]. In spite of the proven SERS-effectiveness and ease of preparation of hydroxylamine-reduced (HR) Ag colloid, originally demonstrated by Leopold and Lendl [33], and HR-Ag colloids possessing several distinct advantages over other alternatives as demonstrated more recently by Larmour *et al.* [36], hydroxylamine is yet to establish itself in the SERS

community as a comprehensively used reducing agent for the fabrication of SERS-active Ag colloids.

Hydroxylamine was used in this experiment firstly to ascertain its capability to produce SERS-active Ag-agarose, and then to perhaps improve upon reproducibility results obtained using the "standard" reducing agent, SB. The original method of Ag colloid preparation, pioneered by Leopold and Lendl and employing hydroxylamine as a reductant, was adapted for silver salt gel reduction. In the original experiment, Ag^+ (aq) ions were rapidly reduced (in seconds) at room temperature by hydroxylamine in a high-pH environment created by the addition of aqueous sodium hydroxide. The reaction sequence during reduction is complex and probably includes the formation of a complex between the hydroxylamine and the silver ions, in addition to the production of neutral silver [33]; nitrogen gas and water are given off during the reaction [36]. In this chapter, HR-Ag-agarose gels were prepared mainly in the same way as sodium borohydride-reduced (SBR) gels, the only difference being that the 500 mM hydroxylamine (aq) solution was part of a 1000 mM sodium hydroxide (aq) solution to maintain high pH for rapid reduction. The concentration ratio of NaOH to hydroxylamine was thus 2:1, in line with the work by Leopold and Lendl [33].

3.2.2 Experimental

All chemicals were purchased from Sigma Aldrich and used without further purification. L-ascorbic acid (reagent grade, crystalline), *trans*-1,2-bis(4-pyridyl)ethylene (BPE – assay 97%), agarose type IX-A ultra-low gelling temperature, sodium borohydride (SB, purum p.a., ≥96% (gas-volumetric)) silver

nitrate ($AgNO_3$, ReagentPlus grade ≥ 99.0% (titration)) hydroxylamine hydrochloride (ReagentPlus, 99%), sodium hydroxyide (NaOH, HPCE-grade)..

Blank agarose squares (prepared using the same procedure described in chapter two, section 2.2.2.1), approximately 10 × 10 × 1.5 mm^3, were placed in vials containing $AgNO_3$ (aq) solutions (1 square per 3 ml of 10, 60 and 150 mM) for 3 h, ensuring that both square sides of the agarose were exposed to the salt solution. They were then removed, dried on filter paper and placed immediately in either 500 mM SB (aq), or 500 mM hydroxylamine (aq) as part of a 1000 mM NaOH (aq) solution for 3 h (1 square per 3 ml). The concentration of both reductants was held constant. After removal from the reducing solutions, the Ag-agarose gels were carefully washed in distilled water, and then dialysed for 1 h. They were then steeped overnight in 1.00 × 10^{-5} M BPE (aq), (1 square per 3 ml) in preparation for SERS analysis.

SERS analysis at 633 nm excitation was conducted using the same experimental setup described in chapter two, section 2.2.2.3. The unfocussed power at the sample was approximately 1 mW, and the collection time was 5 s. OriginPro 8.6 software was used to measure the average 1200 cm^{-1} peak intensity of BPE from twenty-six baseline-corrected spectra from each sample.

3.2.3 Results and discussion

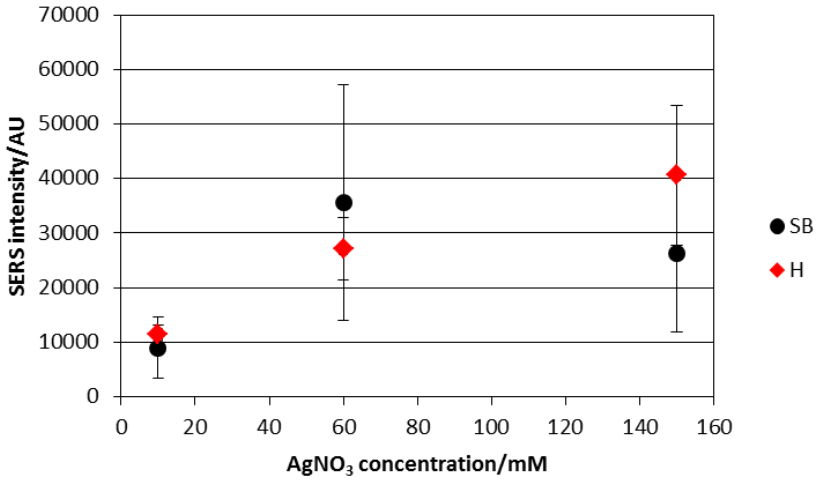

Figure 3.8. SERS intensity versus 10, 60, 150 mM silver nitrate feed solution concentration: a SB and hydroxylamine (H) comparison. Each data point is the 1200 cm^{-1} peak height of BPE averaged from twenty-six spectra, each collected over 5 s at about 1 mW from the entire surface of the substrate, with error bars representing the standard deviation.

Both HR and SBR gels generate similar signal strengths within the considered feed concentration range as illustrated in figure 3.8. The adapted hydroxylamine-reduction technique for Ag-agarose fabrication indeed proves highly successful in generating a SERS-active substrate. As might be expected for both reductants, 60 and 150 mM $AgNO_3$ solutions generate a stronger signal than 10 mM, possibly due to a combination of increased AgNP loading and an increase in average particle size, however care should be taken over this interpretation, as no transmission electron microscopy (TEM) was conducted on these samples, and only three different concentrations were examined. Figure 3.8 illustrates that hydroxylamine proves a viable alternative to SB with respect to Ag-agarose fabrication in terms of SERS signal strength.

Interestingly, the error bars are larger for SB than hydroxylamine, suggesting that overall, hydroxylamine might turn out to be better in terms of reproducibility under these conditions. This is in fact confirmed by figure 3.9

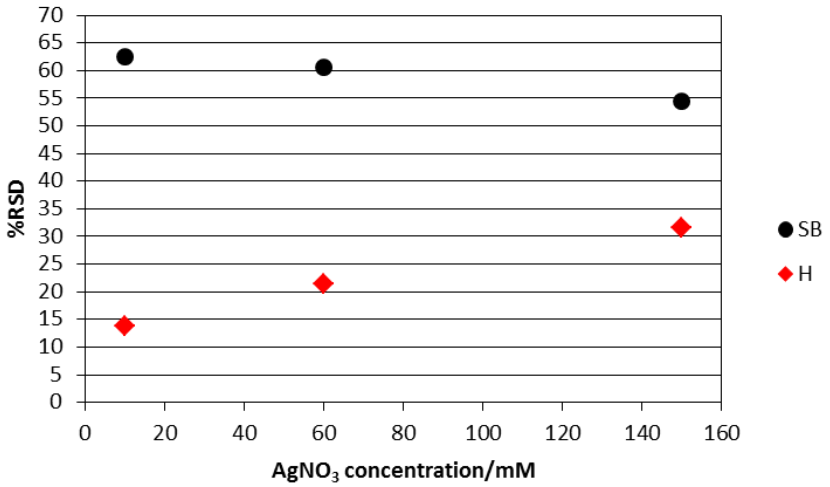

Figure 3.9. %RSD in SERS signal strength for 10, 60, 150 mM $AgNO_3$ HR and SBR Ag gels. Each data point represents the % relative standard deviation of the 1200 cm^{-1} peak height of BPE averaged from twenty-six spectra, each collected over 5s at approximately 1 mW from the entire surface of the substrate.

Figure 3.9 shows a clear division in gel reproducibility between SBR and HR gels, with HR gels proving superior in this regard.

The results summarised in figures 3.8 and 3.9 illustrate that in addition to generating a signal intensity comparable to that of SBR samples, HR gels exhibit superior reproducibility. This suggests that the AgNP number density and average particle size in both gels should be fairly similar, but that the size distribution of the SBR gel should be broader. TEM analysis would of course be required to prove this definitively. Better reproducibility in HR samples implies that high-pH hydroxylamine induces a shorter nucleation period compared with SB. Moreover, as reduction progressed, significantly less bubbling was evident in HR samples which

resulted in less physical disruption during NP formation – another factor which could be conducive to better reproducibility. Further analysis of HR-Ag-agarose and, in addition, HR-Au-agarose which more closely examines signal strength and reproducibility is included later in chapter four.

Interestingly, the exact same fabrication and SERS analysis procedures were followed using ascorbic acid (AA) as a reducing agent. The AA gels for all three salt concentrations however failed completely to produce viable substrates. Of over twenty spectra collected from each sample, only a few were of BPE, the rest being identical to AA-reduced controls, meaning that under these experimental conditions, AA reduction is unsuccessful. This is most likely due to AA being a relatively weak reducing agent and consequently, there being insufficient time for the salt to become adequately reduced.

3.2.4 Conclusion

An adapted reduction method using high-pH hydroxylamine was employed to produce Ag-agarose which was comparable with sodium borohydride-reduced gel in terms of SERS intensity, but which surpassed it with respect to reproducibility. This suggests that the AgNP number density and average particle size in both gels were fairly similar, but that the SB samples possessed a broader size distribution than their hydroxylamine counterparts.

3.3 Potential issues during spectral analysis

3.3.1 Introduction

It is interesting to note that, under the experimental conditions described in section 3.2, the control spectra of 10, 60 and 150 mM HR-Ag-agarose all have prominent Raman bands, something which should be remembered during SERS analysis of BPE.

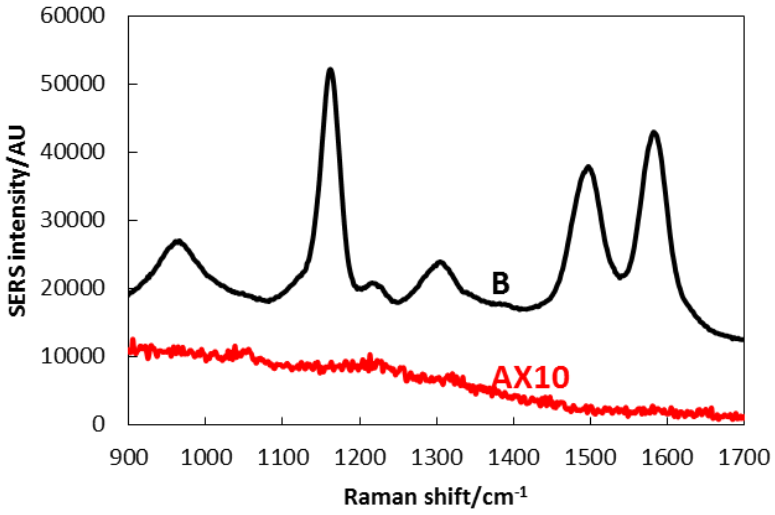

Figure 3.10. Representative SERS spectra of blank (A) SBR- (scaled up by ten) and (B) HR-Ag-agarose gels, both from a 60 mM $AgNO_3$ feed solution. Spectra have been shifted for clarity.

The control SERS spectrum of blank HR-Ag-agarose, illustrated in figure 3.10 (B), exhibits prominent Raman bands at 965, 1162, 1216, 1304, 1498, and 1582 cm^{-1}, in contrast with that of SBR Ag-agarose which, even at X10 magnification, is virtually featureless. In their study of spurious Raman bands arising from different Ag colloids and aggregating agents, Yaffe and Blanch [37], warn that the experimental system must be characterised in terms of SERS before examination of the analyte under consideration. This is because Raman bands which are taken as originating

from the analyte may rather be generated by the colloid-aggregating agent system and could thus confuse or prevent proper analysis. In their work, they report for the first time several Raman bands arising from HR-Ag-colloid, which they cannot confidently ascribe to specific vibrational modes. Without further information, it is difficult to attribute specific vibrations to any bands of the HR-Ag-agarose control with certainty. However, in their study of Raman scattering of a single crystal of hydroxylamine hydrochloride, Krishnan and Balasubramanian assign the bands in the right hand column of table 3.1 to the vibrations of the NH_3OH^+ (hydroxylammonium) ion [38]. These bands closely match four of the six bands found in the HR-Ag-agarose spectrum (shown in the left-hand column), strongly suggesting that there exists residual unreacted hydroxylamine hydrochloride in the gels post-reduction.

Table 3.1. Raman bands of HR-Ag-agarose with possible corresponding bands from a single crystal of hydroxylamine hydrochloride (the latter taken from [38]).

Selected bands of HR-Ag-agarose/cm^{-1}	Bands of hydroxylamine hydrochloride crystal/cm^{-1}
1162	1168
1216	1204
1498	1496
1582	1590

Although no aggregating agent is required when using the already SERS-active Ag gel, SERS characterisation of the sample without the analyte should always be conducted for reference and possible background removal during data analysis.

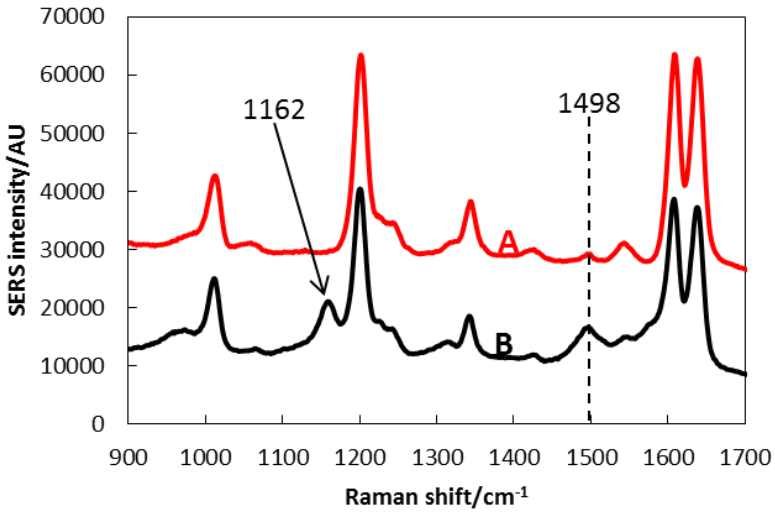

Figure 3.11. SERS spectra of BPE in Ag-agarose gel prepared using (A) SB and (B) hydroxylamine as reducing solutions. The band at 1162 cm^{-1} in (B) arises from blank HR-Ag-agarose, and BPE and blank Ag-agarose happen to have coincident peaks at around 1498 cm^{-1}. Spectra have been shifted for clarity.

Figure 3.11 shows two BPE SERS spectra produced by SBR- and HR-Ag gels. Each possesses the prominent bands of BPE [39], however, there are small, but important differences in the spectra. The "HR-Ag-agarose + BPE" spectrum (spectrum B) has a spurious band at 1162 cm^{-1}, resulting from a superposition of the HR-Ag-agarose background (illustrated in figure 3.10 (B)) onto the BPE spectrum. In contrast, the spectrum of blank SBR gel in figure 3.10 (A) is virtually featureless, supporting the earlier proposal that Raman bands in the hydroxylamine control gel originate from residual unreacted hydroxylamine hydrochloride. Interestingly, in chapter four section 4.1.3.1, the same background in the controls is absent when substantially lower concentrations of hydroxylamine are employed.

It also happens that the spectra of BPE and blank HR-Ag-agarose have coincident peaks around 1498 cm^{-1}, a phenomenon which exaggerates the 1498 cm^{-1} peak height of BPE in the "HR-Ag-agarose + BPE" spectrum, (figure 3.11 (B)).

While the background in this case presents no particular problem, especially since the baseline-corrected 1200 cm^{-1} peak height of BPE is measured, which is absent in the HR control, it is nonetheless prudent in general to ascertain which peaks belong to the analyte and which to the substrate, to avoid potential pitfalls during data analysis. This is analogous to distinguishing between analyte and colloid-aggregating agent peaks as discussed in [37].

One main difference between Ag-gel and a colloid-aggregating agent system is that, for gel, an aggregating agent is redundant. The NPs are already fixed in the matrix close enough together to facilitate coupling of localised surface plasmons, and as discussed in chapter two section 2.1.2, the matrix can be collapsed upon drying to strengthen the SERS signal. Citrate-reduced colloid was produced and used alongside two common aggregating agents, sodium sulphate and sodium chloride to emphasise graphically how the intrinsic spectrum of BPE can become distorted depending on the aggregating agent used, an issue that does not arise in the use of metal-agarose gels which do not require aggregation.

3.3.2 Experimental

All chemicals were purchased from Sigma Aldrich and used without further purification. *trans*-1,2-bis(4-pyridyl)ethylene (BPE - assay 97%), silver nitrate ($AgNO_3$, ReagentPlus grade ≥ 99.0% (titration)), sodium sulphate (Na_2SO_4, ACS reagent, anhydrous, ≥ 99.0%), sodium chloride (NaCl, premium 99.0-100.5%), sodium citrate (monobasic, purum p.a., anhydrous, ≥99.0%).

Preparation of citrate-reduced silver colloid (CRSC) was adapted from the procedure introduced by Lee and Meisel (method C from their paper) [40]. Briefly, $AgNO_3$ (45 mg) was dissolved in 250 ml of distilled water in a conical flask and brought to boiling, upon which, 5 ml of 1% sodium citrate were added and the solution left to boil for 1 h. The Ag colloid was left to cool and stored in the fridge until required. Aqueous solutions of 1.00 M Na_2SO4 and NaCl were synthesised.

For SERS analysis, the colloid (200 µl) was placed in a quartz micro-cuvette to which BPE (20 µl, 1.00×10^{-5} M (aq)) was added. This was followed sequentially by aqueous Na_2SO_4 or NaCl, (each 200 µl, 1.00 M), making the final concentration of BPE about 4.8×10^{-7} M. Analysis was conducted using the Renishaw Ramascope System 2000 described in chapter two, at 633 nm excitation and with a cuvette adapter fitted. Five 2 s collections at around 4 mW were performed on each sample with the average 1200 cm^{-1} BPE peak intensity recorded using OriginPro 8.6 software.

3.3.3 Results and discussion

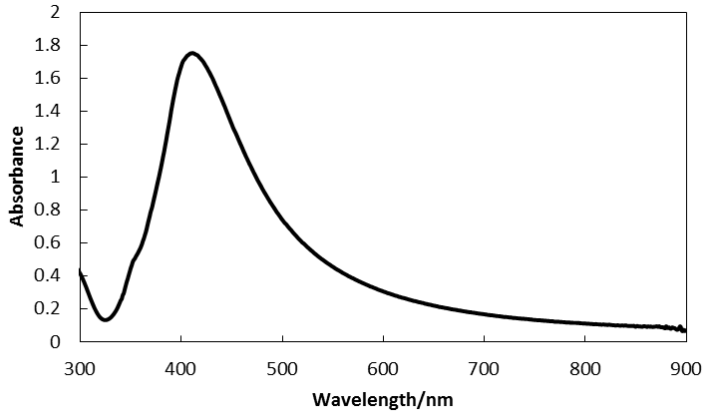

Figure 3.12. Absorption spectrum of citrate-reduced silver colloid with the plasmon band centred on 411 nm.

Figure 3.12 is an absorption spectrum of CRSC with the silver plasmon band centred on 411 nm which is in close agreement with the literature [36].

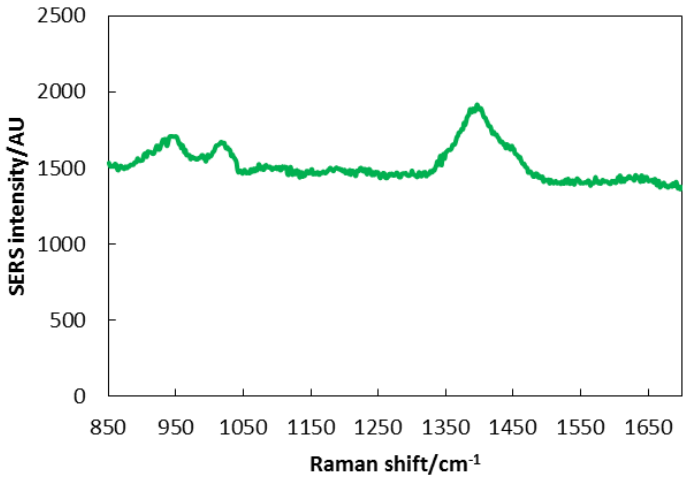

Figure 3.13 SERS spectrum of citrate-reduced Ag colloid.

Figure 3.13 is a SERS spectrum of CRSC, possessing several small peaks on a weak background. SERS spectra of "CRSC + BPE" using the two aggregating agents are shown in figure 3.14.

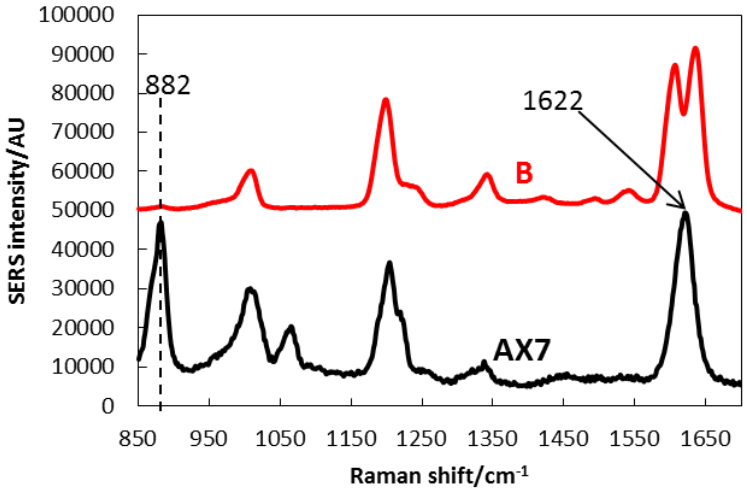

Figure 3.14. SERS spectra of BPE (final concentration approximately 4.8×10^{-7} M) using (A) CRSC + NaCl (× 7 magnification) and (B) CRSC + Na_2SO_4. Spectra have been shifted for clarity.

Figure 3.14 highlights important spectral differences which can arise during SERS of BPE depending on the choice of aggregating agent. When Na_2SO_4 is employed, the standard SERS spectrum of BPE (figure 3.14 (B)) is generated [39], however when NaCl is used, various changes in the spectrum are evident, most notably the substantial increase in relative intensity of the 882 cm^{-1} band, and the merging of bands 1607 and 1637 cm^{-1} into a single band centred on 1622 cm^{-1}. This result reemphasises how a specific aggregating agent might fundamentally alter the spectral profile of an analyte. Given the merging of bands 1607 and 1637 cm^{-1}, it would appear that the alteration does not merely originate from a superposition of spurious bands from the "CRSC + NaCl" solution onto the BPE spectrum, but rather from fundamental changes to the SERS spectrum of BPE itself. It is noteworthy that, despite minor qualitative changes in the peak height ratios of BPE as seen by the naked eye, depending on whichever metal-agarose hydrogel was under analysis, none of the gels in this thesis ever induced such a fundamental distortion of the intrinsic spectrum of BPE. Moreover, although high-concentration HR-Ag-agarose controls possess definite Raman bands, probably arising from residual, unreacted hydroxylamine hydrochloride left over from reduction, samples fabricated at lower hydroxylamine concentrations are distinctly lacking in these and are largely featureless as discussed later in chapter four section 4.1.3.1. In other words, employing metal gels as SERS substrates is one possible way of avoiding potential pitfalls regarding spectral distortion arising from the use of aggregating agents.

Although a comparison between silver colloids and Ag-agarose is beyond the scope of this thesis, one final point of interest is that after normalisation of spectra to a silicon standard, the 200 mM Ag-agarose sample mentioned in chapter two section

2.3 produces an average 1200 cm^{-1} BPE peak height similar to that of the "CRSC + NaCl" system (within 15%). This is despite the concentration of BPE being around five times less in the gel (1.0×10^{-7} M in the gel and 4.8×10^{-7} M in the colloidal system). This highlights that even without further refinement, the silver gel can at least produce a SERS signal comparable in strength to one generated by a standard colloidal substrate.

3.3.4 Conclusion

Section 3.3 discussed potential pitfalls which might arise during analysis from SERS spectra of the substrate itself, which could confuse or prevent proper examination of the analyte. In the case of HR-Ag-agarose, prominent Raman bands were present in control spectra taken from the bare substrate, and were seen to be superimposed onto the BPE spectra. While this did not pose any serious analytical problem, it is an important reminder that the system should always be characterised by SERS before examination of the analyte to determine which peaks belong to the analyte and which to the substrate itself.

Citrate-reduced colloid was used alongside two common aggregating agents, sodium sulphate and sodium chloride, to illustrate how a Raman spectrum can suffer intrinsic distortion depending on the aggregating agent used. One major advantage that metal-agarose gels have over sols is that they do not require the use of aggregating agents to engage SERS activity, thus automatically avoiding potential problems arising from a poor choice of such.

3.4 Summary

This chapter investigated an adapted reduction method using high-pH hydroxylamine to produce Ag-agarose, comparable with sodium borohydride-reduced gel with respect to SERS intensity, but surpassing it in reproducibility. This suggests that the AgNP number density and average particle size in both gels were fairly similar, but that the SB samples possessed a broader size distribution than their hydroxylamine counterparts.

The importance of characterising the system in terms of SERS prior to analysis of a molecular probe was highlighted, as Raman bands arising solely from the substrate can become superimposed on the molecular spectrum, potentially confusing analysis.

Citrate-reduced colloid was used alongside two common aggregating agents, sodium sulphate and sodium chloride, to illustrate how a Raman spectrum can suffer intrinsic distortion depending on the aggregating agent used. This is avoided when using metal-agarose gels which do not require aggregating agents to engage SERS activity.

References

[1] D. Das, T. Kar, and P. K. Das, "Gel-nanocomposites: materials with promising applications," *Soft Matter*, vol. 8, no. 8, pp. 2348–2365, 2012.

[2] P. Yu, Q. Qian, Y. Lin, and L. Mao, "In situ formation of three-dimensional uniform Pt/carbon nanotube nanocomposites from ionic liquid/carbon nanotube gel matrix with enhanced electrocatalytic activity toward methanol oxidation," *J. Phys. Chem. C*, vol. 114, no. 8, pp. 3575–3579, 2010.

[3] G. Ionita, G. Marinescu, C. Ilie, D. F. Anghel, D. K. Smith, and V. Chechik, "Sorption of metal ions by poly(ethylene glycol)/β-CD hydrogels leads to gel-embedded metal nanoparticles," *Langmuir*, vol. 29, no. 29, pp. 9173–9178, 2013.

[4] T. Maneerung, S. Tokura, and R. Rujiravanit, "Impregnation of silver nanoparticles into bacterial cellulose for antimicrobial wound dressing," *Carbohydr. Polym.*, vol. 72, no. 1, pp. 43–51, 2008.

[5] S. Ghosh, A. Saraswathi, S. S. Indi, S. L. Hoti, and H. N. Vasan, "Ag@AgI, core@shell structure in agarose matrix as hybrid: synthesis, characterization, and antimicrobial activity," *Langmuir*, vol. 28, no. 22, pp. 8550–8561, 2012.

[6] S. Ghosh, R. Kaushik, K. Nagalakshmi, S. L. Hoti, G. A. Menezes, B. N. Harish, and H. N. Vasan, "Antimicrobial activity of highly stable silver nanoparticles embedded in agar-agar matrix as a thin film," *Carbohydr. Res.*, vol. 345, no. 15, pp. 2220–2227, 2010.

[7] S. Saha, A. Pal, S. Pande, S. Sarkar, S. Panigrahi, and T. Pal, "Alginate gel-mediated photochemical growth of mono- and bimetallic gold and silver nanoclusters and their application to surface-enhanced Raman scattering," *J. Phys. Chem. C*, vol. 113, no. 18, pp. 7553–7560, 2009.

[8] J. M. Köhler, A. März, J. Popp, A. Knauer, I. Kraus, J. Faerber, and C. Serra, "Polyacrylamide/silver composite particles produced via microfluidic photopolymerization for single particle-based SERS microsensorics.," *Anal. Chem.*, vol. 85, no. 1, pp. 313–318, 2013.

[9] S. Abalde-Cela, B. Auguié, M. Fischlechner, W. T. S. Huck, R. A. Alvarez-Puebla, L. M. Liz-Marzán, and C. Abell, "Microdroplet fabrication of silver–agarose nanocomposite beads for SERS optical accumulation," *Soft Matter*, vol. 7, no. 4, pp. 1321–1325, 2011.

[10] Sigma-Aldrich, "Hydrazine gas: safety and documentation," 2014. [Online]. Available: http://www.sigmaaldrich.com/catalog/product/sial/215155?lang=en&region=GB. [Accessed: 08-May-2014].

[11] S. Yao, C. Zhou, and D. Chen, “A highly porous PVA dried gel with gold nanoparticles embedded in the network as a stable and ultrasensitive SERS substrate.,” *Chem. Commun.*, vol. 49, no. 57, pp. 6409–6411, 2013.

[12] K. Shin, K. Ryu, H. Lee, K. Kim, H. Chung, and D. Sohn, “Au nanoparticle-encapsulated hydrogel substrates for robust and reproducible SERS measurement,” *Analyst*, vol. 138, no. 3, pp. 932–938, 2013.

[13] M. Leona, P. Decuzzi, T. A. Kubic, G. Gates, and J. R. Lombardi, “Nondestructive identification of natural and synthetic organic colorants in works of art by surface enhanced Raman scattering,” *Anal. Chem.*, vol. 83, no. 11, pp. 3990–3993, 2011.

[14] C. Lofrumento, M. Ricci, E. Platania, M. Becucci, and E. Castellucci, “SERS detection of red organic dyes in Ag-agar gel,” *J. Raman Spectrosc.*, vol. 44, no. 1, pp. 47–54, 2013.

[15] R. Armisen, F. Galatas, and S. A. Hispanagar, “Agar,” in *Handbook of Hydrocolloids*, Second Ed., G. O. Phillips and P. A. Williams, Eds. Cambridge: Woodhead Publishing Limited, 2009, pp. 82–89.

[16] X. Wang, C. E. Egan, M. Zhou, K. Prince, D. R. G. Mitchell, and R. A. Caruso, “Effective gel for gold nanoparticle formation, support and metal oxide templating,” *Chem. Commun.*, no. 29, pp. 3060–3062, Aug. 2007.

[17] M. Keating, Y. Chen, I. A. Larmour, K. Faulds, and D. Graham, “Growth and surface-enhanced Raman scattering of Ag nanoparticle assembly in agarose gel,” *Meas. Sci. Technol.*, vol. 23, no. 8, p. 084006, 2012.

[18] E. Faoucher, P. Nativo, K. Black, J. B. Claridge, M. Gass, S. Romani, A. L. Bleloch, and M. Brust, “In situ preparation of network forming gold nanoparticles in agarose hydrogels,” *Chem. Commun.*, no. 43, pp. 6661–6663, 2009.

[19] P. Aldeanueva-Potel, E. Faoucher, R. A. Alvarez-Puebla, L. M. Liz-Marzan, and M. Brust, “Recyclable molecular trapping and SERS detection in silver-loaded agarose gels with dynamic hot spots,” *Anal. Chem.*, vol. 81, no. 22, pp. 9233–9238, 2009.

[20] J.-L. Li, X.-Y. Liu, X.-G. Wang, and R.-Y. Wang, “Controlling nanoparticle formation via sizable cages of supramolecular soft materials,” *Langmuir*, vol. 27, no. 12, pp. 7820–7827, 2011.

[21] N. Du, J. Chou, E. Kulla, P. N. Floriano, N. Christodoulides, and J. T. McDevitt, “A disposable bio-nano-chip using agarose beads for high performance immunoassays,” *Biosens. Bioelectron.*, vol. 28, no. 1, pp. 251–256, 2011.

[22] G. Kang, J.-H. Lee, C.-S. Lee, and Y. Nam, “Agarose microwell based neuronal micro-circuit arrays on microelectrode arrays for high throughput drug testing,” *Lab Chip*, vol. 9, no. 22, pp. 3236–3242, 2009.

[23] J. V. Jokerst, J. Chou, J. P. Camp, J. Wong, A. Lennart, A. A. Pollard, P. N. Floriano, N. Christodoulides, G. W. Simmons, Y. Zhou, M. F. Ali, and J. T. McDevitt, “Location of biomarkers and reagents within agarose beads of a programmable bio-nano-chip,” *Small*, vol. 7, no. 5, pp. 613–624, 2011.

[24] S. S. Smith, T. E. Gilroy, and F. A. Ferrari, “The influence of agarose-DNA affinity on the electrophoretic separation of DNA fragments in agarose gels,” *Anal. Biochem.*, vol. 128, no. 1, pp. 138–151, 1983.

[25] N. Guarrotxena and G. Braun, “Ag-nanoparticle fractionation by low melting point agarose gel electrophoresis,” *J. Nanoparticle Res.*, vol. 14, no. 10, p. 1199, 2012.

[26] V. Kattumuri, M. Chandrasekhar, S. Guha, K. Raghuraman, K. V. Katti, K. Ghosh, and R. J. Patel, “Agarose-stabilized gold nanoparticles for surface-enhanced Raman spectroscopic detection of DNA nucleosides,” *Appl. Phys. Lett.*, vol. 88, no. 15, p. 153114, 2006.

[27] A. Raza and B. Saha, “Silver nanoparticles doped agarose disk: highly sensitive surface-enhanced Raman scattering substrate for in situ analysis of ink dyes,” *Forensic Sci. Int.*, vol. 233, no. 1–3, pp. 21–27, 2013.

[28] V. A. Sivakov, K. Höflich, M. Becker, A. Berger, T. Stelzner, K.-E. Elers, V. Pore, M. Ritala, and S. H. Christiansen, “Silver coated platinum core-shell nanostructures on etched Si nanowires: atomic layer deposition (ALD) processing and application in SERS,” *ChemPhysChem*, vol. 11, no. 9, pp. 1995–2000, 2010.

[29] R. F. Aroca, R. E. Clavijo, M. D. Halls, and H. B. Schlegel, “Surface-enhanced raman spectra of phthalimide. Interpretation of the SERS spectra of the surface complex formed on silver islands and colloids,” *J. Phys. Chem. A*, vol. 104, no. 42, pp. 9500–9505, 2000.

[30] S. E. J. Bell and N. M. S. Sirimuthu, “Quantitative surface-enhanced Raman spectroscopy.,” *Chem. Soc. Rev.*, vol. 37, no. 5, pp. 1012–24, 2008.

[31] A. Raza and B. Saha, “In situ silver nanoparticles synthesis in agarose film supported on filter paper and its application as highly efficient SERS test stripes,” *Forensic Sci. Int.*, vol. 237, pp. e42–e46, 2014.

[32] W.-L. Zhai, D.-W. Li, L.-L. Qu, J. S. Fossey, and Y.-T. Long, “Multiple depositions of Ag nanoparticles on chemically modified agarose films for surface-enhanced Raman spectroscopy,” *Nanoscale*, vol. 4, no. 1, pp. 137–142, 2012.

[33] N. Leopold and B. Lendl, “A new method for fast preparation of highly surface-enhanced Raman scattering (SERS) active silver colloids at room temperature by reduction of silver nitrate with hydroxylamine hydrochloride,” *J. Phys. Chem. B*, vol. 107, no. 24, pp. 5723–5727, 2003.

[34] B. K. Jena and C. R. Raj, “Electrochemical biosensor based on integrated assembly of dehydrogenase enzymes and gold nanoparticles,” *Anal. Chem.*, vol. 78, no. 18, pp. 6332–6339, 2006.

[35] S. Link and M. A. El-Sayed, “Size and temperature dependence of the plasmon absorption of colloidal gold nanoparticles,” *J. Phys. Chem. B*, vol. 103, no. 21, pp. 4212–4217, 1999.

[36] I. A. Larmour, K. Faulds, and D. Graham, “SERS activity and stability of the most frequently used silver colloids,” *J. Raman Spectrosc.*, vol. 43, no. 2, pp. 202–206, 2012.

[37] N. R. Yaffe and E. W. Blanch, “Effects and anomalies that can occur in SERS spectra of biological molecules when using a wide range of aggregating agents for hydroxylamine-reduced and citrate-reduced silver colloids,” *Vib. Spectrosc.*, vol. 48, no. 2, pp. 196–201, 2008.

[38] R. S. Krishnan and K. Balasubramanian, “Raman spectrum of hydroxylamine hydrochloride (NH3OH.Cl),” *Proc. Indian Acad. Sci. - Sect. A*, vol. 59, no. 5, pp. 285–291, 1964.

[39] W. Yang, J. Hulteen, G. C. Schatz, and R. P. Van Duyne, “A surface-enhanced hyper-Raman and surface-enhanced Raman scattering study of *trans*-1,2-bis(4-pyridyl)ethylene adsorbed onto silver film over nanosphere electrodes. Vibrational Assignments: experiment and theory,” *J. Chem. Phys.*, vol. 104, no. 11, pp. 4313–4323, 1996.

[40] P. C. Lee and D. Meisel, “Adsorption and surface-enhanced Raman of dyes on silver and gold sols,” *J. Phys. Chem.*, vol. 86, no. 17, pp. 3391–3395, 1982.

Chapter 4 SERS of hydroxylamine-reduced Au and Ag nanoparticle-agarose

In chapter three, the most promising reductant between sodium borohydride and high-pH hydroxylamine with respect to the combined qualities of SERS signal strength and reproducibility, proved to be the latter, so this chapter focusses on SERS of Ag- and Au-agarose, reduced by hydroxylamine.

4.1 SERS of hydroxylamine-reduced Ag-agarose gels

4.1.1 Introduction

It was shown in chapter two, section 2.4, that reproducibility in high-concentration silver-agarose (200 mM $AgNO_3$) remains poor even when a heavy excess of sodium borohydride (SB) is used, suggesting that lower-feed-concentration gels possess better reproducibility in general. Consequently, hydroxylamine-reduced (HR)-Ag-agarose gels in the low-feed-concentration range of 1 – 10 mM were fabricated and the SERS response examined.

4.1.2 Experimental

All chemicals were purchased from Sigma Aldrich and used without further purification: *trans*-1,2-bis(4-pyridyl)ethylene (BPE - assay 97%), agarose type IX-A (ultra-low gelling temperature), silver nitrate ($AgNO_3$, ReagentPlus grade ≥ 99.0% (titration)), hydroxylamine hydrochloride (ReagentPlus, 99%), and sodium hydroxyide (NaOH, HPCE-grade).

Blank agarose gel was prepared as described previously in chapter two, section 2.2.2.1. Gel squares measuring approximately $1.5\times10\times10\ mm^3$ were immersed in $AgNO_3$ solutions (1 square per 3 ml: 1, 2, 3,….10 mM) for 2 h, removed and dried on filter paper, and then placed immediately in vials containing reducing solutions of high-pH hydroxylamine (1 square per 3ml: 2, 4, 6,….20 mM) for 2 h, ensuring both square planar sides of the gel were fully exposed to the solution. The hydroxylamine solutions were rendered alkaline by the addition of NaOH (aq) – the ratio of NaOH to hydroxylamine was maintained at 2:1. An excess of reductant, [reductant]:[Ag salt] = 2:1, was used to ensure complete reduction of the Ag-salt gels. After *in situ* reduction, Ag gels were dialysed in distilled water for 1 h and then placed in 1.00×10^{-5} M BPE (aq) overnight for SERS analysis.

SERS analysis was conducted the next day using 633 and 785 nm excitation wavelengths on the Renishaw Ramascope System 2000, set up as described previously in chapter two section 2.2.2.3. The unfocussed power at the sample was 2.425 mW, with a collection time of 5 s at 633 nm excitation and 5.25 mW, 5s at 785 nm excitation. All gels were taken from BPE solutions and dried on filter paper before analysis. For clarity, all spectra were normalised for power and collection time, giving intensity units of photon counts per second per milliwatt ($c\ s^{-1}\ mW^{-1}$). Each data point in the "SERS intensity versus $AgNO_3$ concentration" graphs, represents the 1200 cm^{-1} baseline-corrected peak height of BPE, measured using OriginPro 8.6 software and averaged from twenty-two spectra collected from across the surface of the substrate (approximately 1 cm^2), with error bars representing the standard deviation.

Absorption spectra were recorded on a Jasco V-660 UV-VIS spectrometer. A method of gel preparation, as reported by Aldeanueva-Potel *et al.* [1], was used, whereupon a small piece of blank agarose gel was compressed between two fused silica slides and used as a baseline, with the same done for Ag-agarose.

4.1.3 Results and discussion

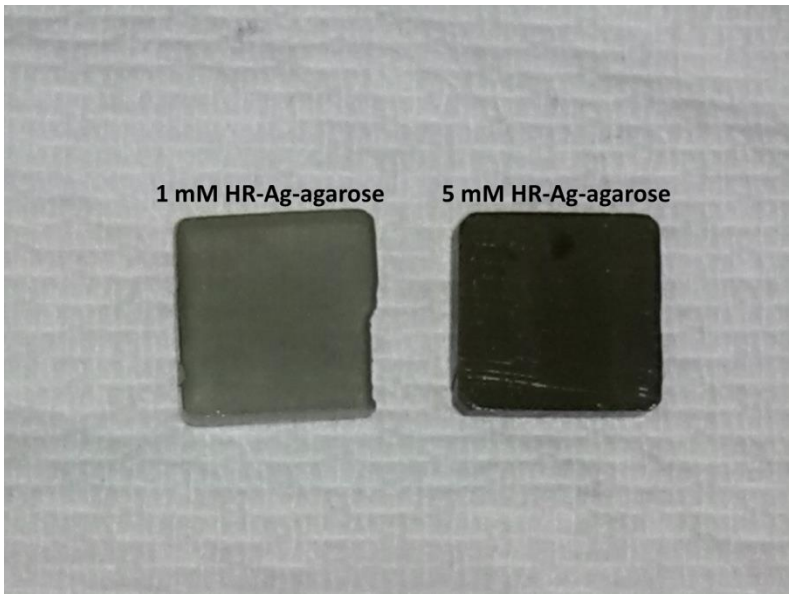

Figure 4.1. HR-Ag-agarose gels as-labelled. Each side measures 1 cm.

Figure 4.1 shows 1 mM HR-Ag-agarose on the left hand side of the image, which is far paler in comparison to 5 mM HR-Ag-agarose on the right. In fact, the 1 mM gel was virtually transparent and a spatula could be seen easily when placed underneath. Interestingly it was found that in general, the lowest-concentration silver or gold samples could withstand the highest laser powers at 633 and 785 nm excitations, which could prove advantageous in limit of detection experiments for example or in improving the signal to noise ratio generally. The reason is due to less

power absorption at these concentrations, as the gels are more translucent and less opaque.

4.1.3.1 SERS of blank Ag-agarose

Figure 4.2 is a SERS spectrum of blank HR-Ag-agarose, using a 6 mM $AgNO_3$ feed solution.

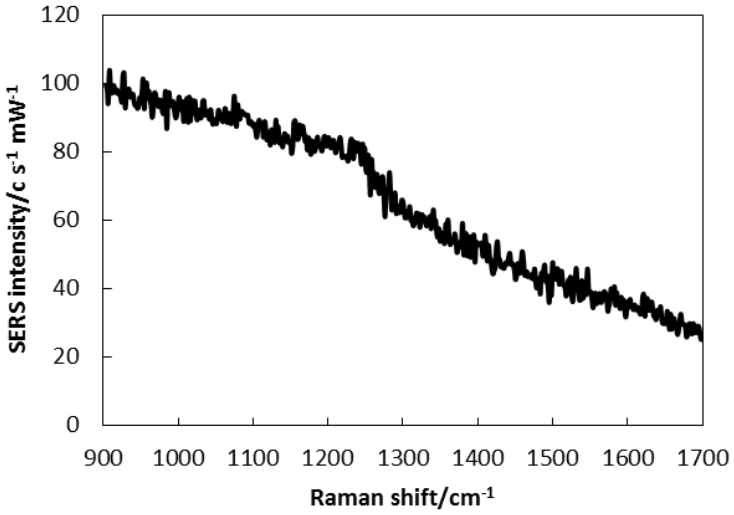

Figure 4.2. SERS spectrum of blank 6 mM HR-Ag-agarose at 633 nm excitation. The original laser power was about 1.2 mW with a collection time of 5 s.

Interestingly, the spectrum is virtually featureless and lacks the prominent bands present in the control samples fabricated using excess hydroxylamine, discussed in chapter three, despite being subjected to the same 633 nm excitation. Why such bands should be lacking in all of the current control spectra from 1 – 10 mM is at first unclear, especially since there is an overlap in $AgNO_3$ concentration between the previous and current experiments at 10 mM.

The main difference between the two experiments however, is that the one in chapter three used a high concentration of 500 mM hydroxylamine, while the highest

concentration in the current experiment is only 20 mM (for the 10 mM $AgNO_3$ sample). Moreover, it appears absolute concentration is the deciding factor in band production, rather than the molar ratio of hydroxylamine to $AgNO_3$, as the ratio in the previous experiment for the 150 mM $AgNO_3$ sample for instance, was only 3.33:1, which is close to the current ratio of 2:1. In terms of absolute hydroxylamine concentration however, that of the previous study was 25 times greater than that in the current work.

4.1.3.2 SERS of Ag-agarose at 633 and 785 nm excitations

The amount of light scattering, whether Raman or Rayleigh, is not only dependent on the scattering medium, but is crucially dependent on the wavelength as $1/\lambda^4$, so that 633 nm photons are Raman-scattered $(785/633)^4 \approx 2.37$ times more than 785 nm photons [2]. With all other things being equal for a given sample, the signal will therefore be more intense at shorter wavelengths which can, if necessary, be corrected for during analysis. In analytical work however, the total *observed* signal is paramount [3], and consequently in this chapter, powers and acquisition times, for the most part, have been normalised for both wavelengths to give units of counts per second per milliwatt (c s^{-1} mW^{-1}) without scattering corrections, to facilitate a direct comparison.

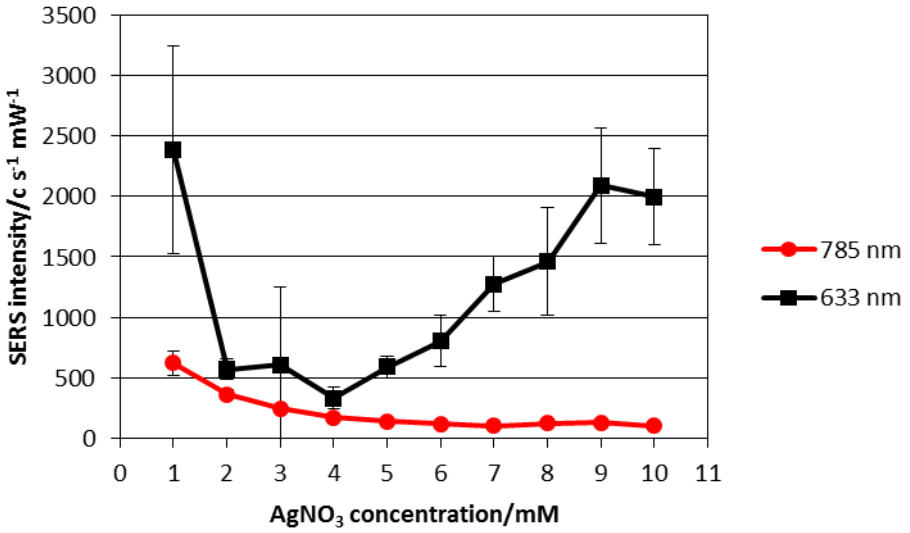

Figure 4.3. SERS intensity versus $AgNO_3$ feed solution concentration of the same HR-Ag-agarose samples at 633 and 785 nm excitations. Each data point represents the 1200 cm^{-1} peak height of BPE averaged from twenty-two spectra, each collected from across the surface of the substrate (approximately 1 cm^2). Powers and acquisition times have been normalised (counts per second per milliwatt or c s^{-1} mW^{-1}).

Figure 4.3 is a graph of SERS intensity versus $AgNO_3$ feed concentration for the same HR-Ag-agarose samples at 633 and 785 excitations. Remarkably, in this low-concentration regime, the SERS intensity of 1 mM at 633 nm is similar to that of 9 and 10 mM. Without TEM analysis, there is no way to gauge nanoparticle size and/or the degree of aggregation, however as precursor concentration was increased in both silver and gold gels, gel opacity quickly rose to a qualitative maximum at around 4 mM due to increased particle loading. Counterintuitively, and despite visual evidence of substantially less particle loading in the 1 mM sample as seen in figure 4.1, this gel generates a signal about 4 times stronger than the 5 mM sample. The signal intensity falls sharply however between 1 and 2 mM, reaching a minimum at 4 mM, after which it starts to climb steadily, eventually almost reaching the initial value.

It is curious why the lowest concentration gel, evidently with a considerably lower NP density, should generate such a strong signal, roughly the same as that of the 9 and 10 mM samples. It was observed that the high whitish-grey semi-transparency of the 1 mM sample promoted very strong scattering of the laser light, which perhaps produced a compensatory effect in that greater numbers of Raman-scattered photons were created, generating the stronger-than-expected signal (which did not originate from outliers). There was only one 1 mM sample however, and it would be interesting to see if this result were repeatable. Gel opacity quickly rose after 1 mM concentration, which resulted in greater absorption, less scattering and a concomitant temporary reduction in signal strength. At 4 mM however, NP density became high enough to begin to offset this reduction, producing a rising trend from 5 – 10 mM. In contrast, the 785 nm excitation intensity profile of HR-Ag-agarose turns out to be quite different.

At this wavelength, the intensity falls after 1 mM and fails to recover, reaching a plateau at around 7 mM, and overall, SERS intensity is lower at 785 nm excitation. Given its longer wavelength, 785 nm light penetrates the samples comparatively easily, so the initial reduction in intensity cannot be attributed to an inverse relation between opacity and scattering, especially since the reduction is more gradual than at 633 nm. Rather, it should originate from a reduction in the density of NPs amenable to 785 nm excitation as a function of concentration. If particle size became smaller and particle density became not so great as to significantly compensate for the observed signal reduction via increased LSP-coupling, then 785 nm intensity should diminish as the particles become progressively less attuned to this wavelength. Concurrent decreasing particle

size and rising numbers of NPs as a function of concentration, could both reduce the 785 nm profile whilst simultaneously increasing that of 633 nm after 4 mM, as greater numbers of smaller particles amenable to 633 nm excitation are produced; this is provided there is minimal LSP-coupling between the smaller particles.

Why particle size might decrease as numbers increase with rising concentration could perhaps be due to greater numbers of Ag^0 nuclei being formed at higher feed concentrations, reducing the reservoir of Ag^+ ions for subsequent growth as reduction progresses. It would of course require TEM analysis to confirm this growth hypothesis and its influence on the SERS response, something which could be carried out in future studies.

It should be noted that although each data point is averaged from only 22 spectra for both wavelengths, and mapping studies would provide a more accurate picture of the SERS response, these results provide a good overall view nonetheless. In any case, even if alternate extreme values of the error bars were plotted in place of the averages, the overall trends would remain reasonably similar – a dip and then a recovery in 633 nm intensity and a reduction in 785 nm intensity which eventually levels off, with the values for 2 and 4 mM remaining about equal for both plots.

One other important point which should be highlighted is that it is impossible, for practical reasons, to illuminate a sample at the exact same location for both excitation wavelengths, but this does not present significant problems, and possible issues are largely overcome with averaging. Occasionally however, outliers in intensity arise with the potential to skew results, but it was found that whether these are included or removed, the trends in figure 4.3 remain remarkably similar.

Removal of outliers has been avoided, so that results presented therefore are as-recorded. Raman mapping, which is capable of recording vast numbers of spectra, surmounts potential problems posed by outliers, and mapping studies which confirm the reproducibility of both metal-agarose gels are included at the end of the chapter.

As mentioned at the start of this section, it is desirable to make a direct analytical comparison between the SERS responses at 633 and 785 nm excitations, which does not require a scattering correction to be made, and to this end, each intensity value at 633 nm is divided by its correspondent at 785 nm. These relative intensities are then averaged and quoted with the standard deviation. On average, 633 nm excitation induces an intensity about 7.9 ± 6.3 times that at 785 nm over the entire feed concentration range. The large standard deviation reflects the divergent nature of the profiles from 4 mM.

4.1.4 Conclusion

SERS of hydroxylamine-reduced Ag-agarose gels was conducted at 633 and 785 nm excitations. It was found that SERS intensity was greater overall at 633 nm, with an increasing trend from 4 mM. 785 nm intensity fell fairly sharply and then levelled. The results point to a simultaneous increase in number and decrease in size of the NPs, producing a greater proportion amenable to 633 nm excitation as a function of feed concentration, and conversely, a decreasing proportion amenable to 785 nm.

4.2 SERS of hydroxylamine-reduced Au-agarose gels

4.2.1 Introduction

In addition to silver, gold is another widely-used SERS metal [4], and it was crucial therefore to establish whether the adapted hydroxylamine-reduction method, used to fabricate Ag-agarose, could be extended to deliver SERS-active Au-agarose substrates.

4.2.2 Experimental

All chemicals were purchased as described in section 4.1.2 in addition to gold (III) chloride trihydrate (Sigma-Aldrich, ACS reagent, ≥ 49.0% Au basis).

Blank agarose gel was prepared as described previously in chapter two, section 2.2.2.1. Gel squares measuring approximately $1.5\times10\times10\ mm^3$ were immersed in gold salt ($HAuCl_4.3H_2O$) solutions (1 square per 3 ml: 1, 2, 3,….10 mM) for 2 h, dried on filter paper and then placed immediately in vials containing reducing solutions of high-pH hydroxylamine (1 square per 3ml: 2, 4, 6,….20 mM) for 2 h, ensuring both square planar sides of the gel were fully exposed to the solution. The hydroxylamine solutions were rendered alkaline by the addition of NaOH (aq) – the ratio of NaOH to hydroxylamine was maintained at 2:1. An excess of reductant, [reductant]:[Au salt] = 2:1, was used to ensure complete reduction of the Au-salt gels. After *in situ* reduction, Au gels were dialysed in distilled water for 1 h then placed in 1.00×10^{-5} M BPE (aq) overnight for SERS analysis.

SERS analysis was conducted the next day using 633 and 785 nm excitation wavelengths on the Renishaw Ramascope System 2000, set up as described

previously in chapter two, section 2.2.2.3. The unfocussed power at the sample was 1.165 mW, with a 1s collection time at 633 nm excitation and 3.575 mW, 1s at 785 nm. All gels were taken from BPE solution and dried on filter paper before analysis. For clarity, all spectra were normalised for power and collection time giving intensity units of photon counts per second per milliwatt (c s^{-1} mW^{-1}). Each data point in the "SERS intensity versus Au salt concentration" graphs, represents the 1200 cm^{-1} peak height of BPE, measured using OriginPro 8.6 software, averaged from twenty-two spectra collected from across the surface of the substrate (approximately 1 cm^2), with error bars representing the standard deviation.

Absorption spectra were recorded on a Jasco V-660 UV-VIS spectrometer using the same set up and sample preparation procedure as in section 4.1.2.

As with HR-Ag-agarose, gel squares were immersed carefully in salt and reducing solutions in vials, allowing full exposure to both square-planar sides of the gel. Figure 4.4 illustrates what can happen when HR-Au-salt-agarose sinks to the bottom of the container, remaining immobilised during reduction. The unexposed side flush with the bottom ("red underside") which experiences less diffusion of hydroxylamine, turns reddish due to a relatively low NP density, while the exposed side ("black top") turns almost black due to greater diffusion and, in turn, a relatively high NP density. The red underside of the gel has a black border, where the edges have had freer access to hydroxylamine solution and where more gold NPs have formed as a result.

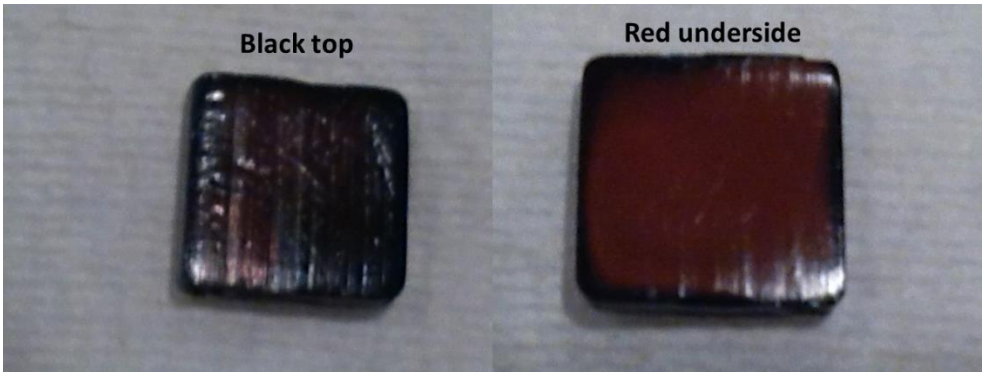

Figure 4.4. 5 mM HR-Au-agarose. Uneven formation of AuNPs has occurred, as evidenced by differences in colour. The black top is the exposed side of the gel and the reddish underside is the side flush with the bottom of the bottle during reduction. Pictures are from the same sample, but taken at slightly different magnifications. Each side measures 1 cm.

Figure 4.4 illustrates the importance of allowing full gel-exposure to solution during salt and reductant immersion. All gels in this thesis were arranged as such, resulting in an even formation of nanoparticles within the agarose.

4.2.3 Results and discussion

4.2.3.1 UV-VIS spectroscopy

Chapter two, section 2.3.3 concluded that given both the nature of the gel and the sample preparation, it is impossible to conduct a quantitative analysis of UV-VIS spectra. Compression of a small piece of Ag gel between two fused silica slides for example, can really only deliver spectra which approximate the location of the Ag plasmon band, which is useful to an extent but only allows a qualitative analysis at best. Obviously this is also the case for UV-VIS of Au-agarose, and some results are included here to support the findings of chapter two.

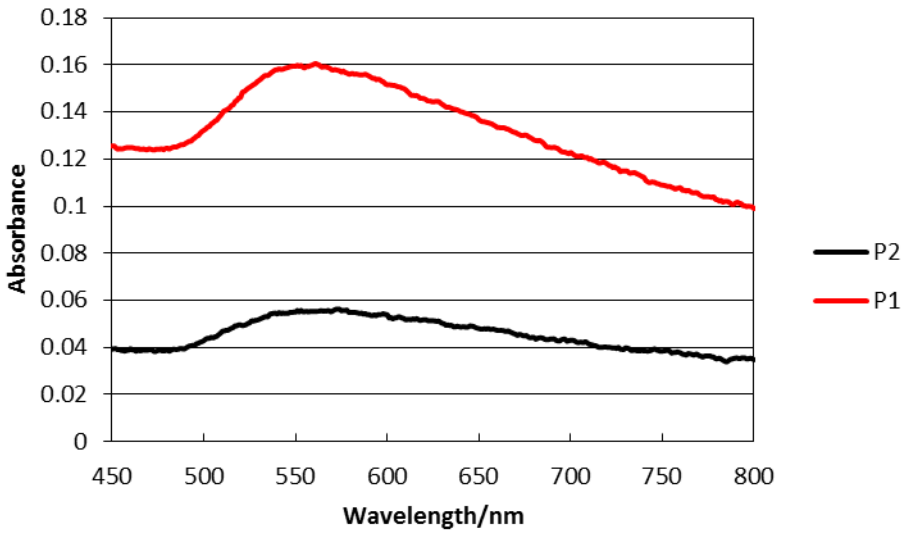

Figure 4.5. UV-VIS absorption spectra of 5 mM Au-agarose, prepared for absorption analysis using the compression technique explained above. Different peak positions, full-width-at-half-maximums (FWHMs) and intensities are evident, even though they originate from the same piece of gel. A small sample was cut from the gel and pressed between two silica slides. P1 is the resultant spectrum after pressing the silica slides together for the first time. P2 is the spectrum recorded after the second pressing. NEITHER of the spectra has been shifted for clarity.

Figure 4.5 shows that although the same piece of Au gel has been used for analysis, the spectra look quite different. The results are summarised in table 4.1

Table 4.1. Results from the graph in figure 4.5.

Pressing	Absorbance Peak/nm	Absorbance	FWHM/nm
P1	557	0.04	90
P2	565	0.02	79

Table 4.1 displays the plasmon band positions, absorbances and FWHMs for 5 mM Au-agarose gel. Upon pressing the sample between the slides for the second time, the plasmon peak redshifts by 8 nm, the absorbance halves and the FWHM decreases by 11 nm. These results confirm that the compression technique produces qualitative results at best. This is discouraging, as it is desirable to characterise the gels as they

are without having to resort to additional steps such as chemical or physical extraction of the nanoparticles for analysis. There is however no way to control either how much material is deposited between the slides or the degree of compression, and hence the path-length of the sample, thus ruling out quantitative UV-VIS characterisation. One way around this could be to pour the molten agarose solution into very thin moulds, so that all blank gels have exactly the same (short) path-length before immersion in salt and reducing solutions, but it would be still be necessary to minimise opacity of the gel by using a low salt concentration.

4.2.3.2 SERS of Au-agarose at 633 and 785 nm excitations

Figure 4.6 shows the SERS intensity profiles of Au-agarose gels at 633 and 785 nm excitations.

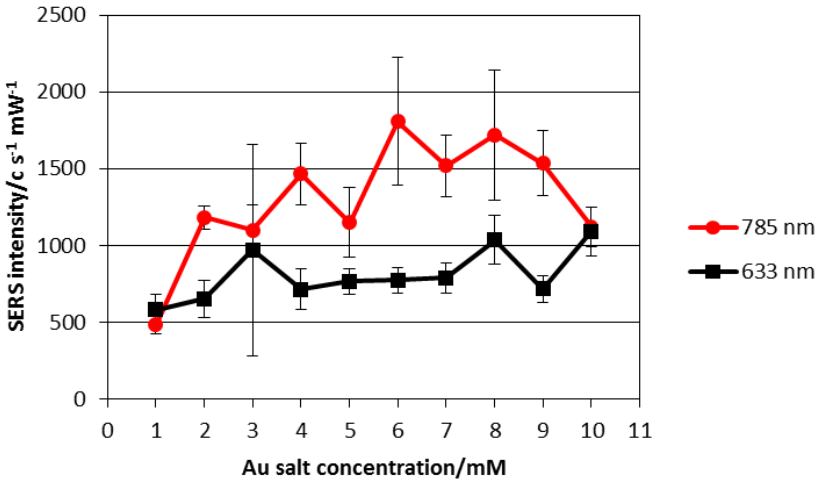

Figure 4.6. SERS intensity versus gold salt feed solution concentration of the same HR-Au-agarose samples at 633 and 785 nm excitations. Each data point represents the 1200 cm^{-1} peak height of BPE averaged from twenty-two spectra, each collected from across the surface of the substrate (approximately 1 cm^2). Powers and acquisition times have been normalised (counts per second per milliwatt or c s^{-1} mW^{-1}).

The overall increase in intensity at 785 nm excitation is marginally steeper than at 633 nm, and the SERS response overall is slightly stronger at 1.6 ± 0.5 times, but the signal peaks at 6 mM and falls gradually thereafter. This means the size and arrangement of AuNPs are reasonably amenable to both excitation wavelengths over the entire concentration range.

4.2.4 Conclusion

Hydroxylamine-reduced Au-agarose gels were produced in the 1-10 mM Au-salt range and their SERS response examined under 633 and 785 nm excitations. It was found overall that 785 nm excitation produced a slightly stronger signal than 633 nm excitation.

4.3 SERS of hydroxylamine-reduced Ag- and Au-agarose: a comparison

4.3.1 Introduction

In addition to examining the SERS response at 633 and 785 nm excitation wavelengths for gold and silver gels separately, SERS optimisation necessitates a direct comparison between the two metals if metal-agarose is eventually to find utility in applications. This section groups all of the results so far in this chapter in order to facilitate a direct comparison.

4.3.2 Results and discussion

Figure 4.7 provides a summary of the intensity profiles of HR-Ag- and Au-agarose at 633 and 785 nm excitations.

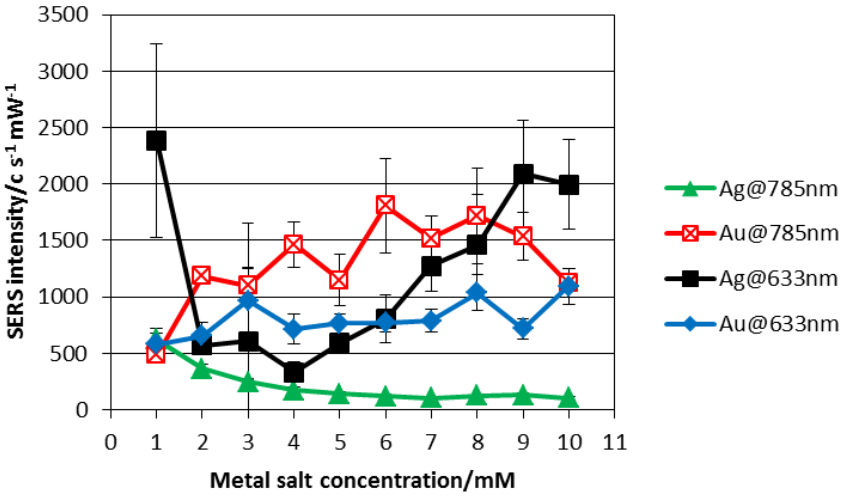

Figure 4.7. Summary of SERS intensity versus metal salt concentration for hydroxylamine-reduced Ag- and Au-agarose gels at 633 and 785 nm excitation wavelengths. Each data point represents the 1200 cm^{-1} peak height of BPE averaged from twenty-two spectra, each collected from across the surface of the substrate (approximately 1 cm^2). Powers and acquisition times have been normalised (counts per second per milliwatt or c s^{-1} mW^{-1}).

At 633 nm excitation, Ag-agarose produces on average a SERS signal roughly similar to that of Au-agarose. The reason at first is not clear, because in a colloidal context for example, AgNPs generally provide a much larger Raman enhancement than Au nanoparticles in the visible region (at least up to ≈ 600-650 nm) [5]. The reason must therefore be down to a particular size/arrangement of the AuNPs which offsets the expected stronger response of Ag. With regard to Ag- and Au-agarose at 785 nm excitation however, there is a significant difference between the two intensity profiles, with Au producing an average intensity 9.1 ± 4.9 times that of Ag over the entire concentration range. This could be attributed to the gold plasmon

band at around 520 nm [6] being closer to 785 nm than the 400 nm silver plasmon band.

Figure 4.7 confirms that under these experimental conditions, the best overall substrate in terms of SERS intensity is Au-agarose at 785 nm excitation. No feed concentration in particular stands out as the overall winner, but as a rule of thumb, it is probably better to used gold salt concentrations below 5 mM, as the error bars in intensity measurements are generally smaller in that sub-range.

4.3.3 Conclusion

It was found that at 633 nm excitation, the SERS intensity profiles of Ag- and Au-agarose were roughly similar. This might be due to the expected higher intensity of Ag in part of the visible range (up to ≈ 600-650 nm) being offset by a particular size/arrangement of the AuNPs. At 785 nm excitation, there was a significant difference between the intensity profiles of the two metal gels, with Au samples producing far stronger SERS on average. This was ascribed to the gold plasmon band at around 520 nm being closer to 785 nm than the 400 nm silver plasmon band. The best overall substrate therefore proved to be Au-agarose at 785 nm excitation. No particular feed concentration stood out as the overall winner, but as a rule of thumb, it is probably better to used gold salt concentrations of below 5 mM, as the error bars in intensity measurements are generally smaller in that sub-range.

4.4 SERS mapping of selected hydroxylamine-reduced Ag- and Au-agarose gels

4.4.1 Introduction

In addition to the capacity for strong signal generation, one other fundamental requirement of any SERS substrate to be used in applications is good reproducibility [7]. Several HR-Au- and Ag-agarose gels described in this chapter were further examined using Raman mapping to better assess reproducibility. Mapping provides a rigorous evaluation of gel uniformity, as in this case, 4800 spectra per sample are analysed. Given the large number, the effects of any potential outliers are practically eliminated.

4.4.2 Experimental

SERS mapping of the integrated intensity of the 1200 cm^{-1} peak of BPE (1.00×10^{-5} M (aq)) of Ag- and Au-agarose gels was performed using 633 and 785 nm laser lines on a WITec Confocal Raman Microscope alpha300 R. Each of the 12 maps taken from the surface of each sample (with an approximate area of 1 cm^2) consisted of 400 spectra, collected over an area 100 µm x 100 µm (20 points per line, 20 lines per image), using a 10 × 0.25 objective, equating to 4800 spectra from each sample. Two mM Ag-agarose was mapped using 785 nm at 1.0 mW, with a 0.1 s collection time. Two mM Au-agarose was mapped using 785 nm at 1.46 mW with a collection time of 0.25 s, while 6 and 7 mM Au-agarose gels were mapped using 633 nm at 0.40 mW with a 0.25 s collection time. Data analysis was carried out using WITec Project 2.10 software.

4.4.3 Results and discussion

Figure 4.8 shows representative SERS maps of the integrated 1200 cm^{-1} peak intensity of BPE at (a) 785 nm excitation of 2 mM HR-silver-gel, and (b) at 633 nm excitation of 6 mM HR-gold-gel. Maps were collected from across the entire surfaces of the samples (approximately 1 cm^2).

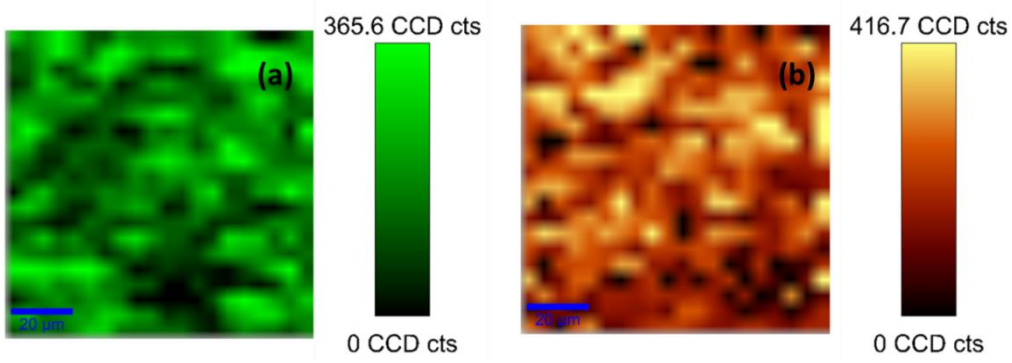

Figure 4.8. SERS mapping of BPE at (a) 785 nm excitation of 2 mM HR-Ag-agarose at 1.0 mW, with a 0.1 s collection time; (b) 633 nm excitation of 6 mM HR-Au-agarose at 0.40 mW with a 0.25 s collection time. Each image is a map of the integrated 1200 cm^{-1} peak intensity of BPE, taken over an area 100 µm x 100 µm producing 400 spectra. The scale bar in the bottom-left of each image represents 20 µm.

Two maps have been extracted from the data and are shown in figure 4.8 as examples of the even distribution of SERS activity in both Ag and Au gels (one for each metal). The four samples for mapping were chosen not because they related to maximal SERS intensity, but rather because they possessed the best reproducibility, as established from the "spot-to-spot spectra" studies discussed earlier in the chapter. The primary intention therefore was not to map samples with high intensity, but rather to prove at least that highly uniform samples could be fabricated using the described technique. Later work could perhaps look at optimising both signal strength and gel uniformity.

The relative standard error of the mean signal intensity (RSE) and the overall % relative standard deviation in signal intensity (RSD), were used in conjunction to thoroughly test the reproducibility of four gels exhibiting good reproducibility. The RSE for a given sample is the standard deviation of the 12 mean peak intensities (each calculated from 400 spectra comprising a map) divided by the mean of the 12 mean intensities. The overall %RSD for a given sample is the total standard deviation in peak intensity calculated from all 4800 spectra, divided by the overall mean intensity from all 4800 spectra – the latter happens to be the exact same as the mean of the 12 mean intensities. Both measurements provide a robust measure of gel reproducibility. The graphs for these results are shown in figures 4.9 and 4.10.

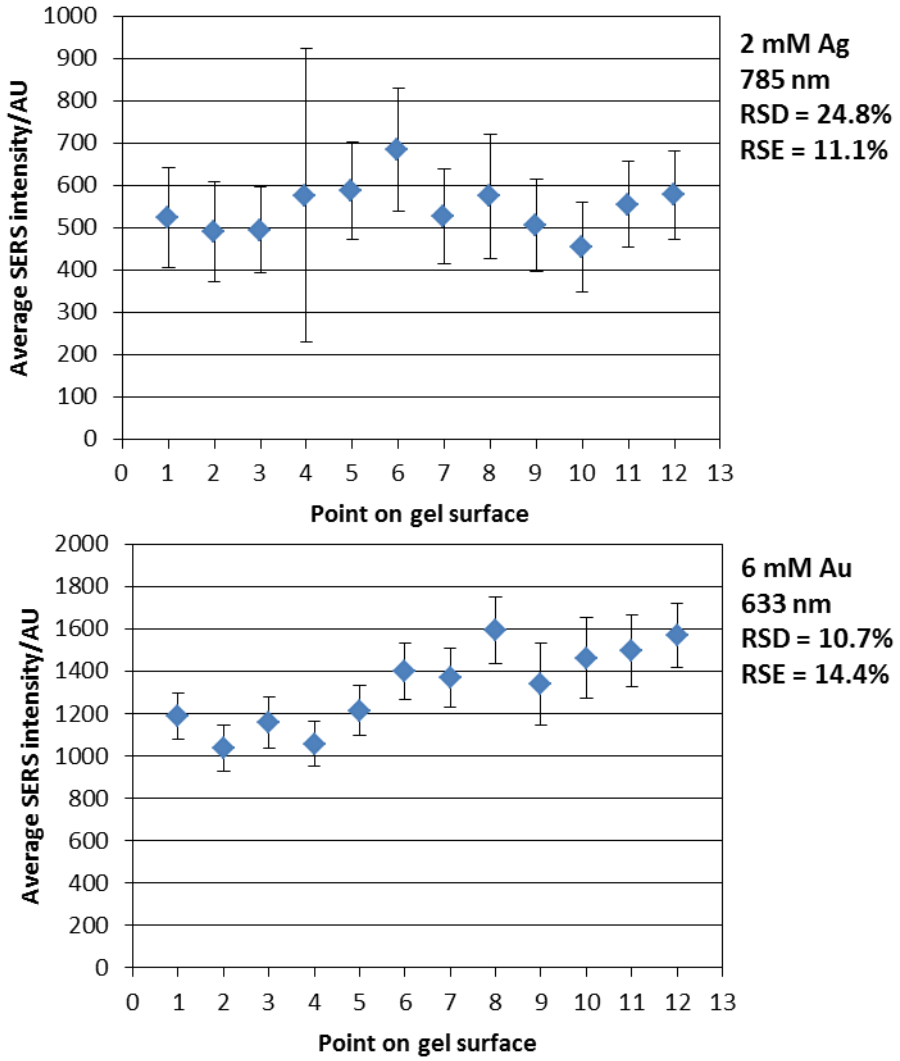

Figure 4.9. SERS mapping of hydroxylamine gels as-labelled. Each data point on the graph is the integrated 1200 cm^{-1} peak intensity of BPE, averaged from 400 spectra comprising a map (100 µm x 100 µm) with error bars representing the standard deviation, with 12 maps collected per sample over an area of approximately 1 cm^2. "RSD" is the Relative Standard Deviation of all 4800 integrated peak intensities for a given sample, while "RSE" is the Relative Standard Error of the mean, that is, the standard deviation of the twelve mean intensities for a given sample divided by the mean of the twelve mean intensities.

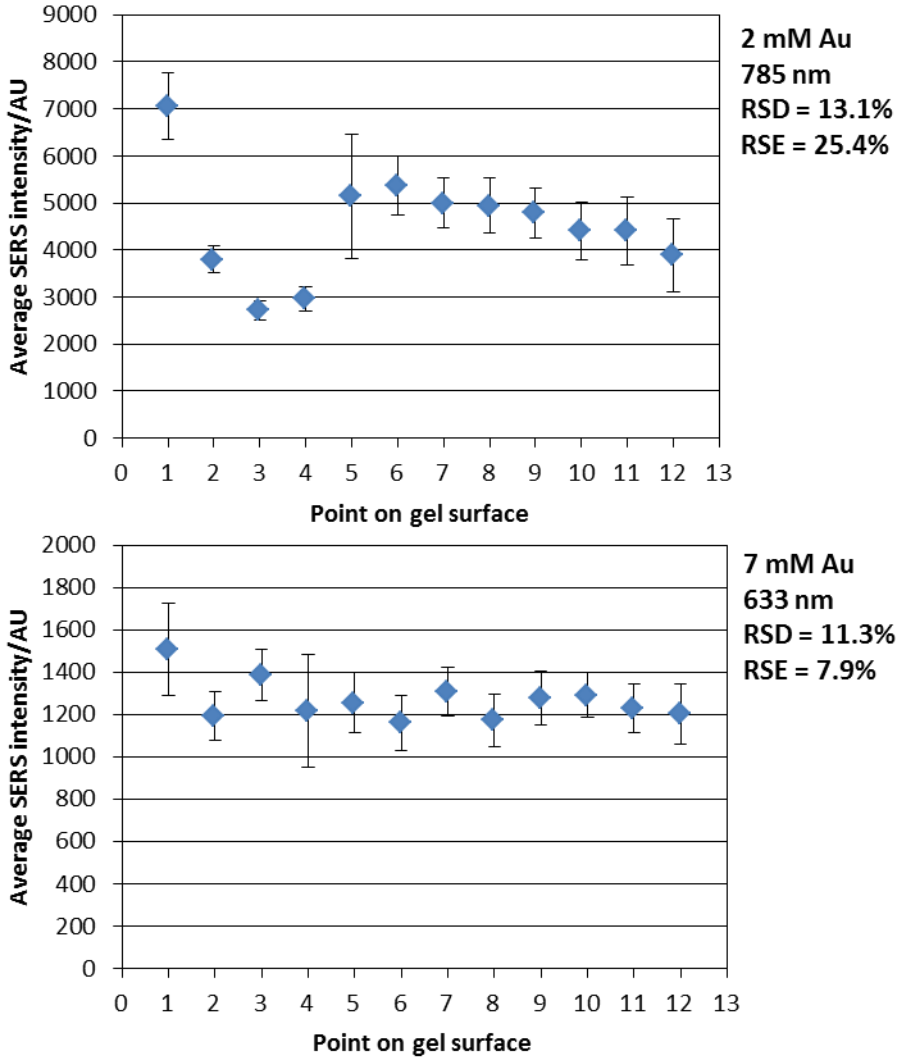

Figure 4.10. SERS mapping of hydroxylamine gels as-labelled. Each data point on the graph is the integrated 1200 cm^{-1} peak intensity of BPE, averaged from 400 spectra comprising a map (100 µm x 100 µm) with error bars representing the standard deviation, with 12 maps collected per sample over an area of approximately 1 cm^2. "RSD" is the Relative Standard Deviation of all 4800 integrated peak intensities for a given sample, while "RSE" is the Relative Standard Error of the mean, that is, the standard deviation of the twelve mean intensities for a given sample divided by the mean of the twelve mean intensities.

Mapping graphs clearly indicate that the adapted method for HR-metal-agarose production generates substrates with good reproducibility. It is true that of the four samples selected for mapping, two, namely 2 mM Au and 2 mM Ag, have a slightly poorer RSE and a better %RSD or vice versa. Six and 7 mM Au samples however,

have RSEs and %RSDs both under 15%, below the upper threshold of 20% for SERS detection and identification purposes [8], [9], although it is acknowledged that these results were obtained under controlled conditions, and that the gel must be able to perform to same high standard in the field. Moreover, mapping studies were limited to gels from one batch, so further experimentation is required to carefully assess inter-batch variability before introduction of the substrate to applications; the results are encouraging nonetheless. Inter-batch variability could be investigated after maximisation of both the SERS signal strength and reproducibility within the same batch by, for example, examining in greater depth the effect of altering the molar ratio of hydroxylamine to metal salt using the current immersion technique. Work in chapter two showed that the SERS intensity for sodium borohydride-reduced gels was greatest when the $[AgNO_3]$:$[NaBH_4]$ ratio was greater than 1:1 (more $AgNO_3$, less $NaBH_4$). The same could be tried for hydroxylamine-reduced gels, despite the potential danger of elongating the nucleation period and increasing nanoparticle dispersity. There would inevitably be a trade-off between intensity and reproducibility, but trial and error should result in an optimised substrate. Chapter two also showed that even when the $[AgNO_3]$:$[NaBH_4]$ ratio is fixed, lower-concentration gels provide greater SERS signal uniformity, so it would be prudent to fix the feed concentration relatively low and then alter the concentration of hydroxylamine around that point.

One final point of note is that an important advantage exists in the *in situ* reduction technique described in this thesis compared with the assimilation of pre-manufactured colloid, in that greater control over growth conditions can be realised, resulting in a stronger influence over nanoparticle size and arrangement. Indirectly,

this affords the experimentalist a greater degree of control over the plasmonic characteristics of the substrate and, consequently, the associated SERS response.

4.4.4 Conclusion

Four of the gel samples described earlier in this chapter which exhibited not necessarily the strongest SERS signal, but instead the smallest error bars (best reproducibility) were selected for Raman mapping. This provided a rigorous evaluation of gel uniformity, confirming that the fabrication technique employed in this thesis is successful in the synthesis of reproducible metal-agarose gels. While the results are very encouraging, mapping studies were limited to gels from one batch, so further experimentation is required to assess inter-batch variability before these substrates can be used confidently in applications. This could be done after optimisation of both SERS signal strength and reproducibility, by for example, examining in more depth the effect of altering the molar ratio of hydroxylamine to metal salt at low salt concentration.

4.5 Summary

Hydroxylamine-reduced Au- and Ag-agarose gels were produced in the low salt-concentration range of 1 – 10 mM. Low-concentration feed solutions generally give rise to gels with better uniformity, so it is important to understand how the SERS response develops within this range. SERS at 633 and 785 nm was conducted on the samples, and the SERS intensity examined as a function of salt concentration.

With respect to the Ag samples, the strongest SERS signal was produced on average at 633 nm excitation. A hypothesised simultaneous increase in number and decrease in size of NPs as a function of concentration, explained the substantially different plots for both 633 and 785 nm wavelengths. Regarding the Au gels, the intensity was only marginally greater overall at 785 nm compared with 633 nm.

Upon comparing Ag- and Au-agarose gels at 633 nm excitation, it was found that the intensity profiles were largely similar, which initially seemed puzzling as Ag nanoparticles generally provide a much larger Raman enhancement than Au nanoparticles in the visible region (at least up to ≈ 600-650 nm). The reason therefore must have been down to a particular size/arrangement of the AuNPs, such that it offset the expected higher Ag intensity. A comparison of gold and silver gels at 785 nm excitation, showed that Au-agarose produced on average by far the strongest SERS signal, so the best overall substrate, in terms of SERS intensity was Au-agarose at 785 nm excitation. No feed concentration in particular stood out as the overall winner, but as a rule of thumb, it is probably better to used gold salt concentrations below 5 mM, as the error bars are comparatively small suggesting better reproducibility.

SERS mapping on selected Ag and Au gels provided a rigorous evaluation of gel uniformity, and confirmed that the fabrication technique employed in this thesis is successful in the synthesis of reproducible metal-agarose gels. Mapping studies however, were limited to gels from one batch, so further experimentation is required to assess inter-batch repeatability before gels can be utilised confidently in applications.

References

[1] P. Aldeanueva-Potel, E. Faoucher, R. A. Alvarez-Puebla, L. M. Liz-Marzan, and M. Brust, "Recyclable molecular trapping and SERS detection in silver-loaded agarose gels with dynamic hot spots," *Anal. Chem.*, vol. 81, no. 22, pp. 9233–9238, 2009.

[2] J. R. Ferraro, K. Nakamoto, and C. W. Brown, *Introductory Raman Spectroscopy*, Second Ed. London: Academic Press, 2003, pp. 122–123.

[3] N. G. Greeneltch, M. G. Blaber, G. C. Schatz, and R. P. Van Duyne, "Plasmon-sampled surface-enhanced Raman excitation spectroscopy on silver immobilized nanorod assemblies and optimization for Near Infrared (λ_{ex} = 1064 nm) studies," *J. Phys. Chem. C*, vol. 117, no. 6, pp. 2554–2558, 2013.

[4] K. Faulds, W. E. Smith, D. Graham, and R. J. Lacey, "Assessment of silver and gold substrates for the detection of amphetamine sulfate by surface enhanced Raman scattering (SERS)," *Analyst*, vol. 127, no. 2, pp. 282–286, 2002.

[5] E. C. Le Ru and P. G. Etchegoin, *Principles of Surface-Enhanced Raman Spectroscopy and related plasmonic effects*. Oxford: Elsevier, 2009, p. 368.

[6] I. A. Larmour and D. Graham, "Surface-enhanced optical spectroscopies for bioanalysis," *Analyst*, vol. 136, no. 19, pp. 3831–3853, 2011.

[7] S. E. J. Bell and N. M. S. Sirimuthu, "Quantitative surface-enhanced Raman spectroscopy," *Chem. Soc. Rev.*, vol. 37, no. 5, pp. 1012–1024, 2008.

[8] X.-M. Lin, Y. Cui, Y.-H. Xu, B. Ren, and Z.-Q. Tian, "Surface-enhanced Raman spectroscopy: substrate-related issues," *Anal. Bioanal. Chem.*, vol. 394, no. 7, pp. 1729–1745, 2009.

[9] M. Kahraman, I. Sur, and M. Culha, "Label-free detection of proteins from selfassembled protein-silver nanoparticle structures using surface-enhancedRaman scattering," *Anal. Chem.*, vol. 82, no. 18, pp. 7596–7602, 2010.

Chapter 5 Metal nanorod arrays for SERS created by oblique angle deposition

This chapter presents results concerning the manufacture of metal nanorod arrays using oblique angle deposition (OAD) and their role as SERS substrates. It begins by investigating the relationship between film surface roughness, porosity and the associated SERS response before moving onto an examination of highly ordered silver and copper arrays formed on pre-patterned polymer sheets. Unlike normal OAD, where nanorods are randomly distributed on flat supports, the patterned polymer support defines nucleation sites which guide subsequent growth of nanorods, resulting in enhanced SERS intensities for Ag arrays on polymer compared with an Ag-silica control. The SERS response of Ag nanorod arrays of various structures is investigated alongside results obtained from discrete dipole approximation simulations, which reveals that narrow gaps between nanorods, formed by guided nucleation during OAD, are responsible for this dramatic enhancement. Ordered Cu nanorod arrays are also examined, which offer the possibility of constructing cheap, high-throughput substrates with great potential for applications.

5.1 Varying the deposition angle of Ag nanorods on silicon: the link between film porosity, surface roughness and SERS

5.1.1 Introduction: oblique angle deposition for Ag-Si SERS substrates

Figure 5.1 (a) [1] shows a reminder of the setup for OAD, first encountered in the review of SERS substrates in chapter two, and figure 5.1 (b) and (c) [1] shows the "shadowing effect", crucial for the construction of metal nanorods.

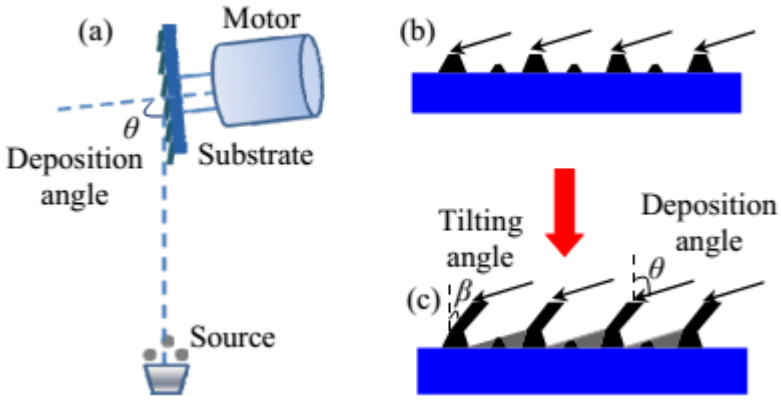

Figure 5.1. (a) A representation of oblique angle deposition; (b) and (c) the shadowing effect [1].

The "source" in figure 5.1 (a) is the metal which is to be evaporated inside the physical deposition chamber (evacuated to about 10^{-6} Torr) by an impinging electron beam, resulting in a flux of metal vapour incident on the "substrate" at a deposition angle, θ to the substrate normal. As shall be discussed in the next section, metal films formed using the largest deposition angles ($\sim 85^{o}$) are required for SERS, as

these generate the strongest signal. The actual angle of the nanorods to the substrate normal, β however, is always less than θ, because the rods grow into the vapour flux.

OAD relies on the so-called "shadowing effect" and adatom diffusion. Adatoms in the vapour randomly strike and condense onto the flat substrate, diffusing on the surface, forming separate nuclei whose sizes are largely dependent on adatom mobility; greater mobility creates larger nuclei. Because the vapour flux impinges on the target at a very large angle to the substrate normal, and consequently a very small angle to the substrate plane, larger (taller) nuclei become shadowing centres, blocking further deposition "downwind" of the flux. Consequently, there is no further growth within the shadowed regions, meaning that only these taller nuclei go on to form eventual nanorods which grow into the incident vapour flux. In addition to a large deposition angle being required, it is necessary that deposition itself take place in a low pressure environment (~10^{-6} Torr) to drastically reduce the interaction between air molecules and both the electron beam which irradiates the metal, and the metal vapour flux itself. The process is also carried out at room temperature which reduces surface adatom diffusivity, helping to maintain the integrity of the columnar structure of the nanorods. At higher temperatures the diffusion length increases, resulting in metal filling the shadowed regions and consequently, a breakdown in nanorod structure [1].

As mentioned earlier, only the highest angles yield substrates which have a strong SERS signal. This is due to their having much higher degrees of porosity and surface roughness, and consequently, better scattering abilities. Ag films were formed on silicon with deposition angles 0, 45, 75, and 85^{o}, and the SERS response

examined alongside reflectance spectra to investigate the dependence of SERS activity on film porosity and surface roughness.

5.1.2 Experimental

5.1.2.1 Preparation and imaging of Ag films

Ag (99.99%, Kurt J. Lesker and Co.) films were created using e-beam evaporation (Satis) at various vapour incident angles: 0, 45, 75, and 85^{o}. The deposition angle of the sample can be manually controlled through a motion feedthrough. Blank fused silica and silicon wafer substrates were immersed in a 3% solution of Decon-90 overnight, rinsed in copious amounts of distilled water and then dried in N_2 (g) before film deposition. Sample thicknesses at various vapour incident angles were controlled using a quartz crystal monitor; the same sample thickness was maintained to an extent by adjustment of the projection of silver vapour flux to the normal direction of the substrate. A Hitachi S-4100 was used to capture SEM images of silver films.

5.1.2.2 Reflectance of Ag films

An Aquila nkd8000 was used to measure s- and p-polarised reflectances at a 30^{o} incident angle within the wavelength range of 350 to 1000 nm. As the nanorods on the substrate are tilted at an angle (not perpendicular to the substrate surface), the angle between the incident plane of the measuring light beam and the incident plane of silver vapour flux was fixed (90^{o} in this study) so that the reflectances of different polarisations of various samples could be compared. Reflectances of s- and p-

polarisations for a sample were obtained from the same position on the sample surface.

5.1.2.3 SERS of Ag films

SERS was investigated using *trans*-1,2-bis(4-pyridyl)ethylene (BPE) (Sigma Aldrich) at an excitation wavelength of 633 nm, using a Renishaw Ramascope System 2000 with the same experimental setup as in section 2.2.2.3. A droplet of methanolic BPE, 10^{-5} M concentration, was dispensed on the surface of the substrates and allowed to dry. All samples were scanned before applying BPE as a comparison. The **E**-vector of the laser was fixed in the direction of the vapour flux plane for all samples to treat them equally. Spectra were collected over a time of 1 s at approximately 4.7 mW unfocussed power at the sample surface and were normalised to a silicon standard. The 1200 cm^{-1} peak height, averaged from five spectra and acquired from across the surface of substrate, was measured using OriginPro 8.6 software and used as a measure of SERS intensity.

5.1.3 Results and discussion

5.1.3.1 Morphology of Ag substrates

Figure 5.2 shows images of silver films deposited at various vapour incident angles.

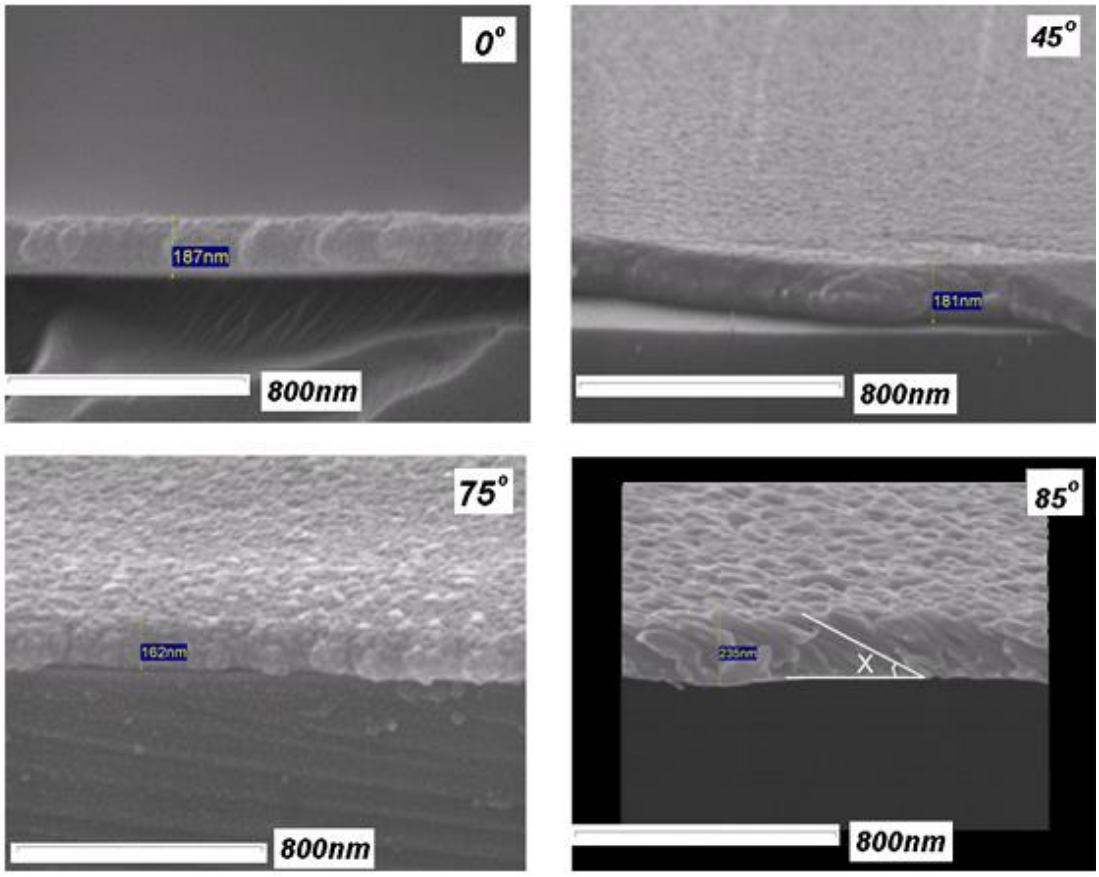

Figure 5.2. SEM images of silver films deposited at various vapour incident angles, as-labelled.

The surface becomes rougher as the vapour incident angle is increased. Only the sample deposited at 85^{o} however shows a clear, oblique columnar structure, which results directly from self-shadowing at the length-scale of the arriving adatoms during deposition, either by atomic nucleation at the starting point of film deposition or nucleation induced by substrate defects. The columns generally point in the direction of the incoming vapour flux, as represented schematically in figure 5.3. Here, χ_v is the vapour flux angle and χ, the angle of the oblique columns. In this

study, the manually controlled deposition angle θ is equal to $90^o - \chi_v$, and there is an empirical relation between the vapour flux angle and column angle known as the tangent rule, i.e. $\tan(\chi) = 2\tan(\chi_v)$ [2].

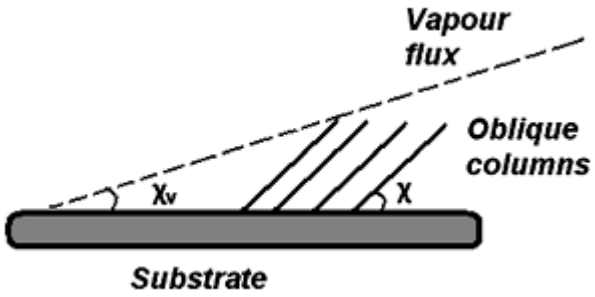

Figure 5.3. Schematic of oblique columns at an oblique vapour incident angle.

For an 85^o deposition angle, the vapour flux angle is 5^o. According to the tangent rule, the oblique column angle should be about 10^o. However, the actual column oblique angle is about 34^o, which is obtained from the SEM image in figure 5.2. This is very different from the calculated angle obtained using the tangent rule, implying that adatom mobility is very high under these conditions.

5.1.3.2 Quantifying film porosity and surface roughness

As seen from figure 5.2, the silver films have varying porosity and surface roughness, governed by the deposition angle, and only the sample deposited at 85^o with the highest values for both shows a clear, oblique columnar structure. Table 5.1 is a summary of silver volume fraction (a measure of porosity), and surface roughness for all films excepting the 0^o sample, due to its structure being virtually identical to that of bulk metal.

Table 5.1 Surface roughnesses of the Ag films.

Vapour incident angle	Silver volume fraction	Surface roughness
45^o	0.995	2.48 nm
75^o	0.963	3.70 nm
85^o S polarisation	0.949	11.5 nm
85^o P polarisation	0.580	12.8 nm

The silver volume fraction is obtained simply from an SEM image, by calculating the percentage of 2D space in a surface profile which is occupied by the metal. Surface roughness, R_q, is defined by the root mean square (RMS) equation [3]:

$$R_q = \sqrt{\frac{1}{L}\int_0^L y^2(x)\,dx} \tag{5.1}$$

where $y(x)$ is the surface profile which has mean value $\bar{y}$, and L is the assessment length of the substrate. The schematic in figure 5.4 illustrates these parameters.

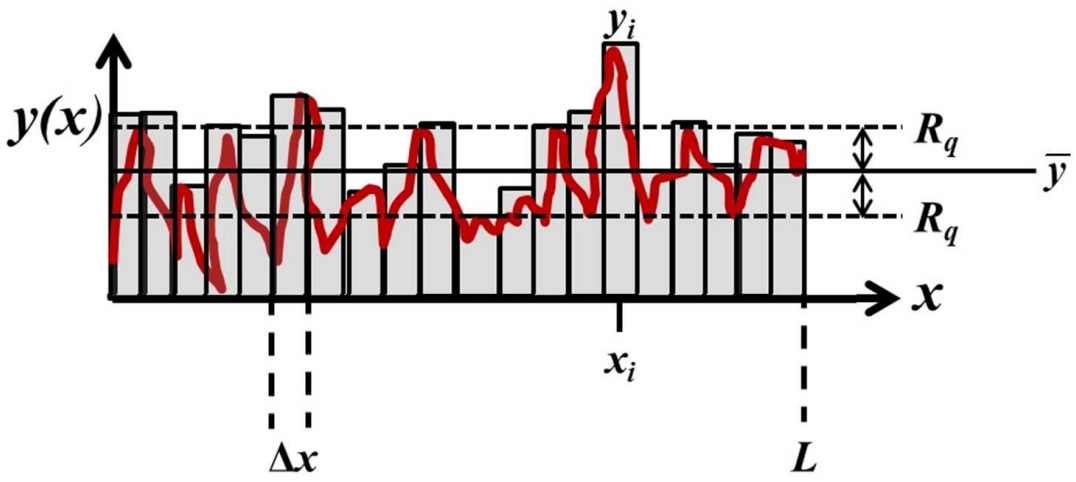

Figure 5.4. Schematic of the surface roughness profile of Ag-Si film, *y* (*x*) (the rough line in red). y-bar is the mean height of the structures.

As observed in the schematic in figure 5.4, the roughness R_q is a deviation from the mean height, $\bar{y}$ of y (x), the surface profile function of the nanorod substrate. The y-values are all different heights from the x-axis, which is in contact with the deepest "crevice" of the profile function where $y = 0$. Once the mean height of the structures is determined, the value is set to zero for convenience, for input into the function R_q. It should be remembered that the surface profile of the film, $y(x)$ in equation 5.1 is a function which must be integrated, rather than an individual y-value.

The 85^o sample has by far the greatest surface-roughness at both s- and p-polarisations, which boosts the scattering ability of the substrate tremendously and hence its capacity for Raman enhancement. With respect to porosity, the closer the volume fraction is to 1, the less porous a film. Because of the high anisotropy at 85^o there are two volume fractions for this deposition angle relating to the two distinct film profiles: one where the laser is p-polarised and the **E**-vector is at 30^o to the normal of the silver flux plane, in a direction where the volume fraction is low (high porosity), and another where the laser is s-polarised and the **E**-vector lies in the flux plane, in a direction where the volume fraction is high and porosity is low. The surface roughness for the 85^o sample in the p-polarisation direction is slightly higher than that under s-polarisation.

5.1.3.3 Reflectances of Ag films

The high anisotropy of the 85^{o} film is confirmed by the reflectance spectra shown in figure 5.5.

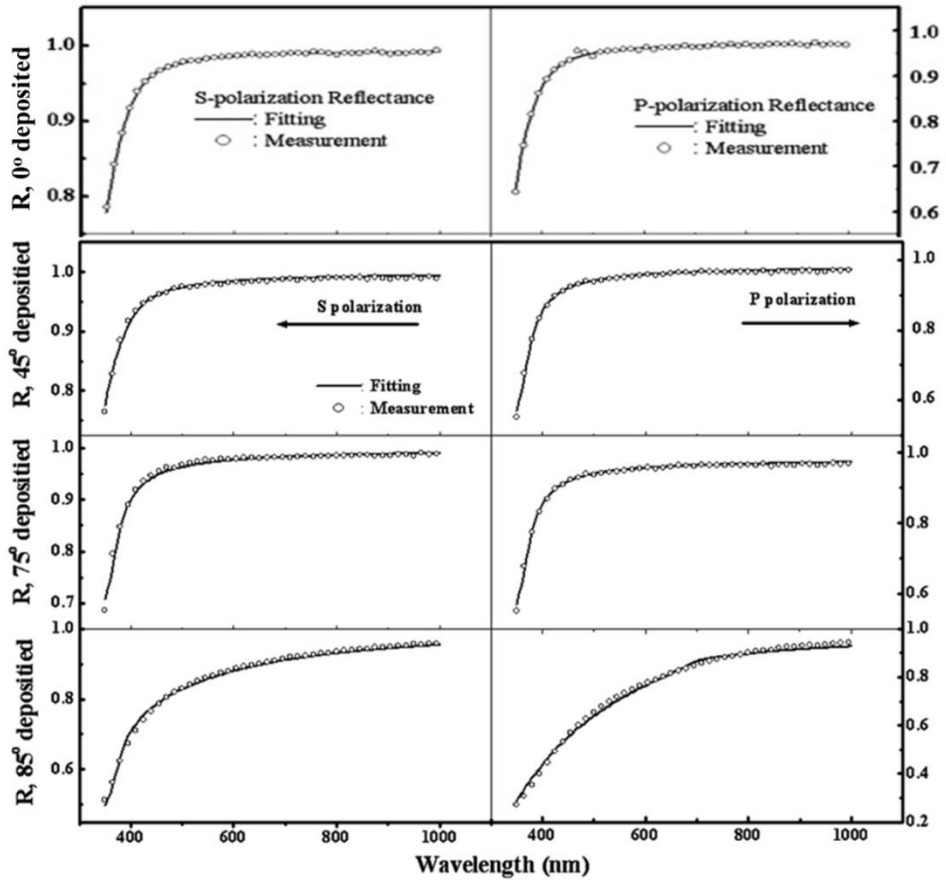

Figure 5.5. Reflectances of Ag coatings deposited at various vapour incident angles as-labelled.

Only reflectance spectra at both s- and p-polarisations for the 85^{o} array, which has the highest porosity and surface roughness, show any substantial difference in shape to those of 0^{o} which resembles bulk silver. The spectra for 45, and 75^{o} substrates differ only slightly, meaning they are relatively similar optically, and by extension structurally, to the 0^{o} film which is confirmed by the SEM images in figure 5.2, table 5.1 and Raman measurements which are discussed shortly. The s- and p-spectra for the lower angles tend to maximum reflection (approximately just

under 1) at about 500 nm, while those of 85° do so at a significantly larger value of around 950 nm due to the high scattering ability at both polarisations. Interestingly, the 85° p-polarisation plot climbs less sharply than that of s-polarisation, corresponding well with greater porosity and slightly better surface roughness in this direction, leading to a higher degree of scattering.

5.1.3.4 SERS of Ag films

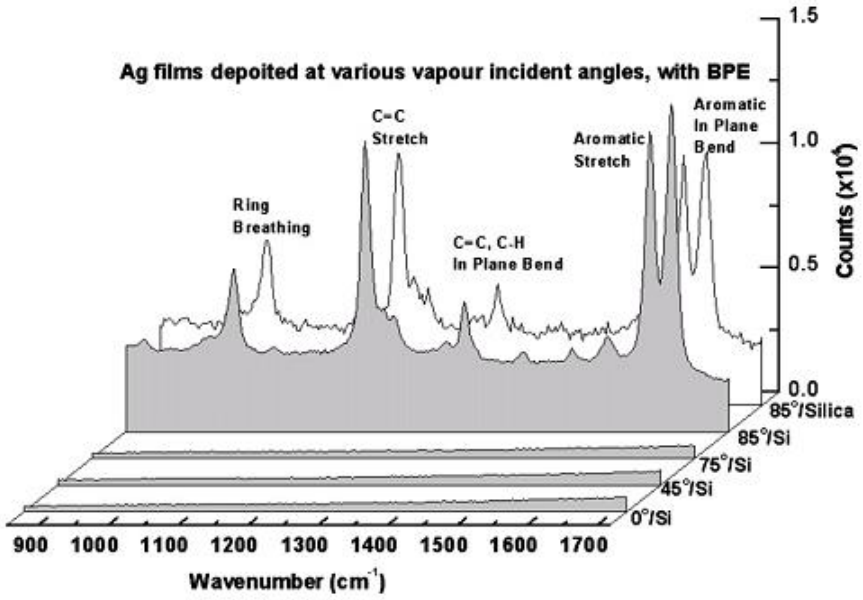

Figure 5.6. SERS measurements for the Ag coatings deposited at various vapour incident angles, as-labelled.

Figure 5.6 shows SERS spectra deposited at various vapour incident angles, as-labelled. Immediately obvious is the lack of a BPE profile for all deposition angles save 85° (the spectra are all virtually featureless even when magnified), which can be understood in terms of what has just been discussed regarding film morphologies and reflectance spectra – only the 85° substrate has the required columnar structure

for higher scattering to allow strong SERS. The mean amplitudes of the 1200 cm^{-1} mode are 11263 counts and 13547 counts for silicon and silica substrates, respectively, and both spectra show the typical vibrational modes of BPE [4]. These comparable SERS intensities (less than 10% of a difference) suggest similar enhancement factors, although the background level from the silica substrate is larger. For this observation however, it is important to note that the silica sample signal was recorded at 0.1 the integration time of the silicon sample and then multiplied by 10 for comparison. Also, as a reference, the samples were scanned before application of BPE and these scans were largely featureless.

These findings differ somewhat to those from Liu *et al.* [5], who investigated the SERS response of manufactured OAD silver nanorod arrays on silicon deposited at various deposition angles, in that they managed to obtain a clear SERS signal of BPE for deposition angles less than 85^{o}. They, however, laid down a 500 nm film on the blank Si substrate before nanorod deposition which would almost certainly have affected both nucleation and, in turn, subsequent rod growth. This current experiment emphasises how acutely the SERS response can be affected by film porosity and surface roughness.

5.1.4 Conclusion

Silver films were deposited on silicon and fused silica substrates at various vapour incident angles using OAD. Film surfaces became rougher and porosity increased as the vapour incident angle was widened. Only the sample deposited at 85^{o} exhibited a clear oblique columnar structure and the actual column oblique angle

for this sample was much greater than the calculated angle obtained using the tangent rule. This implies that adatom mobility was very high in this study. Reflectance spectra confirmed the positive relation between porosity and deposition angle and the high anisotropy of the 85^{o} sample due to the inclined columnar structure (sliver nanorod arrays). With respect to SERS spectra, only the 85^{o} deposition angles on Si and silica substrates gave strong SERS of a similar intensity. Scans of the other samples were largely featureless.

5.2 Ordered silver and copper nanorod arrays for enhanced Raman scattering created via guided oblique angle deposition on polymer

5.2.1 Introduction

Part of the review in chapter two covered nanorod arrays fabricated by OAD and several of the advantages they possess. However, despite their obvious success, it has proven difficult to control the gap size and diameter of nanorods during OAD fabrication, hindering the optimisation of geometrical parameters which directly affect the SERS response. The dimensions of nanorod arrays are initially influenced by nucleation, which is a random process on flat supports, meaning nanorods created by OAD are randomly distributed. To obtain a high-order nanorod array via the suppression of random nucleation events during OAD, Liu *et al*. used two-dimensional Au nanopost arrays manufactured using electron beam lithography (EBL), where the posts acted as periodically arranged shadowing centres during Ag

deposition [6]. While a dependence of the SERS response on gap size and diameter was found, the arrays produced were only semiordered. Moreover, the size of the arrays was very small (50 μm × 50 μm) [6], which is not suitable for sensing applications, so there exists considerable room for improvement in the construction of ordered metal nanorod arrays for SERS using OAD. In this section, polycarbonate sheet, pre-patterned using nanoimprint lithography (NIL), is applied as a large-area, highly uniform template to tightly control the nucleation process during OAD and, in turn, the subsequent growth of ordered metal nanorod arrays for SERS. Potentially, guided nucleation makes optimisation of SERS possible, based on template design which steers gap size and diameter towards the most favourable values.

5.2.2 Experimental

5.2.2.1 Materials

The materials used were silver and copper (99.99%, Kurt J. Lesker and Co.), *trans*-1,2-bis(4-pyridyl)ethylene (BPE; Sigma Aldrich – assay, 97%), and rhodamine B isothiocyanate (RBITC; Sigma Aldrich); polycarbonate sheets were prototypes supplied courtesy of MacDermid Autotype Ltd.

5.2.2.2 Nanoimprint lithography

Nanoimprint lithography (NIL) is a relatively new technique, where the desired pattern is transferred from a stamp onto a polymer resist, as illustrated in figure 5.7, taken from [7].

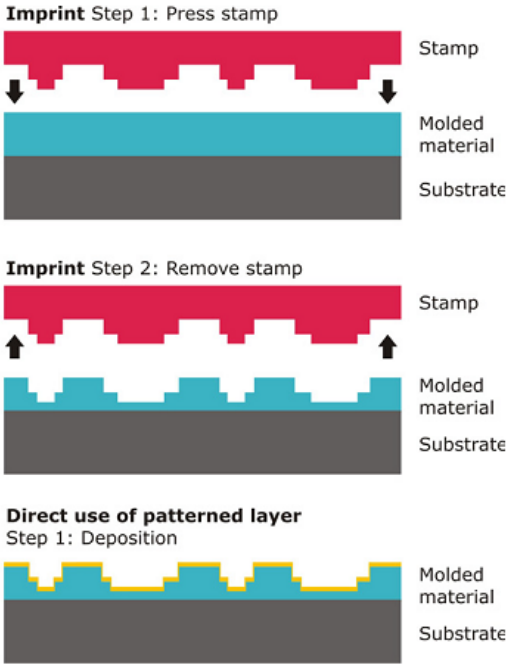

Figure 5.7. The type of nanoimprint lithography used to create the polymer substrate in this experiment, with the diagram taken from [7]. A stamp imprints directly onto the polymer ("moulded material", step 1), leaving its mark on the polymer when lifted off (step 2). The final deposition step (not in this thesis) is where a thin layer of metal is sputtered onto the now-patterned polymer. In this thesis, nanorods are instead deposited by OAD.

Unlike traditional lithographies whose patterns rely on the alteration of the physical and chemical properties of a resist by the bombardment of electrons or photons, NIL depends solely on direct physical distortion of the resist material by a stamp. After transferral of the pattern from stamp to polymer, a nanoscale layer of metal can be overlaid through sputtering, for example, to render the substrate SERS-active. This technique not only has the advantage of being cheap, but it can also generate large-area, highly reproducible, high-throughput substrates, especially suited to sensing, which other techniques such as EBL cannot [7].

5.2.2.3 Nanoimprinted polycarbonate

Polycarbonate sheet (A4 size) with an inverted hemispherical structure in a closely packed hexagonal arrangement, fabricated using nanoimprint lithography, was used as received and is shown in figure 5.8.

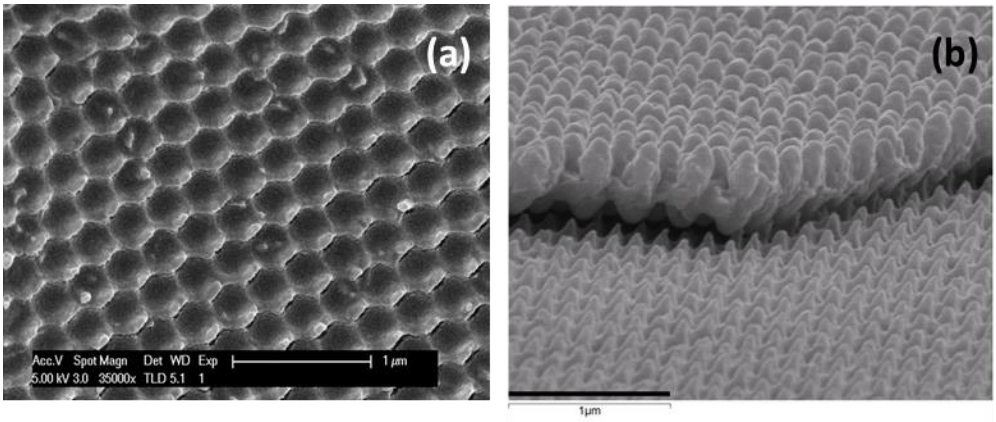

Figure 5.8. SEM: (a) surface image of the underside of the polymer, with an inverted structure of nanosphere assembly in closely packed hexagonal arrangement. (b) Oblique surface image of the topside of the polymer with deposited Ag nanorods (0° deposition, upper-half of the image) and bare polymer (lower-half of the image); the scale bar in both is 1 µm. The Ag array has become partly dislodged from the polymer during preparation for SEM imaging.

Figure 5.8 shows (a) the underside and (b) the topside of polymer – the latter with Ag nanorods (0° deposition), which have slightly risen from it during preparation for SEM, exposing bumps at the bottom which trace the structure of the polymer. Nanoimprinted polymers have been employed previously in generating plasmonic structures [7]–[9] via the deposition of metallic layers on patterned polymer. Flat polymer bases have also been used, in Ag nanorod OAD for example, to create flexible, large-area SERS substrates resistant to mechanical strain which could potentially be used as flexible SERS "labels" [10]. Underlying polymer layers, patterned or flat, can generate highly reproducible and high-throughput SERS

substrates at low cost. In this experiment, the polymer serves as a seed template during OAD.

5.2.2.4 Oblique angle deposition of Ag and Cu nanorod arrays

Nanorod fabrication using OAD has been described in detail elsewhere [11], [12]. Here, polycarbonate substrates cut to approximately 10 × 13 mm^2 and adhered to glass slides, were loaded for metal deposition together with silicon, silica, or glass substrates for comparison. A Satis e-beam evaporation system was used for thin film deposition, with the chamber vacuum maintained at about 1×10^{-6} Torr. Deposition along the surface normal (0°) resulted in conformal growth and an ordered Ag nanorod array, as previously shown in figure 5.8 (b) and again in figure 5.10 (a). Before OAD, a 10 nm layer of the respective metal (monitored by a quartz crystal microbalance) was deposited onto the substrates in the normal direction to increase nanorod adhesion. This thin metallic layer also serves to help protect the polymer from laser illumination while simultaneously blocking the polymer background signal during a Raman measurement [13]. OAD was then performed at 85° with a nominal growth rate of 0.2 nm s^{-1}. Micrographs of thus-manufactured nanorod arrays were taken using a scanning electron microscope (SEM; Hitachi S-4100).

5.2.2.5 Spot-to-spot collection of SERS spectra

With regard to optimal sample excitation, it has been reported previously that both the incident angle and polarization of the laser beam, with respect to nanorod direction, may influence SERS signal strength [14], [15]. This however is beyond the scope of this thesis, and in order to minimise the number of variables, all

substrates were treated equally with a fixed angle of 0° between the substrate plane and the **E**-vector, and also between the longitudinal planes of the nanorods and the **E**-vector.

Prior to SERS analysis, all Ag and Cu substrates were immersed overnight in aqueous solutions of BPE (1.00×10^{-5} M for Ag and 1.00×10^{-4} M for Cu), and then dried in an N_2 stream. Ten and 20 spectra were collected for Ag and Cu, respectively, from the entire surface of each substrate (about 1 cm^2) using the same Raman spectrometer and set up as in 2.2.2.3. The 632.8 nm line of a helium-neon laser was used as the excitation source. Unfocussed output power at the sample was measured to be approximately 3.2 and 3.5 mW, with collection times of 0.1 and 30 s for Ag and Cu, respectively. For Ag, SERS intensity of BPE was recorded by averaging the height of the 1200 cm^{-1} peak after baseline correction of 10 spectra. For Cu substrates, the 1636 cm^{-1} peak height was averaged from 20 spectra and OriginPro 8.6 software was used for data analysis. Spectra were acquired during a collection time of 0.1s for the Ag-silica control, 85 and 85:85^o Ag polymers and 1s for the 0:85 and 0:85:85^o polymers which were corrected to 0.1s for comparison.

5.2.2.6 SERS mapping

SERS mapping of the integrated 1200 cm^{-1} peak intensity of 1.00×10^{-5} M BPE (aq) on the 85^o Ag polymer array was performed using 632.8 and 785 nm laser lines on a Witec Confocal Raman Microscope alpha300 R. Five maps at each wavelength, each comprising 100 spectra over an area of 10 µm x 10 µm (10 points per line, 10 lines per image) were collected, using a 100 × 0.9 objective and a 50 ms collection time, totalling 500 spectra per wavelength. The unfocussed power at the

sample was 1.5 mW at both excitations. Data analysis was carried out using WITec Project 2.10 software.

Mapping of Cu polymer and Si arrays with 1.00×10^{-5} M methanolic BPE was carried out on a DXR Raman microscope (Thermo Scientific) using 780 nm excitation and a 50 × 0.9 objective with a 1 s collection time. Each of five maps per sample was constructed using the height of the 1636 cm^{-1} peak, with 150 spectra collected over an area of 90×140 μm^2, totalling 750 spectra per sample.

SERS mapping of Cu substrates with 1.156×10^{-5} M rhodamine B ITC (aq) was conducted on a Witec Confocal Raman Microscope alpha300 R, with a 10 × 0.25 objective at 632.8 nm excitation, with a 2.5 s collection time and an unfocussed power at the sample of 24.3 mW. Each of two maps per sample was constructed using the integrated intensity of the 1190 cm^{-1} peak, with 400 spectra collected over an area of 100×100 μm^2, totalling 800 spectra per sample. Data analysis was carried out using WITec Project 2.10 software.

5.2.2.7 Simulations

Mr Guoke Wei of the Photophysics group at the University of Strathclyde used the discrete dipole approximation (DDA) to simulate the interaction between metal nanorods and light at the excitation wavelengths used in the SERS experiments. Simulation results were obtained using the EPSRC funded ARCHIE-WeSt High Performance Computer (www.archie-west.ac.uk). A detailed discussion of the computing parameters used in the simulations, i.e. those concerning the manipulation and limitations of the computer code or the simulation run-times for

example is beyond the scope of this thesis, and the background discussion in this section covers only those items which help elucidate how light interacts with the nanorod structure in terms of amplification of the incident field.

Originally developed to model light interaction with astronomical dust grains, the DDA is now a standard technique deployed to calculate the absorption and scattering of electromagnetic radiation by targets of arbitrary geometries. It is especially suited however, to simulating spatially periodic and anisotropic materials, even when near substrates, making it ideal for work on nanorod arrays. A dipole array of polarisable points inside cubic "building blocks", with pre-programmed polarisabilities, approximates the same volume or area as the target. Maxwell's equations can then be solved for the array to an arbitrarily accurate degree, depending on available computer power. An incident monochromatic plane wave causes the polarisations of the target dipoles to oscillate coherently, and in addition to being affected by the wave, each dipole experiences the combined electric fields of all of the other point dipoles [16].

Figure 5.9 is a pictorial summary of the nanorod dimensions used in the simulations; the real nanorods are shown in figure 5.10.

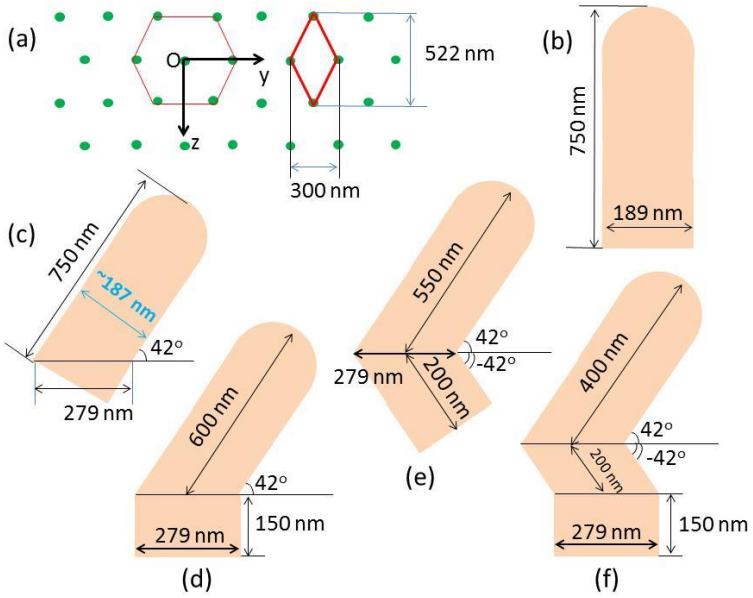

Figure 5.9. Schematic of (a) hexagonal pattern substrate, and five different target units simulating Ag nanorods on polymer prepared under (b) 0° deposition, (c) 85° deposition, (d) 0°:85° deposition, (e) 85°:−85° deposition (mirror image), and (f) 0°:85°:−85° deposition (mirror image).

To simplify the nanorods calculations, the *effective*- and *vertical*-base diameters were all set to 279 nm, in line with the effective-base diameter of the actual 85° Ag nanorod sample – the sample depicted schematically in figure 5.9 (c); *effective*-base diameters are those found in figure 5.9 (c) and (e), where there is no *vertical* base (279 nm × 150 nm), as present in the structures in figure 5.9 (d) and (f). Instead, the effective base diameter is the major axis of the oval plane of the rod (away from the tip), parallel to the y-z plane. It should be noted that differences existed between the vertical-base diameters in simulation structures and those in actual nanorod samples (represented in 5.9 (d) and (f)), causing a discrepancy between experimental and simulation results which is examined later. The 0° sample retained its actual base diameter during the simulations, due to its transverse plane being parallel to the y-z plane.

The SERS enhancement factor (EF) was introduced in chapter one, and the average EF over the surface area, s, of an Ag rod is calculated thus: $\langle EF \rangle = \int g^4 ds / \int ds$ [17]. The local EF value, i.e. g^4 is calculated half a grid point away from each exposed cube surface and the normalised electric field, $g = |E|/|E_0|$, where E and E_0 are the local and incident fields respectively, is a function of position on the rod surface.

5.2.3 Results and discussion

5.2.3.1 Ag nanorod arrays

Figure 5.10 (b) shows an SEM surface image of the 85^o deposition angle nanorod array (note that parts of the arrays have become dislodged from the underlying polymer during preparation for SEM imaging).

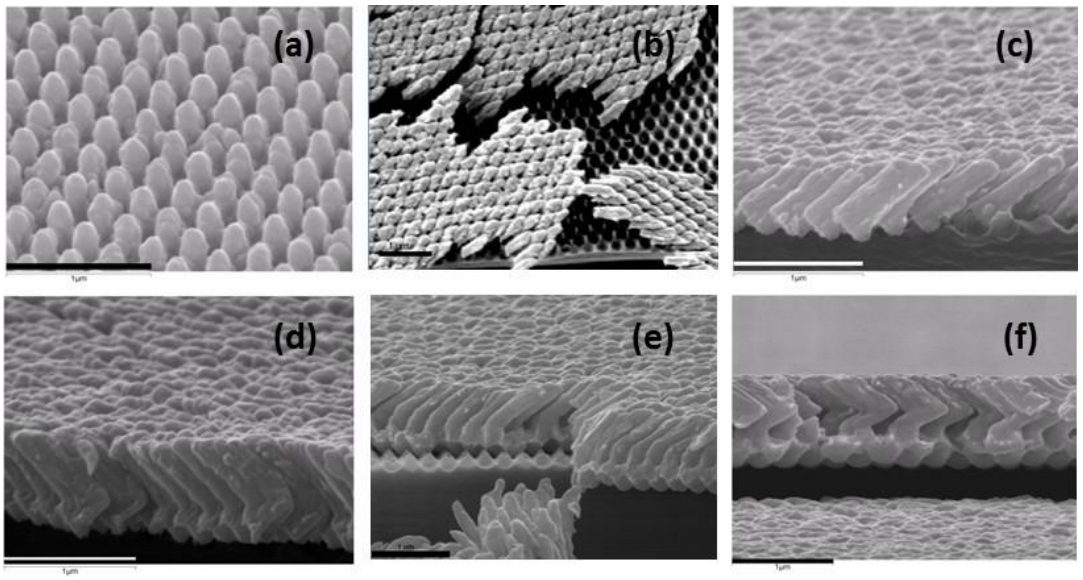

Figure 5.10. SEM images of Ag nanorod arrays on polymer films prepared under (a) 0° deposition, (b) 85° deposition (top view), (c) 85° deposition (cross-section), (d) 85°:−85° deposition, (e) 0°:85° deposition, and (f) 0°:85°:−85° deposition. The scale bar in each image represents 1μm. Note: parts of arrays were lifted off when the samples were cut to create cross-sections.

Ordered arrangement of the array following a hexagonal polymer pattern, in contrast with random nanorods grown on silicon at 85^{o} deposition, as seen in the surface image in figure 5.11, confirms that guided nucleation of nanorods has taken place.

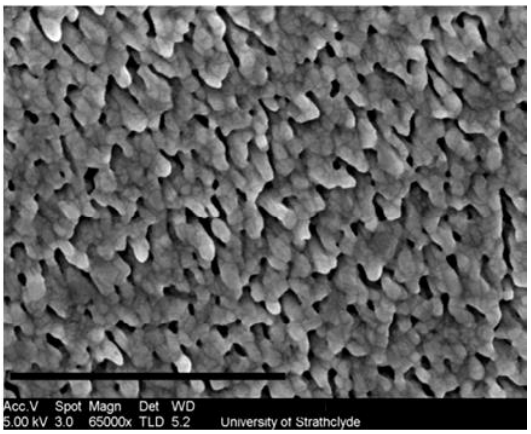

Figure 5.11. SEM surface image of OAD Ag nanorod array grown on silicon showing random distribution. The scale bar represents 1 μm.

Figure 5.10 (c) shows an SEM image of a cross-section of the 85^{o} nanorod array on polymer. The diameter of the rods is about 187 nm and the length about 750 nm. Subsequent depositions at 85° and −85° (denoted by 85°:−85°) resulted in a zigzag rod structure, as shown in figure 5.10 (d). Two other nanostructured arrays were produced by growing tilted (85°) and zigzag (85°:−85°) nanorods on short vertical bases (denoted 0°:85° and 0°:85°:−85° and shown in figure 5.10 (e), (f), respectively). Figure 5.12 shows SERS spectra of bare Ag nanorods.

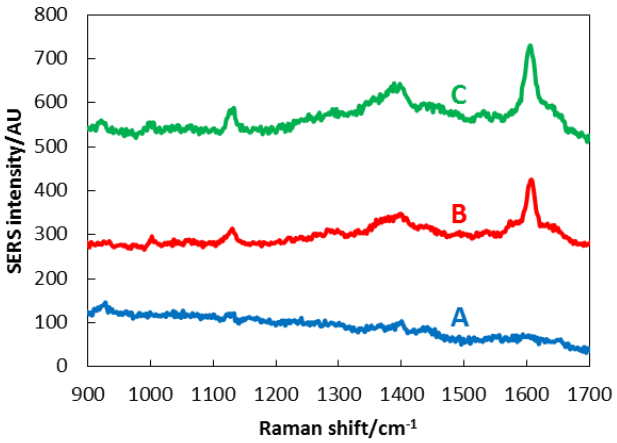

Figure 5.12. SERS spectra of bare Ag nanorods (632.8 nm excitation, 3.2 mW unfocussed power, acquisition time 0.1 s): (A) 85° silica control; (B) 85°:−85° polymer; (C) 85° polymer.

Background spectra of the Ag polymer arrays in figure 5.12 (B) and (C) have peaks at 1130 cm^{-1}, 1394 cm^{-1}, and 1608 cm^{-1}, while the Ag silica substrate possesses the first two only, which are just visible above background noise. The features are not as prominent in the Ag-silica substrate as it does not provide as strong a signal as the other two; the band at 1608 cm^{-1} in this sample is either absent or it has been subsumed by spectral noise. The most prominent band (1608 cm^{-1}) in figure 5.12 (B) and (C) can be assigned to graphite; graphite has a strong band at 1580 cm^{-1} (the G band ascribed to the in-plane stretching mode). Importantly, this band shifts to higher frequencies as graphitic material decreases in size, meaning that the band at 1608 cm^{-1} can be assigned to the G band of nanographitic flakes placed on the surface of the substrate during deposition, while other small peaks are likely generated by organic contaminants outgassing from the deposition chamber [18].

Figure 5.13 (a) shows typical SERS spectra of BPE on ordered 85°:−85° and 85° Ag nanorod arrays on polymer (B and C, respectively) in comparison with 85° Ag nanorod arrays on silica (A); the most prominent vibrational modes of BPE

appear at 1200, 1607, and 1637 cm^{-1} corresponding to the C = C stretching, aromatic ring stretching, and in-plane ring modes, respectively [4].

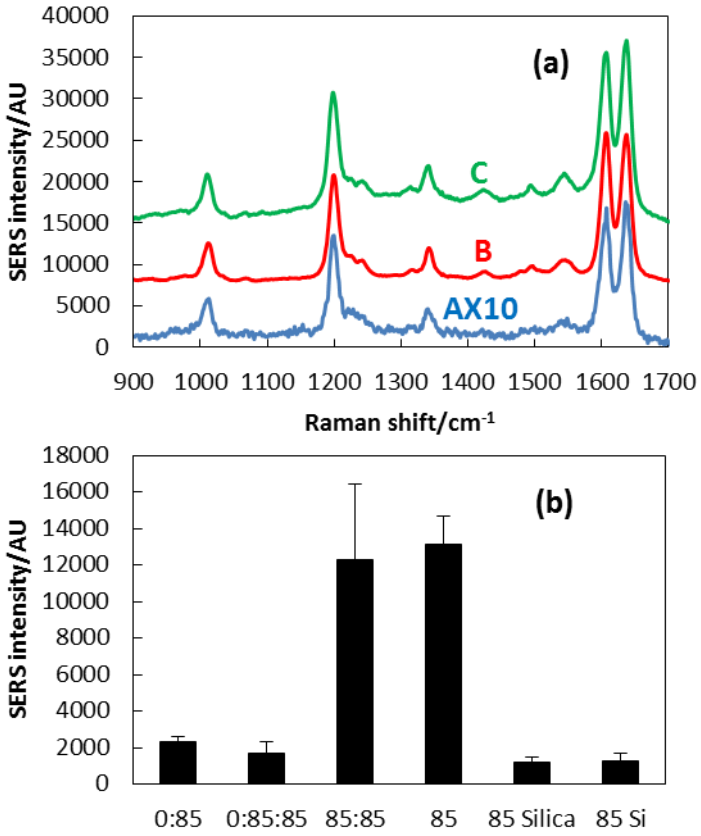

Figure 5.13 (a) Representative SERS spectra of BPE on Ag nanorods (632.8 nm excitation, 3.2 mW unfocussed power, acquisition time 0.1 s): (A) 85° silica control; (B) 85°:−85° polymer; (C) 85° polymer. (b) Intensity of 1200 cm^{-1} peak, averaged from 10 spectra from various Ag nanorod arrays as-labelled.

It is clear from figure 5.13 (b) that both 85° and 85°:−85° arrays on polymer generate a strong SERS signal, up to about 10 times that of the other polymer substrates and the silica control. In terms of reproducibility, the 85° and 0:85° arrays have comparably low relative standard deviations (RSDs) of 11.8% and 10.3%, respectively, which are better than the 24.4% for 85° arrays on silica, 34.0% on silicon, and 33.4% for the 85°:−85° array on polymer. The 85° array on polymer therefore surpasses all others when SERS intensity and reproducibility are

considered in conjunction. Good reproducibility (< 20%) also qualifies the 85° polymer array for SERS detection and identification purposes [19]. All arrays, excepting 0°, have similar diameters and overall lengths as confirmed by SEM images. Their overall surface areas are comparable as shown in figure 5.14, meaning there is no significant correspondence between SERS signal strength and nanorod surface area in this case.

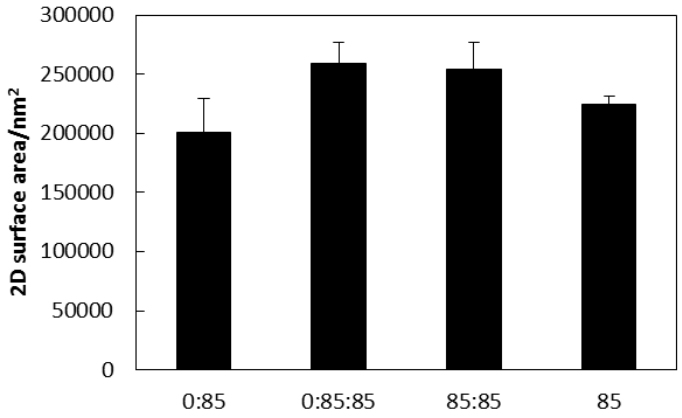

Figure 5.14. 2-D surface areas of Ag nanorods on polymer as measured from SEM images.

The nanorod array of 0° deposition on polymer (figure 5.10 (a)) produces a weak but definite SERS spectrum (plot B, figure 5.15 (a)) of BPE, 250 times weaker than 85° deposition on polymer, while in contrast, 0° rods on silicon (plot A, figure 5.15 (a)) produces none at all. Control spectra of bare arrays deposited at 0^{o} on (A) silicon and (B) polymer substrate are included in figure 5.15 (b) for comparison.

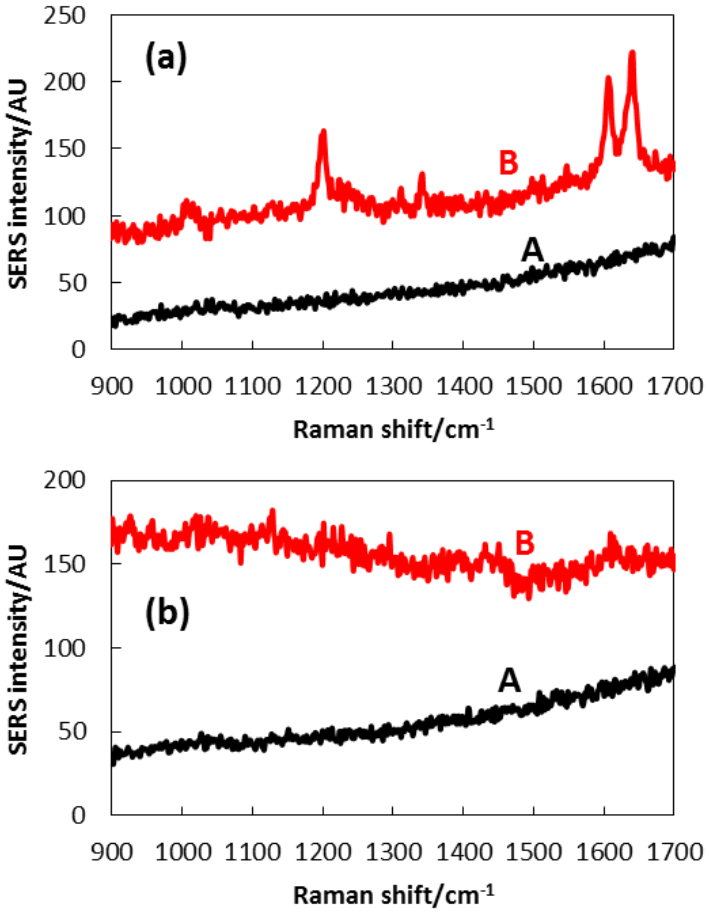

Figure 5.15 (a) SERS spectra of BPE on Ag nanorod arrays deposited at 0^{o} on (A) silicon and (B) polymer substrate; (b) SERS spectra of bare arrays deposited at 0^{o} on (A) silicon and (B) polymer substrate. (For all spectra: 632.8 nm excitation, 3.2 mW unfocussed power, acquisition time 0.1 s).

These findings are in line with those discussed previously in this chapter – that the porosity and surface roughness of Ag film deposited at 0° on planar silicon are virtually zero, as in bulk silver, so a SERS signal from this substrate should not be expected. In contrast, 0° deposition on polymer produces a BPE spectrum due to the comparatively porous and roughened structure of the Ag film generated by guided nucleation; figure 5.10 (a) clearly shows regular gaps in the film.

It is not surprising therefore that 0° deposition on planar silicon generates no SERS. However, this cannot account for the substantial differences in signal strength between vertical polymer/nanorod arrays (0°), arrays supported by vertical bases (0°:85°, 0°:85°:−85°), and tilted arrays (85°and 85°:−85°).

5.2.3.2 Simulations

Figure 5.16 shows the magnitude of the normalized electric field, when 85°, 85°:−85°, 0°:85° and 0°:85°:−85° arrays are excited at 632.8 nm.

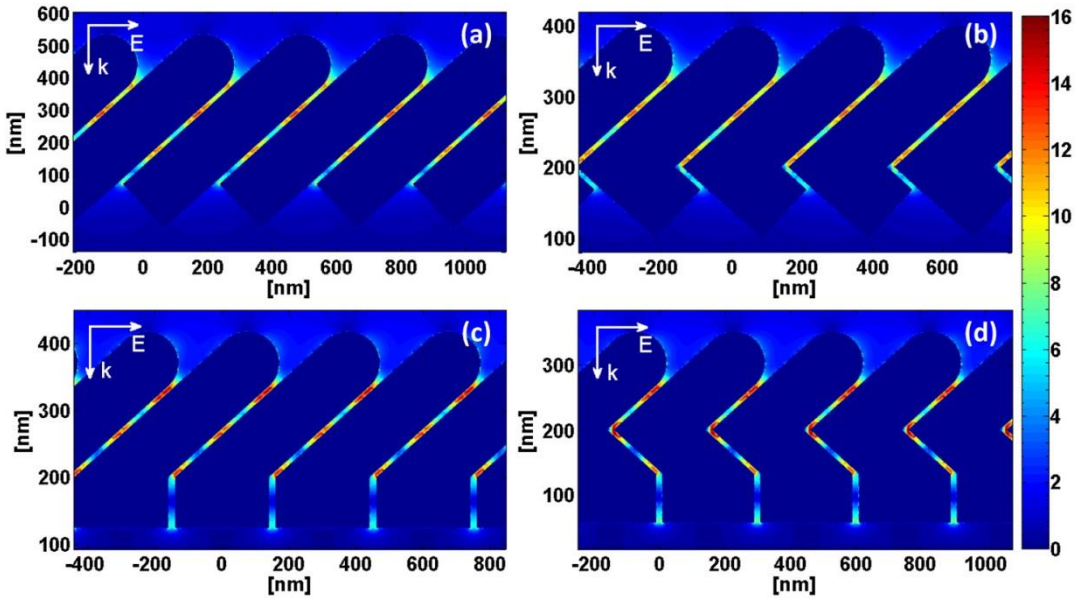

Figure 5.16. Magnitude of normalized electric field, $g = |E|/|E_0|$, where E and E_0 are the local and incident fields, respectively, of (a) 85°, (b) 85°:−85°, (c) 0°:85°, and (d) 0°:85°:−85° arrays. **k** and **E** are the wave and electric field vectors respectively. All internal fields were set to zero for clarity.

g^4 ($g = |E|/|E_0|$) is the enhancement factor, where E and E_0 are the local and incident fields respectively. Regions of strong EM enhancement (commonly known as "hotspots") are found in the gaps between adjacent nanorods in all of the polymer arrays, with the exception of the 0° array shown in figure 5.17, which produces by

far the least enhancement due to a relatively large gap size and weaker electromagnetic coupling between neighbouring nanorods.

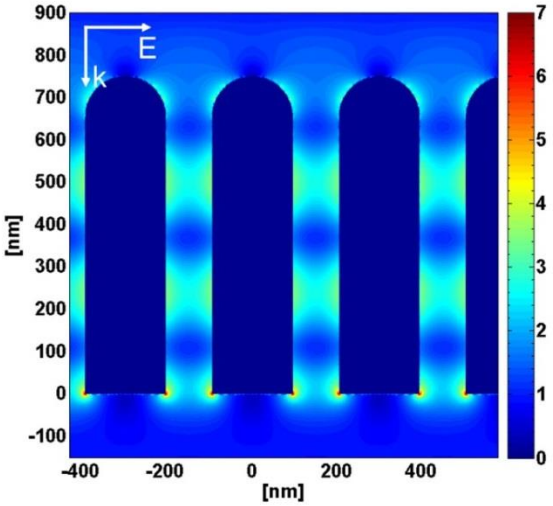

Figure 5.17. Magnitude of normalized electric field, $g = |E|/|E_0|$, where E and E_0 are the local and incident fields respectively, of the Ag nanorod array deposited at 0^o on polymer. The enhancement factor is 29. **k** and **E** are the wave and electric field vectors respectively. All internal fields were set to zero for clarity.

At nanoparticle surfaces, the electromagnetic enhancement factor (EF) in SERS is g^4. To help explain the results, the average EF over the surface area of an Ag rod was calculated, $\langle EF \rangle = \int g^4 ds / \int ds$ [17]. The g^4 value was calculated half a grid point away from each exposed cube surface. The average enhancement factors for 85° and 85°:−85° arrays, 438 and 459, respectively, are comparable and in line with experimental results. The slightly higher EF of the 85°:−85° array may be due to the sharp corners where the rods bend in the simulation structures. A much smaller EF of 29 was found for the 0° array, also consistent with Raman measurements. Calculation of 0°:85° and 0°:85°:−85° arrays however, generates EFs of 575 and 696 respectively, higher than those of the 85° and 85°:−85° arrays. This inconsistency is due to the discrepancy between the gap sizes found in simulation structures and those

in actual arrays, a discrepancy arising because of the simplifications made before the calculations. The magnitude of EM enhancement strongly depends on gap size, as seen in figure 5.18.

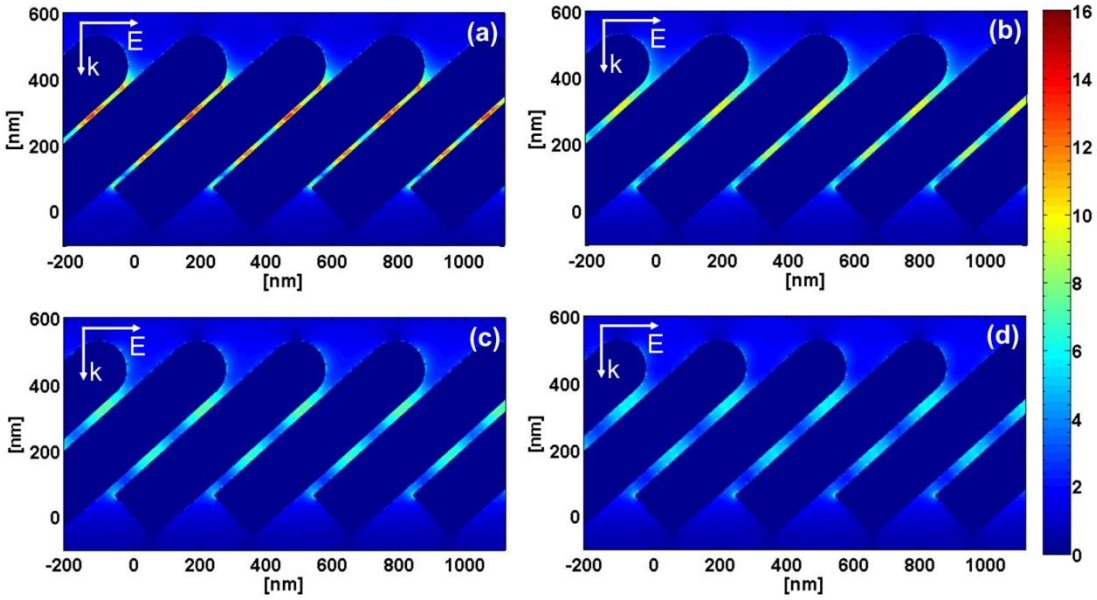

Figure 5.18. Magnitude of normalized electric field, $g = |E|/|E_0|$, where E and E_0 are the local and incident fields respectively, of Ag nanorod arrays with (a) 21, (b) 27, (c) 39 and (d) 51 nm gaps. **k** and **E** are the wave and electric field vectors respectively. All internal fields were set to zero for clarity.

In the experiment, the diameter of real vertical rods, approximately 182 nm (resulting from conformal growth under 0° deposition) was smaller than that used in the simulation (279 nm), resulting in larger gaps and a weaker EM field strength. Taking this into account, the calculations show a relatively weak EM enhancement from the 0°:85° array compared with the 85° array. Figure 5.19 highlights the dramatic difference in g when only the diameter of the base is changed in 0°:85° rods.

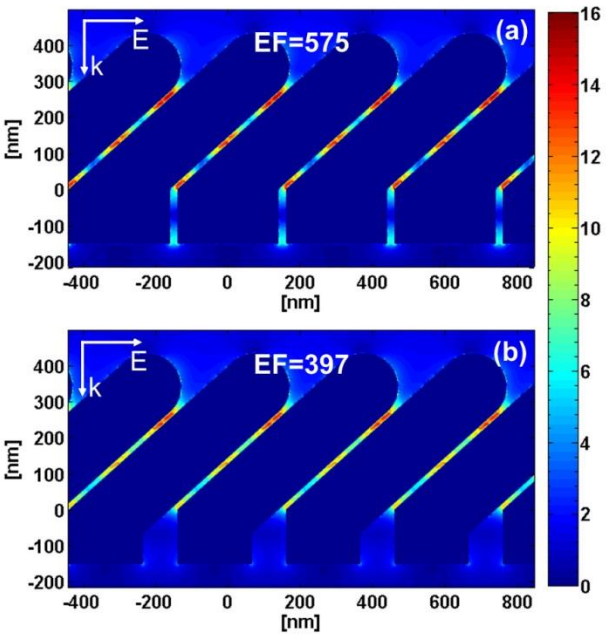

Figure 5.19. Magnitude of normalized electric field of 0:85° Ag nanorod arrays with different vertical pillar diameters. **k** and **E** are the wave and electric field vectors respectively. All internal fields were set to zero for clarity.

The dependence of rod diameter and the associated plasmonic properties on polymer template dimensions would certainly merit further investigation.

For the 85° polymer array, frequency-corrected mapping data of the 1200 cm^{-1} peak of BPE, taken at both 633 and 785 nm excitations, show SERS intensity at 633 nm to be about 5 times that at 785 nm. As described in chapter four, section 4.1.3.2, with all other things being equal for a given sample, the SERS signal will be more intense at 633 nm excitation compared with 785 nm by a factor, $(785/633)^4$, which can, if necessary, be corrected for during analysis. Although in analytical work the total *observed* signal is paramount, it is necessary to employ the correction here when considering theoretical results from simulations, as these describe local amplification of the incident electric field for each wavelength, rather than wavelength-dependent scattering efficiencies. Representative maps without

frequency correction, with excitation wavelengths as-labelled (top-right) and taken from different locations on the substrate are shown in figure 5.20

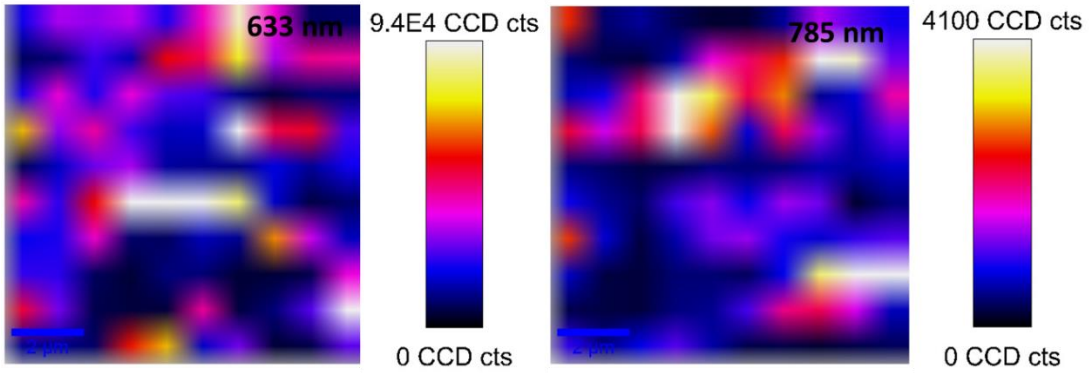

Figure 5.20. Representative maps of 85° Ag on polymer array with excitation wavelengths as-labelled, both comprising 100 spectra over an area of 10 µm x 10 µm (10 points per line, 10 lines per image), with an unfocussed power at the sample of 1.5 mW for each. The scale bar in the bottom left represents 2 micrometres.

Maps in figure 5.20 retain their own scale to illustrate the distribution of SERS activity across the surface locations at both wavelengths. As the peak number of counts at 633 nm excitation is about 23 times that at 785 nm, the 785 nm map would become featureless if a mutual scale were inserted. It should be noted that mapping data were not employed to determine substrate reproducibility, as the maps were recorded several months after fabrication of the array. Stored in ambient conditions, the silver became oxidised and reproducibility was adversely affected, but the array remained highly SERS-active nonetheless. Five hundred mapping spectra however for each wavelength showed a broad distribution, but an absence of outliers in SERS intensity measurements meaning that the comparison of intensities between both wavelengths is valid, despite the age and decreased uniformity of the substrate.

It may be that a physical change in the substrate over time renders it more amenable to 633 nm excitation, but this is unlikely given simulation results. Figure

5.21 shows the magnitude of the normalised electric field of Ag nanorod arrays under 633 and 785 nm excitations simulated using the DDA. The average enhancement factors were found to be 437 and 336 for excitations at 633 and 785 nm respectively, in line with frequency-corrected experimental results.

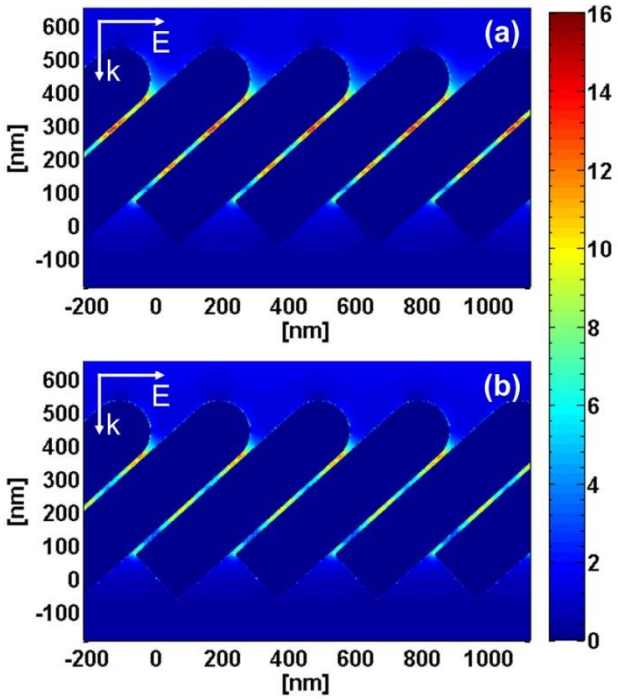

Figure 5.21. Magnitude of normalized electric field, $g = |E|/|E_0|$, where E and E_0 are the local and incident fields respectively, of the 85° Ag nanorod-polymer array under (a) 633nm and (b) 785nm excitation. All internal fields were set to zero for clarity.

The influence of excitation wavelength on SERS of Ag nanorod arrays depends on their geometric structures as well as the nature of the probe molecule under consideration. Further investigation is required to reveal the mechanism behind the different enhancements.

5.2.3.3 Cu nanorod arrays

A number of metals have been employed successfully in SERS, the most common being silver, gold, and copper [20]. Although the SERS signal is generally weaker when it is employed, copper is nonetheless highly attractive as a SERS metal as it has a scrap value much less than that of either of its counterparts. Recently, great efforts have been made to construct Cu-based SERS-active platforms, including for example, nanowires, nanoparticles, and hollow copper microcages [21]–[24]. Zhao *et al*. synthesised vertical, SERS-active Cu nanorods using potentiostatic electrodeposition inside nanochannels of porous anodic alumina membrane (PAAM) [25], while SERS-active Cu nanorod arrays were created via OAD on glass slides by Kahn *et al*. [26].

Given the effectiveness of Ag polymer substrates, 85^{o} copper nanorod arrays on polymer were fabricated using this guided OAD approach. An ordered array was created, as shown in figure 5.22 (a) for 671 nm nanorods. Substrates were immersed overnight in aqueous BPE (1.00×10^{-4} M) and interrogated using 633 nm excitation. Figure 5.22 (b) shows typical SERS spectra of BPE for Cu nanorod arrays of lengths 671 and 989 nm on polymer support and on glass as a control.

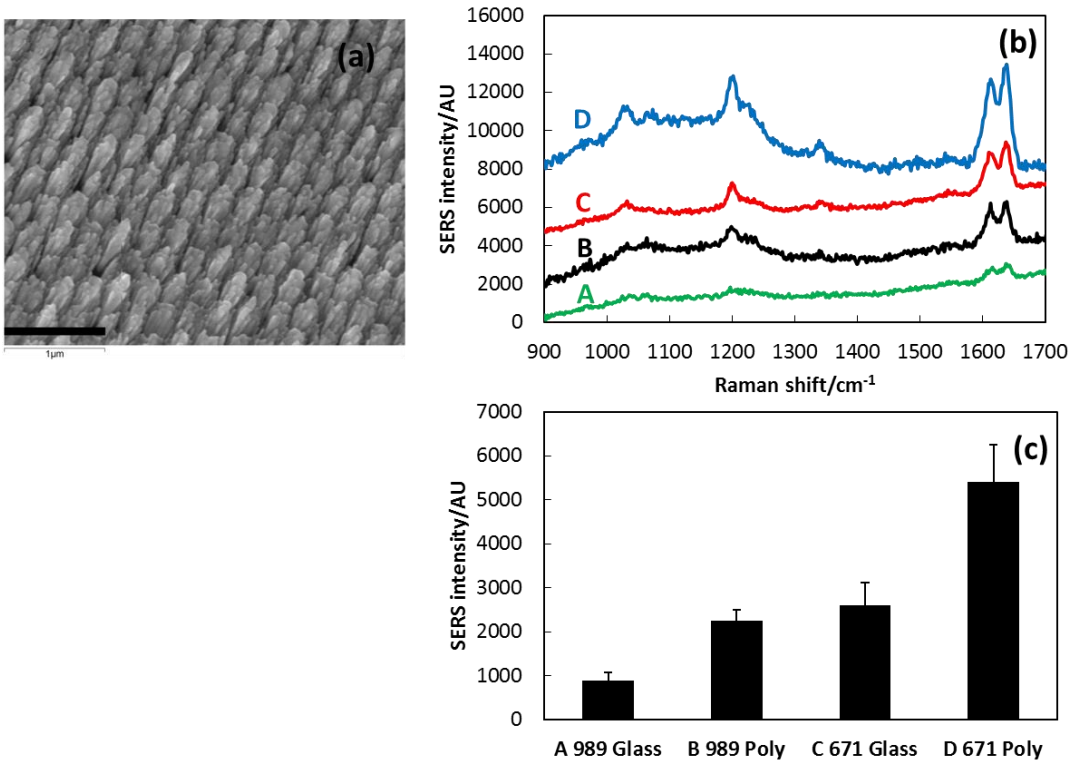

Figure 5.22 85° Cu arrays: (a) SEM surface image of 671 nm Cu-polymer array. (b) SERS spectra of nanorod arrays of lengths (A) 989 nm on glass, (B) 989 nm on polymer, (C) 671 nm on glass and (D) 671 nm on polymer. (c) Average intensity of 1636 cm^{-1} peak from 20 spectra from Cu nanorod arrays as labelled. At 633 nm excitation, the approximate unfocussed power at the sample was 3.5 mW with a 30 s collection time.

Twenty spectra were collected from each substrate, with the 1636 cm^{-1} peak height used for analysis, as the 1200 cm^{-1} was not resolved clearly in the "989 Glass" sample; the arrays on polymer produce a SERS signal strength roughly twice that of their Cu-glass counterparts as seen in figure 5.22 (c). Table 5.2 displays the %RSDs of the 20 spectra for each sample, and control spectra are included in figure 5.23 as a comparison.

Table 5.2. %RSDs of Cu substrates.

Sample	989 Glass	989 Poly	671 Glass	671 Poly
%RSD in signal strength	19.6%	11.6%	20.2%	15.6%

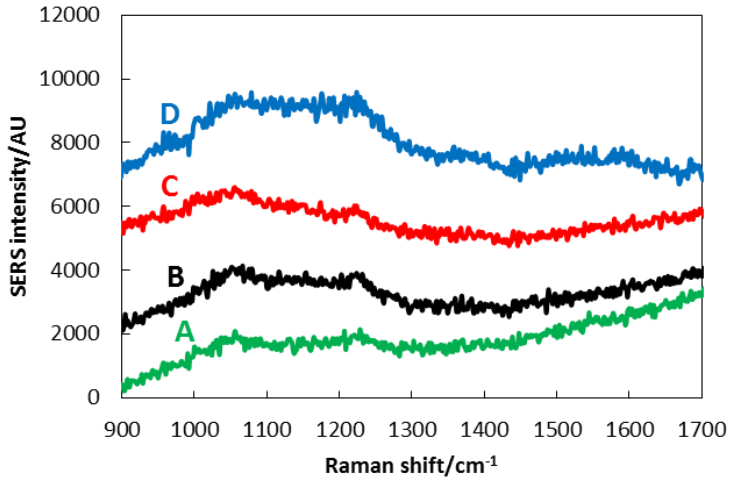

Figure 5.23. Largely featureless control SERS spectra of nanorod arrays of lengths (A) 989 nm on glass, (B) 989 nm on polymer, (C) 671 nm on glass and (D) 671 nm on polymer. Approximate unfocussed power at the sample was 3.5 mW, with a 30 s collection time at 633 nm excitation.

Control spectra in figure 5.23 for Cu arrays turn out to be virtually featureless. The polymer array of rod-length 989 nm, with a RSD of 11.6%, produces a SERS signal strength about 2.5 times that of the Cu-glass control, and about half that of the 671 nm polymer array. The magnitude of the normalised electric field of Cu nanorod arrays on polymer for both lengths was simulated using the DDA, the results for which are illustrated in figure 5.24.

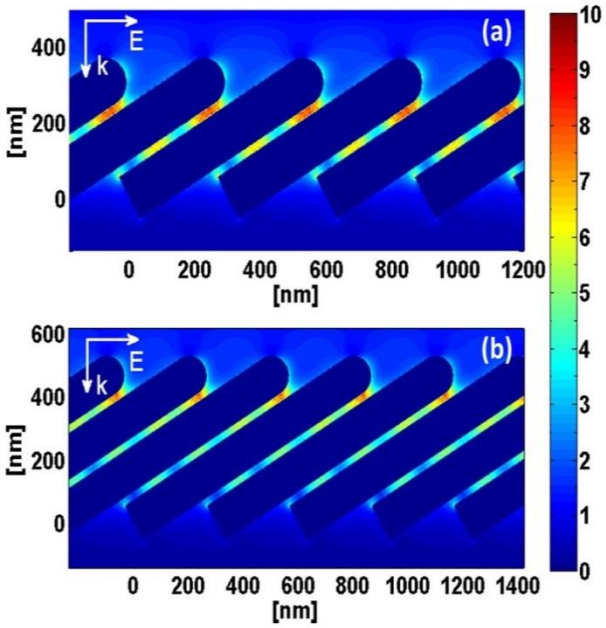

Figure 5.24. Magnitude of normalized electric field, $g = |E|/|E_0|$, where E and E_0 are the local and incident fields, respectively, of 85° Cu nanorod arrays on polymer of (a) 671 and (b) 989 nm length (diameter ~ 127 nm; tilted angle ~ 30°, as taken from SEM measurements). All internal fields were set to zero for clarity.

The average enhancement factors of 671 and 989 nm arrays were found to be 83.5 and 52.7 respectively, which is consistent with experimental results. This suggests that SERS intensity is not simply proportional to rod surface area and that aspect ratio changes which give control over the longitudinal and transverse plasmons play an important role, making it possible to optimise rod length for the best SERS effect.

The effectiveness of Cu nanorod arrays on polymer substrates was further confirmed by SERS mapping of BPE, as shown in Figure 5.25.

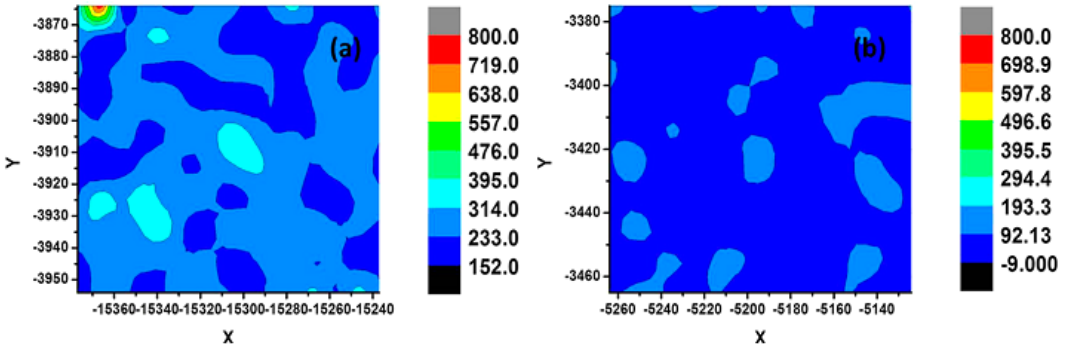

Figure 5.25. SERS maps of methanolic BPE (10^{-5} M) on (a) Cu-polymer and (b) Cu-Si. Each map corresponds to an area on the substrate of 90 × 140 μm^2, with the height of the 1636 cm^{-1} peak used and 150 spectra collected.

A 2μL aliquot of BPE in methanol (10^{-5} M) was placed on Cu-Si and Cu-polymer substrates and allowed to dry before SERS analysis. Each map corresponds to an area on the substrate of 90 × 140 μm^2, with the 1636 cm^{-1} peak height used for analysis and 150 spectra collected. Mapping results averaged from 750 spectra from each substrate indicate that the Cu-polymer array generates an average SERS intensity about 3 times that of the Cu-Si array. Cu-polymer also shows better reproducibility at 23.9%, compared with that of Cu-Si (32.5%).

In addition to BPE, another common SERS probe, RBITC (aq) (1.156×10^{-5} M) was used to test the Cu-polymer substrate. Figure 5.26 (a) shows SERS spectra of RBITC on Cu-polymer and Cu-Si substrates, each averaged from 800 individual spectra collected from mapping, where characteristic peaks match those described in the literature [27], [28]. To the right of the spectra is the molecular structure of the probe taken from [29].

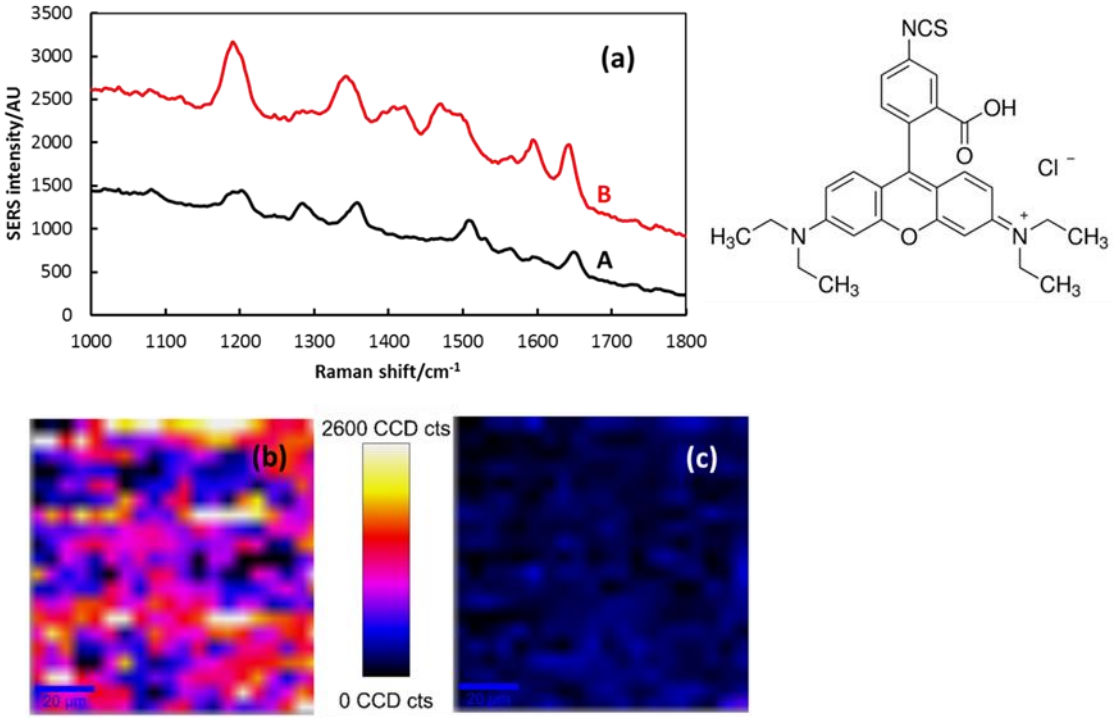

Figure 5.26 (a) SERS spectra of RBITC on (A) Cu nanorod array on Si substrate (Cu-Si) and (B) Cu nanorod array on polymer substrate (Cu-polymer). (b) SERS mapping (from 400 spectra) of the 1190 cm^{-1} band of RBITC on Cu-polymer and on (c) Cu-Si substrate. Each map corresponds to an area on the substrate of 100 × 100 μm^2 with an excitation wavelength of 633 nm. The substrate was immersed in 1.156 × 10^{-5} M (aq) RBITC for 15 min and then dried in N_2 immediately before SERS measurement. The molecular schematic is taken from [29].

Selected prominent bands are the 1344 and 1644 cm^{-1}, ascribed to aromatic C – C stretching, and the 1190 cm^{-1}, arising from aromatic C – H bending [28].

Integrated peak intensity of the 1190 cm^{-1} band for the Cu-polymer substrate is about 3 times that of its Cu-Si counterpart along with a good reproducibility of 11.0% as observed from SERS mapping, figure 5.26 (b), (c). It is worth pointing out that although the improvement in SERS performance in the case of copper is not as pronounced as that of silver, the possibility of manufacturing nanorod arrays with designed gaps and diameters using this guided OAD method should allow further

structural optimisation. This added to the low cost of polymer substrates makes this novel method an attractive approach for fabricating large-scale, highly effective SERS-active substrates.

5.2.4 Conclusion

A fabrication method using patterned polymer, for the production of highly ordered nanorod arrays which, in principle, could circumvent the problems of gap size and diameter control was investigated. The polymer template tightly controls the nucleation process during OAD, producing nanorod arrays which are highly SERS-active and reproducible. In the case of Ag, an enhanced SERS intensity about 10 times that of the Ag-silica control was observed for the 85° Ag-polymer array. The SERS response of Ag-polymer arrays was compared to results obtained from discrete dipole approximation simulations, which revealed that narrow gaps between nanorods, formed by this guided-nucleation approach, were responsible for this dramatic enhancement. Ordered Cu-polymer arrays were also successfully fabricated, which likewise, exhibited strong SERS combined with good reproducibility, as confirmed via mapping studies of BPE and RBITC. Although only one nanopattern is employed in this work, the results highlight that potentially, such templates could be created to desired specifications before rod deposition. Future studies could focus on optimisation of polymer template design and, in turn, plasmonic characteristics to maximize SERS performance. This work opens the door not only to an efficient, cheap, and reproducible method of producing high-quality, high-order nanorod arrays as SERS substrates, but to their wider application in other areas such as nanophotonic devices and solar cells.

5.3 Summary

This chapter examined the role of different types of metal nanorod arrays as SERS substrates. The relationship between deposition angle, film surface roughness, porosity and SERS was examined, and it was found that film surfaces became rougher and porosity increased as the angle was widened. Only the sample deposited at 85^{o} exhibited a clear oblique columnar structure which was capable of generating SERS of BPE. Reflectance spectra confirmed the positive relation between porosity and deposition angle and the high anisotropy of the 85^{o} nanorods.

A fabrication method using patterned polymer, for the production of highly ordered Ag and Cu nanorod arrays which, in principle, could circumvent the problems of gap size and diameter control was investigated. The polymer template tightly controlled the nucleation process during OAD, producing nanorod arrays which were highly SERS-active and reproducible. Despite only one nanopattern being employed in this work, the results highlight that potentially, such templates could be created to desired specifications before rod deposition. Future studies could focus on optimisation of polymer template design and, in turn, plasmonic characteristics to maximize SERS performance.

References

[1] Y. Liu, "Surface-enhanced Raman scattering from silver nanorod arrays fabricated by oblique angle deposition," pp. 39–40, Georgia, 2010.

[2] Y.-C. Yao, M.-T. Tsai, H.-C. Hsu, L.-W. She, C.-M. Cheng, Y.-C. Chen, C.-J. Wu, and Y.-J. Lee, "Use of two-dimensional nanorod arrays with slanted ITO film to enhance optical absorption for photovoltaic applications," Opt. Express, vol. 20, no. 4, pp. 3479–3489, 2012.

[3] J. H. Rakels, "Influence of the surface height distribution on the total integrated scatter (TIS) formula," *Nanotechnology*, vol. 7, no. 1, pp. 43–46, 1996.

[4] W. Yang, J. Hulteen, G. C. Schatz, and R. P. Van Duyne, "A surface-enhanced hyper-Raman and surface-enhanced Raman scattering study of *trans*-1,2-bis(4-pyridyl)ethylene adsorbed onto silver film over nanosphere electrodes. Vibrational assignments: Experiment and theory," *J. Chem. Phys.*, vol. 104, no. 11, pp. 4313–4323, 1996.

[5] Y.-J. Liu, H. Y. Chu, and Y.-P. Zhao, "Silver nanorod array substrates fabricated by oblique angle deposition: morphological, optical, and SERS characterizations," *J. Phys. Chem. C*, vol. 114, no. 18, pp. 8176–8183, 2010.

[6] Y.-J. Liu, Z.-Y. Zhang, R. A. Dluhy, and Y.-P. Zhao, "The SERS response of semiordered Ag nanorod arrays fabricated by template oblique angle deposition," *J. Raman Spectrosc.*, vol. 41, no. 10, pp. 1112–1118, 2010.

[7] A. Boltasseva, "Plasmonic components fabrication via nanoimprint," *J. Opt. A Pure Appl. Opt.*, vol. 11, no. 11, p. 114001, 2009.

[8] W. Wu, M. Hu, F. S. Ou, Z. Li, and R. S. Williams, "Cones fabricated by 3D nanoimprint lithography for highly sensitive surface enhanced Raman spectroscopy," *Nanotechnology*, vol. 21, no. 25, p. 255502, 2010.

[9] R. Alvarez-Puebla, B. Cui, J.-P. Bravo-Vasquez, T. Veres, and H. Fenniri, "Nanoimprinted SERS-active substrates with tunable surface plasmon resonances," *J. Phys. Chem. C*, vol. 111, no. 18, pp. 6720–6723, 2007.

[10] J. P. Singh, H. Chu, J. Abell, R. A. Tripp, and Y. Zhao, "Flexible and mechanical strain resistant large area SERS active substrates," *Nanoscale*, vol. 4, no. 11, pp. 3410–3414, 2012.

[11] S. B. Chaney, S. Shanmukh, R. A. Dluhy, and Y.-P. Zhao, "Aligned silver nanorod arrays produce high sensitivity surface-enhanced Raman spectroscopy substrates," *Appl. Phys. Lett.*, vol. 87, no. 3, p. 031908, 2005.

[12] Q. Zhou, Y. He, J. Abell, Z. Zhang, and Y. Zhao, “Optical properties and surface enhanced Raman scattering of L-shaped silver nanorod arrays,” *J. Phys. Chem. C*, vol. 115, no. 29, pp. 14131–14140, 2011.

[13] M. Geissler, K. Li, B. Cui, L. Clime, and T. Veres, “Plastic substrates for surface-enhanced Raman scattering,” *J. Phys. Chem. C*, vol. 113, no. 40, pp. 17296–17300, 2009.

[14] Y. Liu, J. Fan, Y.-P. Zhao, S. Shanmukh, and R. A. Dluhy, “Angle dependent surface enhanced Raman scattering obtained from a Ag nanorod array substrate,” *Appl. Phys. Lett.*, vol. 89, no. 17, p. 173134, 2006.

[15] C. L. Leverette, S. A. Jacobs, S. Shanmukh, S. B. Chaney, R. A. Dluhy, and Y.-P. Zhao, “Aligned silver nanorod arrays as substrates for surface-enhanced infrared absorption spectroscopy,” *Appl. Spectrosc.*, vol. 60, no. 8, pp. 906–913, 2006.

[16] B. T. Draine and P. J. Flatau, “Discrete-dipole approximation for periodic targets: theory and tests,” *J. Opt. Soc. Am. A*, vol. 25, no. 11, pp. 2693–2703, 2008.

[17] S. Li, M. L. Pedano, S.-H. Chang, C. A. Mirkin, and G. C. Schatz, “Gap structure effects on surface-enhanced Raman scattering intensities for gold gapped rods,” *Nano Lett.*, vol. 10, no. 5, pp. 1722–1727, 2010.

[18] J. D. Driskell, S. Shanmukh, Y. Liu, S. B. Chaney, X.-J. Tang, Y.-P. Zhao, and R. A. Dluhy, “The use of aligned silver nanorod arrays prepared by oblique angle deposition as surface-enhanced Raman scattering substrates,” *J. Phys. Chem. C*, vol. 112, no. 4, pp. 895–901, 2008.

[19] M. Kahraman, I. Sur, and M. Culha, “Label-free detection of proteins from self-assembled protein-silver nanoparticle structures using surface-enhanced Raman scattering,” *Anal. Chem.*, vol. 82, no. 18, pp. 7596–7602, 2010.

[20] K. Faulds, W. E. Smith, D. Graham, and R. J. Lacey, “Assessment of silver and gold substrates for the detection of amphetamine sulfate by surface enhanced Raman scattering (SERS),” *Analyst*, vol. 127, no. 2, pp. 282–286, 2002.

[21] M. Muniz-Miranda, C. Gellini, and E. Giorgetti, “Surface-enhanced Raman scattering from copper nanoparticles obtained by laser ablation,” *J. Phys. Chem. C*, vol. 115, no. 12, pp. 5021–5027, 2011.

[22] C. Kong, S. Sun, X. Zhang, X. Song, and Z. Yang, “Nanoparticle-aggregated hollow copper microcages and their surface-enhanced Raman scattering activity,” *CrystEngComm*, vol. 15, no. 31, pp. 6136–6139, 2013.

[23] Q. Shao, R. Que, M. Shao, L. Cheng, and S.-T. Lee, “Copper nanoparticles grafted on a silicon wafer and their excellent surface-enhanced Raman scattering,” *Adv. Funct. Mater.*, vol. 22, no. 10, pp. 2067–2070, 2012.

[24] D. Xu, Z. Dong, and J.-L. Sun, “Fabrication of copper nanowires by a solid-state ionics method and their surface enhanced Raman scattering effect,” *Mater. Lett.*, vol. 92, pp. 143–146, 2013.

[25] A. Zhao, T. Mei, X. Lin, L. Ni, and A. Wu, “Aligned copper nanorod arrays for surface-enhanced Raman scattering,” in *2007 International Conference on Information Acquisition*, 2007, pp. 79–82.

[26] M. A. Khan, T. P. Hogan, and B. Shanker, “Metallic nanorods synthesis and application in surface-enhanced Raman spectroscopy,” *J. Nano Syst. Technol.*, vol. 1, no. 1, pp. 1–11, 2009.

[27] C. Fang, A. Agarwal, K. D. Buddharaju, N. M. Khalid, S. M. Salim, E. Widjaja, M. V Garland, N. Balasubramanian, and D.-L. Kwong, “DNA detection using nanostructured SERS substrates with Rhodamine B as Raman label,” *Biosens. Bioelectron.*, vol. 24, no. 2, pp. 216–221, 2008.

[28] J. Chen, J. Jiang, X. Gao, J. Gong, G. Shen, and R. Yu, “Gold-aggregated, dye-embedded, polymer-protected nanoparticles (GDPNs): A new type of tags for detection with SERS,” *Colloids and Surfaces A: Physicochem. Eng. Asp.*, vol. 294, no. 1–3, pp. 80–85, 2007.

[29] Sigma-Aldrich, “Rhodamine B Isothiocyanate schematic.” [Online]. Available: http://www.sigmaaldrich.com/catalog/product/aldrich/283924?lang=en&region=GB. [Accessed: 19-May-2015].

Chapter 6 Conclusion and future work

This thesis has focussed on SERS of both metal nanoparticle-agarose gel and highly ordered metal nanorod arrays created via guided oblique angle deposition (OAD). The influence of nanoparticle growth conditions on gel structure and the associated SERS response was investigated. With respect to metal nanorod substrates, this thesis examined the use of large-scale, pre-patterned polymer as a template to tightly control nucleation and, in turn, the subsequent growth of Ag (and Cu) nanorods during OAD, to construct highly ordered, SERS-active nanorod arrays.

Chapter one laid out motivation for the research and examined, in detail, theoretical aspects underpinning the thesis. In chapter two, initial testing of Ag-agarose gel successfully replicated previous work in readily producing SERS of various molecular probes. SERRS of NBA at nanomolar concentrations was detected. The effect of silver nitrate feed solution concentration on the resultant nanoparticle morphology, gel homogeneity, SERS signal intensity and spot-to-spot signal variation was examined in depth. Initially, SERS signal strength increased approximately linearly as a function of feed concentration but then fluctuated with no further overall increase. TEM studies confirmed that this rise in lower-concentration gels was due mainly to a higher nanoparticle density along with a modest increase in aggregation. In higher-concentration gels, larger symmetric particles not only produced stronger SERS on their own, but tended to form large aggregates conducive to 'hotspot' formation, further increasing the signal. The overall increasing spot-to-spot signal variation was attributed to the increasing size distribution leading to a decrease in gel homogeneity. Generally, as the size %RSD rose, the less

homogeneous a sample was and the larger the spread in SERS measurements became. In addition, no appreciable rise in the number of larger particles after 150 mM $AgNO_3$ was evident which accounted for the subsequent lack of overall increase in SERS signal strength. La Mer's theory explained why lower-concentration gels had narrower size distributions than higher-concentration gels whose distributions were heavily skewed.

High-concentration Ag-agarose was fabricated using a fixed concentration of $AgNO_3$ and heavy excesses of $NaBH_4$, alongside lower concentrations of the reductant as a control. The aim was to construct gels which had undergone a short nucleation period, and thus possessed better uniformity. The greatest SERS intensity was observed when the $NaBH_4$ concentration was less than that of $AgNO_3$. Strangely, SERS intensity fell to zero at high $NaBH_4$ concentration and began to recover; this probably reflected increasing numbers of Ag nanoparticles being produced, as more nuclei were formed due to a high concentration of $NaBH_4$, but so many that there was now insufficient Ag^+ (aq) in the gel to act as a reservoir for growth, resulting in very small nanoparticles with reduced plasmonic activity and a concomitant reduction in signal strength.

While the concentration ratio of $NaBH_4$ to $AgNO_3$ (with a fixed $AgNO_3$ concentration) did influence gel reproducibility, overall, it remained poor whatever the molarity of borohydride, and it appeared that the concentration of *both* reactants must be reasonably low to maximise reproducibility. However, even at relatively low reactant concentrations, $NaBH_4$ may not turn out to be a good choice as regards reproducibility.

Chapter three investigated an adapted reduction method using high-pH hydroxylamine to produce Ag-agarose, comparable with sodium borohydride-reduced gel with respect to SERS intensity, but surpassing it in reproducibility. This suggests that the AgNP number density and the average particle size in both gels were fairly similar, but that the SB samples possessed a broader size distribution than their hydroxylamine counterparts.

The importance of characterising the system in terms of SERS prior to the analysis of a molecular probe was highlighted, as Raman bands arising solely from the substrate can become superimposed on the molecular spectrum, potentially confusing analysis. Citrate-reduced colloid was used alongside two common aggregating agents, sodium sulphate and sodium chloride, to illustrate how a Raman spectrum can suffer intrinsic distortion depending on the aggregating agent used. This is avoided when using metal-agarose gels which do not require aggregating agents to engage SERS activity.

As hydroxylamine-reduced Ag-agarose possessed significantly better signal uniformity than sodium borohydride-reduced Ag-agarose in chapter three, Au- and Ag-agarose gels in chapter four were produced using the adapted hydroxylamine-reduction technique in the low salt-concentration range of 1 – 10 mM. Low-concentration feed solutions generally give rise to gels with better uniformity, so it is important to understand how the SERS response develops within this range. SERS at 633 and 785 nm was conducted on the samples, and the SERS intensity examined as a function of salt concentration. With respect to the Ag samples, the strongest SERS signal was produced on average at 633 nm excitation. A simultaneous increase in number and decrease in size of NPs as a function of concentration

explained the substantially different plots for both 633 and 785 nm wavelengths. Regarding the Au gels, SERS intensity was only marginally greater overall at 785 nm compared with 633 nm.

Upon comparing Ag- and Au-agarose gels at 633 nm excitation, it was found that the intensity profiles were largely similar, which initially seemed puzzling as Ag nanoparticles generally provide a much larger Raman enhancement than Au nanoparticles in the visible region (at least up to ≈ 600-650 nm). The reason therefore must have been down to a particular size/arrangement of the AuNPs, such that it offset the expected higher Ag intensity. A comparison of gold and silver gels at 785 nm excitation, showed that Au-agarose produced on average by far the strongest SERS signal, so the best overall substrate, in terms of SERS intensity was Au-agarose at 785 nm excitation. No feed concentration in particular stood out as the overall winner, but as a rule of thumb, it is probably better to used gold salt concentrations below 5 mM, as the error bars are comparatively small suggesting better reproducibility.

SERS mapping of selected hydroxylamine-reduced Ag- and Au-agarose gels provided a rigorous evaluation of substrate uniformity, and confirmed that the hydroxylamine-reduction technique employed in this thesis is successful in the synthesis of reproducible metal-agarose gels. Mapping studies however, were limited to gels from one batch, so further experimentation is required to assess inter-batch repeatability before gels can be utilised confidently in applications.

Chapter five examined the role of metal nanorod arrays as SERS substrates. The relationship between deposition angle, film surface-roughness, porosity and

SERS intensity was examined, and it was found that film surfaces became rougher and porosity increased as the angle was widened. Only the sample deposited at 85^{o} exhibited a clear oblique columnar structure and was capable of generating SERS of BPE. Reflectance spectra confirmed the positive relation between porosity and surface roughness and deposition angle, and the high anisotropy of the 85^{o} nanorods.

A fabrication method using patterned polymer, for the production of highly ordered Ag and Cu nanorod arrays which, in principle, could circumvent the problems of gap size and diameter control was investigated. The polymer template tightly controlled the nucleation process during OAD, producing nanorod arrays which were highly SERS-active and reproducible. Despite only one nanopattern being employed in this work, the results highlighted that potentially, such templates could be created to desired specifications prior to rod deposition, to gain greater control over geometrical nanorod parameters which influence the SERS response.

Future work:

Although the results for SERS intensity and reproducibility concerning hydroxylamine-reduced metal nanoparticle agarose in chapters three and four are very encouraging, mapping results from chapter four related only to one batch and so further work is required to establish repeatability of the substrates, i.e. that reproducibility continues between batches using the described hydroxylamine-reduction technique. Moreover, gel formation must be tweaked in terms of the overall SERS response, using different salt and reducing solution concentrations; this is a matter of trial and error, although low-reactant concentration gels should be used

as these generally prove more reproducible. In addition to hydroxylamine, future work could focus on different reducing solutions, with a view to creating larger, more monodisperse particles which should create a stronger SERS signal with less variation. In addition, metal salt solution and subsequent reducing solution could be introduced to molten agarose to observe the effects of temperature on NP size and dispersity. As temperature rises, the nucleation rate increases, but a detailed examination of gel formation at elevated temperature is required to better understand the impact of altering this parameter during gel synthesis. This should further optimise a substrate which already holds great potential for SERS analysis.

With respect to highly ordered metal nanorod arrays, although only one nanopattern was employed in the work, potentially, such templates could be created to desired specifications before rod deposition. Future studies could focus on optimisation of polymer template design and, in turn, plasmonic characteristics to maximize SERS capability. Work might begin on Cu-polymer arrays, as although these do not produce as strong a signal as their Ag-polymer counterparts, there are obvious economic incentives for further research into these substrates, as copper is considerably cheaper than silver or gold. Moreover, there remains the potential to influence geometrical nanorod parameters via template design, potentially leading to a much-improved SERS performance in the case of Cu arrays.

Publications and presentations

1. M. Keating, S. Song, G. Wei, D. Graham, Y. Chen, and F. Placido, "Ordered silver and copper nanorod arrays for enhanced Raman scattering created via guided oblique angle deposition on polymer," *J. Phys. Chem. C*, vol. 118, no. 9, pp. 4878–4884, 2014.

2. M. Keating, Y. Chen, I. A. Larmour, K. Faulds, and D. Graham, "Growth and surface-enhanced Raman scattering of Ag nanoparticle assembly in agarose gel," *Meas. Sci. Technol.*, vol. 23, no. 8, p. 084006, 2012.

3. S. Song, M. Keating, Y. Chen, and F. Placido, "Reflectance and surface enhanced Raman scattering (SERS) of sculptured silver films deposited at various vapor incident angles", *Meas. Sci. Technol.*, vol. 23, no. 8, p. 084007, 2012.

4. M. Keating, Y. Chen, I. A. Larmour, K. Faulds, and D. Graham, "Silver nanoparticle assembly in agarose gel for surface-enhanced Raman scattering (SERS)," *Nano Meets Spectroscopy Conference*, 2012.

THE JOURNAL OF PHYSICAL CHEMISTRY C

Article

pubs.acs.org/JPCC

Ordered Silver and Copper Nanorod Arrays for Enhanced Raman Scattering Created via Guided Oblique Angle Deposition on Polymer

M. Keating,[†] S. Song,[‡] G. Wei,[†,§] D. Graham,[∥] Y. Chen,*[,†] and F. Placido[‡]

[†]Photophysics Group, Centre for Molecular Nanometrology, Department of Physics, SUPA, University of Strathclyde, John Anderson Building, 107 Rottenrow, Glasgow G4 0NG, U.K.

[‡]Thin Film Centre, SUPA, University of the West of Scotland, Ayr KA8 0SX, U.K.

[§]Department of Physics, Beihang University, Beijing 100191, China

[∥]Centre for Molecular Nanometrology, WestCHEM, Department of Pure and Applied Chemistry, University of Strathclyde, Glasgow G1 1XL, U.K.

Supporting Information

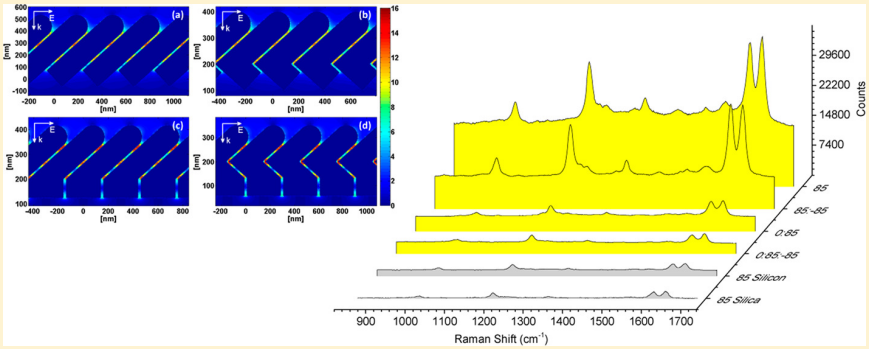

ABSTRACT: We report the manufacture of ordered silver and copper nanorod arrays for surface-enhanced Raman scattering using oblique angle deposition (OAD) on prepatterned polymer sheets. It was found that the patterned polymer substrate defined nucleation sites which guided subsequent growth of nanorods. Enhanced surface-enhanced Raman spectroscopy (SERS) intensities of the Raman probe molecule *trans*-1,2-bis(4-pyridyl)ethylene (BPE) were found for Ag arrays on polymer, up to about 10 times that of the Ag−silica control. The SERS response of Ag nanorod arrays of different structures was investigated alongside results obtained from discrete dipole approximation simulations. This revealed that narrow gaps between nanorods, formed by guided nucleation during OAD, were responsible for this dramatic enhancement. Ordered Cu nanorod arrays were also successfully fabricated, producing a SERS intensity about 3 times that of Cu on silicon for both BPE and another Raman probe—rhodamine B isothiocyanate (RBITC)—highlighting the potential of this large-scale, low-cost, SERS-active substrate.

INTRODUCTION

Surface-enhanced Raman spectroscopy (SERS) combines molecular fingerprint specificity with potential single-molecule sensitivity and so is an attractive tool in biological sensing and chemical analysis. To establish SERS as a routine analytical tool, however, it is essential to produce powerful, reproducible SERS-active substrates in a cost-effective way. Tremendous efforts have been made in the past decade to develop various effective SERS substrates. Using numerous fabrication methods, a wide range of metallic nanostructures can be produced,[1−3] DNA-conjugated nanoparticle clusters,[4] nanoparticle arrays formed through molecular self-recognition,[5] and nanoparticle self-assembly within a matrix.[6,7] Alternatively, metallic films of various structures have also been created for use in SERS applications. In particular, aligned Ag nanorod arrays created by oblique angle deposition (OAD) have recently been demonstrated to be highly effective SERS substrates.[8−11] Producing strong SERS with high sensitivity, these arrays also show good reproducibility in signal strength and can be fabricated with substantial uniform areas for applications such as sensing. In addition, the OAD approach is relatively straightforward compared with other methods employed to generate nanostructured arrays, such as photolithography or electron beam lithography (EBL), and avoids the time-consuming, complex, and expensive steps inherent in those methods.[12,13] Ag nanorods have also been applied successfully in "real world" applications, for example, in the detection and differentiation of several human pathogens.[14] However, despite their obvious success, it has proved difficult to control the gap size and diameter of nanorods during OAD fabrication, hindering the optimization of geometrical parameters which directly affect the SERS response.

Received: October 11, 2013
Revised: February 11, 2014
Published: February 11, 2014

dx.doi.org/10.1021/jp410116h | *J. Phys. Chem. C* 2014, 118, 4878−4884

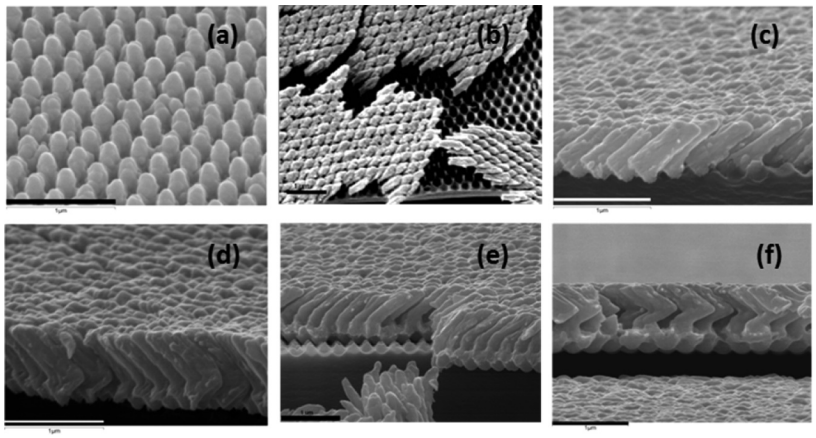

Figure 1. SEM images of Ag nanorod arrays on polymer films prepared under (a) 0° deposition, (b) 85° deposition (top view), (c) 85° deposition (cross-section), (d) 85°:−85° deposition, (e) 0°:85° deposition, and (f) 0°:85°:−85° deposition. The scale bar in each image represents 1 μm. Note: parts of arrays were lifted off when the samples were cut to create cross-sections.

The dimensions of nanorod arrays are initially influenced by nucleation, which is a random process on flat substrates, meaning nanorods created by OAD are randomly distributed. To obtain a high-order nanorod array via the suppression of random nucleation events during OAD, Liu et al. used two-dimensional Au nanopost arrays manufactured using EBL, where the posts acted as periodically arranged shadowing centers during Ag deposition. While a dependence of the SERS response on gap size and diameter was found, the arrays produced were only semiordered. Moreover, the size of the arrays was very small (50 μm × 50 μm),[15] which is not suitable for sensing applications.

In this work, we demonstrate for the first time the application of a polycarbonate sheet, prepatterned using nanoimprint lithography (NIL), as a large-area, highly uniform template to tightly control the nucleation process during OAD and, in turn, the subsequent growth of ordered metallic nanorod arrays for SERS. Guided nucleation makes optimization of SERS possible, based on template design which steers gap size and diameter toward the most favorable values.

■ EXPERIMENTAL SECTION

Materials. The materials used were silver and copper (99.99%, Kurt J. Lesker and Co.), BPE (Sigma Aldrich; assay, 97%), and RBITC (Sigma Aldrich); polycarbonate sheets were prototypes supplied courtesy of MacDermid Autotype Ltd.

Nanoimprinted Polycarbonate. Polycarbonate sheets (A4 size) with an inverted hemispherical structure in a closely packed hexagonal arrangement (SEM image in Figure.S1 of the Supporting Information), fabricated using nanoimprint lithography were used as received. Nanoimprinted polymers have been employed previously in generating plasmonic structures[16−18] via the deposition of metallic layers on patterned polymer. Flat polymer bases have also been used, in Ag nanorod OAD for example, to create flexible, large-area SERS substrates resistant to mechanical strain which could potentially be used as flexible SERS "labels".[19] Underlying polymer layers, patterned or flat, can generate highly reproducible and high-throughput SERS substrates at low cost. In this work the polymer serves as a seed template during OAD.

Oblique Angle Deposition of Ag and Cu Nanorod Arrays. Nanorod fabrication using OAD has been described in detail elsewhere.[20,21] Briefly, polycarbonate substrates, cut to approximately 10 × 13 mm^2 and adhered to glass slides, were loaded for metal deposition, together with silicon, silica, or glass substrates for comparison. A Satis e-beam evaporation system was used for thin film deposition, with the chamber vacuum maintained at about 1 × 10^{-6} Torr. Deposition along the surface normal (0°) resulted in conformal growth and an ordered Ag nanorod array as shown in Figure 1a (also large scale in Figure.S2 of the Supporting Information).

Before oblique angle deposition, a 10 nm layer of the respective metal (monitored by a quartz crystal microbalance) was deposited onto the substrates in the normal direction to increase nanorod adhesion. This thin metallic layer also serves to protect the polymer from laser illumination while simultaneously blocking the polymer background signal during a Raman measurement.[22] OAD was then performed at 85° with a nominal growth rate of 0.2 nm s^{-1}. Micrographs of thus manufactured nanorod arrays were taken using a scanning electron microscope (SEM; Hitachi S-4100).

SERS of Ag and Cu Nanorod Arrays. Prior to SERS analysis, all Ag and Cu substrates were immersed overnight in an aqueous solution of BPE (10^{-5} M for Ag and 10^{-4} M for Cu), a common SERS probe, and then dried in an N_2 stream. Ten and 20 spectra were collected for Ag and Cu, respectively, from the entire surface of each substrate (about 1 cm^2) using a Renishaw Ramascope System 2000 with the 632.8 nm line of a helium−neon laser as the excitation source. Unfocused output power at the sample was measured to be approximately 3.2 and 3.5 mW, with collection times of 0.1 and 30 s for Ag and Cu, respectively. (More details are in the Supporting Information).

SERS mapping of Cu substrates with 1.156 × 10^{-5} M (aq) rhodamine B ITC was conducted on a Witec confocal Raman microscope alpha300 R at 632.8 nm excitation, with a 2.5 s collection time and an unfocused power at the sample of 24.3 mW. Mapping of Cu polymer and Si arrays with 10^{-5} M methanolic BPE was carried out on a DXR Raman microscope (Thermo Scientific) using 780 nm excitation and a 50× objective with a 1 s collection time. (More details are in the Supporting Information).

With regard to optimal sample excitation, it has been reported previously that incident angle and polarization of the laser beam with respect to nanorod direction may influence SERS signal strength.[23,24] This however is not the subject of the current study, and in order to reduce the number of variables,

dx.doi.org/10.1021/jp410116h | J. Phys. Chem. C 2014, 118, 4878−4884

all substrates were treated equally with a fixed angle of 0° between the substrate plane and the **E**-vector, and also between the longitudinal planes of the nanorods and the **E**-vector.

RESULTS AND DISCUSSION

Ag Nanorod Arrays. Figure 1b shows a SEM image of the nanorod array (note that parts of the arrays have become dislocated from the underlying polymer during preparation for SEM imaging). Ordered arrangement of the array following a hexagonal polymer pattern, in contrast to random nanorods grown on a silicon surface (Figure S4 of the Supporting Information), confirms that guided nucleation of nanorods has taken place. Figure 1c shows a SEM image of a cross-section of a nanorod array on polymer. The diameter of the rods is about 187 nm and the length about 750 nm. Subsequent depositions at 85° and −85° (denoted by 85°:−85°) resulted in a zigzag rod structure, as shown in Figure 1d. Two other nanostructured arrays were produced by growing tilted (85°) and zigzag (85°:−85°) nanorods on short vertical bases (denoted by 0°:85° and 0°:85°:−85° and shown in Figure 1e,f, respectively).

Figure 2a shows typical SERS spectra of BPE on ordered 85°:−85° and 85° Ag nanorod arrays on polymer (B and C, respectively) in comparison with 85° Ag nanorod arrays on silica (A); the most prominent vibrational modes of BPE appear at 1200, 1607, and 1637 cm^{-1} corresponding to the C=C stretching, aromatic ring stretching, and in-plane ring modes, respectively.[25]

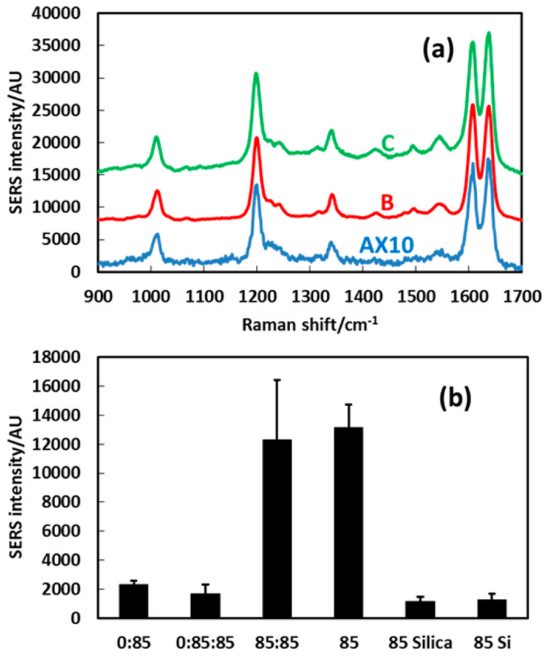

Figure 2. (a) Representative SERS spectra of BPE on Ag nanorods (excitation, 632.8 nm; acquisition time, 0.1 s): (A) 85° silica control; (B) 85°:−85° polymer; (C) 85° polymer. (b) Average intensity of 1200 cm^{-1} peak over 10 spectra from various Ag nanorod arrays as labeled.

It is clear from Figure 2 that both arrays on polymer generate a strong SERS signal, up to about 10 times that of the other polymer substrates and the silica control. In terms of reproducibility, the 85° and 0:85° arrays have comparably low relative standard deviations (RSDs) of 11.8% and 10.3%, respectively, which are better than the 24.4% for 85° arrays on silica, 34.0% on silicon, and 33.4% for the 85°:−85° array on polymer. The 85° array on polymer therefore surpasses all others when SERS intensity and reproducibility are considered in conjunction. Good reproducibility also qualifies the 85° polymer array for SERS detection and identification purposes.[26]

All arrays, excepting 0°, have similar diameters and overall lengths as confirmed by SEM images. Their overall surface areas are comparable as shown in Figure S5 of the Supporting Information, meaning there is no significant correspondence between SERS signal strength and nanorod surface area in this case.

Simulations. The nanorod array of 0° deposition on polymer (Figure 1a) produces a weak but definite SERS spectrum of BPE, 250 times weaker than does 85° deposition on polymer, while, in contrast, 0° rods on silicon produce none at all (Figure.S6 of the Supporting Information). Our previous study found that the porosity of Ag film on planar silicon decreases dramatically when the deposition angle is reduced from 85° to 75°, resulting in no discernible SERS of BPE at 75° or less.[27] It is not surprising therefore that 0° deposition on planar silicon generates no SERS. However, this cannot account for the substantial differences in signal strength between vertical nanorod arrays (0°), arrays supported by vertical bases (0°:85°, 0°:85°:−85°), and tilted arrays (85° and 85°:−85°).

To understand the SERS effect in terms of the electromagnetic (EM) enhancement mechanism, the local fields of infinite Ag nanorod arrays were simulated using the discrete dipole approximation (DDA) method, employing DDSCAT 7.2 code.[28−31] The dielectric constants of Ag were obtained from the experimental data of Johnson and Christy[32] without size corrections, as the size dependence can be neglected in our studies. The value of the interaction cutoff parameter γ was taken to be 0.01. Five target units, corresponding to 85°, 85°:−85°, 0°, 0°:85°, and 0°:85°:−85° arrays, were calculated using geometrical parameters shown in Figure S7 of the Supporting Information. The orientation of the oblique nanorods was chosen to be along the *y*-direction, and the tilted angle was set to 42°. The upper oblique parts of the nanorods were modeled as tilted cylinders with a hemispherical cap at each end, to smooth sharp edges and so avoid the "lightning rod effect". Gaps between adjacent nanorods were 111 nm for 0° arrays (estimated from SEM measurements) and 21 nm for other arrays. The total lengths of individual nanorods were all fixed to be 750 nm in order to investigate the structural effect on the near-field properties. The polarization of incident light was parallel to the *y*-direction.

Figure 3 shows the magnitude of the normalized electric field, when 85°, 85°:−85°, 0°:85° and 0°:85°:−85° arrays are excited at 632.8 nm. $g = |E|/|E_0|$ is the enhancement factor, where E and E_0 are the local and incident fields, respectively. Regions of strong EM enhancement (commonly known as "hotspots") are found in the gaps between adjacent nanorods in all of the polymer arrays, with the exception of the 0° array which produces by far the least enhancement due to a relatively large gap size which promotes weaker coupling between neighboring nanorods (Figure S8 of the Supporting Information). At nanoparticle surfaces, the electromagnetic enhancement factor (EF) in SERS is proportional to g^4. To help explain our results, we calculated the average EF over the surface area of an Ag rod, $\langle EF \rangle = \int g^4 \, ds / \int ds$.[33] Note that the g^4 value was calculated half a grid point away from each exposed cube surface. The average enhancement factors of 85° and 85°:−85°

dx.doi.org/10.1021/jp410116h | J. Phys. Chem. C 2014, 118, 4878−4884

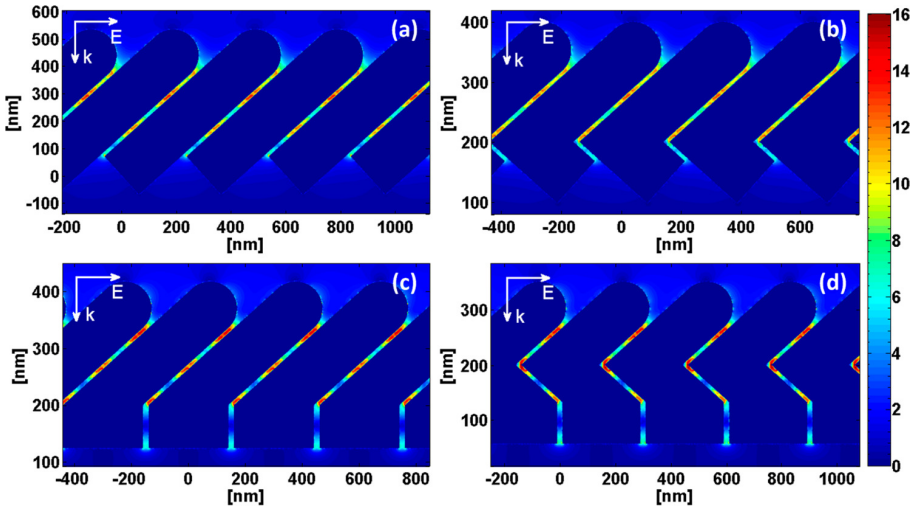

Figure 3. Magnitude of normalized electric field, $g = |E|/|E_0|$, where E and E_0 are the local and incident fields, respectively, of (a) 85°, (b) 85°:−85°, (c) 0°:85°, and (d) 0°:85°:−85° arrays. All internal fields were set to zero for clarity.

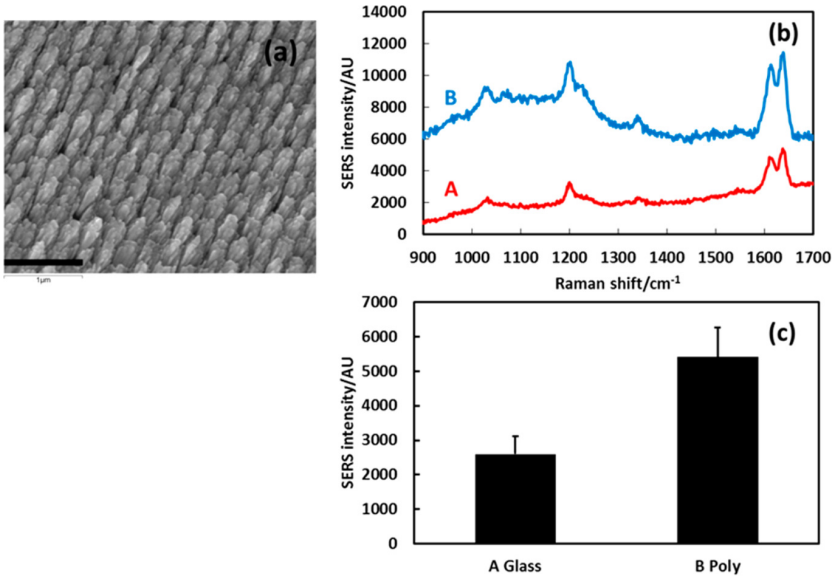

Figure 4. (a) SEM image of 671 nm Cu nanorod array created under 85° deposition on polymer showing ordered arrangement; The scale bar represents 1 μm. (b) Representative SERS spectra of BPE on (A) Cu array on glass (Cu−glass) and (B) Cu array on polymer (Cu−polymer). (c) Average intensity of 1636 cm^{-1} peak over 20 spectra from Cu nanorod arrays as labeled.

arrays, 438 and 459, respectively, are comparable to each other and in line with experimental results. The slightly higher EF of the 85°:−85° array may be due to the sharp corners where the rods bend in the simulation structures. A much smaller EF of 29 was found for the 0° array, also consistent with Raman measurements. Calculation of 0°:85° and 0°:85°:−85° arrays, however, generate EFs of 575 and 696, respectively, higher than those of the 85° and 85°:−85° arrays. This inconsistency is due to the discrepancy in gap sizes between simulation structures and actual arrays. The magnitude of EM enhancement strongly depends on gap size, as shown in Figure S9 of the Supporting Information. In the experiment, the diameter of real vertical rods, approximately 182 nm (resulting from conformal growth under 0° deposition) was smaller than that used in the simulation (279 nm), resulting in larger gaps and a weaker EM field strength. Taking this into account, the calculations show a relatively weak EM enhancement from the 0°:85° array compared with the 85° array (Figure S10 of the Supporting Information). Therefore, in this guided OAD approach, the inverted hemispherical hexagonal pattern on polymer defines the periodic arrangement of the nanorod array and OAD produces tilted thick rods, resulting in narrow gaps between adjacent rods and in turn, a dramatic enhancement of the EM field. The dependence of rod size and associated plasmonic properties on polymer template dimensions needs further investigation.

For 85° polymer arrays, BPE spectra taken under both 633 and 785 nm excitations show that the SERS intensity at 633 nm is about 5 times that at 785 nm (Figure S11 of the Supporting Information). Supporting Information Figure S12 shows the magnitude of the normalized electric field of Ag nanorod arrays under different excitations simulated using DDA. The average

dx.doi.org/10.1021/jp410116h | J. Phys. Chem. C 2014, 118, 4878−4884

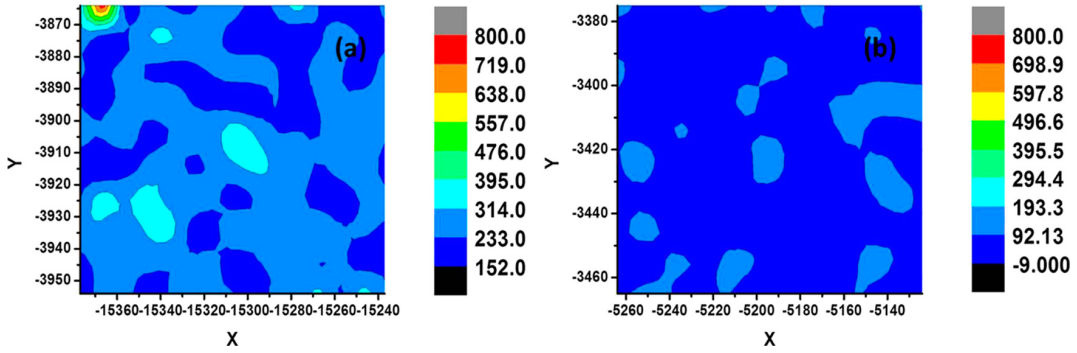

Figure 5. SERS maps of BPE (10^{-5} M) on (a) Cu−polymer and (b) Cu−Si. Each map corresponds to an area on the substrate of 90 × 140 μm^2, with the height of the 1636 cm^{-1} peak being used and 150 spectra collected.

enhancement factors were found to be 437 and 336 for excitations at 633 and 785 nm, respectively, which is in line with experimental results. The influence of excitation wavelength on SERS of Ag nanorod arrays depends on their geometric structures as well as the nature of the probe molecule under consideration. Further investigation is required to reveal the mechanism behind the different enhancements.

Cu Nanorod Arrays. A number of metals have been employed successfully in SERS, the most common being silver, gold, and copper.[34] Although the SERS signal is generally weaker when it is employed, copper is nonetheless highly attractive as a SERS metal, as it has a scrap value much less than that of either silver or gold. Recently, great efforts have been made to construct Cu based SERS-active platforms, including, for example, nanowires, nanoparticles, and hollow copper microcages.[35−38] Zhao et al. synthesized SERS-active vertical Cu nanorods using potentiostatic electrodeposition inside nanochannels of porous anodic alumina membrane (PAAM),[39] while SERS-active Cu nanorod arrays were created via OAD on glass slides by Kahn et al.[40]

Given the effectiveness of Ag polymer substrates, we fabricated copper nanorod arrays on polymer using this guided OAD approach. An ordered array was created, as shown in Figure 4a. Substrates were immersed overnight in aqueous BPE (10^{-4} M) and interrogated using 633 nm excitation. Figure 4b shows typical SERS spectra of BPE for Cu nanorod arrays of 671 nm length on polymer substrate and on glass as a control. Twenty spectra were collected from each substrate. The array on polymer produces a SERS signal strength about twice that of the Cu−glass control as seen in 4c and the substrates have RSDs of 15.6% and 20.2%, respectively.

The effectiveness of Cu nanorod arrays on polymer substrates was further confirmed by SERS mapping of BPE, as shown in Figure 5. A 2 μL aliquot of BPE in methanol (10^{-5} M) was placed on Cu−Si and Cu−polymer substrates and allowed to dry before SERS analysis. Each map corresponds to an area on the substrate of 90 × 140 μm^2, with the 1636 cm^{-1} peak height used and 150 spectra collected. Mapping results averaged from 750 spectra from each substrate indicate that the Cu array on polymer (Cu−polymer) generates an average SERS intensity about 3 times that of the Cu silicon substrate (Cu−Si). Cu−polymer also shows good reproducibility at 23.9%, which is better than that of Cu−Si (32.5%)

In addition to BPE, another common SERS probe, RBITC(aq) (1.156 × 10^{-5} M) was used to test the Cu−polymer substrate. Figure 6a shows SERS spectra of RBITC on Cu−polymer and Cu−Si substrates, each averaged from 800

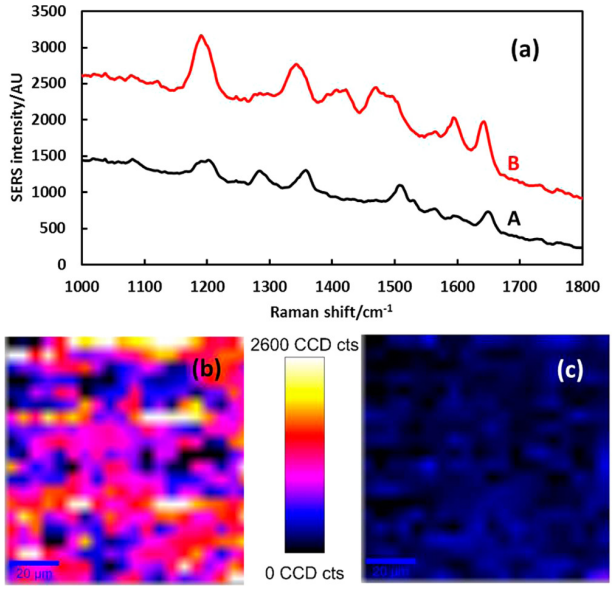

Figure 6. (a) SERS spectra of RBITC on (A) Cu nanorod arrays on Si substrate (Cu−Si) and (B) Cu nanorod arrays on polymer substrate (Cu−polymer). (b) SERS mapping (from 400 spectra) of RBITC on Cu−polymer and on (c) Cu−Si substrate. Each map corresponds to an area on the substrate of 100 × 100 μm^2 with an excitation wavelength of 633 nm. The substrate was immersed in 1.156 × 10^{-5} M (aq) RBITC for 15 min and then dried in N_2 before SERS measurement.

individual spectra collected from mapping, where characteristic peaks match those described in the literature.[41]

Integrated peak intensity of the 1200 cm^{-1} band for the Cu−polymer substrate is about 3 times that of its Cu−Si counterpart along with a good reproducibility of 11.0% as observed from SERS mapping, Figure 6b,c. It is worth pointing out that although the improvement in SERS performance in the case of copper is not as significant as that of silver, the possibility of manufacturing nanorod arrays with designed gaps and diameters using this guided OAD method should allow further structural optimization. This added to the low cost of polymer substrates makes this novel method an attractive approach for fabricating large-scale, highly effective SERS-active substrates.

Another Cu nanorod polymer array of rod length 989 nm was manufactured, with the height of the 1636 cm^{-1} band averaged from 20 BPE spectra. This array produces a SERS

dx.doi.org/10.1021/jp410116h | J. Phys. Chem. C 2014, 118, 4878−4884

signal strength about 2.5 times that of the Cu−glass control, and about half that of the 671 nm polymer array, with a RSD of 11.6%. The magnitude of the normalized electric field of Cu nanorod arrays of both lengths was simulated using DDA, the results for which are illustrated in Figure 7. The average

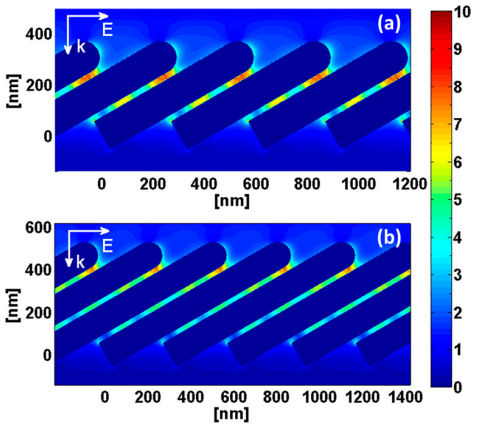

Figure 7. Magnitude of normalized electric field, $g = |E|/|E_0|$, where E and E_0 are the local and incident fields, respectively, of Cu nanorod arrays of (a) 671 and (b) 989 nm length (diameter ∼ 127 nm; tilted angle ∼ 30°, as taken from SEM measurements). The dielectric constants of Cu were from Johnson and Christy.[32] All internal fields were set to zero for clarity.

enhancement factors of 671 and 989 nm arrays were found to be 83.5 and 52.7, respectively, which is consistent with experimental results. This suggests that SERS intensity is not simply proportional to rod surface area and that aspect ratio changes which give control over the longitudinal and transverse plasmons play an important role. Therefore it is possible to optimize rod length for the best SERS effect.

CONCLUSION

In summary, we have demonstrated a proof-of-principle fabrication method for highly ordered nanorod arrays which, in principle, could circumvent the problems of gap size and diameter control. The polymer template tightly controls the nucleation process during OAD, producing nanorod arrays which are highly SERS-active and reproducible. In the case of Ag, an enhanced SERS intensity about 10 times that of the Ag−silica control was observed for the 85° Ag−polymer array. The SERS response of Ag−polymer arrays was compared to results obtained from discrete dipole approximation simulations, which revealed that narrow gaps between nanorods, formed by this guided nucleation approach, were responsible for this dramatic enhancement. Ordered Cu−polymer arrays were also successfully fabricated, which, likewise, exhibited strong SERS combined with good reproducibility, as confirmed via mapping studies of BPE and RBITC. Although we employ only one nanopattern in this experiment, the results highlight that potentially such templates could be created to desired specifications before rod deposition. Future studies could focus on optimization of polymer template design and, in turn, plasmonic characteristics to maximize SERS performance. This work opens the door not only to an efficient, cheap, and reproducible method of producing high-quality, high-order nanorod arrays as SERS substrates but to their wider application in other areas such as nanophotonic devices and solar cells.

ASSOCIATED CONTENT

Supporting Information

Text describing further experimental details and numerical calculations, figures showing SEM images of bare polymer, 0° Ag on polymer, and 85° Ag on Si, 2-D Ag nanorod surface areas as measured from SEM, SERS spectra, simulation structures, and magnitudes of normalized electric field. This material is available free of charge via the Internet at http://pubs.acs.org.

AUTHOR INFORMATION

Corresponding Author

*Tel.: +44 (0)141 548 3087. E-mail: y.chen@strath.ac.uk.

Notes

The authors declare no competing financial interest.

ACKNOWLEDGMENTS

We thank Dr. S. Mabbott for his assistance in experimental work. M.K. acknowledges the financial support of an EPSRC Doctoral Training Grant. G.W. thanks the China Scholarship Council (CSC) for financial support. Simulation results were obtained using the EPSRC funded ARCHIE-WeSt High Performance Computer (www.archie-west.ac.uk; EPSRC Grant No. EP/K000586/1).

REFERENCES

(1) Willets, K. A.; Van Duyne, R. P. Localized Surface Plasmon Resonance Spectroscopy and Sensing. *Annu. Rev. Phys. Chem.* **2007**, *58*, 267−297.

(2) Li, J. F.; Huang, Y. F.; Ding, Y.; Yang, Z. L.; Li, S. B.; Zhou, X. S.; Fan, F. R.; Zhang, W.; Zhou, Z. Y.; Wu, D. Y. Shell-Isolated Nanoparticle-Enhanced Raman Spectroscopy. *Nature* **2010**, *464*, 392−395.

(3) Camden, J. P.; Dieringer, J. A.; Wang, Y. M.; Masiello, D. J.; Marks, L. D.; Schatz, G. C.; Van Duyne, R. P. Probing the Structure of Single-Molecule Surface-Enhanced Raman Scattering Hot Spots. *J. Am. Chem. Soc.* **2008**, *130*, 12616−12617.

(4) Graham, D.; Thompson, D. G.; Smith, W. E.; Faulds, K. Control of Enhanced Raman Scattering Using a DNA-Based Assembly Process of Dye-Coded Nanoparticles. *Nat. Nanotechnol.* **2008**, *3*, 548−551.

(5) Sisco, P. N.; Murphy, C. J. Surface-Coverage Dependence of Surface-Enhanced Raman Scattering from Gold Nanocubes on Self-Assembled Monolayers of Analyte. *J. Phys. Chem. A* **2009**, *113*, 3973−3978.

(6) Mahmoud, M. A.; Tabor, C. E.; El-Sayed, M. A. Surface-Enhanced Raman Scattering Enhancement by Aggregated Silver Nanocube Monolayers Assembled by the Langmuir−Blodgett Technique at Different Surface Pressures. *J. Phys. Chem. C* **2009**, *113*, 5493−5501.

(7) Keating, M.; Chen, Y.; Larmour, I. A.; Faulds, K.; Graham, D. Growth and Surface-Enhanced Raman Scattering of Ag Nanoparticle Assembly in Agarose Gel. *Meas. Sci. Technol.* **2012**, *23*, No. 084006.

(8) Driskell, J. D.; Shanmukh, S.; Liu, Y.; Chaney, S. B.; Tang, X.-J.; Zhao, Y.-P.; Dluhy, R. A. The Use of Aligned Silver Nanorod Arrays Prepared by Oblique Angle Deposition as Surface Enhanced Raman Scattering Substrates. *J. Phys. Chem. C* **2008**, *112*, 895−901.

(9) Liu, Y.-J.; Zhang, Z.-Y.; Zhao, Q.; Dluhy, R. A.; Zhao, Y.-P. Surface Enhanced Raman Scattering from an Ag Nanorod Array Substrate: The Site Dependent Enhancement and Layer Absorbance Effect. *J. Phys. Chem. C* **2009**, *113*, 9664−9669.

(10) Liu, Y.-J.; Chu, H. Y.; Zhao, Y.-P. Silver Nanorod Array Substrates Fabricated by Oblique Angle Deposition: Morphological, Optical, and SERS Characterizations. *J. Phys. Chem. C* **2010**, *114*, 8176−8183.

(11) Song, C.; Abell, J. L.; He, Y.; Murph, S. H.; Cui, Y.; Zhao, Y. Gold-Modified Silver Nanorod Arrays: Growth Dynamics and Improved SERS Properties. *J. Mater. Chem.* **2012**, *22*, 1150−1159.
(12) Vossen, D. L. J.; Fific, D.; Penninkhof, J.; van Dillen, T.; Polman, A.; van Blaaderen, A. Combined Optical Tweezers/ion Beam Technique to Tune Colloidal Masks for Nanolithography. *Nano Lett.* **2005**, *5*, 1175−1179.
(13) Plaza, J. L.; Chen, Y.; Jacke, S.; Palmer, R. E. Nanoparticle Arrays Patterned by Electron-Beam Writing: Structure, Composition, and Electrical Properties. *Langmuir* **2005**, *21*, 1556−1559.
(14) Driskell, J. D.; Shanmukh, S.; Liu, Y.-J.; Hennigan, S.; Jones, L.; Zhao, Y.-P.; Dluhy, R. A.; Krause, D. C.; Tripp, R. A. Infectious Agent Detection With SERS-Active Silver Nanorod Arrays Prepared by Oblique Angle Deposition. *IEEE Sens. J.* **2008**, *8*, 863−870.
(15) Liu, Y.-J.; Zhang, Z.-Y.; Dluhy, R. A.; Zhao, Y.-P. The SERS Response of Semiordered Ag Nanorod Arrays Fabricated by Template Oblique Angle Deposition. *J. Raman Spectrosc.* **2010**, *41*, 1112−1118.
(16) Boltasseva, A. Plasmonic Components Fabrication via Nanoimprint. *J. Opt. A: Pure Appl. Opt.* **2009**, *11*, 114001.
(17) Wu, W.; Hu, M.; Ou, F. S.; Li, Z.; Williams, R. S. Cones Fabricated by 3D Nanoimprint Lithography for Highly Sensitive Surface Enhanced Raman Spectroscopy. *Nanotechnology* **2010**, *21*, 255502.
(18) Alvarez-Puebla, R.; Cui, B.; Bravo-Vasquez, J.-P.; Veres, T.; Fenniri, H. Nanoimprinted SERS-Active Substrates with Tunable Surface Plasmon Resonances. *J. Phys. Chem. C* **2007**, *111*, 6720−6723.
(19) Singh, J. P.; Chu, H.; Abell, J.; Tripp, R. A.; Zhao, Y. Flexible and Mechanical Strain Resistant Large Area SERS Active Substrates. *Nanoscale* **2012**, *4*, 3410−3414.
(20) Chaney, S. B.; Shanmukh, S.; Dluhy, R. A.; Zhao, Y.-P. Aligned Silver Nanorod Arrays Produce High Sensitivity Surface-Enhanced Raman Spectroscopy Substrates. *Appl. Phys. Lett.* **2005**, *87*, 031908.
(21) Zhou, Q.; He, Y.; Abell, J.; Zhang, Z.; Zhao, Y. Optical Properties and Surface Enhanced Raman Scattering of L-Shaped Silver Nanorod Arrays. *J. Phys. Chem. C* **2011**, *115*, 14131−14140.
(22) Geissler, M.; Li, K.; Cui, B.; Clime, L.; Veres, T. Plastic Substrates for Surface-Enhanced Raman Scattering. *J. Phys. Chem. C* **2009**, *113*, 17296−17300.
(23) Liu, Y.; Fan, J.; Zhao, Y.-P.; Shanmukh, S.; Dluhy, R. A. Angle Dependent Surface Enhanced Raman Scattering Obtained from a Ag Nanorod Array Substrate. *Appl. Phys. Lett.* **2006**, *89*, 173134.
(24) Leverette, C. L.; Jacobs, S. A.; Shanmukh, S.; Chaney, S. B.; Dluhy, R. A.; Zhao, Y.-P. Aligned Silver Nanorod Arrays as Substrates for Surface-Enhanced Infrared Absorption Spectroscopy. *Appl. Spectrosc.* **2006**, *60*, 906−913.
(25) Yang, W.; Hulteen, J.; Schatz, G. C.; Van Duyne, R. P. A Surface-Enhanced Hyper-Raman and Surface-Enhanced Raman Scattering Study of Trans-1,2-bis(4-Pyridyl)ethylene Adsorbed Onto Silver Film Over Nanosphere Electrodes. Vibrational Assignments: Experiment and Theory. *J. Chem. Phys.* **1996**, *104*, 4313−4323.
(26) Kahraman, M.; Sur, I.; Culha, M. Label-Free Detection of Proteins from Self-Assembled Protein-Silver Nanoparticle Structures Using Surface-Enhanced Raman Scattering. *Anal. Chem.* **2010**, *82*, 7596−7602.
(27) Song, S.; Keating, M.; Chen, Y.; Placido, F. Reflectance and Surface Enhanced Raman Scattering (SERS) of Sculptured Silver Films Deposited at Various Vapor Incident Angles. *Meas. Sci. Technol.* **2012**, *23*, 084007.
(28) Draine, B. T.; Flatau, P. J. Discrete-Dipole Approximation for Scattering Calculations. *J. Opt. Soc. Am. A* **1994**, *11*, 1491−1499.
(29) Draine, B. T.; Flatau, P. J. Discrete-Dipole Approximation for Periodic Targets: Theory and Tests. *J. Opt. Soc. Am. A* **2008**, *25*, 2693−2703.
(30) Flatau, P. J.; Draine, B. T. Fast Near Field Calculations in the Discrete Dipole Approximation for Regular Rectilinear Grids. *Opt. Express* **2012**, *20*, 1247−1252.
(31) Draine, B. T.; Flatau, P. J. *User Guide for the Discrete Dipole Approximation Code DDSCAT 7.2*, http://arxiv.org/abs/1202.3424 (accessed Mar. 18, 2013).
(32) Johnson, P. B.; Christy, R. W. Optical Constants of the Noble Metals. *Phys. Rev. B* **1972**, *6*, 4370−4379.
(33) Li, S.; Pedano, M. L.; Chang, S.-H.; Mirkin, C. A.; Schatz, G. C. Gap Structure Effects on Surface-Enhanced Raman Scattering Intensities for Gold Gapped Rods. *Nano Lett.* **2010**, *10*, 1722−1727.
(34) Faulds, K.; Smith, W. E.; Graham, D.; Lacey, R. J. Assessment of Silver and Gold Substrates for the Detection of Amphetamine Sulfate by Surface Enhanced Raman Scattering (SERS). *Analyst* **2002**, *127*, 282−286.
(35) Muniz-Miranda, M.; Gellini, C.; Giorgetti, E. Surface-Enhanced Raman Scattering from Copper Nanoparticles Obtained by Laser Ablation. *J. Phys. Chem. C* **2011**, *115*, 5021−5027.
(36) Kong, C.; Sun, S.; Zhang, X.; Song, X.; Yang, Z. Nanoparticle-Aggregated Hollow Copper Microcages and Their Surface-Enhanced Raman Scattering Activity. *CrystEngComm* **2013**, *15*, 6136−6139.
(37) Shao, Q.; Que, R.; Shao, M.; Cheng, L.; Lee, S.-T. Copper Nanoparticles Grafted on a Silicon Wafer and Their Excellent Surface-Enhanced Raman Scattering. *Adv. Funct. Mater.* **2012**, *22*, 2067−2070.
(38) Xu, D.; Dong, Z.; Sun, J.-L. Fabrication of Copper Nanowires by a Solid-State Ionics Method and Their Surface Enhanced Raman Scattering Effect. *Mater. Lett.* **2013**, *92*, 143−146.
(39) Zhao, A.; Mei, T.; Lin, X.; Ni, L.; Wu, A. Aligned Copper Nanorod Arrays for Surface-Enhanced Raman Scattering. In *2007 International Conference on Information Acquisition*, Jeju City, Korea; IEEE: New York, 2007; pp 79−82.
(40) Khan, M. A.; Hogan, T. P.; Shanker, B. Metallic Nanorods Synthesis and Application in Surface-Enhanced Raman Spectroscopy. *J. Nano Syst. Technol.* **2009**, *1*, 1−11.
(41) Fang, C.; Agarwal, A.; Buddharaju, K. D.; Khalid, N. M.; Salim, S. M.; Widjaja, E.; Garland, M. V; Balasubramanian, N.; Kwong, D.-L. DNA Detection Using Nanostructured SERS Substrates with Rhodamine B as Raman Label. *Biosens. Bioelectron.* **2008**, *24*, 216−221.

Growth and surface-enhanced Raman scattering of Ag nanoparticle assembly in agarose gel

2012 Meas. Sci. Technol. 23 084006

(http://iopscience.iop.org/0957-0233/23/8/084006)

Meas. Sci. Technol. **23** (2012) 084006 (9pp) doi:10.1088/0957-0233/23/8/084006

Growth and surface-enhanced Raman scattering of Ag nanoparticle assembly in agarose gel

M Keating[1], Y Chen[1], I A Larmour[2], K Faulds[2] and D Graham[2]

[1] Photophysics Group, Centre for Molecular Nanometrology, Department of Physics, SUPA, University of Strathclyde, John Anderson Building, 107 Rottenrow, Glasgow, G4 0NG, UK
[2] Centre for Molecular Nanometrology, WestCHEM, Department of Pure and Applied Chemistry, University of Strathclyde, Glasgow, G1 1XL, UK

E-mail: martin.keating@strath.ac.uk

Received 13 December 2011, in final form 31 March 2012
Published 19 June 2012
Online at stacks.iop.org/MST/23/084006

Abstract
Agarose gel loaded with silver nanoparticles has attracted a lot of attention recently due to its excellent molecular trapping capabilities and strong surface-enhanced Raman scattering (SERS). Despite its potential, the influence of the growth condition on the gel structure and resultant SERS intensity and reproducibility is not clear. In this work, we examine the effect of silver nitrate feed solution concentration, the precursor to neutral silver nanoparticles, on the resultant nanoparticle morphology, gel homogeneity, SERS signal intensity and reproducibility. SERS of *trans*-1,2-bis-(4-pyridyl) ethylene, a non-resonant molecule, was conducted. A substantial rise in SERS signal strength with increasing feed concentration was observed, accompanied by a modest increase in average particle size as disclosed by TEM analysis. At higher concentrations, gels possessed larger particles from broader size distributions which had a higher tendency to aggregate. This created a higher density of SERS 'hotspots', regions of intense electromagnetic field crucial for maximal enhancement of the Raman signal, but also led to increased spot-to-spot signal variation due to a marked change in nanoparticle morphology and gel homogeneity. Beyond an optimal feed concentration, no further increase in overall signal strength was evident, correlating with no appreciable rise in the number of larger particles.

Keywords: surface-enhanced Raman scattering, silver nanoparticles, agarose, metal nanocomposite, nanoparticle morphology

(Some figures may appear in colour only in the online journal)

Introduction

Owing to their extremely small size, metal nanoparticles exhibit extraordinary physical properties which differ substantially from those of bulk metals. Changing one or all of the size, shape or interparticle distance of nanoparticles [1] or the dielectric constant of the surrounding medium [2] can dramatically alter these characteristics, allowing nanoparticles to be tuned for a variety of purposes. Fields such as sensing [3], electronics [4] and catalysis [5] have all greatly benefited from the unique physical and chemical properties that metal nanoparticles possess. In noble metal nanoparticles, for example, collective conduction electron oscillations, known as localized surface plasmons, can be excited when particle size is much smaller than the wavelength of incident light [6]. These create a strong electromagnetic (EM) field at the surface of a metal nanoparticle [7] and are utilized in various surface-enhanced spectroscopies such as localized surface plasmon resonance, surface-enhanced fluorescence and surface-enhanced Raman scattering (SERS) [8]. In SERS, the inherently weak Raman signal [9] arising from the interaction between vibrational modes of a molecule

and incident light [10] experiences both chemical and EM enhancement. Chemical enhancement involves alteration of a molecule's polarizability via formation of a complex with a metal substrate [11] and is thought to strengthen the signal by about 10 to 100 times [13]. EM enhancement consists of two separate multiplicative effects: amplification of both the incident field and the Raman-scattered field of the molecule by localized surface plasmon resonances of a metal nanoparticle [12]. This strengthens the signal considerably more than the chemical effect and is recognized as contributing by far the greatest enhancement in SERS [14] of about 10^6–10^8 [15]. Aggregated particles commonly produce the largest enhancement where small interparticle spacing facilitates coupling of localized surface plasmon resonances between neighbouring nanoparticles, generating nano-sized regions of extremely high field intensity or so-called 'hotspots' [16, 17]. This makes one of the main objectives in SERS substrate design the maximization of hotspots in order to attain the strongest possible signal [18]. In addition to optimizing the enhancement effect, the application of SERS substrates relies on their reproducibility, which is governed by the choice of metal utilized in substrate design, as well as nanoparticle morphology and homogeneity [19].

One SERS platform which is relatively new and which has already been shown to be highly effective is silver agarose gel. The gel structure permits silver nanoparticles to form *in situ* inside nano-sized pores within the matrix, with larger nanoparticles being trapped in the water phase of the gel while smaller nanoparticles pepper the polymeric network [20]. This dispenses with the need for capping agents which might otherwise seriously interfere with molecular adsorption on the nanoparticle surface [21, 22]. In addition to providing significant nanoparticle stability, preparation of metal nanoparticles within a confined area such as the polymeric network of a gel offers a high degree of control over nanoparticle size, morphology and overall three-dimensional structure [23, 24], with a gel matrix proving to be a superb molecular trap. Silver agarose for example has been shown to detect analytes such as the potent environmental toxin dichlorodiphenyl-trichloroethane (DDT) which does not adsorb on to gold or silver, a characteristic which up until now has precluded it from SERS analysis [20]. In such cases, analytes with a low affinity for noble metals can be mechanically trapped in the vicinity of the nanoparticles during shrinkage of the matrix either by physical or chemical means, thus permitting detection [20, 25]. In addition to macro-sized gels being used in SERS, Abalde *et al* recently produced silver nanoparticle-loaded agarose beads on the order of microns which were large enough to be handled one bead at a time and resolved by a normal confocal microscope. The beads produced strong SERS, had a narrow size distribution and were highly morphologically uniform. As only one micro-bead was required for analysis, the amount of analyte needed was significantly reduced [22].

Added to its efficacy in SERS analysis is the inexpensive and straightforward production of metal nanocomposite agarose. This plus its facility in sample preparation and handling combine to make it a robust SERS platform with great potential. However, despite its obvious promise, the influence of the growth condition on silver gel structure and its effect on the SERS response and reproducibility are not clear. In this work, we systematically investigate the effect of silver nitrate feed solution concentration on the resultant nanoparticle morphology, gel homogeneity, SERS signal intensity and signal reproducibility of silver agarose using BPE as a probe.

Experimental

All chemicals were purchased from Sigma Aldrich and used without further purification: Silver Nitrate ReagentPlus grade $\geqslant$ 99.0% (titration), Agarose type IX-A Ultra-low Gelling Temperature, *trans*-1,2-bis-(4-pyridyl) ethylene (assay 97%).

Preparation of silver gel

Silver-loaded agarose gels were prepared using a method similar to that used by Aldeanueva-Potel *et al* [20]. A 5.4% w/v solution of agarose gel was prepared by placing 0.54 g of agarose powder in 10 ml of distilled water. The mixture was heated to about 90 °C and stirred gently until it began to boil, after which it was placed in a heated sonic bath for 5 min to expel air bubbles. After sonification, the hot liquid gel was poured into a standard plastic cuvette (path length 10 mm) and placed in the fridge, where it was cooled for 1 h at 4 °C. Once solidified, the gel was carefully removed from the cuvette with a thin spatula and a blade was used to cut samples about $1.5 \times 10 \times 10$ mm^3. To ensure that silver ions had diffused uniformly throughout the gel and that they had been completely reduced to neutral silver, gels were immersed for 24 h each in different concentrations of aqueous silver nitrate and subsequently sodium borohydride with the molar ratio remaining 1:1 throughout. This ratio was chosen in line with work done by Aldeanueva-Potel *et al* [20] where they employed a 500 mM $AgNO_3$ concentration with the same for $NaBH_4$. Upon removal, samples were washed in distilled water and dialysed for 20 h before being placed in a 10^{-5} M solution of BPE for 12 h prior to recording SERS spectra. A control experiment was also conducted in an attempt to shorten the period of gel immersion in both the precursor and reducing solutions. In this case, blank gel was immersed for 3 h each in silver nitrate and sodium borohydride, followed by rinsing and dialysis in distilled water for 45 min. SERS was conducted using 10^{-5} M BPE to compare this with the established method using the resultant SERS intensity.

TEM and UV-VIS spectroscopy

Absorbance spectra were taken using a Jasco V-660 UV-VIS spectrometer. The samples were prepared using the same method as Aldeanueva-Potel *et al* [20]. A small piece of blank agarose gel was compressed between two fused silica slides and used as a baseline. The same was done for silver gels of each silver nitrate feed concentration and their spectra recorded. Transmission electron micrographs were taken with a FEI Tecnai T20 TEM with a LaB_6 filament and accelerating

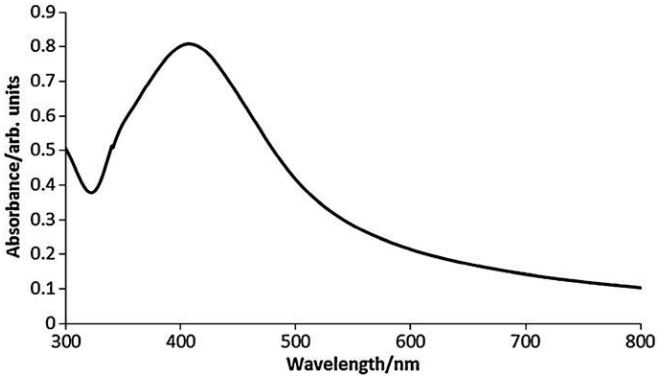

Figure 1. UV-VIS absorption spectrum of 100 mM gel.

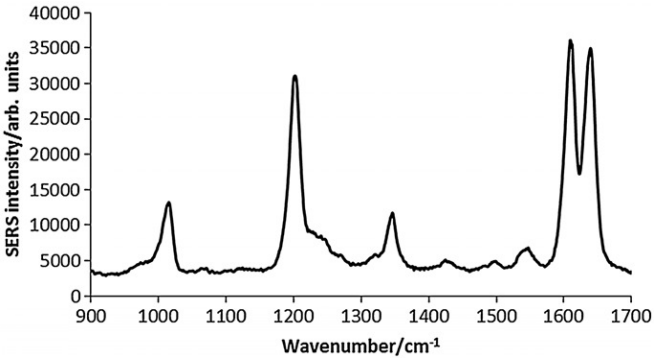

Figure 2. SERS spectrum of 10^{-5} M BPE in 200 mM gel.

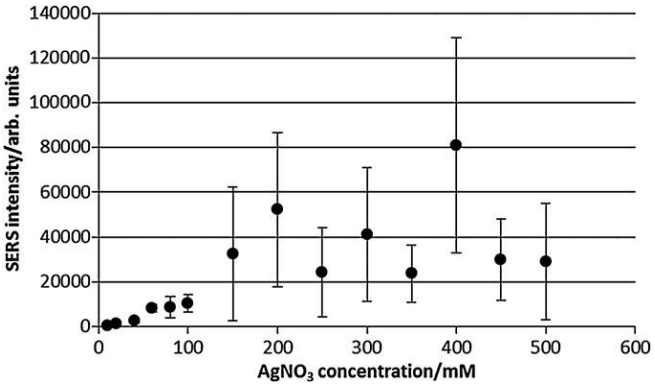

Figure 3. SERS intensity versus silver nitrate feed concentration.

voltage of 200 kV. Images were captured with a Megaview Soft Imaging System and a Gatan Image Filter with an exposure time of 2.0 s. Gel samples were positioned on carbon-coated copper grid substrates and vacuum dried before analysis. ImageJ, the public domain software (version 1.46a), was used to measure nanoparticle size. Size distributions are quoted as the mean measurement ± the standard deviation.

SERS spectra

SERS spectra were recorded on a Leica DM/LM microscope equipped with an Olympus 20 × /N.A. 0.4 long-working distance objective to collect 180° backscattered light. The spectrometer system was a Renishaw Ramascope System 2000 with the 632.8 nm line of a helium–neon laser as the excitation source. At 100% power, the unfocused output was measured to be approximately 4.8 mW at the sample. Dielectric edge filters were used to reject the Rayleigh scattered light. SERS intensity of BPE was recorded by measuring the height of the 1200 cm^{-1} peak. Analysis was carried out using OriginPro 8.5 software. The peak height was averaged from 25 baseline-corrected spectra per silver nitrate concentration taken from different locations on the gel sample. Laser power was maintained at 25% and integration time was adjusted from 5 to 0.2 s to prevent signal saturation. It should be noted that under these conditions, no evidence of gel scorching was observed upon examination through the microscope. All spectra were corrected to an integration time of 1 s for comparison. To compare the two fabrication methods, 25 spectra were taken from different locations on each gel surface.

Results and discussion

A representative absorption spectrum, in this case silver agarose from a 100 mM silver nitrate feed solution or 100 mM gel for ease of reference, is shown in figure 1.

Spectra were taken of all silver nitrate concentration gels which confirmed that silver-loading by reduction of Ag^+ ions had taken place as shown by the presence of the plasmon band around 400 nm. The gels were yellowish to dark brown depending on the concentration of the $AgNO_3$ feed solution. Due both to the nature of the gel and sample preparation, it was not possible to make a quantitative comparison in the absorption intensity, but this is not the subject of the present study. After confirmation of silver-loading, SERS was conducted on the Ag gels using 10^{-5} M BPE as a Raman reporter. A representative SERS spectrum of BPE is shown in figure 2.

Characteristic vibrational modes of BPE appear at 1200, 1604 and 1634 cm^{-1} corresponding to the C=C stretching, aromatic ring stretching and in-plane ring mode respectively [26].

A graph of SERS intensity of the 1200 cm^{-1} peak versus silver nitrate concentration is shown in figure 3.

Error bars on the graph are the standard deviations of SERS intensity measurements. The graph shows that SERS intensity rises substantially as a function of silver nitrate feed solution concentration. The trend is approximately linear between 10 and 100 mM but starts to fluctuate with no subsequent overall increase after 150 mM. It is interesting at this point to note that the gel prepared in the control experiment with greatly reduced gel immersion and dialysing times provided a similar average SERS intensity (merely 13% less) compared with gel fabricated using the established method. In addition, the SERS signal intensity % relative standard deviations (RSDs) for both methods were also very similar, being about 56% and 49% respectively. As there is only a modest reduction in signal strength and the %RSDs lie close to one another, this experiment shows our truncated method is an acceptable alternative in silver agarose production.

Further structural study using TEM analysis was carried out to understand the rise in signal strength with feed

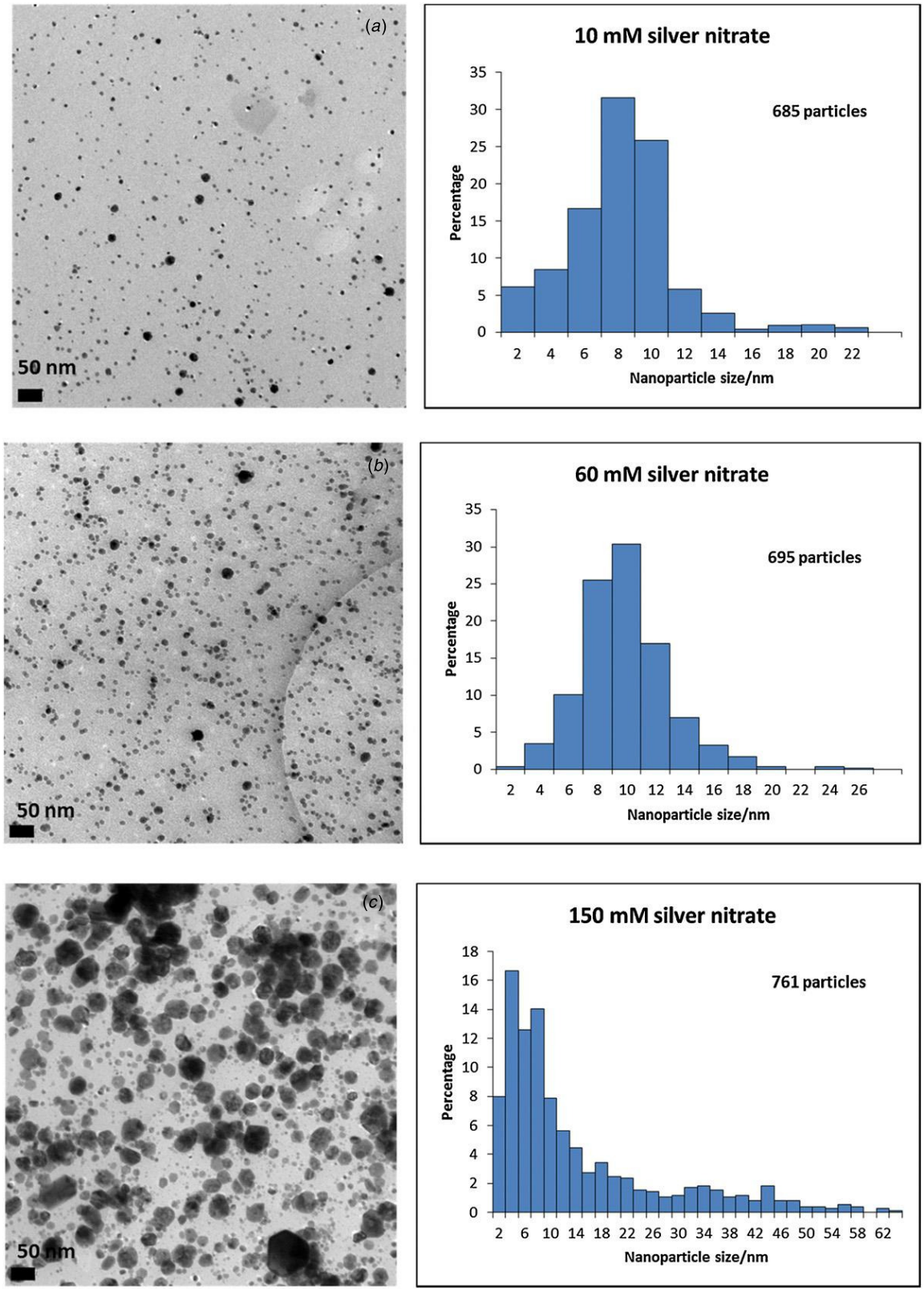

Figure 4. TEM images of (*a*) 10, (*b*) 60, (*c*) 150, (*d*) 200 and (*e*) 300 mM gels with their corresponding size distributions and the number of particles measured for each. All images are at the same scale. The scale bar on the bottom left is 50 nm.

concentration. Figure 4 shows the TEM micrographs taken from gels of various $AgNO_3$ concentrations together with their corresponding size distributions. Average particle size, standard deviation and %RSD are listed in table 1. There is an increase in size from 7.2 ± 3.2 to 11.4 ± 10.4 nm from the 10 mM to the 200 mM gel, the concentration

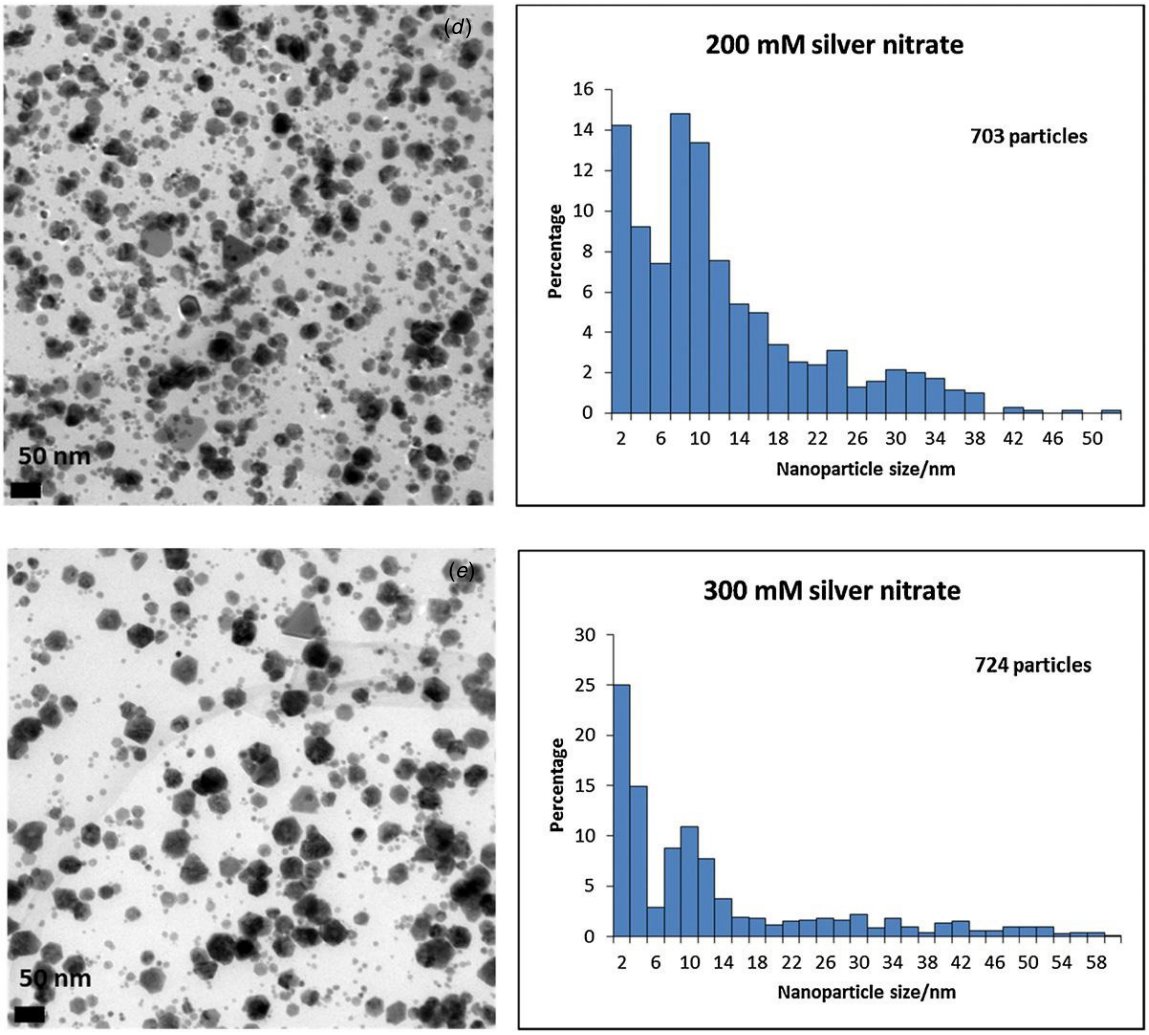

Figure 4. (Continued.)

Table 1. Size distribution of nanoparticles in Ag gel from different $AgNO_3$ concentrations.

$AgNO_3$ concentration (mM)	Average size (nm)	Standard deviation	%RSD
10	7.2	3.2	44.8
60	9.0	3.2	36.2
150	13.4	13.7	102.1
200	11.4	10.4	91.1
300	12.1	13.6	112.4

at which maximum SERS intensity occurs (excluding the extreme value for 400 mM). The average nanoparticle size peaks at 13.4 ± 13.7 nm for the 150 mM gel. Generally, the larger a metal nanoparticle is, the greater its capability of Raman enhancement [9], so increase in average particle size, although modest, does contribute towards the rise in SERS intensity. More important, however, are the shapes of the size distributions themselves. The distributions of the lower concentration gels, namely the 10 and 60 mM gels, closely approximate a normal curve with comparatively small %RSDs around 40% and maximum particle size around 20 nm. Those of the higher concentration gels, namely the 150, 200 and 300 mM gels, however, are all highly skewed, having much larger %RSDs at around 100% and tails covering a wide range of up to 50 nm or more. Although the higher concentration gels possess significantly large numbers of small nanoparticles, they have what the 10 and 60 mM gels lack: particles of up to and over 50 nm.

As nanoparticles become larger, the rise in signal strength may originate from greater molecular adsorption with increasing nanoparticle surface area in addition to increased 'hotspot' density via the formation of larger aggregates. Figure 5 plots the ratio of average SERS intensity to average nanoparticle surface area (with nanoparticles modelled as simple spheres) as a function of feed concentration. An overall increasing trend implies that the rise in signal strength originates mainly from the enhanced local EM field within 'hotspots'.

Indeed, larger particles produce a stronger SERS response on their own compared to their smaller solitary counterparts and are found solely in the higher concentration gels where they have a much stronger tendency to aggregate. Formation of clumps and chains with each other and with smaller particles means they generate significantly more hotspots than smaller, less aggregated particles in lower-content samples. In addition, the geometry of larger particles most likely increases the

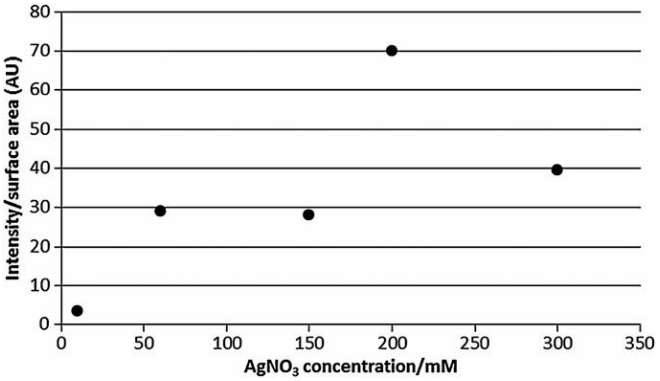

Figure 5. The ratio of SERS signal intensity to nanoparticle surface area versus feed concentration for 10, 60, 150, 200 and 300 mM gels.

number of hotspots even further via the so-called 'lightning rod effect' [27]. Low-content gels consist of mainly spheres, while higher concentration gels include a significant proportion of nonspherical crystals. The EM field for spherical particles is evenly distributed over the entire surface, but in nonspherical particles the distribution is uneven, [8] with fields at sharp metallic structures being significantly stronger [27]. Therefore, the geometry of these structures must also make a significant contribution towards Raman enhancement.

Agglomerations in the lower concentration gels also exist, but as stated, these samples lack larger particles and are much less prone to aggregation. However, 60 mM nanoparticles produce an intensity of about 13 times that of the 10 mM sample. Figures 4(*a*) and (*b*) suggest that this stronger response must originate mainly through a combination of increased particle loading and moderate aggregation. In respect of higher-content gels, the 200 mM sample produces a signal about 80 and 6 times that of the 10 and 60 mM samples respectively. TEM images confirm that SERS intensity in higher-content samples is undoubtedly linked to large aggregates which give rise to a higher density of 'hotspots'. Figure 6 illustrates the different degrees of aggregation in lower and higher-strength gels.

Immediately obvious is the greater degree of aggregation in higher-strength gels which is conducive to 'hotspot' generation, giving rise to comparatively stronger SERS. Going from lower to higher-content samples, the signal becomes stronger as the size distribution broadens, generating larger particles which tend to produce sizeable aggregates. Broadening however also has the effect of increasing spot-to-spot signal variation on the gel surface. Figure 7 shows graphs of the %RSDs of particle size and SERS signal strength.

As seen in figure 7, the trends in both the size and signal graphs are very similar. This points to a close correlation between broadening of the size distribution and the general increase in the spread of SERS intensity measurements. As feed concentration rises, there is an overall increase in the particle size %RSD, making the sample less homogeneous and producing a larger spot-to-spot variation in signal strength on the gel surface. The absence of an overall rise in SERS intensity beyond 150 mM can be explained by the lack of appreciable increase in the number of larger particles beyond this concentration. To optimize silver agarose gel as a SERS substrate therefore, it would be necessary to maximize the number of larger particles whilst simultaneously narrowing the size distribution. This should have the combined effect of producing a stronger SERS response and reducing signal variation.

Sample homogeneity depends critically on how the silver nanoparticles form and grow. Although the science behind particle nucleation and growth is complicated, being governed by thermodynamics and kinetics [28, 29], the La Mer model can adequately explain the evolution of the size distribution in lower to higher-content gels. The reduction of silver nitrate using sodium borohydride to form a critical concentration of silver seed nuclei can be explained by La Mer's burst nucleation theory. Figure 8 illustrates this process.

Formation of silver seed nuclei occurs instantaneously and homogeneously in solution once newly-formed aqueous silver reaches a critical concentration or becomes 'supersaturated'. At supersaturation, nucleation continues until enough silver is removed from solution by seed formation to bring the concentration below critical. Seeds then grow layer-by-layer, forming nanoparticles until the concentration falls to the saturation concentration at equilibrium. When there is only one short nucleation period represented by the 'dot-dash' line in figure 8, the solution is more monodisperse. During a longer nucleation period however, silver is unevenly depleted from solution leading to the creation of different seed particles at different times with a wide range of growth rates, resulting in a more polydisperse solution represented by the solid line in figure 8. A longer nucleation event could occur for example if the rate of consumption of silver by growing nanoparticles was less than the rate of silver atoms added to solution through $AgNO_3$ reduction. This would force the solution to remain above supersaturation for longer, prolonging the nucleation period until sufficient silver had been exhausted to reduce it below critical concentration. Consequently, higher concentration gels which are more polydisperse experience a longer nucleation period than lower concentration gels, which should be expected as they possess significantly more precursor. This was confirmed qualitatively by observation as all samples were reduced. The reduction of silver nitrate by sodium borohydride is governed by the equation

$$AgNO_3 + NaBH_4 \rightarrow Ag + \tfrac{1}{2}H_2 + \tfrac{1}{2}B_2H_6 + NaNO_3.$$

Borohydride also reacts with water relatively slowly:

$$NaBH_4 + 2H_2O \rightarrow NaBO_2 + 4H_2.$$

Before the silver nitrate gels were added to their respective borohydride solutions, bubbling of hydrogen given off by the reaction with water for all borohydride concentrations was minimal. Immediately after gel immersion, copious quantities of bubbles of hydrogen and diborane were generated, with higher-strength gels producing the gases much more vigorously. The low-content gels ceased gas production after about 10 min, suggesting the reaction had terminated, whereas higher-content gels produced gases for up to about 25 min or longer. This suggests that for stronger gels, new silver was still being produced long after weaker gels had ended their reaction, supporting the assertion that higher-strength gels did experience a longer nucleation period.

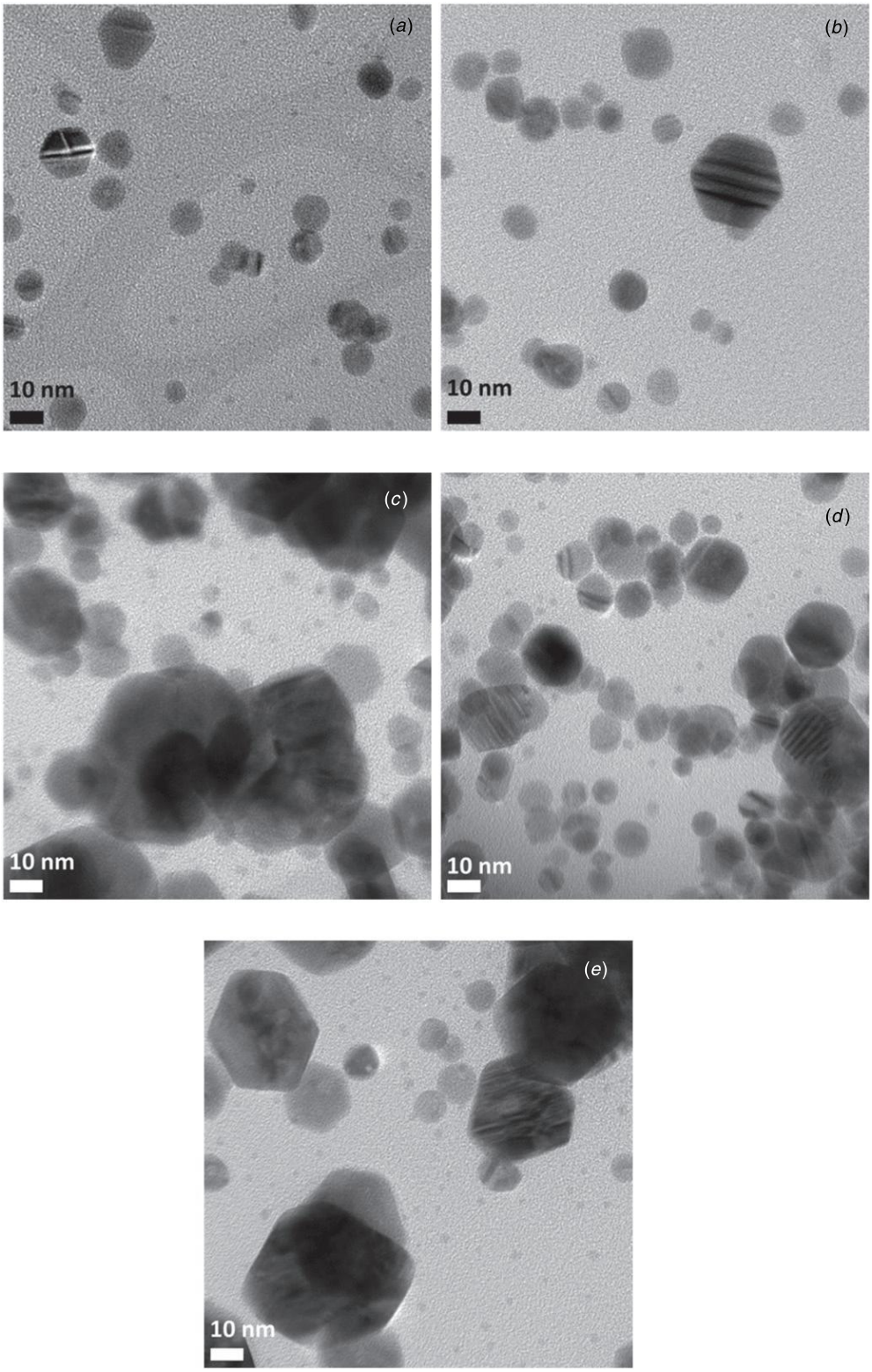

Figure 6. High-magnification TEM images of (*a*) 10, (*b*) 60, (*c*) 150, (*d*) 200 and (*e*) 300 mM samples. All images are at the same scale and the scale bar on the bottom left is 10 nm.

It therefore takes longer for the silver in these gels to be 'spent', elongating the nucleation period and broadening and skewing the size distribution. Although this argument is based on solution chemistry, the governing principles are the same in this context. One difference is that borohydride must diffuse through the gel surface as opposed to solution only. All gel samples were prepared in the same manner however, having the same surface area with a 1:1 ratio of reductant to reactant being maintained throughout. Therefore as all things were equal, the argument is valid. This means that the shape of the

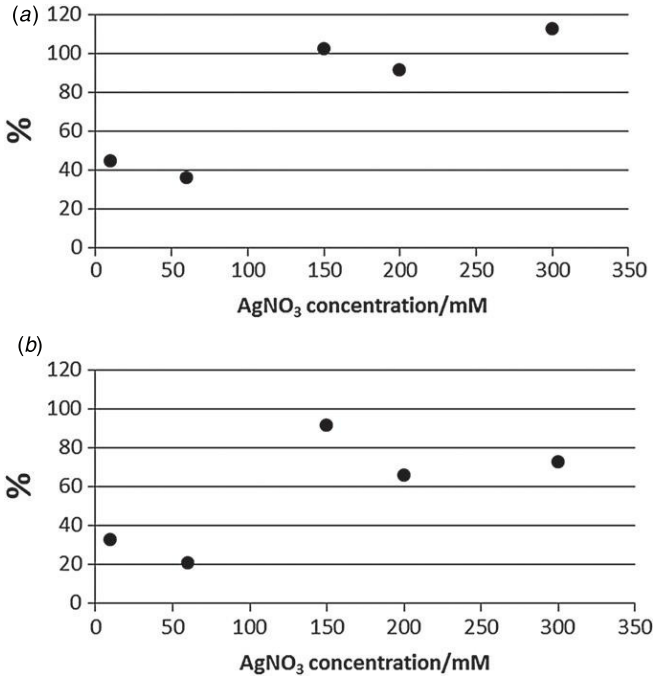

Figure 7. (*a*) Nanoparticle size and (*b*) SERS signal strength %RSDs for 10, 60, 150, 200 and 300 mM gels.

size distribution, which strongly influences spot-to-spot signal variation, directly depends on the nucleation period which is highly sensitive to $AgNO_3$ concentration.

Higher-strength gels do provide notably stronger SERS than gels of lower silver content, but it would be better if their size distributions could be narrowed, with the average position shifted towards larger particle size. This should give rise to stronger SERS with less signal fluctuation. One way to achieve this could be to pre-treat blank agarose gel by steeping it in silver seed solution before slow growth with a mild reducing agent such as ascorbic acid. It has already been shown that adding seeds to a metal precursor solution and introducing a weak reducing agent separates the nucleation and growth periods, offering a high degree of control over the size and shape of nanoparticles. The weakness of the reducing agent permits growth solely on the preformed metal seeds through autocatalysis, precluding the possibility of any nucleation events [30] which would reduce monodispersity. Another method might be to use a heavy excess of $NaBH_4$ or some other strong reducing agent. This could reduce the silver concentration below critical much more quickly, thus shortening the nucleation period.

Conclusion

We examined the effect of silver nitrate feed solution concentration on the resultant nanoparticle morphology, gel homogeneity, SERS signal intensity and spot-to-spot signal variation in silver agarose gel. Initially, SERS signal strength increased approximately linearly as a function of feed concentration but then fluctuated with no further overall increase. TEM studies confirmed that this rise in lower strength gels was due mainly to a higher nanoparticle density along with a modest increase in aggregation. In higher-strength gels, larger asymmetric particles not only produced stronger SERS on their own, but tended to form large aggregates conducive to 'hotspot' formation, further increasing the signal. The overall increasing spot-to-spot signal variation was attributed to the increasing size distribution leading to a decrease in gel homogeneity. Generally, as the size %RSD rose, the less homogeneous a sample was and the larger the spread in SERS measurements became. In addition, no appreciable rise in the number of larger particles after 150 mM $AgNO_3$ was evident, which accounted for the subsequent lack of overall increase in SERS signal strength. La Mer's theory explained why lower-content gels had narrower size distributions than higher-content gels whose distributions were heavily skewed. Future work could focus on different reduction methods to separate the nucleation and growth periods of silver nanoparticles in agarose, with a view to creating larger, more monodisperse particles which should create a stronger SERS response with less signal variation. This would further optimize a substrate which already holds great potential for SERS analysis.

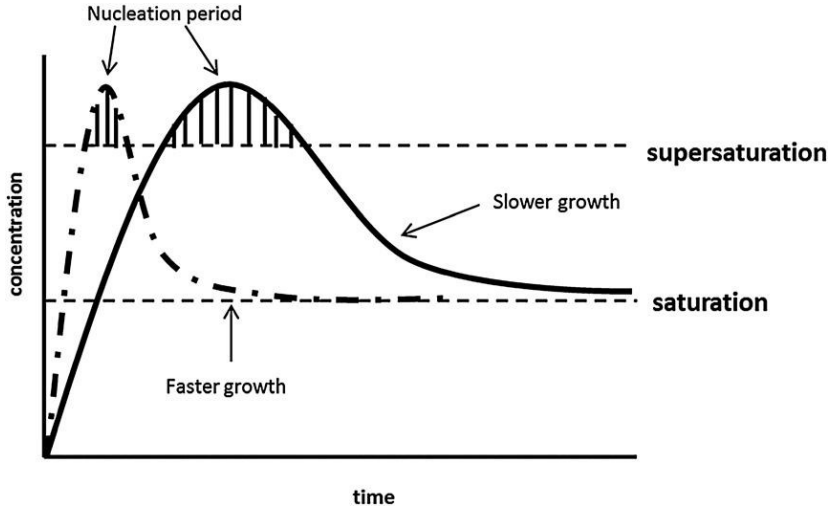

Figure 8. La Mer model of burst nucleation theory.

Acknowledgment

We would like to thank Dr Damien McGrouther for use of the transmission electron microscope and Mr Colin How for his assistance in obtaining the images (School of Physics and Astronomy, University of Glasgow).

References

[1] Link S and El-Sayed M A 2003 Optical properties and ultrafast dynamics of metallic nanocrystals *Annu. Rev. Phys. Chem.* **54** 331–66

[2] Kelly K L, Coronado E, Zhao L L and Schatz G C 2003 The optical properties of metal nanoparticles: the influence of size, shape, and dielectric environment *J. Phys. Chem.* B **107** 668–77

[3] Sau T K, Rogach A L, Jäckel F, Klar T A and Feldmann J 2010 Properties and applications of colloidal nonspherical noble metal nanoparticles *Adv. Mater.* **22** 1805–25

[4] Sau T K and Rogach A L 2010 Nonspherical noble metal nanoparticles: colloid-chemical synthesis and morphology control *Adv. Mater.* **22** 1781–804

[5] Lang S M, Popolan D M and Bernhardt T M 2007 Chemical reactivity and catalytic properties of size-selected gas-phase metal clusters *The Chemical Physics of Solid Surfaces: Atomic Clusters, From Gas Phase to Deposited* (Oxford: Elsevier) pp 65–86

[6] Moores A and Goettmann F 2006 The plasmon band in noble metal nanoparticles: an introduction to theory and applications *New J. Chem.* **30** 1121

[7] Petryayeva E and Krull U J 2011 Localized surface plasmon resonance: nanostructures, bioassays and biosensing—a review *Anal. Chim. Acta* **706** 8–24

[8] Larmour I A and Graham D 2011 Surface enhanced optical spectroscopies for bioanalysis *Analyst* **136** 3831–53

[9] Abalde-Cela S, Aldeanueva-Potel P, Mateo-Mateo C, Rodríguez-Lorenzo L, Alvarez-Puebla R A and Liz-Marzán L M 2010 Surface-enhanced Raman scattering biomedical applications of plasmonic colloidal particles *J. R. Soc. Interface* **7** (Suppl 4) S435–50

[10] Ferraro J R, Nakamoto K and Brown C W 2003 *Introductory Raman Spectroscopy* (London: Academic) pp 13–5

[11] Le Ru E C and Etchegoin P G 2009 *Principles of Surface-Enhanced Raman Spectroscopy and Related Plasmonic Effects* (Oxford: Elsevier) pp 258–61

[12] Le Ru E C and Etchegoin P G 2009 *Principles of Surface-Enhanced Raman Spectroscopy and Related Plasmonic Effects* (Oxford: Elsevier) p 187

[13] Kattumuri V, Chandrasekhar M, Guha S, Raghuraman K, Katti K V, Ghosh K and Patel R J 2006 Agarose-stabilized gold nanoparticles for surface-enhanced Raman spectroscopic detection of DNA nucleosides *Appl. Phys. Lett.* **88** 153114

[14] Meyer M, Le Ru E C and Etchegoin P G 2006 Self-limiting aggregation leads to long-lived metastable clusters in colloidal solutions *J. Phys. Chem.* B **110** 6040–7

[15] Lyandres O, Shah N C, Yonzon C R, Walsh J T, Glucksberg M R and Van Duyne R P 2005 Real-time glucose sensing by surface-enhanced Raman spectroscopy in bovine plasma facilitated by a mixed decanethiol/ mercaptohexanol partition layer *Anal. Chem.* **77** 6134–9

[16] Yang Y, Shi J, Tanaka T and Nogami M 2007 Self-assembled silver nanochains for surface-enhanced Raman scattering *Langmuir* **23** 12042–7

[17] Tay L-L, Hulse J, Kennedy D and Pezacki J P 2010 Surface-enhanced Raman and resonant Rayleigh scatterings from adsorbate saturated nanoparticles *J. Phys. Chem.* C **114** 7356–63

[18] Asiala S M and Schultz Z D 2011 Characterization of hotspots in a highly enhancing SERS substrate *Analyst* **136** 4472–9

[19] Jarvis R M, Rowe W, Yaffe N R, O'Connor R, Knowles J D, Blanch E W and Goodacre R 2010 Multiobjective evolutionary optimisation for surface-enhanced Raman scattering *Anal. Bioanal. Chem.* **397** 1893–901

[20] Aldeanueva-Potel P, Faoucher E, Alvarez-Puebla R A, Liz-Marzan L M and Brust M 2009 Recyclable molecular trapping and SERS detection in silver-loaded agarose gels with dynamic hot spots *Anal. Chem.* **81** 9233–8

[21] Stoerzinger K A, Lin J Y and Odom T W 2011 Nanoparticle SERS substrates with 3D Raman-active volumes *Chem. Sci.* **2** 1435

[22] Abalde-Cela S, Auguié B, Fischlechner M, Huck W T S, Alvarez-Puebla R A, Liz-Marzán L M and Abell C 2011 Microdroplet fabrication of silver-agarose nanocomposite beads for SERS optical accumulation *Soft Matter* **7** 1321

[23] Saha S, Pal A, Pande S, Sarkar S, Panigrahi S and Pal T 2009 Alginate gel-mediated photochemical growth of mono- and bimetallic gold and silver nanoclusters and their application to surface-enhanced Raman scattering *J. Phys. Chem.* C **113** 7553–60

[24] Li J-L, Liu X-Y, Wang X-G and Wang R-Y 2011 Controlling nanoparticle formation via sizable cages of supramolecular soft materials *Langmuir* **27** 7820–7

[25] Alvarez-Puebla R A and Liz-Marzán L M 2012 Traps and cages for universal SERS detection *Chem. Soc. Rev.* **41** 43–51

[26] Liu Y-J, Zhang Z-Y, Dluhy R A and Zhao Y-P 2010 The SERS response of semiordered Ag nanorod arrays fabricated by template oblique angle deposition *J. Raman Spectrosc.* **41** 1112–8

[27] Maier S A 2007 *Plasmonics: Fundamentals and Applications* (New York: Springer) pp 161–2

[28] Burda C, Chen X, Narayanan R and El-Sayed M A 2005 Chemistry and properties of nanocrystals of different shapes *Chem. Rev.* **105** 1025–102

[29] Peng Z, Yang S and Yang H 2009 Approaches to the synthesis and characterisation of spherical and anisotropic platinum nanomaterials *Nanomaterials For The Life Sciences: Metallic Nanomaterials* ed C Kumar (Weinheim: Wiley-VCH) pp 359–65

[30] Tao A R, Habas S and Yang P 2008 Shape control of colloidal metal nanocrystals *Small* **4** 310–25

Reflectance and surface enhanced Raman scattering (SERS) of sculptured silver films deposited at various vapor incident angles

2012 Meas. Sci. Technol. 23 084007

(http://iopscience.iop.org/0957-0233/23/8/084007)

Meas. Sci. Technol. **23** (2012) 084007 (6pp) doi:10.1088/0957-0233/23/8/084007

Reflectance and surface enhanced Raman scattering (SERS) of sculptured silver films deposited at various vapor incident angles

Shigeng Song[1], **Martin Keating**[2], **Yu Chen**[2] **and Frank Placido**[1]

[1] Thin Film Centre, SUPA, University of the West of Scotland, Paisley, UK
[2] Photophysics Group, Centre for Molecular Nanometrology, Department of Physics, SUPA, University of Strathclyde, Glasgow, UK

E-mail: shigeng.song@uws.ac.uk

Received 5 December 2011, in final form 31 March 2012
Published 19 June 2012
Online at stacks.iop.org/MST/23/084007

Abstract
By using e-beam evaporation at various oblique angles, silver nanorod arrays were produced on silicon and fused silica substrates. Reflectance of P and S polarizations was measured at an incident angle of 30°, with the data analyzed by using the appropriate optical dispersive model. The surface enhanced Raman scattering (SERS) was investigated using trans-1,2-bis (4-pyridyl)ethene (BPE) as a probe molecule at an excitation wavelength of 633 nm. The Ag-coated surface become rougher as the vapor incident angle is increased. Only the sample deposited at 85° shows clear oblique column structure. Reflectance fitting confirmed the positive rexlation between roughness and deposition angle and showed an increase of porosity in the film with increasing deposition angle. The reflectance measurements also indicate that the sample deposited at 85° has a very high anisotropic effect due to the inclined column structure. In the RS scans, only the 85° samples on Si and silica substrates gave strong SERS with a similar enhancement factor, with a higher background level and noise signal from the silica substrate.

Keywords: silver nanorod arrays, thin film, reflectance, SERS, e-beam evaporation

(Some figures may appear in colour only in the online journal)

1. Introduction

Noble metals with nanostructures have attracted tremendous attention in the past several decades due to their unique optical properties and subsequent applications, for example, localized surface plasmon resonance (LSPR) and surface enhanced Raman scattering (SERS) [1–3]. Particularly, the SERS has been widely investigated for its potential application in chemical and biological sensing. Many different methods have been employed to produce nanostructured noble metal arrays, e.g., colloidal lithography for discrete nanostructure arrays [4, 5], colloidal mask templates for nanostructured films (nanohole arrays [6]), nanovoid arrays from electrodeposition [7] and electron beam lithography [8]. However, these methods have various issues in expense, efficiency, reproducibility, or production of a large batch of samples. Driskell [9] and Liu [10] have fabricated aligned Ag nanorod arrays on flat substrates using an oblique angle vapor deposition (OAD) method. Their results have shown that highly sensitive and stable SERS substrates can be obtained by using OAD. Also, the OAD method is suitable for producing a large batch of SERS substrates.

Nanostructured films produced by OAD are also known as sculptured thin films. The original research works in these areas can date back to the 1950s [11]. The sculptured films with anisotropic properties can be designed and realized in a controllable manner using physical vapor deposition. By varying the direction of the incident vapor flux (deposition material), a wide range of columnar forms can be obtained: two

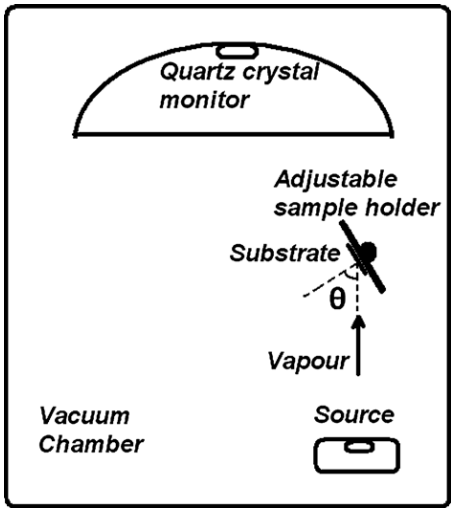

Figure 1. Configuration of e-beam system for oblique angle deposition.

dimensions ranging from simple slanted columns and chevrons to more complex C- and S-shaped morphologies and three dimensions such as simple helixes and superhelixes. High structure variation of sculptured films allows us to optimize morphology and structure to obtain better SERS substrates.

However, the complex morphology and nanostructure of sculptured films cause difficulty for optical characterization [12, 13], e.g., a highly scattering, non-specular surface and porosity. It is necessary to develop an appropriate optical model to analyze noble metal nanorod arrays produced by using OAD. In the research, we have produced Ag nanorod arrays by using e-beam evaporation deposition at various vapor incident angles (OAD method). The samples have been measured by using a novel spectrophotometer with S and P polarizations and various incident angles. The optical dielectric properties of these silver coatings are obtained by use of reflectance data fitting with combined Kim and Drude models for an optical dispersive function, also using the effective medium approximation (EMA) and surface scattering for porous and rough surface modeling. The SERS was also investigated.

2. Experiments

The silver nanorod array samples were deposited by using e-beam evaporation (Satis) at various vapor incident angles: 0°, 45°, 75° and 85°. The inclination angle of the sample can be manually controlled through a motion feedthrough. Fused silica and silicon wafers are used as substrates and cleaned using the standard cleaning process before film deposition. The configuration of the system is shown in figure 1. The thicknesses of samples at various vapor incident angles were controlled by using a quartz crystal monitor; the same sample thickness was maintained to an extent by adjustment of the projection of silver vapor flux to the normal direction of the substrate. A novel spectrophotometer, Aquila nkd8000, is used to measure S and P polarized reflectance at a 30° incident angle within the wavelength range of 350 to 1000 nm. As the nanorods on the substrate tilt at an angle (not perpendicular to the substrate surface), the angle between the incident plane of the measuring light beam and the incident plane of silver vapor flux should be fixed so that the reflectance of different polarizations and various samples can be compared. In our studies, the angle is 90°. Reflectance of S and P polarization for a sample is obtained from the same position on the sample surface. The SERS was investigated using trans-1,2-bis(4-pyridyl)ethene (BPE) as a probe molecule at an excitation wavelength of 633 nm (Renishaw Ramascope System 2000). BPE was chosen because it has a relatively large Raman cross-section and is commonly used as a Raman probe molecule on silver substrates. A droplet of BPE methanol solution with a concentration of 10^{-5} M was dispensed on the surface of silver samples. All samples were also scanned before applying BPE for comparison. The spectra were taken at an integration time of 1 s with 100% laser power (approximately 5.7 mW). The Raman system was calibrated by using a silicon standard before silver sample measurements.

The morphology of silver samples was observed by using SEM.

3. Results and discussion

3.1. Morphology of OAD silver samples

Figure 2 shows the images of silver films deposited at various vapor incident angles. The surface becomes rougher as the vapor incident angle is increased. Only the sample deposited at 85° shows clear oblique column structure. The columnar structure results directly from self-shadowing at the length scale of the arriving adatoms during deposition, either by atomic nucleation at the start point of film deposition or by the defects of substrates. The columns generally point in the direction of the incoming vapor flux, as shown in figure 3. In the figure, χ_v is the vapor flux angle and χ is the oblique angle of columns. In this paper, the manually controlled vapor incident angle θ is equal to $90°-\chi_v$. There is an empirical relation between vapor flux angle and column oblique angle, which is called the tangent rule, i.e. $\tan(\chi) = 2\tan(\chi_v)$ [11]. This relation was confirmed by computer simulation using ballistic aggregation under low adatom mobility conditions. For 85° vapor incident angle, we have the vapor flux angle $\chi = 5°$. According to the tangent rule, the oblique column angle should be about 10°. However, the actual column oblique angle is about 34°, which is obtained from the SEM image in figure 2. This is very different from the calculated angle obtained by using the tangent rule. It implies that adatom mobility is very high in our experiments.

3.2. Reflectance of OAD silver samples and modeling

The dielectric dispersion function of silver films needs to be constructed before reflectance data fitting. The dispersion function includes the Drude model describing plasma resonance absorption of free charge carriers as silver is a metallic material. To simplify the calculation, a classical Drude model [14], in which the damping constant does not depend on frequency, is used. Interband transition absorption also needs

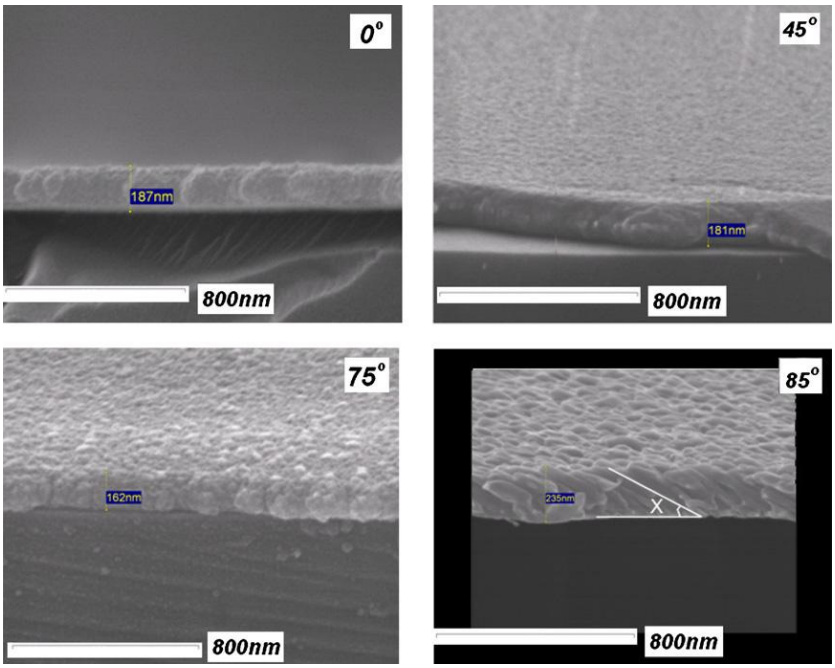

Figure 2. SEM images of silver films deposited at various vapor incident angles.

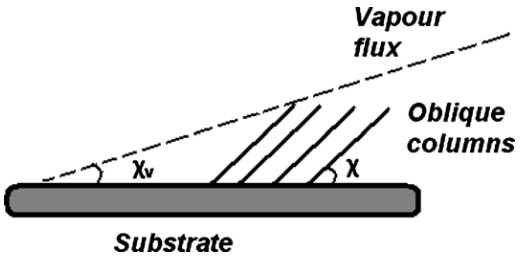

Figure 3. Formation of oblique columns at an oblique vapor incident angle.

to be included in the dispersion model. Here, the Kim oscillator is used for interband transition [15]. Dielectric background χ_{db} is also included in the function. Then, we have the optical dispersion model as: $\varepsilon_{\mathrm{total}} = \chi_{\mathrm{db}} + \chi_{\mathrm{Drude}} + \chi_{\mathrm{Kim}}$. Note that $\varepsilon = 1 + \chi$; here, 1 is included in χ_{db}. The final equation is as follows:

$$\varepsilon(\omega) = \chi_{\mathrm{db}} + \frac{\omega_p^2}{\omega_0^2 - \omega^2 - \mathrm{i}\cdot\omega\cdot\tau(\omega)} - \frac{\omega_{\mathrm{dp}}^2}{\omega^2 + \mathrm{i}\cdot\omega\cdot\tau_d}.$$

The third term on the right-hand side in the equation is the Drude model. ω_{dp} is the resonance frequency and τ_d is the damping constant. The second term on the right-hand side is the Kim oscillator. ω_p is the oscillator strength, ω_0 is the resonance frequency and $\tau(\omega)$ is the frequency dependence of the damping constant:

$$\tau(\omega) = \omega_\tau \cdot \exp\left[-\frac{1}{1+\sigma^2}\cdot\left(\frac{\omega-\omega_0}{\omega_\tau}\right)^2\right].$$

Here, σ is called the Gauss–Lorentz switch, and Gauss line shape is achieved while $\sigma = 0$, whereas Lorentzian line shape is achieved with a large value of σ (e.g. larger than 5).

Light scattering from a rough surface also needs to be taken into account in optical modeling. The total integrated scatter (TIS) formula is used for calculation [16]. The definition of TIS is (specularly reflected light)/(total reflected light). The formula was obtained by assuming that the height distribution function of a rough surface is Gaussian and the roughness compared to the measured wavelength is small; thus, the coherent model can be used to deduce the scattering formula. The height distribution function and TIS formula are as follows:

$$f(z) = \frac{1}{\sqrt{2\pi}\cdot R_a}\cdot\exp\left(-\frac{y^2}{2R_a}\right)$$

$$\mathrm{TIS} = \exp\left[-\left(\frac{4\pi}{\lambda}\cdot R_a\right)^2\right].$$

The EMA is also used here as silver films produced by OAD are highly porous, particularly at a high vapor incident angle. The layer structure consists of silver metal and voids. The Bruggeman model is used in the study:

$$(1-f)\cdot\frac{\varepsilon_{\mathrm{void}} - \varepsilon_{\mathrm{eff}}}{\varepsilon_{\mathrm{void}} + 2\cdot\varepsilon_{\mathrm{eff}}} + f\cdot\frac{\varepsilon_{\mathrm{silver}} - \varepsilon_{\mathrm{eff}}}{\varepsilon_{\mathrm{silver}} + 2\cdot\varepsilon_{\mathrm{eff}}} = 0.$$

Here, $\varepsilon_{\mathrm{void}}$ is 1, $\varepsilon_{\mathrm{eff}}$ is the effective dielectric constant of the silver layer, and f is the fraction of silver in the layer.

Based on above optical models, reflectance data are fitted. Transmittance is not used for optical fitting as it is close to 0 according to the measurement on the samples coated on fused silica substrates. From SEM micrographs, the samples deposited at a vapor incident angle of 0° have the simplest structure and a smooth surface. Thus, the reflectance of these samples can be easily fitted by using a simple optical structure: a single smooth dense silver surface. The reflectance fitting results are shown in figure 4. The fitting parameters obtained for the above optical dispersion model are 4.61 for dielectric background, $\omega_{\mathrm{dp}} = 63\,842\ \mathrm{cm}^{-1}$ and $\tau_d = 486\ \mathrm{cm}^{-1}$ for the Drude model, $\omega_p = 4583\ \mathrm{cm}^{-1}$, $\omega_0 = 27\,227\ \mathrm{cm}^{-1}$ and $\sigma =$

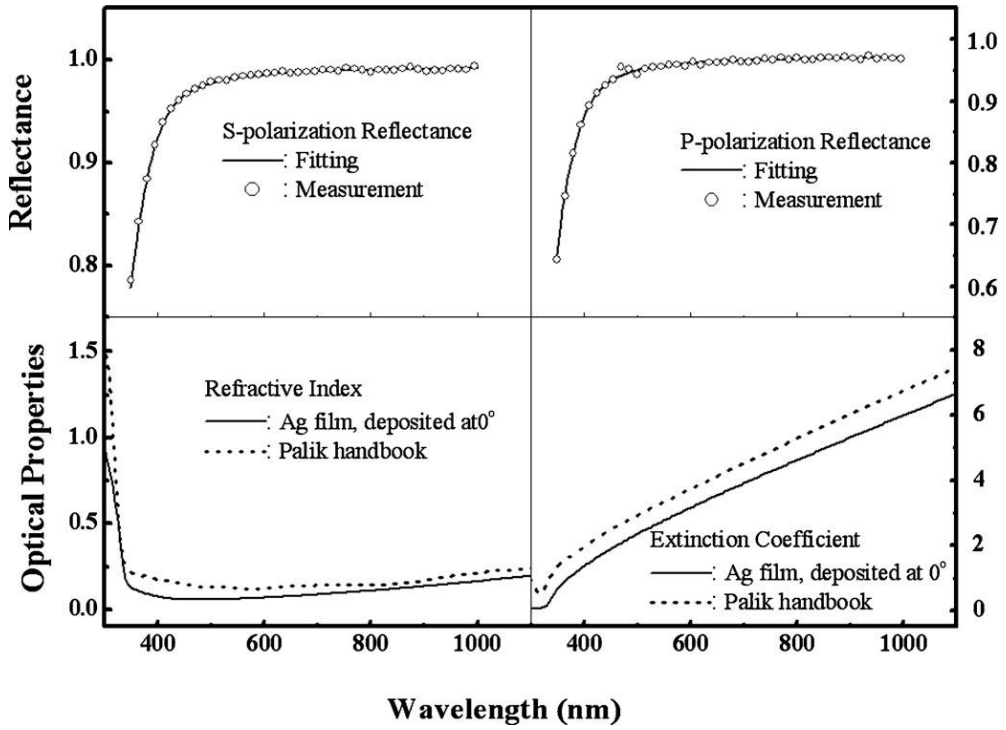

Figure 4. Reflectance of Ag coating deposited at a vapor incident angle of 0° and the fitting results including *n* and *k* data.

51.3 for the Kim oscillator. The fitting refractive index and extinction coefficient are lower than the values from Palik's handbook [17]. This difference originates from the free carrier that is suggested by the optical model. The results also show that the interband transition of the coatings occurs at a similar position given by Palik's handbook.

However, optical fitting for the samples deposited at 45°, 75° and 85° is much more difficult as surface roughness and porosity need to be considered. There is a small change of measured reflectance noted for 45° and 75° deposited silver samples; however, the measured reflectance of the sample deposited at 85° is very different, which shows very high scattering. To simplify calculation for optical fitting, the optical dispersion model obtained from the silver sample deposited at 0° is used for the silver composition of the rest of the samples. As can be seen from the SEM images, the layers have varying porosity depending on depth; thus, we approximate the single layer as a two-layer structure, each layer with uniform density: the top layer is porous and the inner layer is dense. The light scattering model and EMA are used for the top layer. The inner layer has the same optical properties as the samples deposited at 0°. Table 1 gives the properties of the top layer of the samples deposited at high angles. The reflectance data of both S and P polarizations for 45° and 75° deposited samples can be fitted using the same layer structures and optical dispersion model. However, this is not true for the samples deposited at 85° due to their high nanorod array structure; thus, S and P polarized reflectance needs to be analyzed separately. The measurement and fitting results of reflectance are shown in figure 5.

Table 1. The fitting parameters for the samples deposited at high angles.

Vapor incident angle	Silver volume factor	Surface roughness	Top layer thickness
45°	0.995	2.48 nm	8.0 nm
75°	0.963	3.70 nm	16 nm
85° S polarization	0.949	11.5 nm	20 nm
85° P polarization	0.580	12.8 nm	22 nm

3.3. Surface enhanced Raman scattering

As shown in figure 6, Ag films deposited at 0°, 45° and 75° were largely featureless. Only the 85° samples on Si and silica substrates gave strong SERS. Both spectra show typical vibrational modes of BPE that can be assigned as: 1012 cm^{-1}, ring breathing; 1200 cm^{-1}, C=C stretching; 1343 cm^{-1}, in-plane bend of C–H and C=C bonds; 1608 cm^{-1}, aromatic ring stretching; 1638 cm^{-1}, in-plane ring bend mode, respectively. We used the 1200 cm^{-1} mode to characterize the ERS from these substrates. Five individual SERS spectra were acquired from different locations on each substrate. The mean amplitudes of the 1200 cm^{-1} mode were 11 263 counts and 13 547 counts from silicon and silica substrates, respectively. These comparable SERS intensities (less than 10% difference) suggest similar enhancement factors, although the background level from silica substrate was larger. For this observation, it is important to note that the silica sample signal was recorded at 0.1 of the integration time of the silicon sample and was then multiplied by 10 for the comparison of spectra. Also, as a reference, the samples were scanned before application of BPE and these scans were largely featureless.

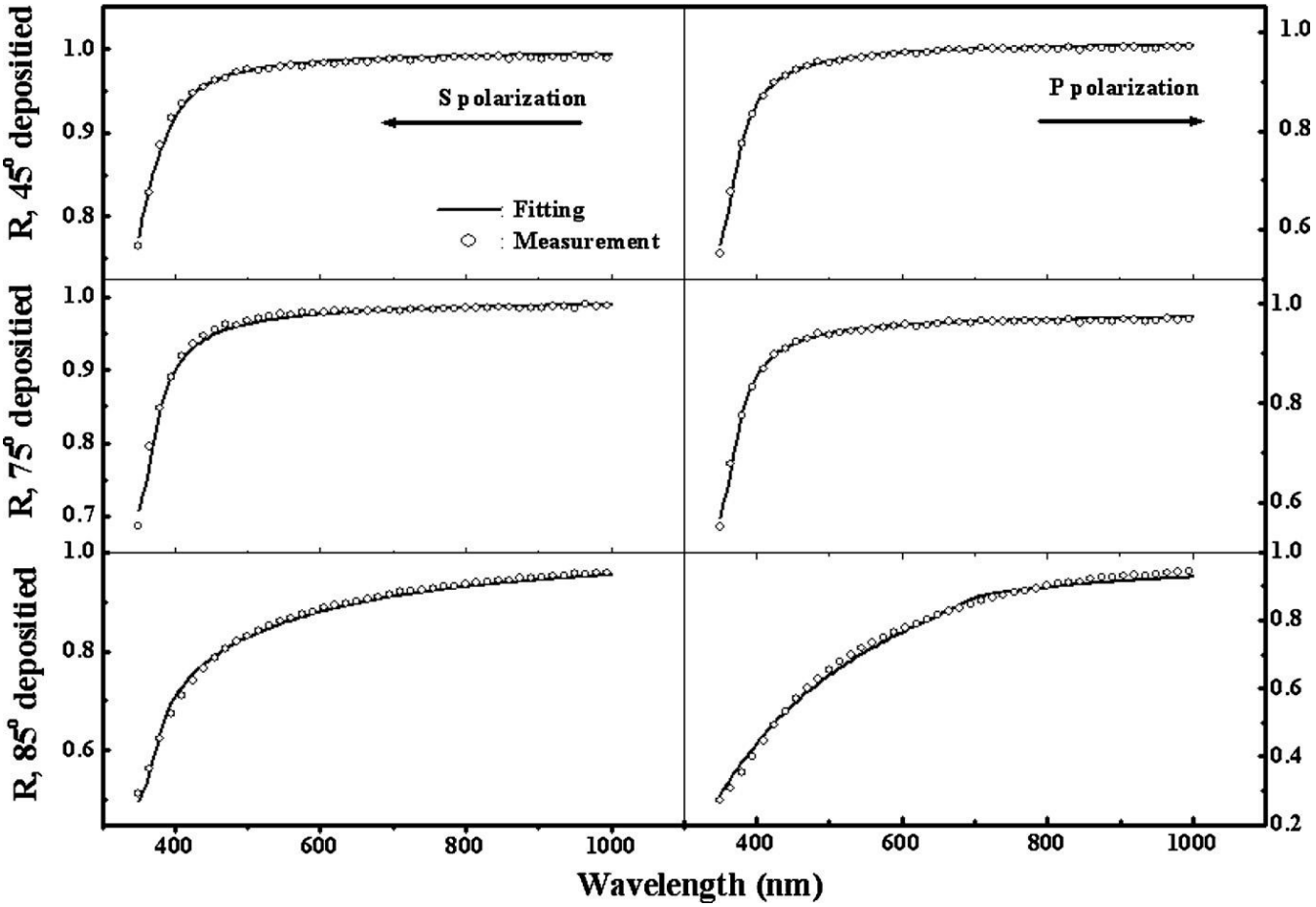

Figure 5. Reflectance of Ag coating deposited at various angles and the fitting results.

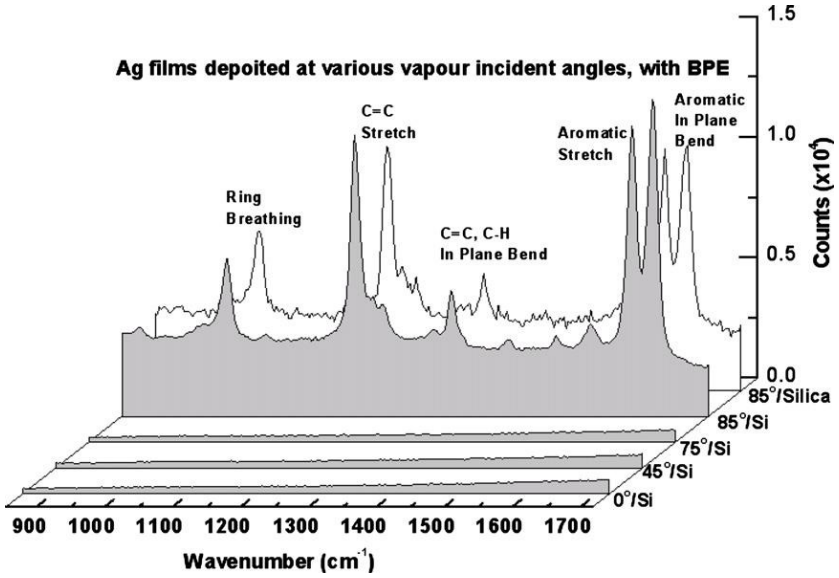

Figure 6. SERS measurements for the Ag coatings deposited at various vapor incident angles.

4. Conclusion

Silver coatings have been deposited on silicon and fused silica substrates at various vapor incident angles using OAD methods. Surfaces become rougher as the vapor incident angle is increased. Only the sample deposited at 85° shows clear oblique column structure and the actual column oblique angle for 85° vapor incident angle is much greater than the calculated

angle obtained by using the tangent rule. This implies that adatom mobility is very high in our experiments. Reflectance data of the samples deposited at 0° can be fitted very well by using a simple optical structure: a single smooth dense silver surface. The fitting refractive index and extinction coefficient are close to the value from Palik's handbook. Reflectance fitting also confirmed the positive relation between roughness and deposition angle and has shown the increase of porosity in the film with increasing deposition angle. The reflectance measurements indicate that the sample deposited at 85° has a very high anisotropic effect due to the inclined column structure (sliver nanorod arrays); this will be discussed in a separate paper. In the RS scans, only the 85° samples on Si and silica substrates gave strong SERS with a similar enhancement factor, with a higher background level and noise signal from the silica substrate. Scans of the other samples were largely featureless.

References

[1] Hartland G V 2011 Optical studies of dynamic in noble metal nanostructures *Chem. Rev.* **111** 3858–87

[2] Mayer K M and Hafner J H 2011 Localized surface plasmon resonance sensors *Chem. Rev.* **111** 3828–57

[3] Giannini V *et al* Plasmonic nanoantennas: fundamentals and their use in controlling the radiative properties of nanoemitters *Chem. Rev.* **111** 3888–912

[4] Jones M *et al* 2011 Templated techniques for the synthesis and assembly of plasmonic nanostructures *Chem. Rev.* **111** 3736–827

[5] Hulteen J and Van Duyne J 1995 Nanosphere lithography: a materials general fabrication process for periodic particle array surfaces *J. Vac. Sci. Technol* A **13** 1553–8

[6] Prikulis J *et al* 2004 Optical spectroscopy of nanometric holes in thin gold films *Nano Lett.* **4** 1003–7

[7] Barlett P, Birkin P and Ghanem M 2000 Electrochemical deposition of macroporous platinum, palladium and cobalt films using polystyrene latex sphere templates *Chem. Commun.* **17** 1671–2

[8] Zhang W, Fischer H, Schmid T, Zenobi R and Martin O 2009 Mode-selective surface-enhanced Raman spectroscopy using nanofabricated plasmonic dipole antennas *J. Phys. Chem.* C **113** 14672–5

[9] Driskell J *et al* 2008 The use of aligned silver nanorod arrays prepared by oblique angle deposition as surface enhanced Raman scattering substrates *J. Phys. Chem.* C **112** 895–901

[10] Liu Y, Chu H and Zhao Y 2010 Silver nanorod array substrates fabricated by oblique angle deposition: morphological, optical, and characterizations *J. Phys. Chem.* C **114** 8176–83

[11] Lakhtakia A and Messier R 2005 *Sculptured Thin Films, Nanoengineered Morphology and Optics* (Bellingham, WA: SPIE Press)

[12] Savaloni H, Babaei F, Song S and Placido F 2011 Influence of substrate rotation speed on the nanostructure of sculptured Cu thin films *Vacuum* **85** 776–81

[13] Savaloni H, Babaei F, Song S and Placido F 2009 Characteristics of sculptured Cu thin films and their optical properties as a function of deposition rate *Appl. Surf. Sci.* **255** 8041–7

[14] Kittel C 1986 *Introduction to Solid State Physics* 6th edn (New York: Wiley)

[15] Kim C *et al* 1992 Modeling the optical dielectric function of semiconductors: extension of the critical-point parabolic-band approximation *Phys. Rev.* B **45** 11749–67

[16] Rakels J 1996 Influence of the surface height distribution on the total integrated scatter (TIS) formula *Nanotechnology* **7** 43–6

[17] Palik E 1985 *Handbook of Optical Constant of Solids* (New York: Academic)